

Study of Polymer Crystalline Structure with (S)TEM imaging

Hui LUO

St. Peter's College

University of Oxford

Supervisors: Prof. Hazel E. Assender, Prof. Peter D. Nellist



A Thesis Submitted for The Degree of Doctor of Philosophy

Department of Materials

Trinity Term 2022

Dedication

To my family

Acknowledgement

First and foremost, I would like to express my sincere gratitude to my supervisors, Prof. Hazel E. Assender and Prof. Peter D. Nellist, for their invaluable advice, support, and patience throughout my PhD study. Throughout my academic research and daily life, their vast knowledge and abundant experience have been an inspiration to me. I would also like to thank my collaborator, Dr Chen Huang, for his high-calibre simulation work. I would also like to thank the members of the research group who provided me with support regarding the microscope. During my first year, Dr Colum O'Leary spent many hours training me on the microscope and ptychography data processing. I received assistance from Dr Alexandra Sheader on EELS. It was fortunate to have Dr Mathias Rothmann share with me his experience of imaging beam sensitive materials at the beginning of my DPhil research. Furthermore, I would like to thank the staff at DCCEM and OMCS: Dr Neil Young from DCCEM trained me on TEM and Dr Nicola Flanagan from OMCS trained me on AFM at the beginning of my DPhil, which enabled me to master the equipment and obtain high quality data as the basis for my DPhil.

Lastly, I would like to express my gratitude to my parents, Mrs. Xiuyan Wei and Mr. Pengyun Luo, who have given me a loving family and all the foundations I need to achieve this goal. They trusted my choices, gave me the freedom to pursue my interests, and offered me full financial and spiritual support. It would have been impossible for me to complete my studies without their tremendous support and encouragement over the past few years. I am grateful for my resilience, which kept me going even during the tough times in COVID lockdown. I feel strong enough to conquer any challenges that may arise in the future. 2022 will be a remarkable year, as it marks the end of my DPhil, but also the beginning of a new chapter in my life.

Disclaimer

I hereby declare that this thesis is my own original work carried out in the Department of Materials, University of Oxford, under the supervision of Prof. Hazel E. Assender and Prof. Peter D. Nellist. No part of this thesis has been submitted to any institution for assessment purposes before.

Further, I have acknowledged all sources used and have cited them in the reference section.

Abstract

The crystallinity of polymers has a significant impact on the material's properties, as polymer solids are usually semi-crystalline in nature. Thus, revealing the local structure through direct (Scanning) Transmission Electron Microscope (S)TEM imaging can greatly enhance our understanding of the material properties. However, there are challenges to obtaining high resolution images of polymers using (S)TEM, including irreversible beam damage and low contrast generated by the light elements. Additionally, low and high spatial frequencies are present in polymer semi-crystalline specimens, which require an advanced imaging techniques to resolve.

In this study, low dose STEM ptychography was used to acquire high resolution images from poly (ethylene 2,6-naphthalate) (PEN) and poly (ethylene terephthalate) (PET). The beam damage was controlled by a low dose condition that ensured the polymer specimen structure was not altered during the data acquisition process, including ptychography and bright-field (BF) STEM imaging. The phase images obtained with single side band (SSB) reconstruction from 4D-STEM dataset have a sufficient level of phase contrast and resolution across a wide range of spatial frequencies.

The critical dose and beam damage of PEN have been studied by tracking the evolution of diffraction intensity versus accumulated dose as part of the development of imaging methodologies. A decay model was constructed with the intention of interpreting the correlation of 'diffraction intensity versus dose' as a latency followed by an exponential decay. The critical dose was determined as $(D_o + D_c)$; where D_o is a "latent dose" from where the exponential decay started, and D_c is the dose at which the intensity had decayed to $1/e$ of the intensity at the start of the exponential decay. The critical dose calculated based on the decay model was

in the range of 700-1000 e/Å², which was relatively high compared to empirical data of organic materials.

The images acquired from semi-crystalline PEN thin film revealed the local molecular conformation of the crystalline structure, and the discrepancy of local structure against the average structure derived from conventional diffraction methods, e.g., XRD, electron diffraction, can be identified. For example, a periodic feature was resolved between planes (2 0 0), and this feature was only observed in experimental images. The periodicity of the feature between strong layers (2 0 0) was identical to the periodicity of a plane within (2 0 0), while the half-spacing of this plane was absent in the experimental image but resolved in the simulated image. Thus, the chemical structure related to the absent half-spacing plane in the experimental image is likely to be the source of the structural discrepancy. A possible explanation for this discrepancy is the rotation of some molecular segments, e.g. the oxygen atoms connected to aliphatic carbons. These discrepancies indicate distinct local structures in comparison to the structure predicted by the model based on XRD data, which implies a modified model. In light of the discrepancy between experimental and simulated ptychography phase images, it was possible to identify the chemical structure from which it may have originated.

In a semi-crystalline PEN or PET thin film specimen with a thickness of around 50nm, multiple grains of varying sizes are dispersed in the film at different depths. The optical sectioning technique with electron as illumination can not only resolve the crystalline structure at different depths, but also reveal the relative orientation of the grains. With optical sectioning, it was discovered that Moiré fringes can be formed by stacking lattices from different domains or by twisting internal lattices within one grain. The depth profiles of PEN specimens indicate that polymer crystalline lattices will tend to bend or twist, which is likely due to the relatively weak intermolecular interactions.

Using established STEM ptychography and optical sectioning techniques, images of PET semi-crystalline specimens revealed new structures. In addition to the fully crystalline 'ordered' structure, a new type of 'partially-ordered' structure, distinct from either crystalline or amorphous, was discovered for the first time. In the partially-ordered regions, there are clear 'peaks' implying a molecular backbone aligned to the viewing direction for 20-30nm, with random short-range periodicity in the lateral dimension, which is in some respects reminiscent of a 'liquid crystal' structure. The 'peaks' could be molecules aligned to the viewing direction, and the peak-to-peak distance might represent intermolecular distance. Theoretically, the intermolecular distance obtained from the close-packed van de Waals radius of atoms should be the smallest distance, and the intermolecular distance should be the smallest in the crystalline state. Across all partially-ordered features from multiple images, the average peak-to-peak distance is consistently much smaller but not far from half of the intermolecular distance in the crystalline model. Assuming the molecules of the partially-ordered feature are aligned with the viewing direction, there may be rotational symmetry along the molecular axis, and the atoms in the side groups may stack and form the peaks.

The ordered features in PET images can be either crystalline or non-crystalline structure depending on their connection with the partially-ordered features. PET models constructed from empirical diffraction data can be used to interpret part of the crystalline structures in the ordered region, particularly the grains in images without partially-ordered features. These ordered features should be crystalline in nature. However, some ordered structures in images containing partially-ordered features show considerable discrepancies with the model, which indicates a significant structural difference with the presence of these partially-ordered features. It appears that these ordered features are a form of more tightly packed molecules of the partially ordered features. This suggests that these ordered features might be in a 'pre-crystalline' state, and together with the junctional partially-ordered feature, a "snapshot" of the

transition status has been obtained. Therefore, PET images involving partially-ordered features might reveal pre-order of molecules before crystallization, and there may be rotational symmetry along the molecular axis. The development of a new model could provide evidence and contribute to the understanding of polymer crystallization mechanisms.

List of Initials and Acronyms

ADF	Annular Dark Field
AFM	atomic force microscope
BF	Bright Field
C_1	defocus value
CBED	convergent-beam electron diffraction
CCD	charge coupled device
CFEG	Cold field emission gun
CTF	contrast transfer function
DCCEM	David Cockayne Centre for Electron Microscopy
DOF	Depth of Field
DP	diffraction pattern
DPC	Differential phase contrast
ED	electron diffraction
FEG	Field emission gun
FT	Fourier Transform
HAADF	High Angle Annular Dark Field
LAADF	Low Angle Annular Dark Field
MAADF	Middle Angle Annular Dark Field
OMCS	Oxford Materials Characterisation Service
PEN	poly (ethylene 2,6-naphthalate)
PET	poly (ethylene terephthalate)
SSB	single side band
STEM	scanning transmission electron microscope

TEM	transmission electron microscope
WDD	Wigner-distribution deconvolution
WPO	weak phase object
XRD	X-ray diffraction

Table of Contents

Dedication	II
Acknowledgement	III
Disclaimer	IV
Abstract	V
List of Abbreviation	IX
Table of Contents	XI
1 Novelty and significance of this thesis	1.1
1.1 Scope of the thesis	1.1
1.2 Imaging beam sensitive and light element material with ptychography	1.2
1.3 Novelty in the methodology established	1.3
1.3.1 Polymer Sample preparation methodology for (S)TEM	1.3
1.3.2 Suitable microscope condition for image acquisition	1.4
1.3.3 Structure analysis with high resolution images of polymer	1.4
2 Literature review	2.6
2.1 Crystallinity of Semi-crystalline polymers	2.6
2.2 Materials of interest	2.6
2.3 State-of-the-art study on crystalline structure of PEN and PET	2.7
2.3.1 Previous studies on PEN crystalline structure	2.7
2.3.2 Crystalline structure of PET	2.12
2.4 Development of EM technique for polymers – the limitations and challenges	2.16
2.4.1 Polymer specimen for (S)TEM preparation methods	2.16
2.4.2 Electron beam damage	2.20
2.5 Principle of (S)TEM imaging and contrast enhancement for polymers	2.32
2.5.1 TEM imaging and phase contrast	2.32
2.5.2 STEM imaging	2.51
2.5.3 STEM ptychography	2.55
2.6 Summary and goal of thesis	2.61
3 Experimental method	3.63
3.1 Sample preparation method development	3.63
3.1.1 New sample preparation method is needed	3.63
3.1.2 Procedure of sample preparation method development	3.64

3.1.3	Advantages of the new sample-preparation method	3.70
3.2	(S)TEM illumination dosage quantification	3.71
3.2.1	Microscope parameters of low-dose condition.....	3.72
3.2.2	Methodology development for <i>in situ</i> dose estimation.....	3.75
3.2.3	Dose quantification in data acquisition experiments	3.80
3.5	(S)TEM imaging microscope setup.....	3.86
3.5.1	4D-STEM data acquisition	3.87
3.5.2	STEM Imaging mode classification based on scattering angle β	3.90
3.6	STEM imaging of PEN, PET with low-dose condition.....	3.92
3.7	STEM ptychography images of polymer	3.94
3.7.1	Single side band (SSB) reconstruction	3.94
3.7.2	Ptychography phase image of polymer.....	3.95
3.5.3	Optical sectioning applied to polymer semi-crystalline thin film	3.97
4	Beam damage study and Critical dose measurement.....	4.100
4.1	Acquisition of time-resolved diffraction patterns from PEN.....	4.100
4.1.1	Microscope setup for low dose condition.....	4.100
4.1.2	Time-resolved electron diffraction patterns acquisition	4.101
4.2	Connect the signal of diffraction planes with exposure time.....	4.101
4.2.1	Quantify the intensity of planes from the DPs	4.101
4.2.2	Time-resolved evolution of DP	4.104
4.3	Damage model construction	4.105
4.3.1	Intensity evolution analysis – model fitting	4.105
4.3.2	Critical dose determined from the decay model	4.107
4.4	Conclusion	4.110
5	Imaging the structure of PEN crystallinity with STEM ptychography.....	5.112
5.1	Images obtained from PEN – a beam sensitive and light element material.....	5.112
5.1.1	Dosage used in PEN image acquisition.....	5.112
5.1.2	Data recording and processing	5.115
5.1.3	Image pixel size calibration	5.116
5.2	Image analysis method development with ptychography data from PEN	5.117
5.2.1	PEN crystal model information	5.117
5.2.2	Measurements of crystalline planes and indexing.....	5.117
5.2.3	PEN crystalline structure investigation with ptychography image.....	5.119

5.2.4	Crystalline structure analysed with ptychography image revealed discrepancy compared to diffraction data	5.128
5.3	Conclusion	5.135
6	Analysis of features dispersed in 3D with 2D images	6.137
6.1	Spatial relation of multiple grains distributing in three dimensions	6.137
6.2	Resolve lattices forming Moiré fringes	6.141
6.2.1	Moiré fringes formed by stacked lattices	6.141
6.2.2	Moiré fringes formed by local plane twisting within one grain	6.143
6.3	Partial plane tilting/defect within one grain measured along the viewing direction	6.146
6.3.1	Identify local plane tilting within one grain	6.146
6.3.2	Local small range defect within a grain	6.150
6.4	Resolve imperfectly aligned planes	6.153
6.5	Conclusion	6.156
7	Structural analysis of semi-crystalline PET with STEM ptychography	7.157
7.1	Models selected for PET structure analysis	7.157
7.1.1	Crystalline structure of PET	7.157
7.1.2	Periodic non-crystalline and pre-crystalline structures in polymer	7.158
7.2	Analysis of PET crystalline feature	7.160
7.2.1	One large crystalline dominant in the image	7.160
7.2.2	Two crystals with grain boundary in between	7.161
7.2.3	Two grains with overlap region	7.167
7.3	Analysis of 'partially-ordered' region in PET semi-crystalline thin film	7.171
7.1.2	Image involving ordered and partially-ordered structures	7.172
7.1.4	Random mixture of ordered and partially-ordered features	7.177
7.4	Discussion about the newly found disordered feature in PET images	7.183
7.4.1	Summary of distances of partially-ordered features	7.183
7.4.2	Intermolecular distance measured from crystalline model	7.184
7.5	Conclusion of PET images analysis	7.185
8	Conclusions and future work	8.187
8.1	Contribution to the field	8.187
8.1.1	New experimental methodology	8.187
8.1.2	New science	8.188
8.2	Future work and potential application	8.189

8.2.1	Future work suggestions	8.189
8.2.2	Potential application proposal.....	8.189
Reference	191

1 Novelty and significance of this thesis

1.1 Scope of the thesis

Polymer solids are often semi-crystalline, and their crystallinity has a significant bearing on their properties. Understanding the local structure of a material can greatly enhance our understanding of its properties. X-ray diffraction has traditionally been used to determine the phase and cell parameters of polymer crystals, but its use in characterizing polymer molecular conformations in crystals has two problems: i. XRD requires a specimen that is micrometre thick to generate a signal, as this contains many crystals in the characterized region, only averaged information can be gathered; ii. The signals generated by local sub-molecular chemical segment rotations would not be captured by XRD, as they are either beyond the resolution limit or the difference in scattered intensity is too low to noticeably affect the diffraction pattern.

An XRD diffraction – Linked-Atom Least-Squares approach provides a framework for refinement of models and compares competing models using statistical tests¹; a preliminary model can be obtained and then be refined. However, this process provides no assurance of a unique solution, because the phase problem and the issue of arbitration remains. Fibrous structures are usually made up of linear polymers with helical conformations – the extensive symmetry in helical molecules makes the asymmetric molecular unit commonly as small as one nucleotide. The Linked-Atom Least-Squares approach shares the idea of other structure analysis methods – comparing the experimental data against refined simulated data to understand the characterized structure. The technique of electron ptychographic imaging used in this thesis overcomes these deficiencies by: ① directly revealing the local atomic structure; ② solving the phase problem in diffraction methods.

High resolution imaging is the suitable approach to resolve the local structure. In this study, of poly (ethylene 2,6-naphthalate) (PEN) and poly (ethylene terephthalate) (PET) are examined. Their molecules are long chains with complex chemical structures - naphthalate and benzene rings - making it challenging to resolve the atoms. Unlike the atomic structure of metals and ceramics, the arrangement of atoms in polymers contains superpositions of complex chemical structures viewed from all perspectives. The rotation of sub-molecular chemical units would induce subtle changes in intensity in the diffraction patterns acquired with X-rays or TEM, so typically it is not possible to determine the details of the structure directly from this. Therefore, a valid imaging technique that can directly resolve local structure is necessary to better understand local polymer crystalline structure.

1.2 Imaging beam sensitive and light element material with ptychography

Scanning transmission electron microscopy (STEM) offers atomic resolution for thin specimens², making it a suitable method for imaging polymer crystallinity. However, polymers are composed of light elements (C, H, O) resulting in low contrast in STEM. On the other hand, polymer specimens will be damaged in an electron beam predominantly due to radiolysis³. Therefore, if the illumination dose is increased to achieve sufficient contrast for a high-resolution imaging from such specimens, irreversible damage will occur.

Ptychography^{2,4} imaging technique uses phase contrast for imaging and is a dose efficient imaging technique with a high resolution enhancement capability. In STEM imaging, the polymer is treated as a weak phase object (WPO), as the amplitude is assumed to be constant when electrons are transmitted. The 4D STEM dataset acquired in ptychography technique can be used to obtain the depth profile (defocus series) of a specimen with only one scan. Therefore, the dose required in STEM ptychography can be controlled to acquire data before

the structure was damaged, in order to acquire data before the crystal structure has been altered by the electron beam.

Using low-dose STEM ptychography, a method for acquiring high-resolution phase images of PEN and PET crystallinity will be demonstrated in this study. The highest contrast achieved from polymers so far allows the local molecular conformation within the crystal in a polymer semi-crystalline thin film to be analysed.

1.3 Novelty in the methodology established

This thesis presents the methodology for preparing samples, the microscope conditions for acquiring data, and analyses data to reveal structural information from semi-crystalline polymer thin films.

1.3.1 Polymer Sample preparation methodology for (S)TEM

Conventional methods can only produce specimens of borderline quality. Typically, thin film specimens are prepared by dropping dilute solutions of polymer onto an anti-solvent, usually water. The thickness is not uniform and is relatively random, and the amount of material is not sufficient to provide much structural information, e.g., in electron diffraction patterns.

An effective method for preparing polymer thin film specimens has been developed in this study. Using spin-casting, polymer thin films were fabricated on a water-soluble substrate; therefore, the thickness of the films can be controlled, and the features of the specimen can be preserved while being transferred to a TEM grid. As a result of the low thickness (<100nm), the different domains of semi-crystal material can be distributed along lateral dimensions, thereby facilitating the imaging of multiple domains in (S)TEM.

1.3.2 Suitable microscope condition for image acquisition

The imaging of beam sensitive materials at room temperature requires a low dose technique accompanied by a high-speed and sensitive camera. The quantification of beam damage to the sample material can be used to guide the selection of microscope parameters for imaging.

A model of intensity degradation correlated to accumulated dose was constructed by recording time-resolved electron diffraction patterns of PEN thin film specimens. In TEM diffraction mode, the dose window applicable to image PEN was estimated based on the critical dose measurement. However, polymer samples were found to tolerate higher doses before being damaged in STEM than in TEM. For imaging materials containing light elements, phase imaging is more efficient⁵, and ptychography is a dose-efficient imaging technique with phase retrieval capabilities. Therefore, high-resolution images were acquired using STEM ptychography under low-dose conditions.

1.3.3 Structure analysis with high resolution images of polymer

PEN and PET have multiple crystalline forms or cell parameters, and they are usually semi-crystalline in nature. The local orientation of each specific domain in semi-crystalline polymers cannot be determined by conventional diffraction methods, such as X-ray and electron diffraction.

The high-resolution phase images of PEN and PET crystallinity were successfully acquired with low dose STEM ptychography, which enabled the identification of various crystalline structures, including crystalline forms and types of symmetry in unit cells. The phase images of PEN and PET has the highest contrast achieved so far for polymers, and the local orientation of specific grains in polycrystals and semi-crystals can be determined. The results of this study

are immensely helpful to reveal molecular packing in crystalline domains, and potentially to investigate the effect of grain boundaries and amorphous domains on the properties of heterogeneous materials.

During the interpretation of crystalline structures in my images, empirical data obtained through diffraction techniques and models derived from the corresponding diffraction data are used as references. The discrepancy between the ptychography images and the model suggests a local structural difference from that proposed in the models that did not measurably alter the diffraction pattern. The high-resolution imaging technique allows for the capture of local molecular conformations in polymer crystallinity, thereby allowing the confirmation or correction of crystal models for polymer materials.

2 Literature review

This chapter will review the state-of-the-art knowledge regarding polymer crystallinity and the imaging methodologies. In order to achieve high-resolution images of polymer crystallinity, the improvement needed, and the methodology development required to overcome challenges will be discussed.

2.1 Crystallinity of Semi-crystalline polymers

Polymers with linear molecular structure are capable of crystallizing⁶, as the molecules require a certain level of flexibility to "pack" into a specific pattern with long-range periodicity. The steric hinderance of molecules with large side groups or branches makes it difficult for them to form into periodic structures. The flexibility of a molecular chain also determines the form of crystalline structure, e.g., symmetry, type of helix in the *c*-axis.

The amount of crystallinity in a material is also affected by the thermal history of the material during the fabrication process. Nucleation is regarded as a random process, and can result in a spread of orientation of the crystals.

2.2 Materials of interest

Polyethylene terephthalate (PET) is a general-purpose thermoplastic polymer which belongs to the polyester family of polymers. Polyester resins are known for their excellent combination of mechanical, thermal, chemical, and dimensional stability properties.

PEN is a heat-resistant version of PET with a higher glass transition temperature (T_g) but a similar melting temperature (T_m). The study of the semi-crystalline structure of PET and PEN

can contribute to a deeper understanding of the structure and its relationship to the material properties.

2.3 State-of-the-art study on crystalline structure of PEN and PET

PEN and PET have been reported to have various forms of crystalline structure. Numerous studies have been conducted to characterize the crystalline structure and understand the mechanism of its formation at the molecular level.

2.3.1 Previous studies on PEN crystalline structure

The first type of PEN crystalline structure, labelled as α -form, was the one-chain triclinic structure, which was determined by Mencik⁷ through crystallization at low temperatures (<200°C) from the unoriented glass or from the melt. Buchner *et al.*⁸ described another four-chain triclinic cell structure referred to as the β -form in their seminal paper on the kinetics of crystallization and melting of PEN. Buchner's results obtained by in-situ crystallization studies under synchrotron XRD (Figure 2.1) and differential scanning calorimetry (DSC) indicated that for samples crystallized at temperatures above 200°C, α -form is observed from a 210°C anneal, while β -form is observed from 240°C annealing. The unit cell parameters of β -form were reported, but the molecular packing in the triclinic cell was not proposed.

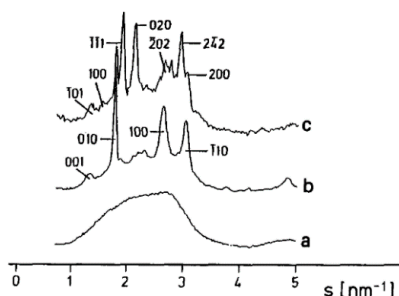


Figure 2.1 Wide angle X-ray scattering of PEN⁸. a. Sample quenched from 290°C in ice-water, amorphous; b. sample quenched as in a and then crystallized for 2h at 210°C, α -modification; c. sample crystallized from the melt for 45min at 240°C, mainly β -modification.

Liu *et al.*⁹ obtained single-crystal electron DPs and proposed models for the molecular packing in both α - and β -form unit cells. The α -form was essentially the same as that determined by Mencik⁷, while the β -form was a monoclinic four-chain unit cell. In α - and β -form unit cells, successive naphthalene units along a molecule are nearly coplanar, but the conformation of the ethylene-carboxyl links varies considerably. In the α -form, the plane of the O-C-C-O bonds is nearly parallel to the plane of the naphthalene rings, whereas in the β -form it is nearly perpendicular (Figure 2.3), while the length of the c -axis is about the same. Liu also found a new crystalline modification as γ -form but had not determined its structure, as they found the study of α - and β -form was more relevant to practical concerns.

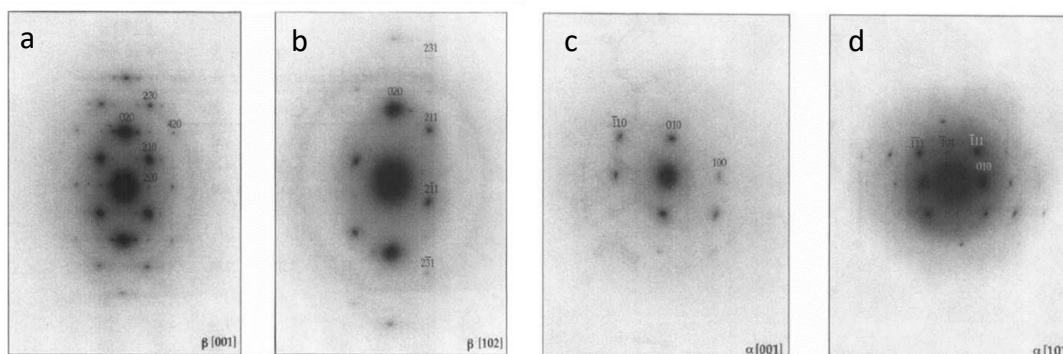


Figure 2.2 ED patterns from the PEN single crystal samples. (a) [001]; (b) $[\bar{1}02]$ are attributed to the β -form. (c) [001]; (d) [101] are attributed to α -form crystal structure.⁹

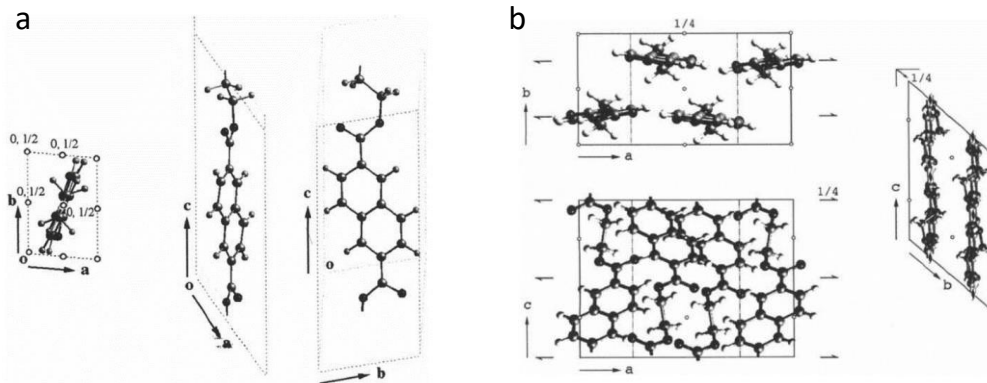


Figure 2.3 (a) Proposed model of the α -form unit cell; this model closely resembles that proposed by Mencik⁷; (b) proposed model of the β -form unit cell. The space group of α and β are P_1 and $P2_1/n 1 1$, respectively.

Heuvel *et al.*¹⁰ proposed explanations for the different origins of crystalline forms caused by molecular conformation by examining the molecular structure of PEN and PET fibres. They found that rotation of the naphthalene ring would induce $\alpha \rightleftharpoons \beta$ and *cis* \rightleftharpoons *trans* conformational transitions in the amorphous domain of PEN yarns. According to their findings, there are two *trans* configurations of the naphthalene ring due to the absence of a twofold rotation axis through the $C_{aliphatic} - C_{aromatic}$ bonds of the ring system, and the PEN molecular conformation can be distinguished by the number of hydrogen atoms at the aromatic ring adjacent to the carbonyl oxygen atom, as shown in Figure 2.5, with one hydrogen atom in the *trans* α -conformation (Figure 2.5a) and two hydrogen atoms in the *trans* β -conformation (Figure 2.5b). Monomer units containing the α -conformation are almost 5% longer than those with more sinusoidal β -conformation (unit lengths of 13.2 and 12.6 Å, respectively).

Heuvel's PEN α -form crystal structure model also matches that described by Mencik⁷, in that the polymer molecules display the α -conformation (Figure 2.6a). This PEN α -form crystal

structure is similar to that of PET (Figure 2.6c) in terms of the extended all-*trans* conformation of the chains and the triclinic one chain unit cell.

The structure of the β -form was determined by Heuvel *et al.*¹⁰ as a monoclinic four chain unit cell with space group $P2_1/a$ and unit cell parameters listed in Table 2.1, using diffraction data from PEN fibres (Figure 2.4). Figure 2.6b illustrates the structure of the polymer chains, which exhibit a sinusoidal conformation. In spite of the fact that the unit cell parameters do not differ much from Liu's results (Table 2.1), Heuvel *et al.* reported a new space group and a different packing of molecules in the unit cell. Also, they noted that the reported PEN β -form structure not only explained their own fibre diffraction pattern in Figure 2.4, but also explained the PEN- β ED patterns obtained by Liu *et al.*⁹. This can be verified by comparing the electron diffraction pattern simulated on the model reported in their work, with the electron diffraction pattern in Figure 2.2 of Liu's work.

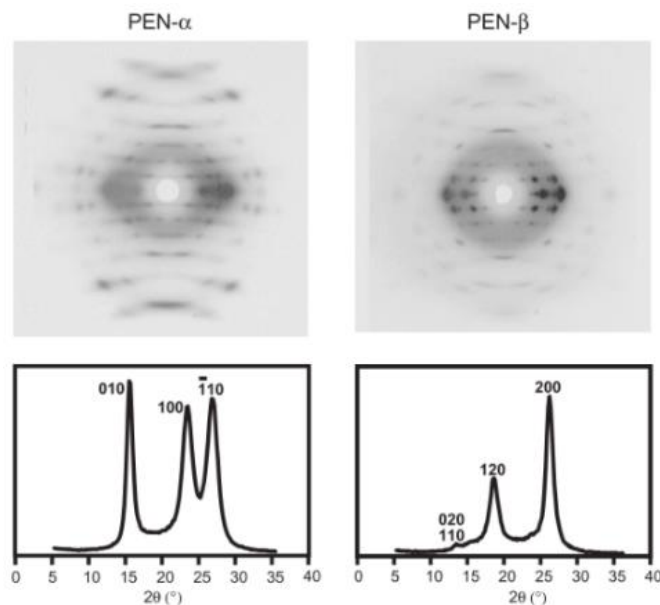


Figure 2.4 Flat plate diffraction patterns (top) and equatorial scans (bottom) of semi-crystalline PEN yarns.¹⁰

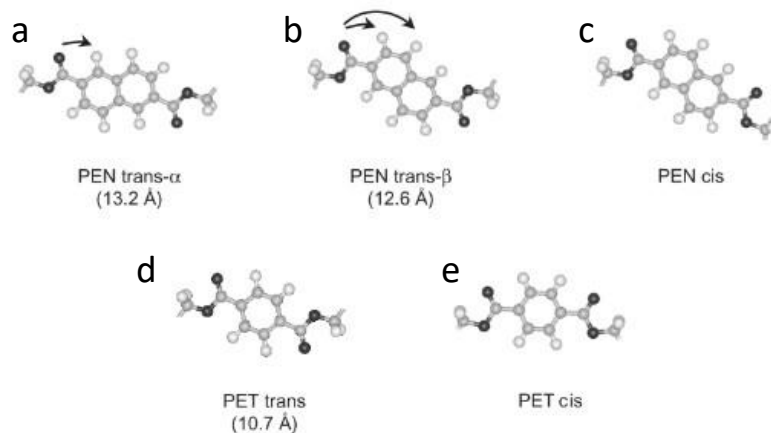


Figure 2.5 Conformation of aromatic rings in PEN and PET. (a) – (b) The two *trans* formations of the naphthalene ring. (c) - (e) The aromatic ring system in both PEN and PET has only one *cis* –conformation.

Table 2.1 Cell parameters of PEN crystal structures

Type	Crystal system	Space group	Unit cell axis (Å)			Unit cell angles (°)			Theoretical crystal density (g/cm ³)	Ref.
			a	b	c*	α	β	γ		
α-form	triclinic	$P\bar{1}$	6.51	5.75	13.20	81.33	144	100	1.407	Mencik ⁷
α-form	triclinic	$P\bar{1}$	6.51	5.62	13.23	81.27	144.59	100.16	1.458	Liu <i>et al.</i> ⁹
β-form	triclinic	$P\bar{1}$	9.26	15.59	12.73	121.6	95.57	122.52	1.439	Buchner <i>et al.</i> ⁸
β-form	monoclinic	$P2_1/n$ 1 1	13.04	9.26	13.00	131.47	90	90	1.368	Liu <i>et al.</i> ⁹
β-form	monoclinic	$P2_1/a$	9.49	13.31	12.61	90	135	90	1.425	Heuvel <i>et al.</i> ¹⁰
β-form	monoclinic	$P2_1/n$ 1 1	13.20	9.62	13.00	131.50	90	90	\	Plummer <i>et al.</i> ¹¹

NOTE: * is molecular chain axis

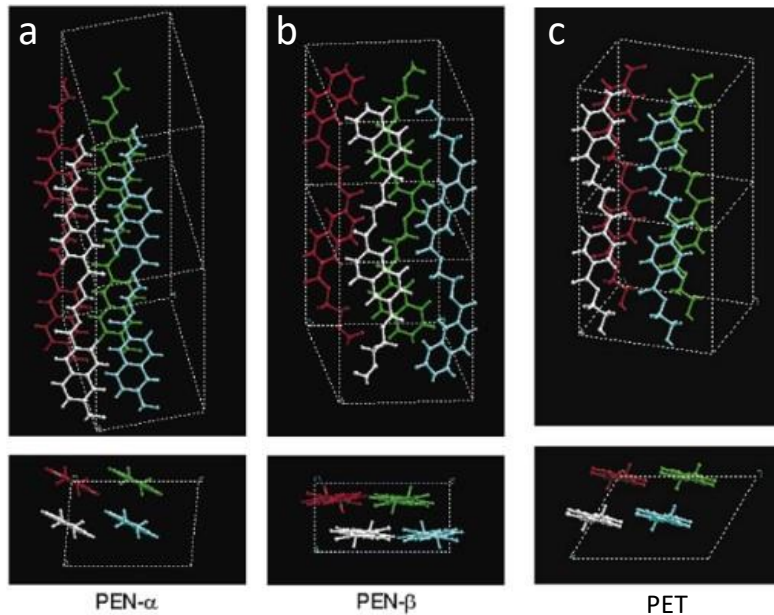


Figure 2.6 (a) Crystal structure of α -form. The structure has extended chains with one chain per unit cell. Crystallographic data: triclinic, $P_{\bar{1}}$, $a=6.51$, $b=5.75$, $c=13.2$ Å, $\alpha=81$, $\beta=144$, $\gamma=100^\circ$, $\rho_c=1.407$ g/cm³. The a and b -axes are drawn twice as large for easy comparison with PEN- β . (b) Crystal structure of β -form. The structure has sinusoidal chains with four chains per unit cell. Crystallographic data: monoclinic, $P12_1/a1$, $a=9.49$, $b=13.31$, $c=12.61$ Å, $\alpha=90$, $\beta=135$, $\gamma=90^\circ$, $\rho_c=1.425$ g/cm³. (c) Crystal structure of PET. The structure has extended chains with one chain per unit cell. Crystallographic data: triclinic, $P_{\bar{1}}$, $a=4.49$, $b=5.88$, $c=10.72$ Å, $\alpha=100$, $\beta=118$, $\gamma=111^\circ$, $\rho_c=1.500$ g/cm³. The a and b -axes are drawn twice as large for easy comparison with PEN- β .

2.3.2 Crystalline structure of PET

The crystalline structure and morphology of poly (ethylene terephthalate) (PET), one of the most important polyesters widely used in electronics and packaging, have been extensively studied for half a century. Among these reports, a few of the most pertinent are considered here.

The PET crystalline structure was found to be a triclinic one chain unit cell (Figure 2.6c) with a variety of cell parameters (Table 2.2), which would be affected by the sample preparation method and the thermal history. The different sets of unit cell parameters listed in Table 2.2 indicate that the unit cell of PET is not as well defined as that of many low molecular weight materials; the effect of these variations can be most readily observed in the ρ_c values listed.

The variation in unit cell parameters can be attributed, at least in part, to variations in sample history.

Astbury and Brown¹² reported the first unit cell dimensions of PET crystals, measured from X-ray fibre diffraction photographs. Daubeny and Bunn¹³ proposed another, now considered the conventional unit cell for PET, based on better oriented specimens, where the chain conformation and atomic positions within the crystals were determined from X-ray reflections.

The unit cell parameters of PET crystals are reported to vary with crystallization temperature, draw ratio, and subsequent annealing temperature and time. For example, using X-ray diffraction, Fakirov *et al.*¹⁴ rechecked the unit cell dimensions from drawn samples annealed at various temperatures between 120°C and 260°C; they suggested another set of unit cell parameters with a higher calculated density ρ_c (1.515 g/cm³). Kitano *et al.*¹⁵ reported a "highly crystalline PET" sample obtained by annealing stepwise under vacuum up to 290°C for a period of 2 years after direct esterification using X-ray diffraction. Their diffraction patterns all showed arced reflections, suggesting that their "highly crystalline PET" samples were still far from being a "perfect" single crystal, despite the extended annealing treatment at high temperatures.

Fakirov *et al.*¹⁴ have shown that the d-spacing varies with crystallization temperature between 100 and 260°C. Crystallized at 100°C, the (010), (100), and (011) spacings are larger than those for samples crystallized at higher temperatures. The calculated ρ_c for 100°C and 250°C crystallized PET samples are 1.484 g/cm³ and 1.515 g/cm³, respectively.

Sun *et al.*¹⁶ have reported the unit cell parameters of stress-induced PET crystal in extrudates as a function of extrusion draw ratio, that is, the higher the extrusion draw ratio, the larger the *c* value, the shorter the *a* and *b* values, and the smaller the unit cell volume would be. The density values reported by Sun are considerably lower than those reported by others, and the *c* dimension is nearly 10% larger than that in Bunn's cell for the highest elongation.

Zhang *et al.*¹⁷ published a paper of particular interest with regard to the relationship between internal stress and unit cell parameters in PET fibres, which reported a crystal density of 1.31 g/cm³ could increase to 1.53 g/cm³, when increasing annealing temperature and time for a PET fibre spun at high speed, as shown in Table 2.2.

Fu *et al.*^{18,19} conducted a comprehensive study of PET fibre crystallites using full-pattern fibre X-ray diffraction refinement and found that both the structure and morphology were affected by the heat and tension treatments. Based on PET4 as the basic fibre, they annealed it with fixed fibre ends to obtain PET4A or under tension to obtain PET4B, then determined the cell dimensions (Table 2.2) and built models for each crystalline form.

Tomashpolskii and Markova²⁰ used electron diffraction (ED) to obtain patterns from solution-cast PET films that had been stretched 700% and subsequently heated at 180°C; they proposed similar but slightly different cell parameters. Wakelyn²¹ found that fibres and films have different (100) and (010) spacings; he suggested that Tomashpolskii and Markova's cell²⁰ is applicable to PET films, and Daubeny and Bunn's cell¹³ to PET fibres.

It is evident that there are no universally valid unit cell parameters for PET crystals prepared by different procedures, e.g., fibres and films; the differences are beyond the scope of experimental error. The internal strain induced during the manufacturing of PET fibres and films can affect the dimensions of the unit cell, and the PET crystals in many (perhaps all) of the samples cannot be in an equilibrium state. Thus, it would be of interest to know the crystal structure and morphology of a "perfect" PET single crystal under equilibrium conditions. Comparing a specific PET crystal structure with the "perfect" PET unit cell might allow one to estimate how much deformation or residual internal stress has been introduced by a specific manufacturing procedure.

Yuhiko²² prepared PET single crystals from dilute solution by slowly evaporating the solvent at a constant crystallization temperature. However, only five independent reflections were observed in a [101] ED pattern from the single crystals, which is insufficient to determine the six parameters of the triclinic PET unit cell.

Liu *et al.*²³ prepared the PET single crystals by confined thin film melt polymerization (CTFMP) method. These single crystals show about 60 (18 independent) reflections in a [001] ED pattern, and nearly 20 (7 additional independent reflections) reflections in a [101] pattern. The information is sufficient to determine the unit cell parameters of the PET single crystal. The crystal structure, including molecular conformation, atomic positions, chain packing, and lattice symmetry, was determined.

Table 2.2 Unit cell parameters of PET crystals

Crystal system	Space group	Unit cell axis (Å)			Unit cell angles (°)			Theoretical crystal density (g/cm ³)	Sample type	Ref.
		a	b	c*	A	β	γ			
triclinic	$P_{\bar{1}}$	5.54	4.14	10.86	107.5	112.2	92.23	1.471	Fibre	Astbury, Brown ¹²
triclinic	$P_{\bar{1}}$	4.56	5.94	10.75	98.5	118	112	1.455	Fibre	Daubeny, Bunn ¹³
triclinic	$P_{\bar{1}}$	4.52	5.98	10.77	101	118	111	1.479	Film	Tomashpolskii, Markova ²⁰
triclinic	$P_{\bar{1}}$	4.48	5.85	10.75	99.5	118.4	111.3	1.515	Fibre	Fakirov et al. ¹⁴
triclinic	$P_{\bar{1}}$	4.50	5.90	10.76	100.3	118.6	110.8	1.501	Fibre	Kitano et al. ¹⁵
triclinic	$P_{\bar{1}}$	4.46	6.06	11.29	99.5	114.5	111.9	1.338	Fibre	Sun et al. ¹⁶
		4.46	5.89	11.31	98.5	113.7	112.0	1.351		
		4.42	5.93	11.43	98.6	114.6	112.7	1.367		
		4.48	5.98	11.38	99.0	114.0	114.0	1.33		
		4.43	5.93	11.45	99.8	113.8	113.8	1.35		
		4.37	5.87	11.57	100.1	113.4	111.4	1.357		
triclinic	$P_{\bar{1}}$	4.81	6.14	11.10	99.2	118.7	111.7	1.312	Fibre	Zhang et al. ¹⁷
		4.77	6.08	10.95	97.6	119.2	112.3	1.353		
		4.68	5.92	10.79	95.1	119.3	113.1	1.421		
		4.64	5.90	10.70	94.2	119.5	113.7	1.454		
		4.64	5.87	10.63	93.9	119.6	113.9	1.473		

		4.61	5.82	10.51	93.8	119.9	114.7	1.533		
triclinic	$P_{\bar{1}}$	4.5609	5.9531	10.7605	99.85	118.20	111.37	1.465	Fibre	Fu et al. ¹⁸
		4.5221	5.9214	10.7792	99.96	118.08	111.19	1.479		
		4.5087	5.8818	10.7873	100.01	118.36	110.56	1.487		
triclinic	$P_{\bar{1}}$	4.657	5.836	10.831	96.26	128.30	106.62	1.559	Single crystal	Liu et al. ²³

NOTE: * is molecular chain axis

2.4 Development of EM technique for polymers – the limitations and challenges

The use of high-resolution electron microscopy is highly promising for revealing the molecular conformation of PEN and PET crystals. Nevertheless, there are challenges in finding new specimen preparation methods, solutions to electron beam damage, and appropriate imaging techniques for light element materials.

2.4.1 Polymer specimen for (S)TEM preparation methods

The specimen used for (S)TEM should be thin enough (~100nm) to achieve sufficient signal on the detectors generated by transmitted electrons. The thinning techniques that are commonly used for metallic and rigid samples are not suitable for polymers, which are soft solids that will typically be damaged by being polished mechanically or thinned using ion beams. Polymer thin films are typically made by solution casting and then annealed to obtain a crystalline structure. However, the heat treatment might deform the specimen and cause it to roll or shrink. Due to the nanometre-sized dimensions of the specimen, even a very small amount of deformation could result in the specimen becoming unusable. Methods have been developed to prepare thin specimens for the purpose of observing the microstructure of polymer specimens.

2.4.1.1 Thin film melt-crystallized (MC) sample

The thin film melt-crystallized (MC) method⁹ was used to produce specimens by direct crystallization from the melt of pre-polymerized polymers. Melt-crystallized samples of PEN, with intrinsic viscosity of 0.86 dL/g, were prepared by dissolving a sample in dimethyl sulfoxide and casting it hot onto a heated coverslip. Upon evaporation and cooling of the solvent, the slide was covered with another slip, heated rapidly to 300°C on a preheated hot stage under an optical microscope for about one minute, cooled rapidly to 260°C (over a period of several minutes), held there for several hours, and cooled rapidly in air to room temperature. Following the splitting of the slips, samples for TEM and ED were shadowed with either platinum/carbon (for TEM) or gold (for ED calibration), removed from the glass by floating on dilute hydrofluoric acid (HF), and picked up with TEM grids.

In this method, two slips were used to obtain the desired thickness, and the whole process was performed in air on a hot plate, but the use of HF required special equipment and high standards of safety management.

2.4.1.2 Single crystal made from confined thin film melt polymerization (CTFMP)

In the confined thin film melt polymerization (CTFMP) sample preparation method⁹, a single crystal polymer specimen was prepared by combining polymerization and annealing in one step. In the CTFMP samples, the monomers for the synthesis of PEN, 2,6-naphthalenedicarbonyl dichloride, and ethylene glycol were dissolved in acetone, cast on a glass coverslip, and then covered with another slip. The slips were heated on a thermostat hot plate at, for instance, 230°C for 14h. This step of heat treatment included both polymerization and annealing. Lastly, the TEM sample preparation was accomplished by shadowing the glass with platinum/carbon that can be used for calibration for TEM, floating the glass on dilute HF, and picking up the grids for TEM.

The method used single crystal monomers for PEN synthesis - small organic molecules, which were relatively easy to obtain compared to polymer single crystals. Furthermore, this method is more time-efficient than dilute solution precipitation, which could take months. But the use of HF still presents a disadvantage, as it was a highly hazardous chemical and requires special facilities.

2.4.1.3 Uniaxially oriented thin films

The objective of this method was to obtain uniaxially oriented thin films²⁴ of PEN, PET, and their blends with suitable thickness and size for TEM characterization. The transferring step in this method was innovative, but it damaged the surface features of the polymer thin film in the specimen.

In the first step, 0.5 wt.% solutions of PET, PEN, and their blends were prepared in 1,1,1,3,3,3-hexafluoro-2-propanol. Each solution was dropped and spread on a glass slide and then covered with another glass slide (both glass slides were pre-heated at 280, 310 and 300°C for PET, PEN, and their blends, respectively). The solution was sandwiched between two glass slides on the hot plate thermostat at the desired temperature. Immediately following evaporation of the solvent, a thin molten polymer film was sheared/crystallized by rapidly displacing one of the two glass slides and then the sample was quenched to room temperature. A digital video camera was used to measure the relative displacement speed of the glass slides, which was found to be 12 m/min on average. If the film thickness is assumed to be 50nm, the shear rate will be approximately $4 \times 10^6 s^{-1}$. The crystallized polymer thin films prepared on the glass slides were then reinforced by vapor deposition of carbon under vacuum. Gold (Au) was vapor-deposited onto some of the films before carbon coating to calibrate the diffraction camera length.

The polymer film was transferred by placing a drop (3~4mm in hemisphere diameter) of polyacrylic acid (PAA) aqueous solution (approximately 25%) on the appropriate portion of the specimen film on the glass slide and drying for one day at room temperature. The hardened PAA with the specimen film was detached from the glass slide and then dissolved in water. Lastly, the floating specimen film was mounted on a copper grid for TEM and dried at ambient temperature.

Reflections of TEM diffraction pattern are associated with both α - and β -modifications similar to those of fibres made by extrusion. So, the uniaxially oriented thin film of PEN prepared for TEM by applying shear strain can be considered as a suitable model specimen for high-speed spun PEN fibre.

2.4.1.4 Advantages and disadvantages of the reported sample preparation methods

Common characteristics have been identified among the specimen fabrication methods developed for TEM characterization. Two glass slides/slips were used to control the thickness. In terms of introducing structural order, the MC method uses annealing, the 'uniaxially oriented' method applies shear strain to create oriented crystals, and the CTFMP method uses a single crystal of monomers to produce a single crystal of polymer.

These methods produce thin film polymer specimens with controllable thickness and sufficient crystallinity for TEM analysis. However, the disadvantages were still apparent. In the case of thin film specimens, the transferring step usually involves the use of HF and the handling would damage the surface features.

2.4.2 Electron beam damage

The primary challenges associated with obtaining high resolution EM images from polymers include beam damage and low contrast generated by light elements within the materials.

2.4.2.1 Observation of damage

Egerton³ reported that beam damage implies some beam-induced change to the specimen, beginning with atoms being displaced from their original positions, which is often accompanied by the breakdown of chemical bonds. The early stages of damage can be observed from the electron diffraction pattern of crystalline samples, where the regular arrangement of atoms produces Bragg spots for single crystals or sharp rings for polycrystal that fade or become blurred as the crystalline order is disrupted, as blurred rings are generated by amorphous materials.

In a poorly conducting specimen, inelastic scattering of the primary electrons results in the emission of secondary electrons, emission of x-rays, Auger electrons and an electrostatic charge. The resulting electric field can cause image drift or distortion, structural change or mass transport, or even complete destruction of the specimen due to local ionization resulting in bond breaking or forming with surface species. Electron beams can also initiate chemical reactions with the sample environment, resulting in hydrocarbon contamination (in a poor vacuum or if the specimen surface is contaminated) or etching for organic specimens if water or water vapor is present.

Elastic scattering implies the presence of electrostatic interaction between the primary electrons and atomic nuclei. The interaction is elastic in the sense that the total kinetic energy of the projectile and target (electron and nucleus, for a localized interaction) is conserved.

2.4.2.2 Effect of electron beam radiation damage on polymers and proposed mechanism

Radiation affects materials by deposition of energy. Energy is transferred through the inelastic scattering of primary electrons by the specimen, which causes the molecules to become electronically excited, and momentum transfer to the atomic nucleus, resulting in the breaking of bonds and changes to the physical and chemical structure of the sample. This is regarded as radiation damage. Radiation damage to polymers is characterized by the alteration of intermolecular spacing²⁵. This is observed as the loss of crystallinity in an ordered structure or the alteration of atomic distances in an amorphous structure²⁶.

Organic molecules have a low electron affinity, which results in a relatively low excitation energy²⁷. In comparison to metals and other inorganic materials, macromolecules have weak intermolecular forces such as van der Waals interactions or, at the strongest, hydrogen bonds. An excited atom in an organic molecule is more likely to dissociate since the Frank-Rabinowitch "cage" effect²⁸, which restricts the excited atom to its original position by surrounding molecules, is relatively weak. In other words, the nature of soft solids⁶ that results in its sensitivity to external disruption also makes them sensitive to electron beam radiation.

Certain molecular structures have been found to be more sensitive to radiation damage than others. In macromolecules, aliphatic groups are more sensitive than aromatic ones²⁹, since the resonant structure of phenyl groups has a large number of energy levels to accommodate electrons at various energy levels, making it easy for absorbed energy to be rapidly dissipated throughout the molecule without causing permanent changes²⁷. It has also been observed that a naphthyl group can "protect" other more sensitive groups by dissipating the energy of excited electrons over a distance of several atoms³⁰. In polymers, an excitation is transferred rapidly along the long chain of molecules, so that the energy may not be localized at any of the bonds for a long enough period to cause the bond to break³¹.

Due to the different sensitivities of chemical structures, specific bonds may be disrupted at preferred sites during the process of excitation energy transfer²⁵. Crystallinity and amorphous structures were also considered to be damaged at different rates. Crystalline structures hold the excited species more firmly in place, so the probability of recombination to almost the original structure is quite high, and the chemical structure may be maintained, while amorphous structures would lead to conformational changes³².

Crystallinity loss is usually attributed to cross-linking and chain scission. It has been suggested that the presence of residue after exposure indicates some cross-linking, while if residue is barely visible then chain scission is dominant³³, though this would only apply to very high levels of exposure and damage.

2.4.2.3 The major type of beam damage in polymers – Radiolysis (ionization damage)

Polymers are primarily damaged by radiolysis in (S)TEM. Radiolysis is caused by the inelastic scattering of electrons, which suffer energy losses ranging from a few eV (for excitation of conduction or valence electrons) to tens or hundreds of eV (for ionization of inner atomic shells). The energy transfer in a conducting specimen such as a metal leaves a vacancy (hole) in the initial state (e.g., conduction band), but this vacancy is rapidly filled by one of the many electrons in the system before atoms can be displaced, so the material is not damaged by ionization.

Nevertheless, in the case of insulators and some semiconductors, holes/vacancies created in the valence band or in an inner atomic shell not being filled by electrons can last long enough for the excited atom to eventually move, resulting in the permanent breakage of chemical bonds and a change in the atomic or molecular structure. The ejected electron may be captured by

the hole (within a few ps.) if its energy is sufficiently low, but this results in a highly excited molecule that may dissociate, causing chemical change²⁵.

Radiolysis can cause cross-linking in organic compounds and the appearance of various chemical species. C-H bonds are easily broken, and the hydrogen may diffuse away, preventing the bond from re-forming, whereas C-C bonds are more resistant to radiation. H_2 production accounts for a significant portion of the absorbed energy in saturated hydrocarbons and alcohols, whereas it is less common in unsaturated and aromatic hydrocarbons, or amino acids³⁴. Generally, aromatic compounds are less radiation sensitive due to the resonance stabilization of the phenyl ring³⁵.

Henderson³⁶ has pointed out that the ratio of energy deposition (and therefore radiolysis damage) to elastic scattering (which provides information in the form of a diffraction pattern or a phase-contrast image) is several hundred times greater for x-rays than for electrons. Secondary electrons or photoelectrons may escape from near-surface atoms without causing damage, so very thin films or small particles should be less sensitive, in agreement with some TEM measurements^{37,38}.

2.4.2.4 Quantitative measurements of damage

A number of properties can be used to quantify the radiation damage. These include mass loss, loss of order or crystallinity, changes in tensile properties (stiffness and strength), changes in electrical conductivity, changes in the coefficient of thermal expansion, and variations in transport properties.

R.M. Glaeser³⁹ measured the radiation dose during TEM imaging as the current density passing through the specimen. Figure 2.7 illustrates the reciprocity between the fading time of DP and the dose rate. The logarithm of fading time is plotted against the logarithm of current

density along a line with a slope of minus one, and the data are within experimental error. The total "dose" needed for complete fading of the diffraction pattern appears to be independent of the intensity (dose rate) of irradiation over the range studied. Figure 2.7 also illustrates the sample degraded faster at 80kV than 500kV, but the damage correlated to accelerating voltage was not discussed.

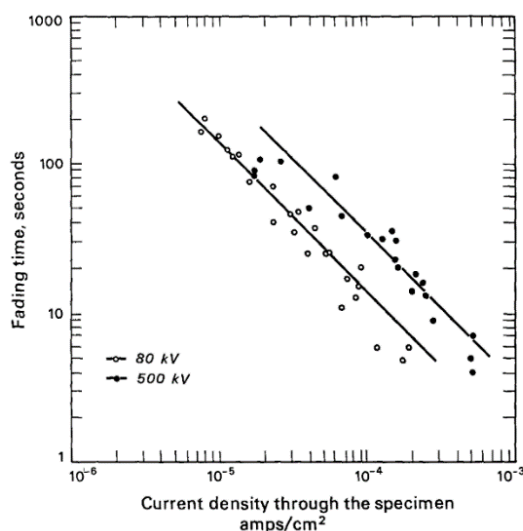


Figure 2.7 Radiation damage of crystalline L-valine in the electron microscope, at accelerating voltages of 80 kV and 500 kV. A line with slope of minus one indicates a constant-dose relationship for complete fading of the diffraction pattern.³⁹

Kumar *et al.*⁴⁰ demonstrated that the sensitivity of a polymer to electron beams is strongly dependent on its thermal stability or melting temperature (Figure 2.8). Kumar used the electron diffraction intensity of one or more reflections as a function of electron dose to quantify the damage. Additionally, they noted some other polymer characteristics continue to change even after crystallinity has disappeared. Martin *et al.* also reported⁴¹ a good correlation between the critical dose for radiolysis and the melting or thermal degradation temperature of polymers.

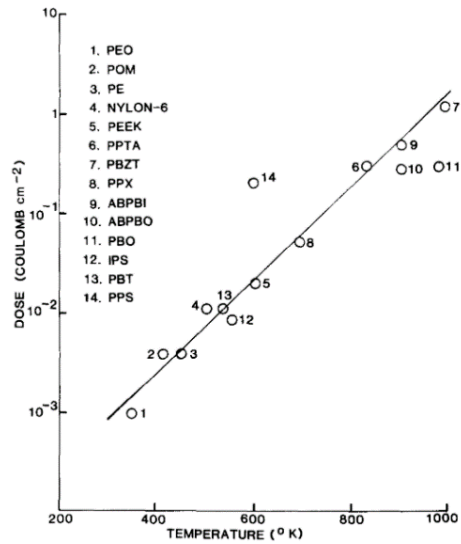


Figure 2.8 Correlation between critical electron dose (D^*) and specimen melt temperature (or onset of degradation temperature for those polymers which degrade before any melting is observed).⁴⁰

Z. Leijten *et al.*⁴² have performed a quantitative analysis of electron beam damage on the photovoltaic nanocomposite polymers P3HT:PCBM. The fading electron diffraction rings allow quantification of the beam sensitivity of each component of the nanocomposite. Using the intensity of the PCBM peak at 0.217\AA^{-1} and the P3HT peak at 0.256\AA^{-1} in radial average of diffraction pattern (Figure 2.9), they showed electron beam damage effects in P3HT-PCBM thin films over multiple length scales. They also confirm that dose rate is not a factor to be concerned about in materials damage, because changing the dose rate from 0.1 to $10 e/(\text{\AA}^2 s)$ has no significant effect on fading of the diffraction rings. This agrees with the conclusion given by Glaeser.³⁹

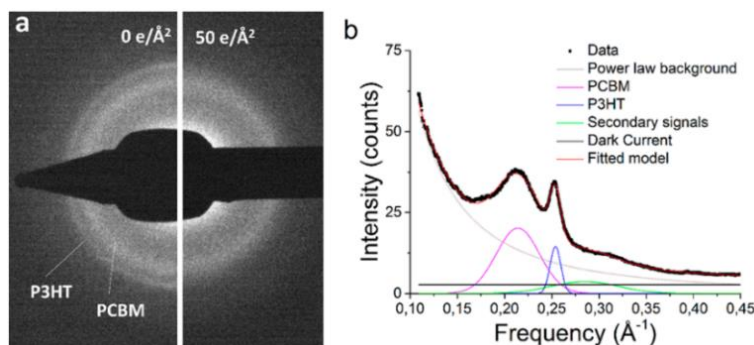


Figure 2.9 ⁴²(a) Fading of diffraction rings of a P3HT:PCBM bulk heterojunction at room temperature, before and after exposure to $50 e/\text{\AA}^2$. (b) Radial average of diffraction pattern as shown in (a) decomposed in its different components by least-squares fitting. The goodness of fit (R^2) for the model is 0.9985.

The cross section of radiolysis was used by Egerton⁴³ to quantify beam damage (Table 2.3). Radiolysis “efficiency” η is measured by the ratio of a damage cross section σ_D (measured as the reciprocal of a characteristic dose) to the total cross section (σ_i *per molecule*) for inelastic scattering, i.e., $\eta = \sigma_D / \langle \sigma_i \rangle$. $\eta < 1$ indicates that more than one inelastic collision per atom is needed to create damage. As a result, large values of η are observed for aliphatic compounds. Radiolysis cross sections⁴³ are of the order of Kb or Mb, while knock-on displacement cross sections are of the order of 100 b ($1b = 10^{-28} \text{m}^2$). Although knock-on displacement (particularly of hydrogen atoms) occurs in organic materials, radiolysis is responsible for nearly all of the damage⁴⁴, even at an incident energy of 1 MeV.

Table 2.3. Characteristic dose D_c , equivalent fluence ($D_{ec} = D_c/e$) and damage cross section ($1/D_{ec}$) determined by several techniques.⁴³ Unless otherwise stated, the data are for 100keV electrons and a specimen at room temperature. The last column shows the factor by which the measured characteristic dose increases when the specimen temperature is reduced to 100K.

Method	Material	dose D_c (C/cm ²)	$D_{ec} = D_c/e$ (e/Å ²)	σ_D (Mb) = 100/ D_{ec}	$D_c(100)/D_c(300)$
Fading of spots in electron diffraction patterns	Bacteriorhodopsin ^f	0.0008	0.5	200	9
	Amino acid (glycine) ^a	0.0025	1.6	64	
	Polyethylene	0.01	6.0	16	
	Coronene ^e	0.11	70	1.5	
	Phthalocyanine (Pc)	0.2	120	0.83	
	Cu-phthalocyanine	2.5	1600	0.06	
	Chlorinated Cu-Pc	20	12000	0.008	
	ZSM-5 zeolite ^d	0.5	300	0.33	
	Calcite (200 kV) ^g	62	39,000	0.0026	
	NaCl (Frenkel pairs) ^b	82	51,000	0.0020	
	KCl (Frenkel pairs) ^b	3.9	2,400	0.041	
	TEM image	Di-glycine ^a	0.03	20	5
Cu-phthalocyanine ^a		0.5	300	0.3	
EELS fine structure	Coronene ^e	1.0	600	0.16	
	Polycrystalline C ₆₀	420	2.6×10^6	4×10^{-4}	2
	Nitrocellulose	0.002	1.2	80	120
N-loss	Nitrocellulose	0.006	3.7	27	90
O-loss (EELS) ^c	Polyvinyl formal	0.03	20	5	30
	PMMA	0.06	40	2.5	8
C-loss	Polycarbonate	0.5	300	0.33	> 10
Cl-loss	PMMA	0.5	300	0.33	1.6
	NaCl ($< 10^{-4}$ A/cm ²) ^c	0.18	110	0.89	
Total mass loss	Glycine	0.012	7.5	13	
	Di-glycine	0.006	4	27	
Calculated knock-on cross sections ^f	Amorphous Al ₂ O ₃ ^h	2500	1.6×10^6	6×10^{-5}	
	H-removal (E _d = 0.1 eV)			5×10^{-4}	
	H-removal (E _d = 4.4 eV)			1×10^{-4}	
	C-removal (E _d = 5 eV)			1.5×10^{-4}	
	C-removal (E _d = 10 eV)			5×10^{-5}	

2.4.2.5 Definition and review of critical dose measurement

The dose is the scale of energy absorbed by the material from the radiation source, usually measured as the energy absorbed per unit mass of the sample. Egerton³ pointed out the correct term to describe this incident in (S)TEM should be ‘fluence’, because the scale here is measured by number of electrons (or energy) per unit area. Critical dose is defined as the dose required to cause an observable change in specimen structure. It is a significant factor in beam sensitive materials characterization with (S)TEM, because it defines the “window” of workable dosage.

Multiple mechanisms and detectors can be used to measure critical dose, for example, EELS, BF images, and ED. ED intensity vanishing tracing is the most commonly used method for polymer crystalline specimens since the transition from crystalline to amorphous indicates the loss of crystalline structure. The critical dose can be measured in several ways with ED: i) End

point dose, which represents the accumulated dose at the point when the diffraction pattern has completely disappeared; ii) Dose at $\exp(-1)$ of the initial signal, which is measured as the accumulated dose at the point when the intensity of the observed diffracted plane drops to $\exp(-1)$ of its initial intensity.

In terms of critical dose measurement, there are three major methods that enable the communication of results from different materials and equipment. They are accumulated dose, dose rate and damage cross-section. The accumulated dose is the most common method because most beam sensitive materials are not sensitive to dose rate and only alter once the accumulated dose reaches a certain level.

The type of beam damage that occurs in polymer specimens is radiolysis³. In the TEM, radiolysis is often approximated by a first-order process with an exponential dose dependence³⁹:

$$S(D) \approx S(0)\exp(-D/D_c) \quad (2.1)$$

where $S(D)$ is a measured signal or property (e.g., diffraction-spot intensity or specimen thickness) recorded after a dose D , and D_c is the characteristic (or critical) dose that reduces the signal by a factor $1/e$.

Time-resolved diffraction intensity has been used as an indicator of crystallinity changes over the accumulation of dosage^{11,39,42}, with a calibrated electron beam current as illumination source. After the entire process of ED vanishing has been recorded, the accumulated dose at each stage of intensity change can be calculated. The disappearance of the ED indicates the amorphization of crystalline material under exposure to an electron beam, so the critical dose for a certain amount of structure change can be determined.

In this work, the time-resolved ED pattern will be acquired using a code developed in-house, which controls the microscope to acquire multiple ED with defined exposure times for each ED and intervals between each ED. The metadata can be used to precisely determine the timing, and when combined with the calibrated dose rate of the electron beam, the actual number of electrons interacting with the specimen can be determined. Therefore, the critical dose could be determined.

2.4.3 Correlation of diffraction pattern and FT of image to crystalline structure

Converting reciprocal-space diffraction pattern back to real-space structure is a direct way to reveal crystalline structure. Diffraction is the reconstructive interference of radiation scattered by atoms in a crystal. Diffraction theory is based on Bragg's Law that measures the path difference ($n\lambda$) between reflection from plane spacing (d): $n\lambda = 2d\sin\theta$; which can be simplified with Small angle approximation: $n\lambda = 2d\theta$, where λ is the wavelength of the radiation.

Considering the amplitude of reflection scattered by a set of parallel planes (hkl) with d spacing in one unit cell (Figure 2.10). The amplitude scattered by a single atom is measured by its *atomic scattering factor*¹². As illustrated in Figure 2.10, we also need to consider the relative position of each atom between a pair of planes: this defines the atom's *phase angle*. For example, if an atom were to lie directly on the plane, it would scatter exactly in phase with the wavefront: its phase angle would be 0° . However, if the atom were half-way between the two planes, it would scatter out-of-phase: its phase angle would be 180° . The total amplitude scattered – the *Structure Factor*, $F(hkl)$, of the reflection – is the *vector sum* of individual scattering factors (f_n) and their phase angle (ϕ_n).

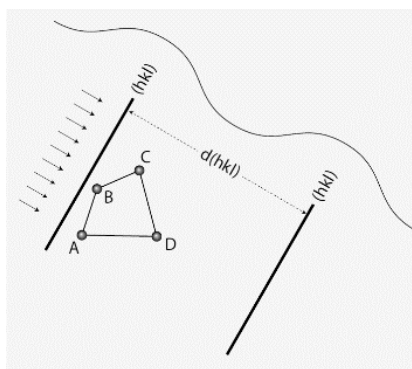


Figure 2.10 In a unit cell, a set of four atoms (ABCD) lie between a pair of planes (hkl) with d spacing. They are irradiated from the top left, as indicated by the array of small arrows. The sine curve indicates the variation of phase along the wavefront.

All that can be recorded in a diffraction experiment is the *intensity* of scattering reflections – the exposure level at a point on a solid-state detector. Intensity (I) is proportional to the square of the amplitude of the Structure Factor (F): $I(hkl) \propto |F(hkl)|^2$. So, we can measure the *amplitude* of scattering from each reflection, but cannot directly recover the *phase* of the scattered beams. This is called “phase problem” and adds difficulty to unify the crystalline structure of organic materials, e.g., polymers, which are usually complex with low symmetry.

It is useful to Fourier transform the crystal lattice into *reciprocal space*¹² in diffraction. Ewald sphere¹² visualizes the relation of reciprocal space and electron wave vectors. In reciprocal space, radius of Ewald sphere ($1/\lambda$) represents possible scattering wave vectors intersecting reciprocal space (Figure 2.11). The radius of sphere is very large compared to reciprocal lattice; hence the sphere circumference is almost flat.

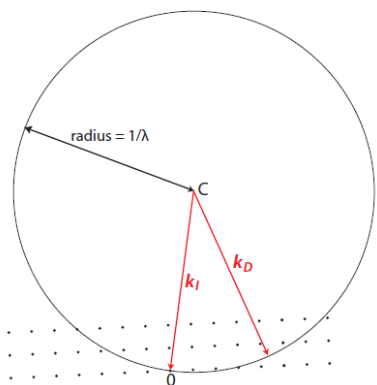


Figure 2.11 The Ewald Sphere. k_I – incident beam wave vector, k_D – diffracted wave vector.

TEM diffraction pattern is Fourier transform (FT) of the specimen. FT of an (S)TEM image represents the spatial frequency of the projected features. The lens aberrations included in the image will also be shown in its FT. To exclude the possible influence of aberration in FT of image, in my work, I use experimental TEM diffraction pattern to ensure the spacing in phase image is real.

FT of ptychography image – reconstructed from 4D-STEM dataset – shows the spatial frequency of projected crystalline structure along one zone axis. By matching the FT to simulated diffraction pattern from the model of target crystal, we can identify the viewing axis. In practice, we run single-crystal diffraction simulation with the model along multiple zone axes to find the one generating diffraction pattern identical to the FT of image.

In summary, FT of image reflects the spatial frequency of projected features, by matching the projection axis to zone axis of crystalline model and generate an identical diffraction pattern with single-crystal simulation, we can identify the orientation of crystalline structure in the specimen. More details are illustrated in analytical chapters: the information of TEM diffraction patterns can be found in Section 4.2.1; the discussion of structure analysis based on its correlation to FT and simulation validation can be found in Section 5.2.3.

2.5 Principle of (S)TEM imaging and contrast enhancement for polymers

2.5.1 TEM imaging and phase contrast

High-resolution imaging provides direct insight into the molecular structure of polymer crystals. TEM images of various polymers have been acquired, along with attempts at damage control. This sector will review previous work on TEM imaging polymers and the corresponding damage control strategies.

Modern high-resolution TEM (HRTEM) instruments typically consist of two to four condenser lenses, an objective lens, and up to six imaging lenses below the specimen. Magnetic lens design⁴⁵ dates back to the late 1920s when it was realized that rotationally symmetric magnetic fields could be used to focus electrons and that to produce a lens of high refractive power, the magnetic field along the axis of rotational symmetry needed to be confined to a small region with a high field strength.

The formation of an HRTEM images as shown in Figure 2.12 from a simplified ray optical perspective and from a wave optical perspective⁴⁵. The scattering of electrons in the specimen results in a diffraction pattern in the back focal plane of the objective lens, and finally, an image in the image plane. The specimen, back focal, and image planes are mathematically related by Fourier transform operations.

The phase contrast of an image can result from differences in the phase of electron waves scattered through a thin specimen. The phase contrast is sensitive to factors including the sample thickness, orientation, or scattering factor of the specimen, and variations in the focus or astigmatism of the objective lens. Phase contrast can be used to image the atomic structure of thin specimens due to its sensitivity. As an example, HRTEM imaging has been used to

study the atomic structure of zeolite – a beam sensitive porous material – under low dose with exit-wave reconstruction⁴⁶.

The phase contrast in TEM formed with the defocus, but the low contrast generated by polymer specimen and the beam damage does not allow defocus adjustment while imaging. Therefore, high resolution TEM phase is not suitable for imaging polymers.

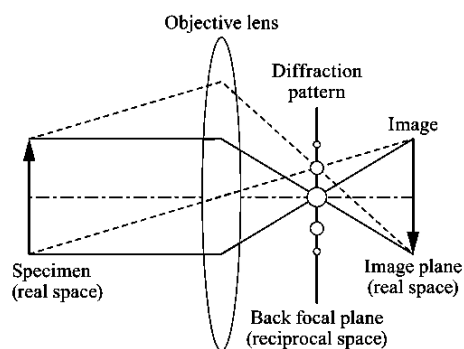


Figure 2.12 Schematic optical ray diagram showing the principles of the imaging process in HRTEM and indicating the reciprocal relationships between specimen, diffraction and image planes⁴⁵.

2.5.1.1 Imaging polymers with TEM

Dobb *et al.*⁴⁷ reported the earliest direct imaging of lattices from beam-sensitive polymers (Figure 2.13a). The image was acquired on poly-(p-phenylene terephthalamide) fibre Kevlar 49 composed of hydrogen-bonded sheets of phenylene rings, with mechanical properties similar to those of PAN-based intermediate-modulus carbon fibres. Despite their emphasis that there is no exact correspondence between layer planes and lattice fringes, they were able to determine the crystallite (grain) size along the fibre axis from such micrographs. The averaged values obtained from the lattice fringes in the image were found to be greater than the values obtained from X-ray and electron diffraction results. Discrepancies in crystal size from different characterization techniques questioned the accuracy of crystallite size results from classical

diffraction methods like XRD, although an alternative explanation is that their observed lattice fringes were derived from the more perfect regions of the structure.

Later, Dobb *et al.*⁴⁸ published a follow-up study on the earliest attempt to monitor polymer specimen damage. A time-lapse series of electron diffraction patterns was recorded at various electron densities to ensure that electron images were recorded within the lifetime of the specimens. They found that different reflections decay at distinct rates during exposure to the electron beam; the (110) reflection (0.4333 nm) was the most stable but did not persist for more than 120s at a beam current density of $1.64 \times 10^{-5} A \cdot mm^{-2}$ ($123 e/\text{\AA}^2$). The structural changes in Kevlar, Kevlar 49, and PRD 49 fibres (Figure 2.13b) were studied using time-lapse electron diffraction, dark-field, and lattice-imaging techniques. These measurements indicate that the decay in molecular order does not fit into either a dose-related or a dose-rate-related degradation pattern.

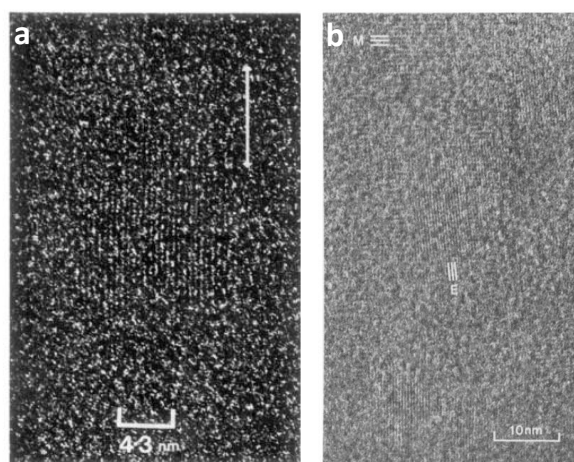


Figure 2.13 (a) Micrograph⁴⁷ showing 0.433nm lattice fringes in Kevlar 49 ($\times 3,200,000$). (b) High resolution micrograph⁴⁸ of a fragment of PRD 49 showing meridional and equatorial lattice fringes.

The study by Galiotis *et al.*⁴⁹ found that certain polydiacetylene crystals are sufficiently resistant to radiation damage in the electron microscope that lattice images can be obtained as shown

in Figure 2.14. The polydiacetylene (polyDCHD) fibres were found to have a high degree of internal perfection by TEM, with the polymer molecules aligned parallel to the fibre axes.

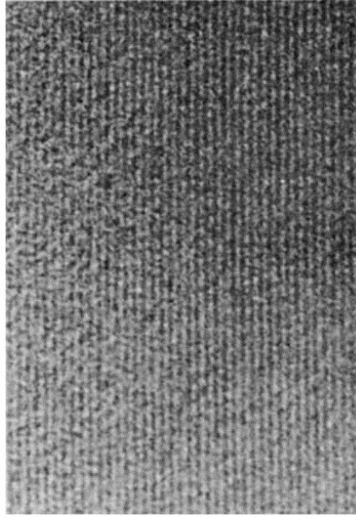


Figure 2.14 (010) lattice image⁴⁹ from a thin polyDCHD crystal showing a spacing of approximately 1.2 nm.

Giorgio *et al.*³⁷ discovered that small crystals were relatively stable in the electron beam, while larger crystals were immediately destroyed when observed at high magnification in TEM. Polyethylene (PE) pyramids (200-1500 Å in length) irradiated in a 100kV TEM showed remarkable stability compared to 1-10 µm sized crystals as a reference, which were damaged and collapsed on the substrate.

In Giorgio's work³⁷, the phase transition and distortion were also noteworthy observations. When the radiation D_c is greater than 800 C/m^2 ($50 \text{ e}/\text{Å}^2$), the orthorhombic \rightarrow hexagonal transition is induced, and slight lattice distortions are visible in the high-resolution image of the hexagonal phase. The molecular distortion factors along the a and b axes were ca. 5%, and along the chain c -axis was ca. 17%; these values agree with x-ray measurements of PE crystallized from the melt. The large difference between these two distortion factors may be

attributed to packing, since the images of PE pyramids did not resolve lattice defects (Figure 2.14). The diffraction pattern disappears at an irradiation dose of $D_c \approx 2400 \text{ C/m}^2$ ($150 \text{ e}/\text{\AA}^2$).

In another work, Giorgio *et al.*³⁸ found that the two-dimensional lamellae (30\AA thick) of Polyalkylacrylate (PAA) were highly resistant to the electron beam, so that high-resolution images (Figure 2.15b,c) could be obtained even when the sample received a fairly high dose of $15,000 \text{ C/m}^2$ ($936 \text{ e}/\text{\AA}^2$). Also, they claimed that grain boundaries in the lamella could be visualized, with molecular holes present in the monocrystalline domains, and even the single molecular holes were quantitatively analysed and averaged.

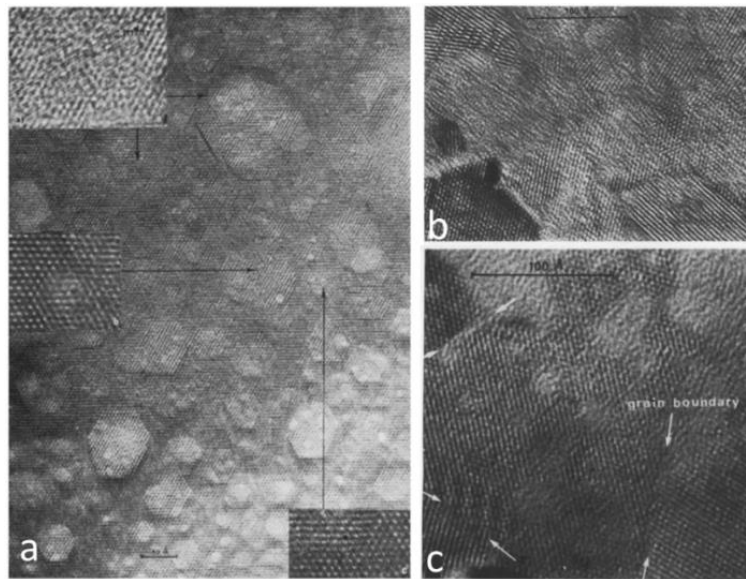


Figure 2.15 High-resolution pattern of a hexagonal PE crystal³⁷. (b) High-resolution pattern of a lamella containing grain boundaries.³⁸ The defocus Δf varies between $\Delta f = -760\text{\AA}$ and $\Delta f = -1030\text{\AA}$ from one end to the other, imaged with the objective diaphragm $40\mu\text{m}$. (c) High-resolution image³⁸ with a quite constant defocus $\Delta f = -900\text{\AA}$ over the lamella acquired with the objective diaphragm $40\mu\text{m}$. (Note: Δf is 'defocus')

Chanzy *et al.*⁵⁰ obtained lattice images of polytetrafluoroethylene (PTFE) single crystals, which is a very sensitive polymer since it lacks an aromatic ring structure throughout the molecule in the same way as PE. In this study, FT filtering was used to facilitate image analysis. The

Fourier-transformed digital image produced a pattern. Each reflection was subjected to a filter and the reversed transform was applied. In Figure 2.15b, a filtered image is shown in the insert. This figure shows a resolved lattice consisting of rows of hexagonally packed white circular dots. The dots are 0.49nm apart and were found to correspond to the projection of individual PTFE chain molecules, which was supported by the perpendicular relationship between the chain axis and the crystal surface. However, the contrast of the images was quite low, and it was difficult to extract more structural information from them.

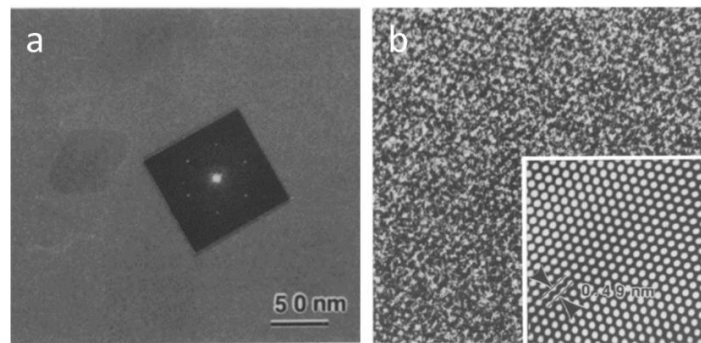


Figure 2.16 (a) Low-dose electron micrograph of one PTFE single crystal⁵⁰ and its optical diffractogram (inset). (b) Further enlargement (same contrast as in a) and filtered image (inset).

Revol *et al.*⁵¹ also used Fourier filtering to denoise the PE lattice image obtained with low dose CTEM. According to their work, the total irradiation dose accumulated for an image (Figure 2.17) was $1.8 \times 10^{-11} \text{C} \cdot \mu\text{m}^2$ ($1.12 \text{ e}/\text{\AA}^2$).

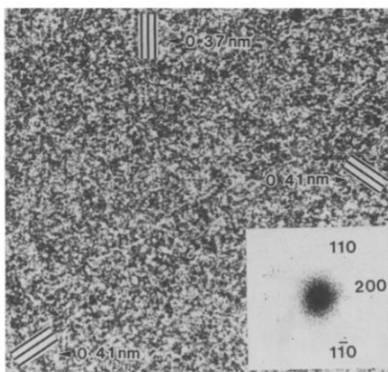


Figure 2.17 Image of a portion of a PE single crystal⁵¹ which on careful inspection shows the (110), ($1\bar{1}0$) and (200) lattice lines. Inset: the corresponding optical diffraction pattern.

Uemura *et al.*⁵² reported that high-resolution images of a crystal in two crystallographic directions are very useful for determining its three-dimensional structure. Poly (*p*-phenylene sulphide) (PPS) images were obtained using the [001] and [$0\bar{1}1$] incident electron beam directions, respectively, which confirmed that the two phenylene groups in a molecular chain in a unit cell have different orientations. Moreover, they measure the change in lattice spacing as dose accumulates (Figure 2.18e).

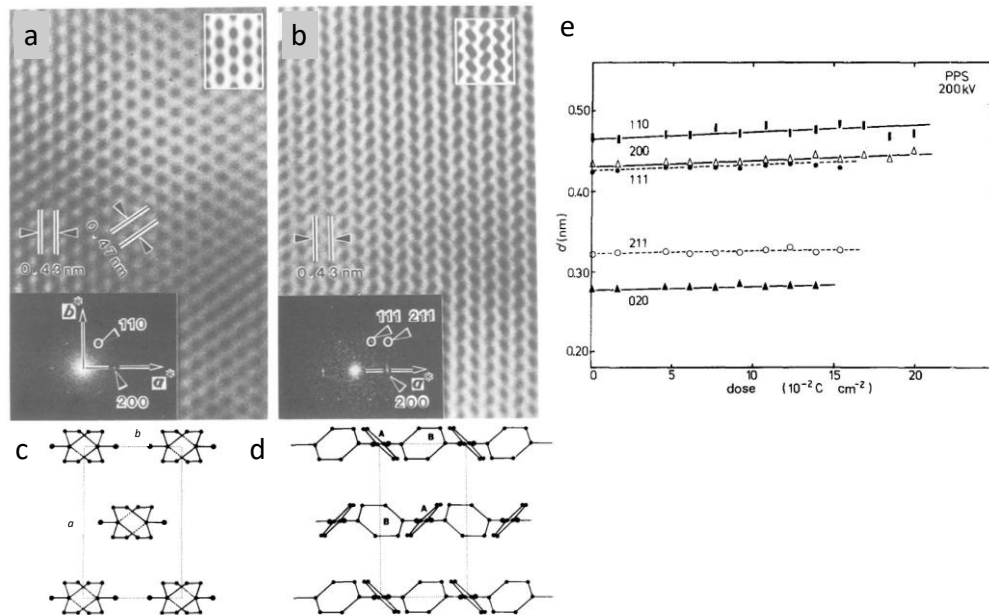


Figure 2.18 ⁵²(a) High-resolution electron microscopic images taken at an accelerating voltage of 200kV for the [001] incidence and (b) [0 $\bar{1}$ 1] incidence. In both, the optical diffraction pattern is given at the lower left-hand corner and the simulated image at Scherzer focus is at the upper right-hand corner. In (a), each dark ellipse corresponds to a single molecular chain projected on the ab plane in the chain direction illustrated in (c). In (b), each dark ellipse corresponds to A in (d) and region between ellipses correspond to B. (e) Changes in lattice spacings with electron irradiation dose at 200kV at room temperature. The lattice spacings are almost invariant with increasing irradiation dose.

M. Tsuji *et al.*⁵³ used ultra-high voltage (500kV) to image poly(*p*-xylylene) (PPX) single crystals, and resolved molecular chains of PPX directly in the β -form single crystal. The ultra-high voltage was used to improve the resolution limit by its smaller wavelength of illumination source. In phase contrast electron microscopy, they found that the image is greatly influenced by the defocus value. Thus, it is important to examine the consistency of the crystal structure of the objective specimen and the high-resolution electron micrograph obtained. Typically, this is accomplished by comparing the electron micrograph obtained with through-focal images simulated from the crystal structure. The computer simulation confirms that the micrograph obtained (Figure 2.19e) does not contradict the results of the X-ray diffraction analysis of the crystal structure. The total end point dose of both the α - and β -form PPX crystals measured at 500kV was approximately $0.5 \text{ C} \cdot \text{cm}^{-2}$ ($312e/\text{\AA}^2$).

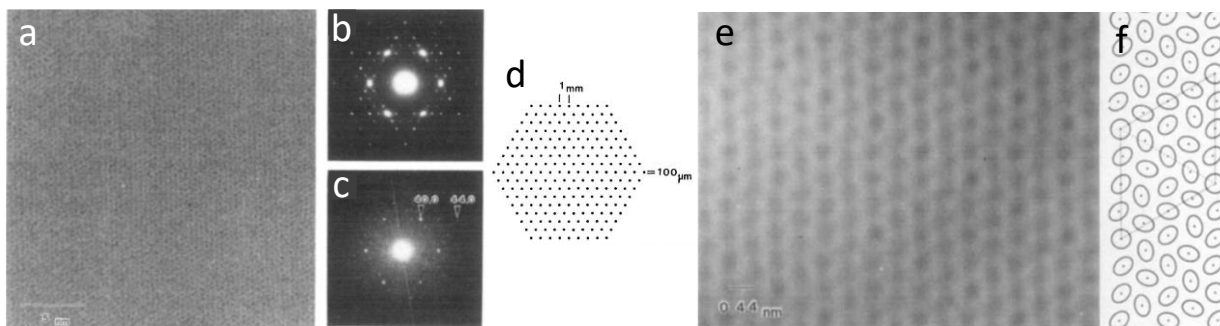


Figure 2.19 (a) High resolution image of a PPX β -form single crystal⁵³, individual molecules are roughly detectable as dark spots. (b) Electron diffraction pattern taken at 500kV. (c) Optical diffractogram of a. (d) Schematic arrangement of pinholes in filter grating used for the optical image processing of the β -form high resolution micrograph. (e) Processed high resolution image of a PPX β -form single crystal. Optically filtered image using the grating in d. (f) Model structure analysed by electron diffraction intensity.

M. Tsuji *et al.*⁵⁴ have also demonstrated the lattice images of polystyrene (i-PS) single crystals obtained in a conventional TEM (CTEM) at 120kV. In i-PS single crystals, lattices with spacings of 1.1nm and 0.55nm were resolved. Additionally, the instrument was equipped with a liquid nitrogen anti-contamination trap and a low dose unit to minimize radiation damage (Figure 2.20). Figure 2.20 shows that the resolution was not as high as that obtained at 500kV as shown in Figure 2.19. It is possible that this is caused by the different accelerating voltages, but it can also be a result of the material properties of the specimen.

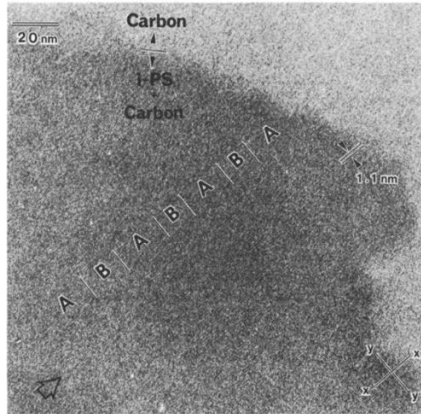


Figure 2.20 Lattice bright field lattice image of the edge of an i-PS single crystal⁵⁴. The 1.1nm lattice fringes can be seen by inspection in the direction indicated by the arrow.

Isoda *et al.*⁵⁵ examined the crystal structure of poly(p-xylylene) (PPX) in its β -form from a high-resolution image of a single crystal, in order to understand the molecular structure. The authors asserted that the high-resolution image corresponded to the projection of molecules onto the ab-plane along the chain axis, illustrating the mutual position of each molecule within a unit cell. The molecules are aligned wavy along the *a*-axis, and the rough positions of their centres in a unit cell are determined from the image. The space group of the β -form was trigonal, P3, and the lattice dimensions are $a=2.052$ nm, $c=0.655$ nm and $\gamma=120^\circ$.

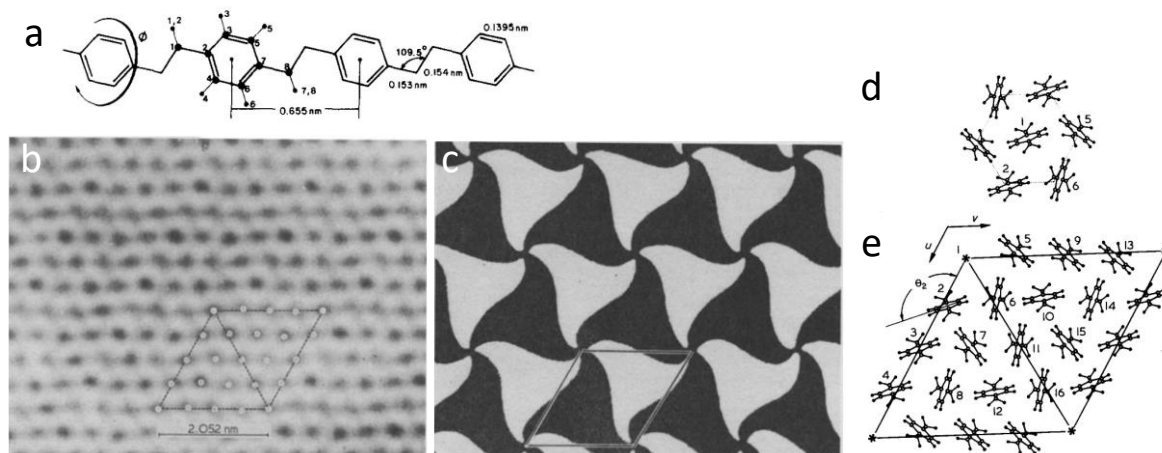


Figure 2.21 ⁵⁵(a) Molecular conformation in PPX crystals. This *trans* zigzag confirmation has the fibre period of 0.655nm. A benzene ring can rotate without a change of fibre period. In the refined β -form structure, the plane containing the benzene ring makes an angle of $\varphi=90^\circ$ with that of a $CH_2 - CH_2$ zigzag unit, just as in the α -form. Eight carbon (large circles) and eight hydrogen (smaller circles) atoms are numbered as in the figure. (b) High-resolution image of a PPX β -form single crystal taken with JEM-500. Each dark portion corresponds to one molecule projected onto the basal plane along the polymer chain axis. The rhombus shows the large unit cell of β -form PPX. One unit cell contains 16 molecules. White circles show the centres of molecules in the unit cell. Molecules are not aligned straight, but in a characteristic wavy fashion along the [100] direction. (c) A two-dimensional pattern called 'Chidori' is a nice representation of wavy alignment of molecules in β -form PPX. The rhombus shows the unit cell corresponding to that of PPX in b. (e) Two-dimensional structure (the *ab*-plane projection) refined by electron diffraction intensity. Open circles denote carbon atoms and fill circles hydrogen atoms. Molecules in the unit cell are numbered as $i=1$ to 16. The orientation of each molecule is defined by θ_i , as shown in the figure. The three 6-fold symmetry axes are on the $i=7, 8$ and 12 by $i=10, 14$ and 15 . From the requirement of $p6$ symmetry, the molecule of $i=1$ may occupy one of three equivalent orientations with equal probability (d).

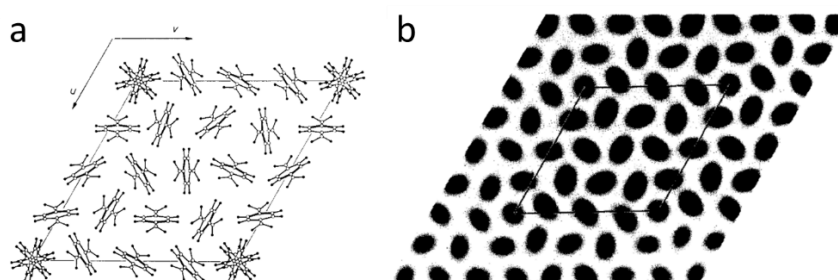


Figure 2.22 Three-dimensional structure of the β -form is shown along the *ab*-plane projection.⁵⁵ Open and filled circles represent carbon and hydrogen atoms, respectively. Bold lines in a molecule represent the upper part of a benzene ring. The molecule of $i=3$ and its equivalents are displaced by $c/2$ along the *c*-axis and the others align on the same level. The molecule of $i=1$ is presented as a superposed molecule with the three equivalent orientations, one of which is occupied in a real crystal.

Young *et al.*⁵⁶ prepared the polyDCHD specimen in the form of relatively perfect polymer single crystals by solid-state polymerization of monomer single crystal. The monomer crystal was

prepared by evaporating droplets of dilute monomer solution on a carbon support film. The monomer crystals were then polymerized by heating or even by exposure to an electron beam in the microscope.

The crystal structure of polyDCHD has been determined with a high degree of accuracy, so it was possible to compute the appearance of the HREM image. Figure 2.23c shows a computer-predicted projected potential for the structure, and the dumbbell nature of the molecules is clearly visible. Due to the need to work rapidly to minimize radiation damage, it was not possible to determine the exact conditions such as defocus and specimen thickness. Nevertheless, the close agreement shown in Figure 2.23c provides considerable confidence in the ability of the technique to reveal a high degree of molecular detail in micrographs.

Polydiacetylene molecules imaged in Young's study contain large carbazolyl side groups that superimpose in stacks and give rise to the dumbbell appearance. Thus, for the first time, it has been possible to resolve the full shape of polymer molecules including their side groups in crystals.

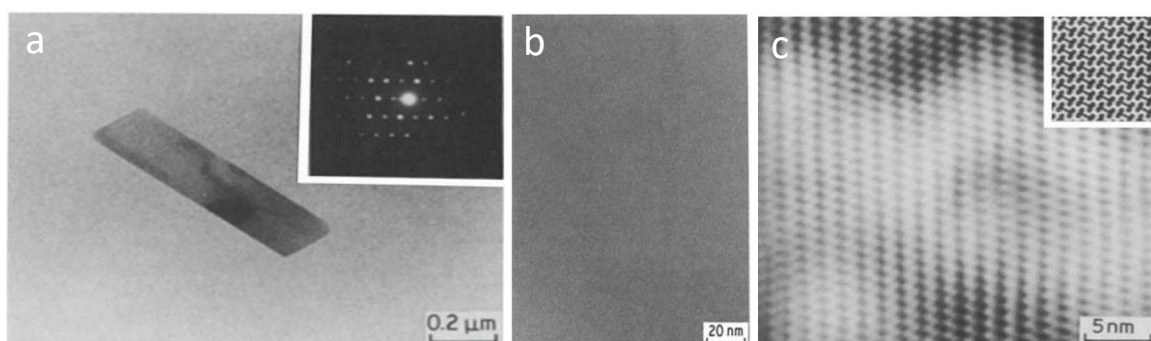


Figure 2.23 (a) Transmission electron micrograph and selected-area electron-diffraction pattern (inset) for a lamellar single crystal of polyDCHD.⁵⁶ The beam direction corresponds to [001] indicating that the polymer-chain direction is perpendicular to the crystal surface. (b) High-resolution electron micrograph from a polyDCHD single crystal similar to that in a. At least three intersecting sets of lattice fringes can be seen. The [100] direction is vertical. (c) Enlarged and filtered image obtained from b showing details of the shape of the individual molecules. The projected potential for polyDCHD parallel to [001] is also shown (inset). The [100] direction is vertical.

In another study by R. J. Young *et al.*⁵⁷, high resolution electron microscopy (HREM) was applied to a substituted polydiacetylene, poly(1,6-di(N-carbazoly)-2,4-hexadiyne). The lattice images of crystal planes with spacings less than 0.5 nm have been obtained from fibrous crystals formed by solid-state polymerization with the polymer chains parallel to the electron beam (Figure 2.24). The experimentally obtained molecular image was digitally filtered to remove background noise, and the enhanced image contained a regular pattern of dark patches resembling dumbbells. In comparison with computer simulations, the image was confirmed to be polydiacetylene molecules viewed along their chain axes with a resolution of better than 0.4nm. It has been demonstrated that lattice images from planes other than $(hk0)$ can be resolved, and images of (hkl) lattice planes have been obtained for the first time in polyDCHD. The crystals are lamellar, with the chains oriented perpendicularly to the substrate.

The electron beam can be parallel to the chain axis of such crystals, allowing lattice and molecular images to be obtained. Furthermore, they claimed that this is the first-time molecular images of a diacetylene polymer have been obtained, and the images have confirmed the crystal structure determined by other researchers.

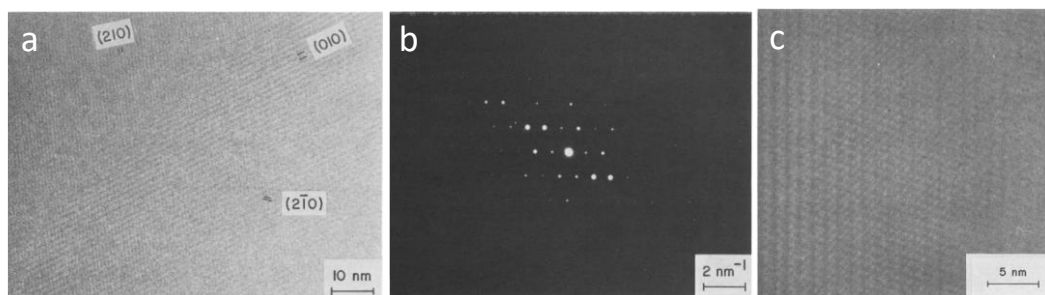


Figure 2.24 (a) Lattice image⁵⁷ of part of a well oriented polyDCHD crystal showing 3 sets of lattice fringes crossing each other. (b) $[001]$ diffraction pattern of the crystal in a. (c) Molecular image of polyDCHD enhanced by the spatial averaging technique using figure in a. The fringes are seen clearly crossing each other and small dark patches are seen at the crossing points.

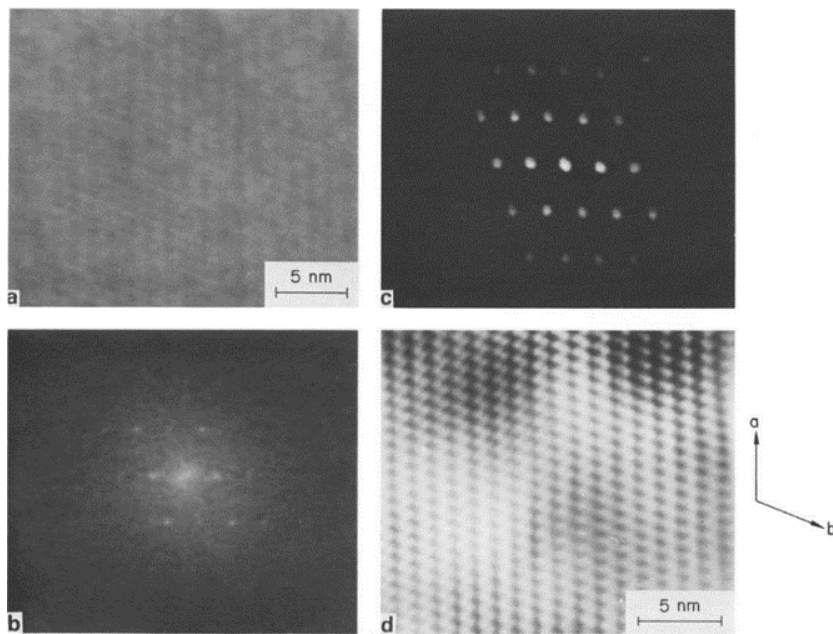


Figure 2.25 (a) Experimental molecular image⁵⁷ of polyDCHD placed in front of video camera. (b) Diffraction pattern of the image in a. There are 5 layers of discrete spots with a total of 22. (c) Diffraction pattern with apertures defined around each discrete spot. (d) Enhanced molecular image with the background noise removed. The vertical direction of the picture is the a-axis of the polymer.

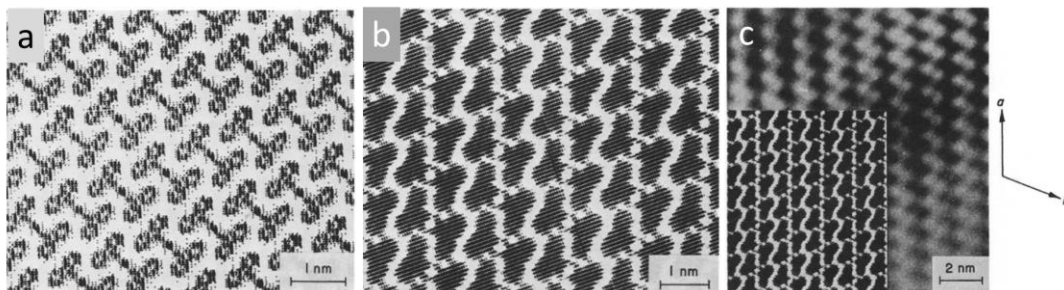


Figure 2.26 Projection of polyDCHD molecules on ab-plane.⁵⁷ (b) Computer simulated polyDCHD molecules viewed along the molecular axis. The image forming parameters are similar to those of the experimental image. (c) Comparison between the experimental enhanced image of polyDCHD molecules with computer simulated image.

C. Plummer¹¹ has revealed the lattice of PEN crystals by direct HRTEM imaging (Figure 2.27). However, the accelerating voltage was not mentioned, and the spacing of (210) and (020) in this work was too large. So far, this is the only lattice image obtained from PEN.

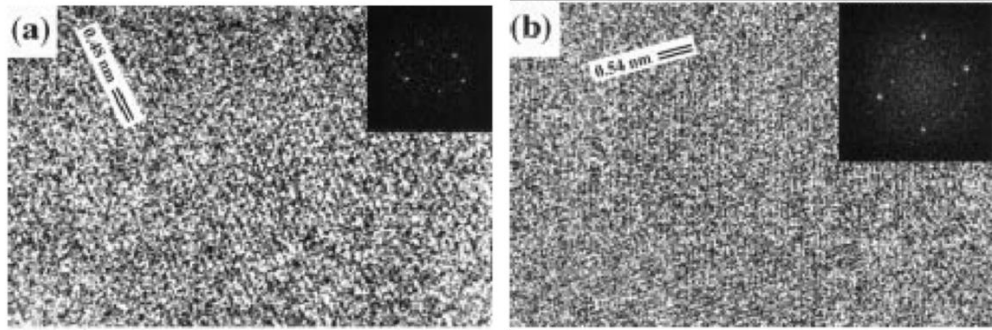
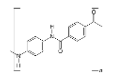
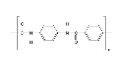
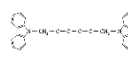
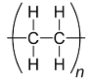
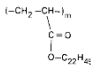

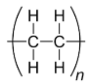
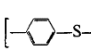


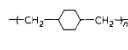
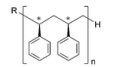
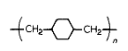

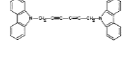
Figure 2.27 HREM micrographs from β phase lamella¹¹ and the corresponding power spectra (insert): (a) $[0\ 0\ 1]$ parallel to the beam and (b) $[0\ 1\ 1]$ parallel to the beam.

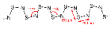
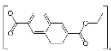
2.5.1.2 Technical details in previous works

Table 2.4 Technical details of TEM imaging of polymers in previous works

Specimen Info.				Microscope Info.		Data Info.		Ref.
Polymer	Chemical Structure	Crystal system	Sample type & preparation method	Accel. voltage (kV)	Microscope condition & damage control method	Data achieved	Key information	
Kevlar 49 Poly-(p-phenylene terephthal amide)		Monoclinic, Pn ⁴⁸	Fibre Fibres fragmented by ultrasonic irradiation, deposited on carbon-coated grids.	100	Beam density $3.28 \times 10^{-4} A \cdot mm^{-2}$	Electron DP, TEM image	Resolved {002} lattice fringes. Assess crystallite size and order. Critical dose of 0.433nm reflection last no longer than 120sec.	M. Dobb <i>et al.</i> ⁴⁷ (1975)
Kevlar, Kevlar 49, PRD 49. Three types of polyamide (PPT).		Monoclinic, Pn	Fibre (a) Ultramicrotomy: fibres embedded in Spur resin cut by diamond knife in a direction perpendicular to the fibre axis. (b) Fragmentation: fibres dispersed by ultrasonic irradiation in water. Sections and fragments deposited on carbon-coated grids.	100	Beam density of $1.64 \times 10^{-5} A \cdot mm^{-2}$.	Electron DP (WAED). TEM image (dark-field image, lattice imaging). Time-lapse series of electron DP.	0.645nm [002] meridional, 0.43nm [110] equatorial.	M. Dobb <i>et al.</i> ⁴⁸ (1977)
Polydiacetylene (PolyDCHD)		Monoclinic ^{58 59}	Single-crystal fibre Dilute solution of DCHD monomer form thin crystals on carbon film of standard TEM grid, polymerized by using γ rays with dose rate of 1Mrad/h.	100	Beam deflected between exposure.	Electron DP, TEM image	(010) lattice imaging with spacing of 1.2 ± 0.1 nm	Galiotis <i>et al.</i> ⁴⁹ (1984)

Polyethylene (PE)	 <p>No ring</p>	Orthorhombic	<p>polyethylene pyramids (200-1500 Å)</p> <p>Self-nucleation method⁶⁰. The lamellar thickness is estimated as 140Å.</p>	100	<p>BF condition, irradiation is 80 $C m^{-2}$ (50 $e/\text{Å}^2$)</p> <p>Focusing on neighbouring crystal, total expo time is 15-25s.</p>	High-resolution images, DP	<p>High-resolution lattice image with 0.4nm spacing resolved.</p> <p>Quantify molecular distortion factor in PE crystalline.</p> <p>Irradiation dose $D_c \approx 2400 C/m^2$ (150 $e/\text{Å}^2$), the DPs disappear.</p>	S. Giorgio <i>et al.</i> ³⁷ (1984)
Polyalkylacrylate (PAA)	 <p>No ring</p>	Hexagonal	<p>Two-dimensional lamellae (30Å)</p> <p>Anti-solvent precipitate</p>	100	magnification 5×10^5 .	High-resolution images, DP	<p>0.42nm spacing resolved</p> <p>Exposed dosage $D=15,000 C/m^2$ (936 $e/\text{Å}^2$)</p>	S. Giorgio <i>et al.</i> ³⁸ (1987)
Polytetrafluoroethylene (PTFE)	 <p>No ring</p>	Trigonal or hexagonal ⁶¹	<p>Single crystal</p> <p>Drops of the PTFE dispersion were deposited on 400-mesh TEM grids covered with a 10nm-thick carbon film, dried.</p>	120	<p>Plate mag$\times 46000$ Under-focus 100nm Expo. 2sec.</p> <p>Illumination accumulated dose 200 $e nm^{-2}$ to specimen</p>	Lattice images, DP Fast-Fourier transformed, filtered and back transformed, to produce a filtered image	0.49nm spacing of (100)	H. Chanzy <i>et al.</i> ⁵⁰ (1986)
Polyethylene (PE)	 <p>No ring</p>	Orthorhombic	<p>Single crystal</p> <p>Crystallized from dilute solution, dispersion drop on TEM grid.</p>	120	Irradiation dose accumulated to record image: $1.8 \times 10^{-11} C \cdot \mu m^{-2}$ (1.12 $e/\text{Å}^2$)	Lattice images Computer reconstruction	0.36nm spacing resolved	J. Revol <i>et al.</i> ⁵¹ (1986)
Poly (p-phenylene sulphide) (PPS)		Orthorhombic ⁶²	<p>Single crystal</p> <p>Fibrillar crystals grow from solution.</p>	200	Microscope operated with a minimum dose system (MDS)	High-resolution images, EDP	<p>0.43nm spacing resolved</p> <p>Total end-point dose (TEPD, dose needed for crystals to lose crystalline reflections in the diffraction pattern) of PPS crystal is $0.2 C \cdot cm^{-2}$ (125 $e/\text{Å}^2$) @200 kV</p>	A. Uemura <i>et al.</i> ⁵² (1988)

Poly(p-xylylene) (PPX)		<p>α-form: monoclinic, $C2/m$⁶³</p> <p>β-form: hexagonal or trigonal⁶⁴</p>	<p>Single crystal</p> <p>Polymer single crystal form in dilute solution, 10nm thick.</p>	500	0.5 coulomb cm^{-2}	<p>High-resolution TEM image</p> <p>Optical filtering performed with a hexagonal filter grating⁶⁵</p>	<p>0.44nm spacing resolved</p> <p>Total end point dose of PPX crystal is $0.5 C \cdot cm^{-2}$ ($312 e/\text{\AA}^2$)</p>	M. Tsuji <i>et al.</i> ⁵³ (1982)
Isotactic polystyrene (i-PS)		Trigonal	<p>Single crystal</p> <p>Crystallized from polymer dilute solution, mounted on TEM grid coated with carbon supporting film and examined without shadowing.</p>	120	Beam intensity controlled – low dose imaging technique was used.	Bright-field lattice imaging using CTEM	<p>Attainable resolution 0.5nm</p> <p>Lattice lines with 1.1 nm and 0.55 nm spacings were resolved.</p>	M. Tsuji <i>et al.</i> ⁵⁴ (1984)
B-form poly(p-xylylene) (PPX)		Trigonal, $P3$ ₅₅	<p>Single crystal</p> <p>Single crystal of polymer crystalized from dilute solution.</p>	500	\	<p>High-resolution TEM image, DP.</p> <p>Optical filtering method to reduce film graininess and to enhance the regularity of the image.</p>	0.25nm spacing resolved	S. Isoda <i>et al.</i> ⁵⁵ (1983)
Polydiacetylene (polyDCHD)		Monoclinic, $P2_1/c$ _{58, 59}	<p>Single crystal fibres</p> <p>Monomers crystalize on carbon support of TEM grid from dilute solution, solid-polymerized in TEM.</p>	200	Spatial-averaging method by photographic superposition over several unit cells ⁶⁶ ; Optical filtering technique ⁶⁵ .	High resolution image, DP	0.4nm spacing resolved	R. J. Young <i>et al.</i> ⁵⁶ (1985)
Polydiacetylene (polyDCHD)		Monoclinic, $P2_1/c$ _{58,59}	<p>Side-on and end-on single crystals</p> <p>Monomers crystalize on TEM grid from dilute solution, solid-polymerized in TEM.</p>	200	<p>Low beam intensity with Condenser aperture 300μm; Spot size 3.</p> <p>Scherzer focus⁶⁷.</p>	<p>High resolution image, DP.</p> <p>Image enhancement using a digital video frame-store system.</p>	<p>0.5nm for polymer chains perpendicular to beam.</p> <p>0.4nm for chains parallel to beam.</p>	R. J. Young <i>et al.</i> ⁵⁷ (1986)

α -form (SN) _x	 No ring	Monoclinic, $P2_1/c$ ⁶⁸ $P2_1/c$ ⁶⁸	Fibrillar or mosaic, fibrous nature crystals Iodinated (SN) _x was crushed into pieces at liquid nitrogen temperature to prevent the crystal lattice from destruction, fine fibrous specimen thus prepared.	200	mag×50000	DP, images Optical transform of the image	0.22nm spacing resolved	A. Kawaguchi <i>et al.</i> ⁶⁹ (1984)
Cellulose microfibrils	\	\	Cellulose microfibril is Single crystal Dehydrated cell-wall embedded in epoxy resin, sectioned with diamond knife.	200	Dose 300 e/nm ² Objective aperture 50μm	TEM images, EDP	0.39nm spacing resolved	J. Sugiyama <i>et al.</i> ⁷⁰ (1985)
Poly (Phthalocyaninato-Germoxane) [Ge(Pc)O] _n	Ge(Pc)(OH) ₂	\	Single crystal Thermal condensation polymerization in solid state from single crystals of monomer.	100	Objective aperture 60μm	Lattice images	1.5nm spacing resolved	X. Zhou <i>et al.</i> ⁷¹ (1985)
Poly (ethylene naphthoate) (PEN)		triclinic	Thin film casted and annealed β phase crystalline was obtained in pellet, then rubbed onto cleaved KCl single crystals, then the KCl was dissolved away.	\	At ambient temperature, with no objective aperture and using standard low dose techniques	HREM micrograph, fibre DP	point to point resolution 2.4Å Total end point dose derived from the extinction of the diffraction patterns was estimated to be 0.1 C · cm ⁻² (62 e/Å ²)	C. Plummer ¹¹ (1999)

2.5.1.3 Summary of previous works about imaging polymers with TEM

Among the previous studies on imaging polymer specimens in TEM, although systematic damage measurement appeared very recently, the methodology has iterated rapidly in recent years and critical doses have been determined for a number of polymers. Although the attempt to correlate beam damage with material properties works well, there is still no direct evidence about electronic excitement and radical generation that would link the observations to theoretical works about radiation chemistry.

Despite the limitations of hardware microscope techniques and the development of computing methods, impressive progress has been made in imaging polymers. Publications have claimed to have obtained lattice images that resolve the chemical structure. But the high-resolution images from these earlier works were obtained by reversed FT or simulation, and the molecular level details in lattice has not achieved from direct imaging.

2.5.2 STEM imaging

STEM imaging involves the use of an electron gun to generate a beam of electrons that is focused by a series of lenses to form an image of the electron source at the specimen. The electron spot, or *probe*, can be scanned over the sample in a raster pattern by stimulating scanning deflection coils. An image is formed by detecting scattered electrons and plotting their intensity as a function of probe position⁷².

The thin sample used in this study results in relatively small probe spreading within the sample, and the spatial resolution of the STEM is primarily determined by the probe size. The crucial image-forming optics are therefore those that are forming the probe before the sample. STEM can produce atomic-resolution images with probe sizes below the interatomic spacings in materials, which is a major strength.

2.5.2.1 STEM optics principle of reciprocity

To understand the optics of STEM, it is important to consider the implications of the *principle of reciprocity*⁷³. Consider elastic scattering so that all electron waves in the microscope have the same energy. Under these conditions, the propagation of the electrons is time reversible. It means points in the original detector plane could be replaced with electron sources, and the original source replaced with a detector, and a similar intensity would be seen (Figure 2.28). Applying this concept to STEM, it becomes clear that the STEM imaging optics (before the sample) are equivalent to the imaging optics (after the sample) in the conventional TEM (CTEM). Similarly, the detector plane in STEM plays a similar role to the illumination configuration in CTEM.

Concepts related to coherence derived from CTEM can be transferred to STEM by applying the principles of reciprocity. STEM imaging optics form a highly demagnified image of the source at the sample, which can be scanned over the sample. A bright-field (BF) image can be formed by detecting plane-wave transmission using a small detector placed on the optic axis in the far field and plotting the intensity as a function of probe position. The principle of reciprocity suggests that the image contrast will have the same form in both the CTEM and STEM cases.

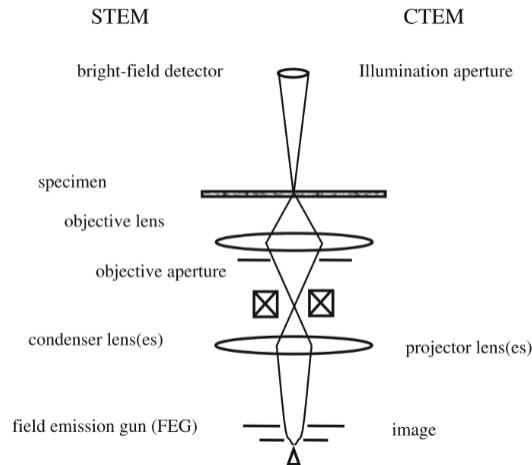


Figure 2.28 A schematic diagram showing the equivalence between bright-field STEM and HRTEM imaging making use of the principle of reciprocity⁷⁴.

2.5.2.2 Bright-Field (BF) and Annular Dark-Field (ADF) imaging

An area detector, such as a CCD, would be used to observe the transmitted electron intensity in the detector plane of the instrument. STEM imaging would detect only one signal, which would be plotted as a function of the probe position.

One such image is a STEM bright-field (BF) image, for which the bright-field disc in the Ronchigram are detected. A Ronchigram is a very large bright-field disc which overlaps with all the diffracted discs when the condenser aperture is removed (or at least set very large). There is lots of interference fringes or speckles if looking at an amorphous sample which are very sensitive to the lens aberrations so Ronchigram is usually used for tuning the aberrations such as astigmatism and comma, hence it is very useful for optical alignment. Typically, the detector will consist of a small scintillator, from which the light generated is directed into a photomultiplier tube. The BF detector will just be summing the intensity over a region of the Ronchigram (Figure 2.29).

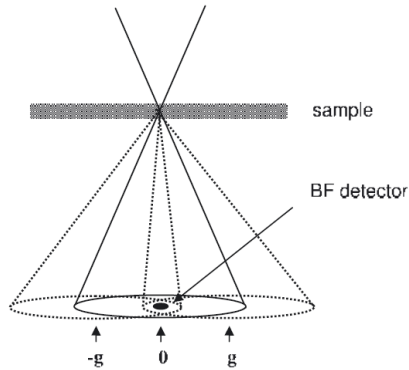


Figure 2.29 A schematic diagram showing that for a crystalline sample, a small, axial bright-field (BF) STEM detector will record changes in intensity due to interference between three beams: the 0 un-scattered beam and the +g and -g Bragg reflections.⁷²

Annular Dark-Field (ADF) imaging⁷² provides images that are relatively insensitive to small focusing errors, in which compositional changes are obvious in the contrast, and give atomic resolution images that are much easier to interpret in terms of atomic structure than their HRTEM counterparts, because it is an incoherent technique using the scattered electrons for imaging and avoids complications such as contrast reversal.

An ADF detector is a scintillator material annulus attached to a photomultiplier tube in a similar manner to a BF detector. Therefore, it measures the total electron signal scattered in an angle between an inner and an outer radius. Both radii can vary widely by changing the camera length, but typically the inner radius is in the range of 30-100 mrad and the outer radius is 100-300 mrad. Often, the centre of the detector is a hole, and electrons scattered to angles lower than the inner radius can pass through the detector to form either a BF image or, more commonly, an electron energy-loss spectrum. STEM makes highly efficient use of the transmitted electrons by combining more than one mode in this manner. In STEM ptychography, ADF and ptychography images can be acquired simultaneously by carefully setting the range of scattering angle each detector is collecting the signal from.

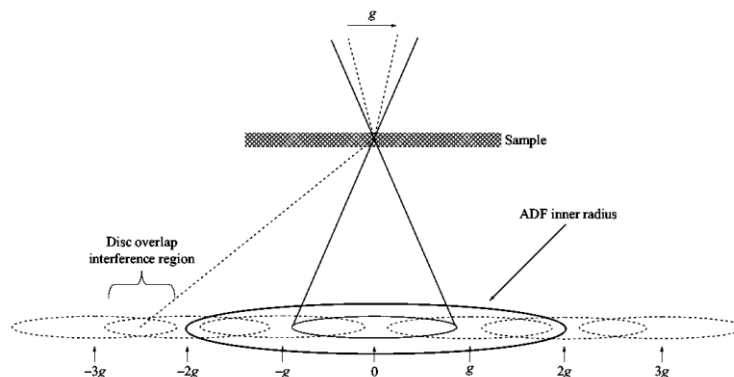


Figure 2.30 A schematic diagram showing the detection of interference in disc overlap regions by the ADF detector⁷². Imaging of a g lattice spacing involves the interference of pairs of beams in the convergent beam that are separated by g . The ADF detector then sums over many overlap interference regions.

M. Rothmann *et al.*⁷⁵ studied hybrid metal halide perovskites with STEM imaging to understand the mechanisms behind their impressive performance in photovoltaic and optoelectronic applications. The low-dose low-angle annular dark field (LAADF) STEM images, which resolve the atomic structure of the perovskites, revealed that the highly adaptive nature of the perovskite structure upon organic cation loss yields exceptional regenerative properties of the partially degraded material. The atomically localized information enabled the design of targeted methods to eliminate defects and optimize interfaces in the materials. Although LAADF is utilizing low-angle scattered electrons and suitable for imaging light element materials, the electron efficiency is not as high as BF imaging technique, because the proportion of scattered electrons is relatively small when imaging light element materials.

2.5.3 STEM ptychography

2.5.3.1 Principle of ptychography

Ptychography is an imaging technique that produces phase contrast by overlapping diffraction discs produced by coherent illumination, and can be applied to both crystalline and amorphous materials. In principle, ptychography can be performed with any coherent radiation source,

which means the waves of the illumination are in phase. Electrons accelerated by high voltage (hundred kilovolts) possess the short wavelength necessary to resolve atomic structure, the wavelength is 2.51pm at 200kV and 1.96pm at 300kV. Therefore, STEM ptychography is the appropriate method for imaging polymer crystallinity to reveal local structure in the semi-crystalline material.

STEM ptychography^{76,77} technique uses a 4D STEM dataset to address the critical challenges of imaging polymers. The data set comprises the two real-space dimensions of the probe scan and the two reciprocal-space dimensions of the diffraction pattern recorded at the STEM detector plane. By using Wigner-Distribution Deconvolution⁷⁷, the phase can be retrieved, and lens aberration can be corrected in post-acquisition computation. The resolution was equivalent to the highest scattered angle recorded in microdiffraction space. The embedded denoise capability in the deconvolution of Aperture Offset Functions improves the signal-to-noise ratio for low contrast specimens⁷⁸.

Additionally, optical sectioning can be used to obtain the structure of specimens along the viewing direction from a 4D STEM dataset recorded in only one scan, because images at various defocus value can be obtained by post-acquisition reconstruction. This is particularly useful for beam sensitive materials. Using a fast pixelated detector, a dataset recorded in low dose illumination could be amplified and provide sufficient signal for reconstruction.

2.5.3.2 Image reconstruction methods for 4D-STEM data

Ptychography reconstruction algorithms include non-iterative methods: Single-Side Band (SSB)⁷⁶ and Wigner-Distribution Deconvolution (WDD)⁷⁷; and iterative methods: Ptychographic Iteration Engine (PIE)⁷⁹ and its further developed version extend Ptychographic Iteration Engine (ePIE)^{80,81}. A major difference between non-iterative and iterative methods is

that the real-space sampling is defined by real-space probe step in SSB and WDD, but limited by reciprocal-space sampling in ePIE.

The assumptions for using WDD are that the specimen's thickness is so thin that it can be assumed to be a weak phase object, there is no multiple scattering of incident beam and that the illumination is fully coherent. Theoretically, all the information collected in the diffraction plane can contribute to WDD reconstruction³. In terms of method suitability judgement, SSB is only suitable for thin samples that can apply Weak Phase Object (WPO) approximation – this condition makes SSB suitable for my work because polymer thin specimen can be treated as WPO. Meanwhile, the contrast transfer function (CTF) of SSB can be modified with convergence semi-angle⁸² for various spatial frequencies of specimen (Figure 3.12).

A powerful extended function – Optical Sectioning is possible in WDD/SSB algorithm because WDD/SSB images can be reconstructed at different defocus besides the experimental value, hence we can obtain focal series image stack. Depth of Field (DOF) is a key factor in optical sectioning, which I made full use for polymer crystalline structure analysis in Chapter 7. To enable optical sectioning, the specimen shouldn't be thinner than the DOF, or too thick that cannot apply WPO approximation.

The ePIE algorithm updates probe function and transmission function of specimen alternatively.^{80,81} ePIE has been experimentally shown to achieve super-resolution beyond conventional diffraction limit. Regarding low frequency transfer, ePIE also shows a good transfer for low spatial frequency signals⁸³ that exists on organic and biological samples. ePIE also shows the capability to reconstruct a high-resolution phase image acquired in low-dose condition. ePIE has multiple advantages, but a lot of technical details about it remain unclear. Although the data collection speed is the same for iterative and non-iterative methods, the speed of data processing of iterative methods is usually slower than non-iterative methods.

Another widely used phase contrast STEM imaging method – Differential phase contrast (DPC)^{84,85} was proposed in 1974. The source of differential phase contrast is the shift of bright field disk on diffraction plane caused by electric or magnetic field in specimen plane⁸⁶. However, DPC is affected by low frequency noise quite easily and has artifacts in low spatial frequency that widely exist in polymer specimen.

Other phase recovery techniques include holography, which requires special optics to split the beam into a reference and transmitted beam, and exit wave reconstruction which is a plane wave TEM method that can precisely measure aberration, but acquisition of the required defocus series is time consuming and not dose efficient, thus not practical in experiments for polymer specimen.

2.5.3.3 Imaging light element, beam sensitive materials with STEM ptychography

Imaging molecular heterostructures like semi-crystalline polymer specimens requires the imaging system to have an efficient phase contrast transfer at both low and high spatial frequencies⁸⁷. According to the phase contrast transfer function (PCTF)⁸⁷, STEM ptychography is capable of resolving low and high spatial frequencies.

The development of fast electron detectors and data processing capabilities has enabled electron ptychography to extend the capabilities of STEM by allowing quantitative phase images to be formed simultaneously with incoherent signals. H. Yang *et al.*⁴ demonstrated this capability as a practical tool for imaging complex structures containing light and heavy elements, and used it to solve the structure of a beam-sensitive carbon nanostructure (Figure 2.31). The contrast of the phase image was maximized through the post-acquisition correction of lens aberration. The compensation of defocus aberrations was also used to measure three-dimensional sample information through post-acquisition optical sectioning.

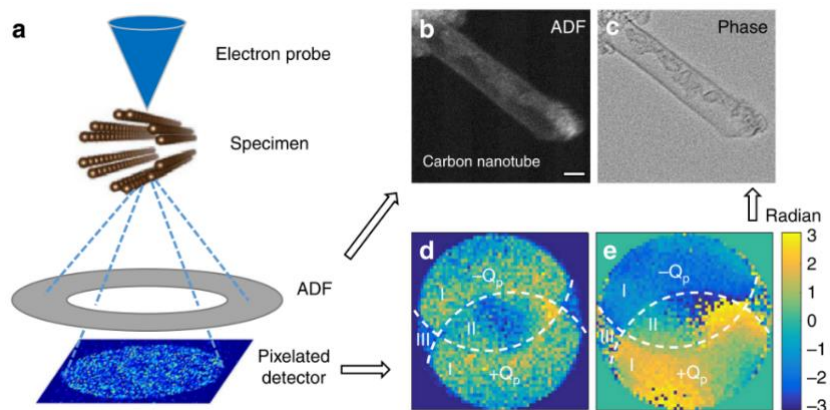


Figure 2.31 Simultaneous atomic resolution incoherent and coherent imaging.⁴ (a) An ADF detector collects the dark-field signal to form (b) an incoherent Z-contrast image. (c) The simultaneous phase image is reconstructed using ptychography. (d, e) An example of the modulus and phase of the complex matrix $G(K_r, Q_p)$ at a single spatial frequency Q_p .

STEM ptychography can also be performed by scanning a defocused probe over the sample with substantially overlapped probe positions. The phase can then be successfully reconstructed with high spatial resolutions by using a relatively small number of probe positions. J. Song *et al.*⁸⁸ used defocused ptychography with a monolayer of MoS_2 as a model system to investigate the effects of electron dose on the phase and resolution of reconstructions, with the aim of finding a viable application in phase reconstruction of biological materials at high resolution without causing damage. The phase of ptychographic reconstruction under low-dose conditions has been evaluated by varying the DP acquisition time and the overlap ratio. They were able to achieve reconstruction at 1.58 Å resolution at a dose of $403 \text{ e}/\text{Å}^2$, indicating potential for further reduction of dosage for phase reconstruction.

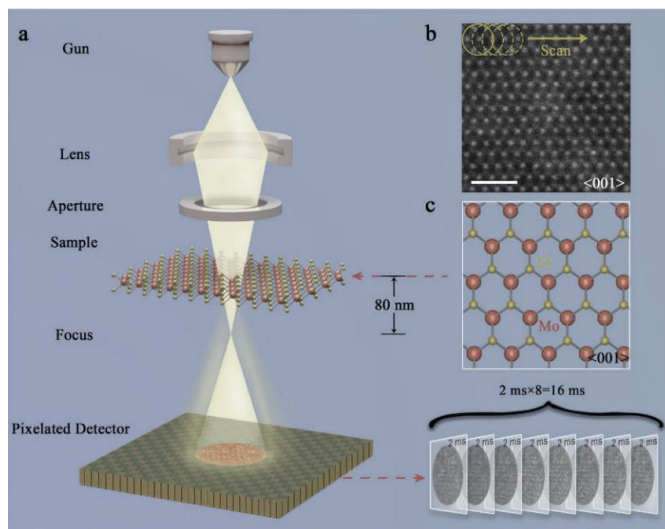


Figure 2.32 (a) Schematic of the experimental optical configuration used for ptychographic reconstruction.⁸⁸ The sample was 80 nm above the beam focus. (b) HAADF image of a MoS₂ monolayer oriented along [001]. The circles represent the probe, and the arrow indicates the direction of the probe movement. Eight diffraction patterns were generated at each position of the probe scan. The acquisition time for each diffraction pattern was 2ms. (c) Projected atomic models of MoS₂ along [001]. The yellow balls represent sulphur atoms, and the red balls molybdenum atoms.

J. Lozano *et al.*⁸⁹ applied electron ptychography to image the lithium-rich cathode which is a beam-sensitive material containing light and heavy elements. The electron ptychography technique allows residual lens aberration to be corrected at the postprocessing stage, thereby avoiding the need for further beam damage and providing an aberration-free reconstructed phase image. They obtained aberration-free reconstructed phase images of Li-rich cathodes in pristine, charged, and discharged states. The images allowed them to determine the position of the lithium and oxygen atomic columns even during the amorphization of the surface induced by the electron beam.

The binary ptychography⁹⁰ was introduced in the work of imaging beam sensitive materials carried out by the P. Nellist group. This paper discusses the use of focused-probe electron ptychography for imaging beam sensitive samples that contain light elements. In focused probe ptychography, a key parameter for controlling the electron irradiation fluence is the detector frame time, which determines the probe dwell time. Data recorded at frame rates up to and

exceeding 10 kHz and with beam currents of less than 1pA will contain only a few hundred electrons. For a typical detector size, most pixels will receive no electrons, while a minority will receive one or more electrons. Despite the very sparse data, ptychographic images can be obtained with a substantial signal-to-noise ratio compared to other STEM modes.

C. O'Leary *et al.*⁸² have reported the application of focused probe ptychography using binary 4D datasets using STEM. By changing the bit depth of a counting detector, such that only values of 0 or 1 can be recorded at each pixel, this technique allows one to reduce dwell time and increase frame rate, thereby reducing the electron exposure of the sample for a given beam current. Atomically resolved phase contrast of aluminosilicate zeolite (ZSM-5) was obtained from the sparse diffraction patterns with isolated individual electrons.

2.6 Summary and goal of thesis

This chapter reviews the state-of-the-art understanding of PET, PEN crystalline structures and characterization methodologies.

In the crystalline form for PET, only one type of 'triclinic one-chain unit cell' was found, but the cell parameters varied due to the thermal history and processing parameters, such as extrusion speed and draw ratio. For PEN, two crystalline forms α and β had been identified. α -form includes only triclinic one-chain unit cells, while β -form includes triclinic one-chain and monoclinic four-chain unit cells. There was also a γ -form two chain cell found, but no further investigation was reported. The crystalline form and unit cell parameters of PEN were found to be closely related to the sample fabrication method and annealing conditions. PET and PEN structural information was obtained primarily through indirect methods, such as X-ray and electron diffraction.

Direct imaging is a useful method for revealing local structure, which is particularly important for semi-crystalline polymers containing multiple domains like PET and PEN. It has been a long-standing challenge to produce a polymer EM sample that contains abundant structural information and is reproducible, because the specimen would only be imaged once due to beam damage. A valid sample preparation method must be developed first, because the sample preparation methods explored in earlier EM characterization studies were not well optimized.

Other challenges for imaging polymers with (S)TEM include beam damage issues and low contrast generated by light elements in polymer materials. Based on the work of other researchers, the critical dose is a significant property of the materials that must be quantified, and a suitable imaging mode has not yet been found for polymers.

Accordingly, the goal of this thesis is to develop a methodology for directly imaging PEN, PET semi-crystalline specimens, and to resolve the local crystalline structure, because a high-resolution image of polymer is essential to a deeper understanding of its crystalline structure.

3 Experimental method

In this chapter, the development of experimental methodology will be described. Firstly, the novel sample preparation method used in this work, including the procedure and logic behind it, will be illustrated. Then, before data acquisition from (S)TEM, the appropriate low-dose condition will be explored, due to the beam-sensitive nature of the polymer specimen and the low contrast generated by light elements. The dose of each data acquisition mode will be calibrated. Thirdly, the appropriate imaging mode and suitable microscope condition selection will be discussed. This includes detectors and imaging mode selection for image acquisition and contrast improvement, which were all under the precondition of low-dose illumination. In the final part, the advantages and reasons to apply ptychography for image acquisition will be discussed. As a result of this methodology, high quality data can be achieved and used for structural analysis of semi-crystalline polymer materials, i.e., PEN and PET. The material PEN was purchased from Goodfellow, and PET was kindly supplied by LOTTE – a polymer manufacturer. The raw material of PEN and PET are both granules fabricated by extrusion with high purity sufficient for crystallization study.

3.1 Sample preparation method development

3.1.1 New sample preparation method is needed

A high-quality and reproducible specimen is essential for imaging with a microscope. The sample preparation method needed to be precisely controlled and reproducible, because specimen thickness is crucial for (S)TEM imaging, which requires a well-controlled procedure, and the polymer specimen cannot be used repeatedly due to irreversible beam damage. Mainstream methods of polymer sample preparation generated specimens of borderline quality and the reproducibility of the results was quite variable. Using a method commonly used in

laboratories for the preparation of polymer specimens, thin film polymer specimens were prepared by dropping dilute solutions of the polymer onto an anti-solvent, usually water, to solidify and form a thin film floating on the surface of the anti-solvent. Once stabilized, the thin film was then picked up with a TEM grid held by tweezers. In this method, the thickness could be controlled by varying the concentration of solution, but the spread-out of the droplets could not be controlled, so the thickness was non consistent, resulting in many failed samples, since thickness can significantly affect the (S)TEM image quality. Furthermore, the amount of material in the thin film was usually very small, and the amount of crystallinity generated by annealing was not sufficient for structural analysis, thereby not providing enough structural information in the material characterization, e.g., TEM ED.

The nature of the material presented a challenge in obtaining a thin and reproducible high quality PEN specimen. Its high surface tension causes shrinkage, because the thin film possesses a very high surface-to-volume ratio, and it tends to reduce its exposed surface by rolling up. In addition, the softness of the material means that it is often impossible to maintain its shape even under very low stresses.

In polymer semi-crystalline materials, multiple orientations of overlapping crystallites as well as amorphous phases are widely present. However, a thin film with distinct orientations distributed across the lateral dimension of the sample-plane would be more suitable for (S)TEM image interpretation. As a result, a novel and reliable sample preparation method had been developed to fabricate specimens of the desired quality for high-resolution (S)TEM imaging.

3.1.2 Procedure of sample preparation method development

This newly developed sample preparation method of polymer specimen for (S)TEM characterization involves spin casting a dilute solution of the polymer onto a water-soluble

substrate to produce thin films (<100nm). The substrates used in this experiment are freshly cleaved single crystal KCl (purchased from Agar) and sugar crystals (purchased from food store). Accordingly, the thickness could be controlled by manipulating the spin-coating parameters and the solution properties, which included the solvent property and solution viscosity.

The advantage of this new sample preparation method was its suitability for characterization with (S)TEM, since the low thickness (<100nm) would facilitate better alignment of the optics. Meanwhile, the specimen transfer process is gentler on the specimen, preventing damage to the soft sample. The substrate is dissolved in water, and the polymer thin film floats on the surface of the water and can then be picked up with a TEM grid. In the following section, the steps involved in the procedure, and technical details for each will be discussed.

3.1.2.1 Thickness of thin film

The thickness of film was controlled by the concentration of solution and spinning speed of spin-coater. In the case of a specific polymer and a particular solvent, the concentration of the solution is a major determinant of its viscosity. Concentration and viscosity typically exhibit a positive correlation beginning with a linear line and then the gradient increasing with concentration, since molecular entanglement begins to affect viscosity when concentration reaches a 'critical point'. Prior to the critical point, the viscosity is positively linearly correlated with concentration, because the concentration of the solution is so low that molecules are assumed not to be entangled with each other. After the critical point, the molecule entanglement would cause the viscosity to increase exponentially. The linear part of the concentration should be chosen here for two reasons. First, the molecules with minimal entanglement would tend to form simpler structures within a domain of the solid-state polymer,

and second, it would be easier to predict the thickness with a linear correlation to concentration.

The targeted film thickness for (S)TEM characterization is less than 100nm for electrons to transmit and generate sufficient signals on detectors, while the upper limit of thickness can slightly vary for different materials. In previous work⁹¹, a mixed solvent was used, and this was achieved with a solution of 1~2 wt.%. This study used the sole solvent 2-chlorophenol and the thickness-concentration relationship was measured in the range of 1~2 wt.%. Figure 3.1 illustrates the relationship between PEN thin film thickness and solution concentration. There was a positive linear correlation between thickness (measured by ellipsometry) and concentration.

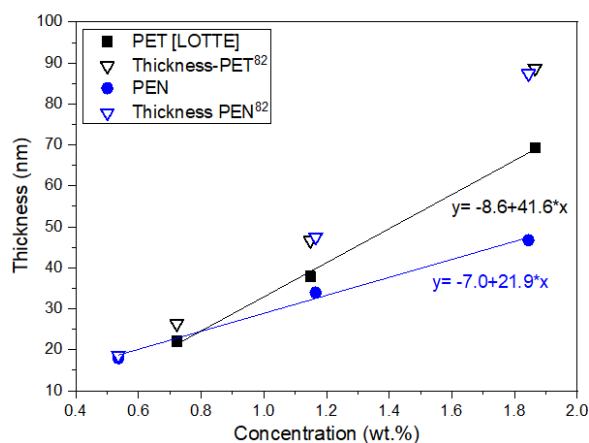


Figure 3.1 Experimental data of correlation between film thickness and concentration of PEN solution.

In some studies^{92,93}, the relationship between thin film thickness, spinning parameters, and polymer solution properties was comprehensively investigated as shown in Figure 3.2. In practice, however, the key factors to ensuring a film with predictable thickness were the concentration of the solution and the speed of spinning. Due to the linear correlation between

thickness and concentration, the formula can be simplified as formula (3.2), which shows the negative power law correlation between thickness and spinning speed:

$$D \propto \omega^{-0.5} \quad (3.2)$$

where D is the thickness of the thin film, and ω stands for spinning speed – round per minute (rpm).

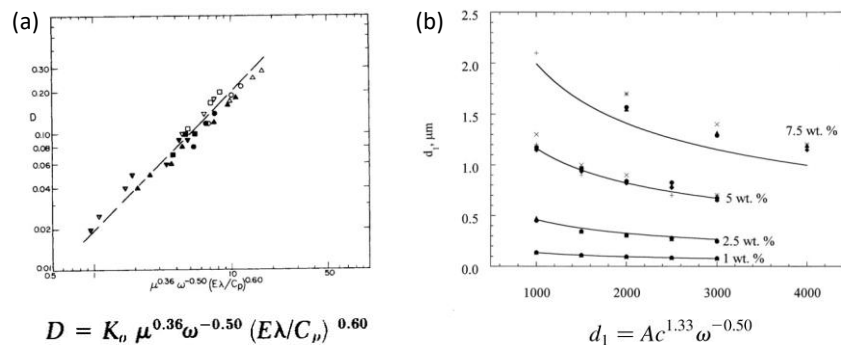


Figure 3.2 Correlation between thin film thickness and solution properties. (a) the straight-line relationship⁹² suggests that the film thickness D can be expressed as $D = K_a \mu^{0.36} \omega^{-0.50} (E\lambda/C_p)^{0.60}$. The range of viscosity covered for the data plotted was 2.99 – 66.1 cP, spin speed ω was 200 – 1000 rpm. Solvent: acetone, methyl ethyl ketone (MEK), and cyclohexanone. The polymers used in the organic solvent coating solutions were poly (vinyl butyral) and cellulose acetate. The polymer used in the aqueous coating solutions was a bone gelatine. (b) PMMA film thicknesses as function of spinning speed and initial coating solution concentration from results of ellipsometry methods⁹³. PMMA was resolve in chloroform.

Spin coating consists of two stages based on the mechanism of spinning, acceleration and stabilization. The parameter 'spinning speed' refers to the speed of the stable stage, whereas the speed of both stages has an impact on the thickness and quality of the thin film. Acceleration speed is selected according to the affinity of the solvent and substrate. In general, the better the affinity, the higher the speed could be used, because the solution tends to attach to the substrate while being pulled out by centrifugal force, whereas a poor affinity would result in pinholes caused by the solution "rolling out".

Usually, the acceleration speed was set to allow the system to reach its stable speed within 10 to 30 seconds, i.e., 100 to 300 rpm if the stable speed is 3000 rpm. In this work, spin-coating parameters were also optimized based on the quality of the sample as viewed in (S)TEM, based on the thin film uniformity on the grid.

Static dispensers are more likely to produce centrosymmetric films than dynamic dispensers in terms of solution dispensing. Because in static dispensers, solution will be dispensed in the centre of substrate before spinning started; while in dynamic dispensers, solution will be dispensed when the spinning speed stabilize. Static dispensers were also more appropriate for a small substrate such as a cleaved KCl crystal.

Table 3.1 Optimized parameters for spin-coating

Substrate	Spin coating			
	Dispense	Speed (rpm.)	Acceleration	Time (sec.)
Glass	Dynamic dispenser	3000	300	60
Silicon	Dynamic dispenser	3000	300	60
Sugar	static dispenser	3000	300	50
Potassium chloride (KCl)	static dispenser	3000	100	40~50

3.1.2.2 Thin film uniformity and substrate-solvent affinity

The affinity of the solvent to the substrate is a factor that is often overlooked but has a significant impact on the uniformity of thin films. If the solution does not adequately wet the substrate, pin-holes may form. Due to the low concentration of solution used in this study, the affinity between solution and substrate would be approximately equivalent to that between solvent and substrate.

The affinity was determined by measuring the contact angle between the substrate and the solvent in use. As shown in Figure 3.3, the affinity of the solvent (2-chlorophenol) is much better

with KCl and sugar than with silicon. The reason for this may be that the solvent is polar, as is KCl and sugar, while pure silicon is non-polar.

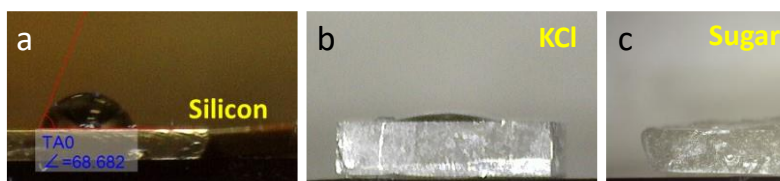


Figure 3.3 Contact angle between 2-chlorophenol and (a) single crystal silicon substrate (68.7°), the water-soluble substrates (b) cleaved single crystal KCl (~13°), and (c) cleaved single crystal sugar (~0°).

3.1.2.3 Annealing for crystallization

The PEN samples in the literature were crystallized from the amorphous state achieved by mechanically extruding^{10,94} the solid or by melting^{8,95}. Despite mechanical mixing in extrusion can remove large amount of crystallinity, it is impossible to eliminate all predominant orientations and residual strains in the sample, which may affect the process of nucleation and growth of crystals. In contrast, the as-spin-cast thin film is thought to be perfectly amorphous and strain free, because it was made from a very dilute solution with rapid solvent evaporation (quench) in which the molecules were well dispersed, and the entanglement of molecules was minimized. The material was in an ideal condition to observe polymer crystallization since it has no thermal history.

These thin film samples were then annealed at a temperature slightly below the melting temperature (T_c) to crystallize. Before annealing, it was important to thoroughly remove the solvent from the thin film to ensure that the crystallization would not be affected by the presence of the solvent. To accomplish this, the solvent can be dried from the surface in a fume hood for several hours, followed by drying in a vacuum oven at 40°C overnight to ensure that the solvent (2-chlorophenol) has been completely evaporated. The PEN and PET specimens were

annealed for crystallization after drying overnight. The PEN thin films did not start crystallizing until the annealing temperature reached 240°C according to the *ex situ* AFM images throughout the process of increasing annealing temperature, which is close to its melting temperature. Hence PEN was annealed at 240°C for 30min on a hot plate. PET specimens were annealed at 130°C for 1.5 hours under vacuum at 10^{-5} mbar to induce crystallization, the condition was optimized with AFM imaging to find the condition of the surface crystallinity formation.

3.1.3 Advantages of the new sample-preparation method

The newly developed sample preparation method allowed for the preparation of very thin polymer specimens of precisely controlled thickness based on the experiments of thin film fabrication optimization, and the procedure was highly reproducible. Due to the modified transfer procedure, the specimen's features were well preserved when it was transferred to the TEM grid following annealing. There is no need to increase contrast with shadowing by metal coating, because the contrast will be improved by the imaging technique.

As shown in Figure 3.4, the sample preparation development has evolved through three versions. The earliest version (Figure 3.4a) was based on a literature method²⁴, which had improved aspects such as thickness control and film peeling off, but in my experiments, the surface features were removed during the sample transfer step. To address this shortcoming, the substrate was changed from silicon to a water-soluble substrate.

The first trial of a water-soluble substrate was with cleaved single crystal sugar used as purchased, which fixed the sample transfer issue. Nevertheless, since sugar decomposes at around 100°C, but the crystallization temperature (T_c) of PEN is above 200°C, it was impossible to anneal PEN thin film on it. Then, another water-soluble substrate was used – single crystal potassium chloride (KCl), a thermally stable material with melting point at 770°C. Consequently,

the thin film can be directly spin-cast onto the substrate for thickness control, the sample annealed on this substrate, and then the water-soluble substrate can be removed without touching the thin film while peeling off it.

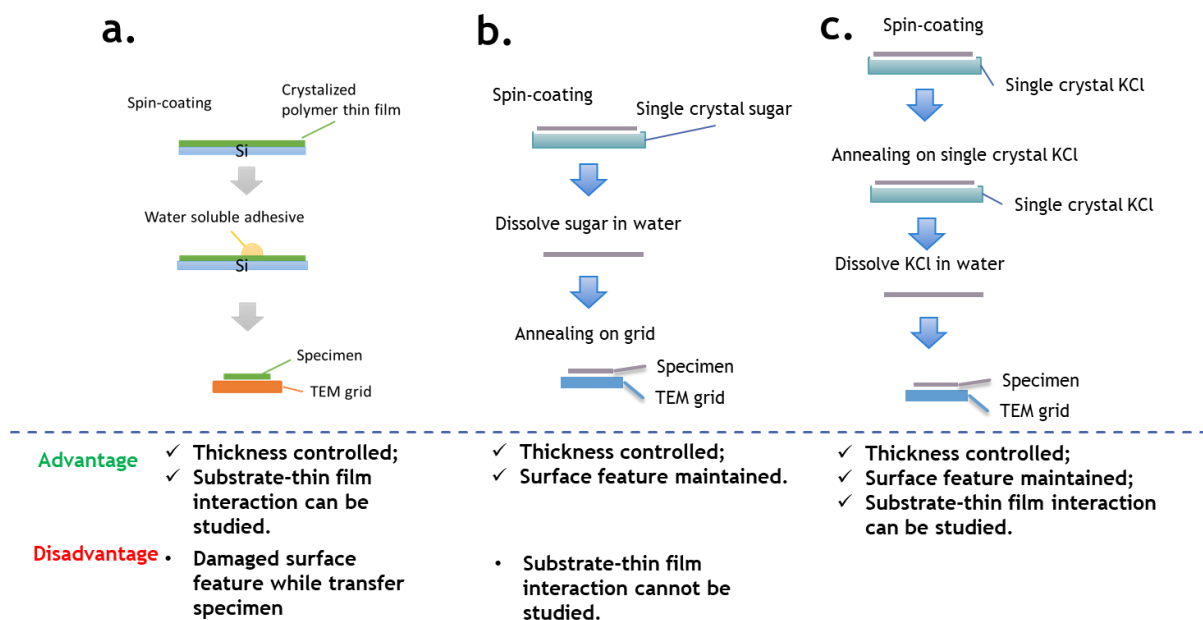


Figure 3.4 Sample-prep method evolution. (a) conventional sample preparation method with Silicon substrate. (b) Sugar single crystal substrate. (c) Single crystal KCl was used as the substrate.

3.2 (S)TEM illumination dosage quantification

Since polymers consist of light elements, and they are easily damaged by an electron beam, it is necessary to make use of phase contrast in the imaging technique, as well as low-dose illumination.

Table 3.2 Equipment information of microscopes used in this work

Microscope model	Source	Accelerating voltage (kV)	Mode used	Camera / Detector
------------------	--------	---------------------------	-----------	-------------------

JEOL 3000F	Field emission gun (FEG)	Max. 300	Diffraction, TEM imaging	CCD camera (4096*4096 pixel)
JEOL ARM200F	Cold field emission source (CFEG)	Max. 200	STEM imaging	JEOL BF/ADF detectors GATAN BF/ADF detectors
			Ptychography imaging	4D Canvas pixelated detector.
JEM ARM300F	CFEG	Max. 300	STEM imaging	JEOL BF/ADF detectors
			Ptychography imaging	4R Medipix

3.2.1 Microscope parameters of low-dose condition

In this work, all data collection will be conducted under low-dose illumination, so the parameters of the microscope that are required to achieve appropriate conditions will be investigated first. The three main factors that can be applied to achieve low dose conditions in (S)TEM are acceleration voltage, beam current, and exposure/dwell time.

3.2.1.1 Accelerating voltage

For high-resolution imaging of polymers, high accelerating voltage is preferred not only because of the low wavelength, but also because of the type of beam damage caused by high voltage, 'knock-on damage', is not a major concern for polymers. It is crucial to determine the range of voltage that is suitable for a beam-sensitive material based on the type of radiation damage. Polymers are primarily damaged by radiolysis as reviewed in Chapter 2. The radiation sensitivity to radiolysis steadily increases as the accelerating voltage is reduced³. Hence high-voltage is preferred for imaging polymer specimens. The accelerating voltages used in this work are 200kV and 300kV for (S)TEM characterization.

3.2.1.2 Beam current

The most straightforward approach to reduce dose is to lower the initial beam current. The initial beam current is set by the 'emission current' on the microscope, and the 'actual' incident beam current that interacts with the specimen can be measured using the methods described in the following section 3.2.2.

The schematic of the beam (Figure 3.5) illustrates the beam current density interacting with the specimen. When a parallel beam illuminates a larger area than the area recorded by the camera, it is challenging to monitor the exposed area of a beam-damaged material. Nevertheless, it is relatively easy to keep the dose per unit area low because the beam is spread out and the density of primary electrons interacting with the specimen is diluted. The illuminated area of a convergent beam is smaller, since the beam is focused on one tiny spot and all electrons in the beam hit the specimen through the probe, therefore it is easier to track the exposed area.

TEM parallel beam will be applied in the 'critical dose' measurement later in this work, with beam current of 192pA calibrated by a Faraday cup, while a convergent beam was applied for the STEM imaging, including BF, ADF-STEM image and ptychography dataset acquisition. The typical emission current used on the ARM200F operated at 200kV was 3~4 μ A, while the incident beam current was ~0.56pA based on calibration with a Faraday cup, which was much lower than the value in TEM diffraction mode. The details of the measurements will be demonstrated in section 3.2.2.

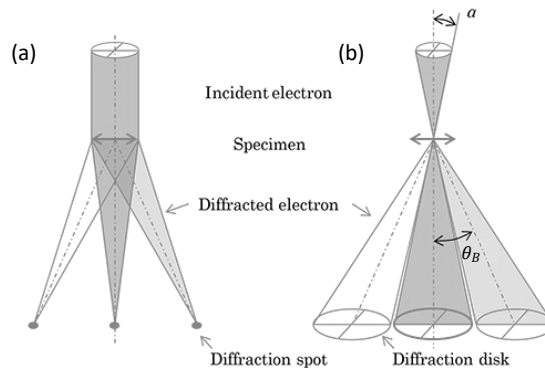


Figure 3.5 Schematic of (a) parallel beam and (b) convergent beam in diffraction mode.

3.2.1.3 Exposure/dwell time

The exposure time will control the dose interacting with the specimen once the beam current and mode have been chosen. The 'dwell time' in STEM imaging is the duration of the exposure, which determines the dose in each pixel, i.e., the probe position. Section 3.2 will illustrate the dose rate calibrations for each data acquisition mode.

Because the objective was to ensure that the data acquired were from the pristine structure rather than the altered structure caused by the electron beam, an area of the sample near to the region of interest was used for optics alignment and specimen focus adjustment, before moving to the nearby region of interest for imaging.

In principle, a sufficient dose is required to produce a reasonable level of signal-to-noise ratio (SNR), and thus generate the contrast in the image. When imaging polymer with low dose illumination, the intrinsic image contrast of polymer, which is low with a standard dose, will be worse because of the low SNR. So, the dwell time was set to be as short as possible to minimize damage, while still generating sufficient contrast to resolve the feature.

3.2.2 Methodology development for *in situ* dose estimation

The dose used for polymers has approached the limit of measurement capability of the detectors, and a small fluctuation in the dose can cause considerable discrepancies. Consequently, a methodology of *in situ* dose estimation was independently developed based on equipment manuals to monitor the dose in real-time and evaluate the validity of data acquired from beam-sensitive specimens. The dose calibration was performed on the microscopes used in this work, including the 'gain' factor for the detectors and the 'dose rate' of the multiple imaging modes employed. Then a vacuum image will be acquired after the dataset with identical microscope condition to estimate the dose. The development of a protocol for dose estimation and measurement ensured reproducibility, and the results were comparable across the different equipment.

3.2.2.1 Dose estimation with vacuum image for electron DP in TEM

The dose estimation method will enable *in situ* dose measurements for DPs acquired at various microscope conditions, with varying beam current and current density. Using this method, regardless of how different the microscope condition may be, all that is required is to acquire a vacuum image under the same conditions as the data acquisition, and the actual dosage can be estimated. In essence, the idea behind this method is to calibrate the conversion factor, or 'gain' of the camera in use, so that every time a dose estimate is required, one can simply acquire an image from vacuum under the same microscope conditions, then convert the intensity (counts) into the number of incident electrons.

Step 1: dark correction of the 'beam image'

During the preparation stage, the 'beam image' and 'dark image' needed to be acquired. The 'beam image' was acquired by arranging the beam to fill most of the camera recording field, so that all electrons in the beam were within the scope and participated in the generation of this image, so that the total intensity reflected the total number of electrons in the beam.

The 'dark image' was used to deduct the counts resulting from 'dark current'. The counts of intensity that were not generated by the electron beam are cataloged as "dark current". As there would be photons from the environment, or electric current generated from resources other than the electron beam, these would also be included in the data recorded by CCD camera. The influence of dark current would be greater in a low-dose work than in a standard illumination situation. Thus, the dark image was recorded without illumination, and the purpose was to record the total "dark current" of the CCD camera so that it could be deducted later. Prior to the collection of each new 'stack of images', a new dark image was acquired with the same exposure time, ensuring that the dark reference was representative of the imaging conditions. 'Stack of images' refers to a series of images acquired with the same parameters, and the intensity of the images can be averaged or summed up.

Additionally, these conditions were essential to ensure the calculation was accurate:

- i. These images were recorded in vacuum to ensure all the electrons in the beam arriving the camera without scattering.
- ii. Magnification was low, e.g., 40k, so that the whole beam would be included into the scope of camera, and all the electrons in the beam would be included in the conversion factor calculation.
- iii. All images were 'raw CCD images', as the raw image would be the original record of the counts on CCD camera, which can be achieved by setting the acquisition on Gatan software as 'unprocessed'.

- iv. The binning parameter was set to 1 in this experiment, so the pixel number in one image is 4096×4096 for this camera on JEOL 3000F (Table 3.2).
- v. The number of images in each stack was set to an even value for convenience in calculating the stack average.

Once the images needed for correction were ready, 'dark correction' could be performed by subtracting the dark image from the targeted image, which will be saved as 'dark-corrected image'. Dark correction could be conducted for multiple images or stack of image, and the dark image and corrected image should be from the same image stack.

Step 2: calibrate the beam current with Faraday cup

It is crucial to calibrate the beam current arriving at the sample plane, which should be much lower than the 'emission current' setting due to the electrons lost at each lens and aperture. A Faraday cup is a metal cup attached to the end of the TEM sample holder. It collects the electrons that fall into it and transfers the current to a picoamp meter connected to the holder outside the microscope. Thus, the beam current can be measured and calibrated.

During the beam current calibration, the microscope was set to various conditions of image acquisition, including the emission current, spot size, and aperture. To measure the current, the beam was condensed into a small probe and made to fall into the Faraday cup. In practice, the movement of the beam to locate the Faraday cup was invisible, because the Faraday cup is not transparent to the electron beam. Thus, the maximum current reading on the connected picometer indicated the location where the entire beam entered the Faraday cup.

Step 3: 'Gain'– 'conversion factor' of camera calibration

In this calibration method, the key step is to determine the conversion factor, which is also called 'gain' in the manuals of cameras and microscopes. This 'gain' value would enable the conversion between the image intensity and the incident electron interacting with the specimen.

The gain of the detector in primary electrons/counts ($e/count$) can be estimated from beam images. Following the previous steps, a dark corrected beam image stack was created. The mean intensity pixel value of this dark corrected image stack was noted down. The gain of detector in $e/count$ can be calculated using the following formula:

$$\text{Conversion factor} = \frac{1}{g} = \frac{n \cdot C_{mean}}{(I \cdot t/e)} \quad (3.3)$$

where g is the 'gain', n is the total number of pixels in the image, C_{mean} is the mean intensity pixel value in counts, $n \cdot C_{mean}$ gives an estimate of the total counts in the image. I is the beam current, t is the acquisition time and e is the absolute value of electron charge. So, the unit of 'Conversion factor' is (counts/primary electron).

Step 4: *in situ* dose estimation with a vacuum image

Once the CCD gain has been calibrated, the dose of images acquired with it in any condition can be estimated *in-situ*. Immediately following the acquisition of an image from a specimen, the microscope condition should be maintained while moving away the specimen and finding a hole in the carbon membrane. This will allow the dose to be estimated during the image acquisition session. A vacuum image was acquired with the same exposure time as the image that requires dose estimation. Then, the mean intensity pixel value of this vacuum image was obtained and could be converted to primary electron number in each pixel with the gain

(*e/count*) measured from the camera in use. Having calculated the number of primary electrons in each pixel and divided by the real pixel size, the electron number interacted with the specimen in real space unit area was known.

3.2.2.2 Dose estimation with phosphor screen

The use of phosphor screens is an alternative method for estimating dose *in situ*. The current displayed on the phosphor screen is a quick method of determining the beam current. Despite the accuracy may be affected by the sensitivity of the phosphor screen, this is a useful method for monitoring the microscope condition during the experiment, which is particularly useful for low-dose work. The delicate microscopes are equipped with highly sensitive phosphor screens and can be used to monitor the beam current conveniently, the essential step is to calibrate it with Faraday cup,

The calibration of the phosphor screen was similar to that of the beam image acquisition. First, the phosphor screen was illuminated with a parallel beam. Because the current density read on the phosphor screen was calculated by: *beam current/screen area*, here it is necessary to ensure that the beam is within the phosphor screen and almost covers the entire screen, hence the area of the phosphor screen would be approximately equal to the area of the 'illuminated area' of the beam. Having noted down the current density (*pA/cm²*), the beam current can be calculated as follows: *beam current = current density × screen area*.

The beam current was measured with a Faraday cup by condensing the beam to a small probe and allowing it to fall into the cup, as indicated by the maximum current read by the picometer. The beam current calculated from the phosphor screen should be calibrated, and therefore identical to the current measured with the Faraday cup.

The diameter of phosphor screens on 3000F: big screen – 160mm; small screen – 25mm; area of small screen: 4.91 cm^2 . The small phosphor screen was used to read the current because of its higher sensitivity.

3.2.3 Dose quantification in data acquisition experiments

The purpose of dose calibration on a microscope is ultimately to quantify the dose to which the specimen was exposed during acquisition. This section will demonstrate how the dose estimation method can be applied in practice, and how the dose used to achieve the corresponding DP or image can be calculated.

3.2.3.1 Dose quantification for electron DP

In the preparation stage, the camera 'gain' value would be calibrated following the steps in Section 3.2.2. Figure 3.6 shows the beam image and dark image that were acquired for the calibration of the camera gain (conversion factor). It is necessary to ensure that all these images are recorded as "raw images" by selecting "unprocessed" in DigitalMicrograph suit. Dark correction was accomplished by subtracting the dark image from each beam image in the same stack; in DigitalMicrograph, this can be achieved by selecting 'process -> simple math -> a-b' and choosing the images (a) and (b) in Figure 3.6. The beam current was 192pA calibrated by the picometer connected to Faraday cup.

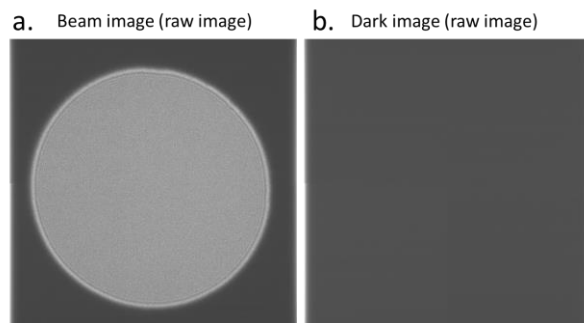


Figure 3.6 Images acquired for camera gain calibration. (a) Beam image. (b) Dark image. All these images are “unprocessed” raw images.

Table 3.3 Parameters of image acquisition for calibration

Data set	Microscope Parameter							Camera setting			Faraday cup	Phosphor screen
	Mode	No. of Image	Mag	Spot Size	ConA	ObjA	SAA	Bin	Expo. Time (sec.)	Frame No.	Beam current (pA)	Current density (pA/cm ²)
dose meas urement_ dataSet t01	beam image	3	40k	5	3	\	\	1	0.04	1	192	14.6
	beam image	4	40k	5	3	\	\	1	0.04	1		
	beam image	5	40k	5	3	\	\	1	0.04	1		
	beam image	6	40k	5	3	\	\	1	0.04	1		
	dark image	7	40k	\	\	\	\	1	0.04	1	\	3.8

Note: ConA – Condenser Aperture. ObjA – Objective Aperture. SAA – Selective Area Aperture.

The stack of dark corrected beam image was used to obtain the mean intensity pixel value. The conversion factor ‘gain’ was calculated with formula (3.3) and the parameters are: $n=4096*4096$, $C_{mean}=245.05$, $I=192$ pA, $t=0.04$ sec., $e=1.602*10^{-19}$ C. Hence, the gain value of the camera was obtained as: Conversion factor = $\frac{1}{g} = \frac{n \cdot C_{mean}}{(I \cdot t / e)} = 85.76$ (counts/primary electron).

Consequently, a vacuum image was acquired under the same illumination as the data acquisition. The key point here was that the brightness of the beam should not be altered. In TEM imaging mode, the intensity is controlled by the current density, so maintaining the

intensity as the same is crucial for dose estimation for the image of interest. In practice, the whole set of apertures and spot-size selected were kept the same while diffraction pattern recording and this vacuum image acquisition.

Here is one example of dose calculation for electron DP of PEN from a vacuum image (Figure 3.7) under the same microscope condition. Figure 3.7 was acquired through a hole of carbon membrane, some amorphous carbon was involved at the corner of the image, but the intensity was not affected to an observable level therefore the influence of the carbon can be negligible.

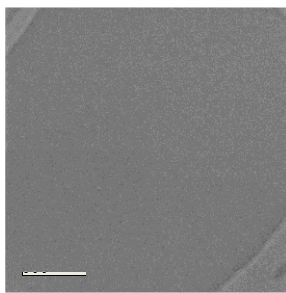


Image Num.	Position	Total exposure time (sec.)	Frame	Mean intensity rate (count/sec. per pixel)
4	Pore (vacuum)	1.0	10	2532.47

Figure 3.7 Vacuum image from same microscope condition. Notes about the term in table – Exposure time: the TOTAL exposure time for Figure 3.7, which was sum of 10 frames. Mean intensity: mean intensity in the Figure 3.7 directly readout in DigitalMicrograph. Mean intensity rate = Mean intensity/Exposure time, where Exposure time = 1sec.

The calculation and parameters obtained are as below:

Mean intensity rate: $2532.47 \text{ count}/(\text{pixel} \cdot \text{sec})$

Convert to electron number in image: $2532.47/85.76 = 29.53 \text{ e}/(\text{pixel} \cdot \text{s})$

Pixel size: $0.22 \times 0.22 \text{ nm}^2$, Magnification = 50k.

Electron number on specimen (real space): $29.53/0.22^2 = 595.59 \text{ e}/(\text{nm}^2 \cdot \text{s}) = 5.96 \text{ e}/(\text{\AA}^2 \cdot \text{s})$

Another example of dose calculation from vacuum image for PEN electron DP. Vacuum image (Figure 3.8) from same microscope condition with same brightness:

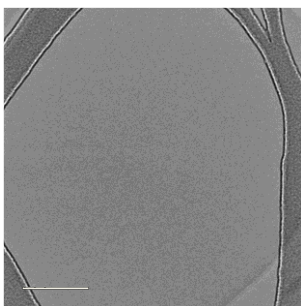


Image Num.	Position	Total exposure time (sec.)	Frame	Mean intensity rate (count/sec. per pixel)
11	Pore (vacuum)	1.0	10	2458.79

Figure 3.8 Vacuum image from same microscope condition of targeted PEN diffraction patterns. Notes about the term in table – *Exposure time*: the TOTAL exposure time for Figure 3.8, which was recorded as sum of 10 frames. *Mean intensity*: mean intensity in the Figure 3.8 directly readout in DigitalMicrograph. *Mean intensity rate* = Mean intensity/Exposure time, where Exposure time = 1sec.

Therefore:

Mean intensity: $2458.79 \text{ count}/(\text{pixel} \cdot \text{sec.})$

Convert to electron number in image: $2458.79/85.7568 = 28.67 \text{ e}/(\text{pixel} \cdot \text{s})$

Pixel size: $0.22 \times 0.22 \text{ nm}^2$, Magnification = 50k

Electron number on specimen: $28.67/0.22^2 = 578.25 \text{ e}/(\text{nm}^2 \cdot \text{s}) = 5.78 \text{ e}/(\text{\AA}^2 \cdot \text{s})$

Using the value of dose rate, the dosage for any diffraction pattern can be calculated with the exposed time.

3.2.3.2 Dose quantification for BF-STEM and ptychography images

The dose calculation method in TEM imaging can be applied to STEM imaging, however, the difference in the data recording mechanism requires a modification of the dose calculation in STEM. STEM images were acquired using the ARM200F.

Gain calibration of CCD camera follows the same protocol. The unprocessed beam image and dark image were acquired using the GIF camera on the ARM200F (Figure 3.9a). Because the GIF camera is located at the end of the entire optics channel, it is relatively easy to include the entire beam within the recording area of the camera. Dark correction was performed by subtracting the dark image (Figure 3.9b) from each beam image in the same stack as described in the established method. The beam current was measured by a Faraday cup to be 14pA.

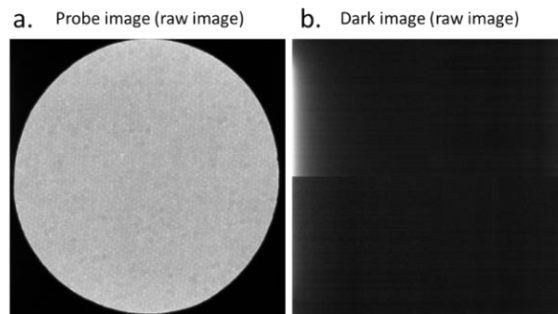


Figure 3.9 (a) probe image and (b) dark Image without processing were acquired on GIF camera (CCD) of JEOL ARM200F for gain calibration.

To get the gain calibration for GIF camera on ARM200F, a dark corrected probe image – an image including all electrons in the probe, was used. Mean intensity pixel value of the averaged dark corrected beam image was 829.50. The conversion factor was calculated with the parameters: $n=1024 \cdot 1024$, $C_{mean}=829.50$, $I=14$ pA, $t=0.4$ sec., $e=1.602E-19$ C, $n \cdot C_{mean} = 87e+7$ counts, Conversion factor = $\frac{n \cdot C_{mean}}{(I \cdot t/e)} = 24.857$ counts/primary electrons.

The following example illustrates typical microscope conditions used for acquiring images from PEN specimens. Figure 3.10 shows a vacuum image acquired under the same illumination conditions as the PEN BF-STEM image.

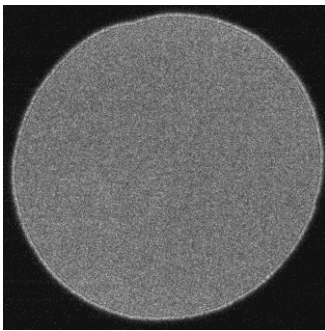


Image Num.	Position	Total exposure time (sec.)	Frame	Mean intensity rate (count/sec.)
1	vacuum	0.4	1	8.823e+7

Figure 3.10 Vacuum image acquired at same microscope image as experimental PEN BF-STEM image for dose estimation.

Sum intensity of this probe image: $3.529e+7$ *count*.

Ratio to the counts in 14pA beam is $(3.529e+7)/(87e+7) \approx 4.06\%$

So, the beam current in this experimental condition also equal to $4.06\% * 14pA = 0.56pA$

By considering exposure time, Mean intensity rate = $8.823e+7$ count/sec. in this probe image

Dwell time for BF-STEM imaging is $1.6\mu S$, each probe position: $8.823e+7 * 1.6e-6 = 141.168$ *count*

Convert to electron number in one probe position (per pixel): $141.168/24.857 \approx 5.68 e$

Alternative calculation of electron from beam current, which can be used for result double-check:

Sum intensity of this probe image: 3.529×10^7 *count*. Also equal to 0.56pA.

$$0.56 \text{pA} \times 1.6 \times 10^{-6} \text{ sec} = 8.96 \times 10^{-19} \text{ C}$$

$$8.96 \times 10^{-19} \text{ C} / 1.602 \times 10^{-19} \text{ C} \approx 5.59 \text{ e (each probe position)}$$

Dwell time for ptychography data acquisition with 4000fps is 2.5^{-4} sec.

$$\text{Each probe position: } 8.823 \times 10^7 * 2.5 \times 10^{-4} = 22057.5 \text{ count}$$

$$\text{Convert to electron number in a probe position: } 22057.5 / 24.857 = 887.38 \text{ e}$$

Electron in unit area of the whole image equals to the value of $e/\text{\AA}^2$ in each pixel:

electron in probe/pixel area

$$\text{For the whole image: } 887.38 / 0.4^2 = 5546 \text{ e}/\text{\AA}^2 = 8.88 \text{ C}/\text{cm}^2$$

3.3 (S)TEM imaging microscope setup

When a probe is scanning through a thin specimen consisting of light elements, the amplitude is not expected to change significantly, and the phase contrast is much more useful. The high resolution phase image was reconstructed from the 4D-STEM dataset by using Single Side Band (SSB) reconstruction⁴, which is suitable for specimens that WPO approximation can be applied. Low dose illumination was also used to acquire 4D-STEM data from PEN and PET specimens. The microscope setup was the same for the acquisition of BF- and ADF-STEM images, as well as for the ptychography datasets. In this section, the criteria for 4D-STEM data acquisition will be discussed regarding ptychography reconstruction.

3.3.1 4D-STEM data acquisition

3.3.1.1 Beam convergent semi-angle α

The STEM beam convergence semi-angle α is the parameter that characterizes the probe because it determines the disc overlapping (Figure 3.11a). With a thin specimen, the probe size dominates the resolution⁹⁶ in STEM images, and the probe size is controlled by α . STEM imaging is useful for beam sensitive materials because the scanning beam can be precisely controlled over a radiated area of the specimen. Additionally, α also defines the collection angle of BF and ABF images, since α controls the radius of the bright field disc and the ratio of overlap between the central and first-order diffraction discs.

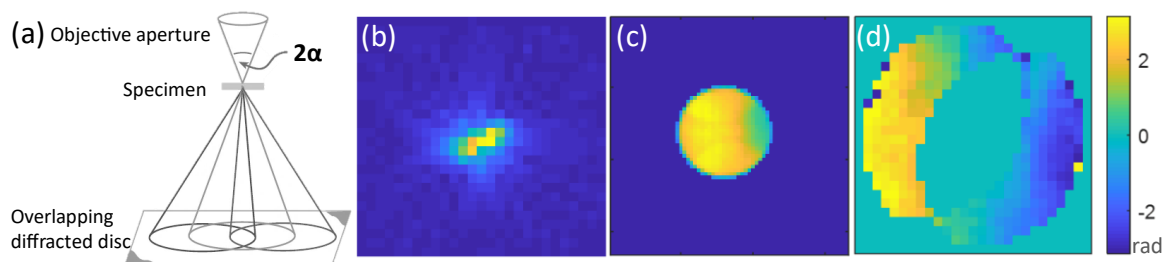


Figure 3.11 (a) The optic schematic showing how the value of beam convergent semi-angle α influence the overlapping of diffracted disc. (b) Probe function plotted from experimental data by including experiment parameters. The probe-step will be used to sample the specimen in real space. (c) Central disc and overlapped regions in one CBED in reciprocal space. This figure also depicts how the disc was sampled by pixels on the detector, which can be applied to 'synthetic bright-field image'. (d) Phase of G function at spatial frequency, which is used for phase image reconstruction.

The beam convergent semi-angle α was adjusted by selecting the objective aperture, which is also referred to as 'the second condenser aperture C2' in microscope manuals. In Figure 3.11c, the central disc overlaps the first order diffraction disc in one CBED, which is desirable for ptychography. To obtain the pattern in Figure 3.11c, the objective aperture should be large enough to form overlapping diffracted discs, so that coherent interference occurs. However,

the aperture should not be too large so that too many electrons are allowed into the beam, since the illumination should be maintained sufficiently low.

The selection of the objective aperture was also influenced by the phase contrast transfer function (PCTF)⁸³ (Figure 3.12). The large objective aperture is preferred for features of high spatial frequency, e.g., 31.5 mrad, which offers coverage across the whole range of spatial frequency, but the transfer efficiency is lower than 0.2 for spatial frequency <10 mrad. Smaller objective apertures are preferred for resolving low spatial frequencies. In polymer crystallinity images, low spatial frequency is also widely observed, and sufficient transferred signals are needed for both high and low spatial frequency.

Polymer images involve both high and low spatial frequencies. In PEN images, the spatial frequency is primarily between 0~20mrad when converted to mrad at accelerating voltage of 200kV. According to the PCTF of ptychography in Figure 3.12, the best choice should be an objective aperture with an α of 14.4mrad. A series of optimization experiments have demonstrated that this selection of objective aperture is suitable for imaging polymer specimens.

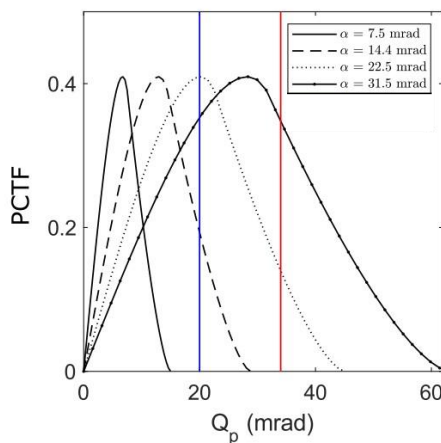


Figure 3.12 PCTF plotted against spatial frequency Q_p for convergence semi-angles of 31.5 mrad, 22.5 mrad, 14.4 mrad, and 7.5 mrad calculated using the intrinsic PCTF for SSB ptychography^{83,5}.

3.3.1.2 Pixel size/probe step

The probe-step in the specimen plane should ensure sufficient sampling in real space. According to Nyquist theory, the pixel size in (S)TEM imaging should not be larger than half of the spacing to resolve it in an image. In polymer crystals, the range of spatial frequency is quite wide, and the smallest spacing in PEN crystalline structure that can be resolved was not known before the images were successfully reconstructed. The pixel size selection was based on the beam damage and the camera capability, since smaller pixels result in a higher dose per unit area with fixed magnification, and a higher frame rate for the camera. Table 3.5 lists the pixel sizes used for imaging PEN and PET.

3.3.1.3 Camera-length for recording specific diffraction signals

Originally, camera-length was used to adjust the magnification of optical devices. (S)TEM uses the concept of camera-length as an analogy to optical devices, but in practice it is achieved by varying the strength of the magnetic field of the lens instead of mechanically moving the lens. In STEM, the camera length influences the magnification of the bright field disc on the detector plane, which determines the outer angle of BF imaging and the inner angle of ADF imaging. This was used to adjust the bright-field disc on the pixelated detector during 4D-STEM data acquisition, to best resolve the discs and overlapped regions, as shown in Figure 3.13. In this work of imaging polymer specimens, a camera length of 12 cm was used because the central disc and overlapped regions could be adequately sampled by pixels in the pixelated detector.

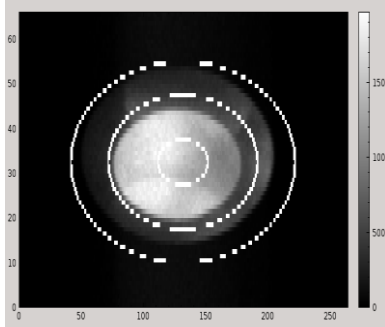


Figure 3.13 Bright field disc on pixelated detector. The central disc involves the overlapping regions and forward scattered beam.

3.3.2 STEM Imaging mode classification based on scattering angle β

The selection of the detector based on the scattering angle of transmitted electrons scattered by the specimen is one of the most important aspects of practical STEM imaging. STEM uses the collection angle of the detector to determine which electrons are selected to produce images (Figure 3.14).

Since the beam convergent semi-angle α has been selected, the boundary between BF and ADF imaging will be the circumference of the central bright-field disc. The signal within the area of the bright field disc collected by a circular detector would produce a BF image, while an annular detector would produce an annular bright-field (ABF) image. Signals with scattering angles β higher than the convergent semi-angle α would be collected with an annular detector, resulting in ADF images. In accordance with the scattering angle range β , ADF images can be further classified as Low Angle ADF (LAADF), Middle Angle ADF (MAADF) and High Angle ADF (HAADF) by the range of signal collecting angles. In synthetic images from 4D STEM datasets, the angles of imaging mode are defined by applying masks (Figure 3.16).

The collecting angles of each detector of the microscope used in this study have been calibrated (Figure 3.15). PEN and PET are composed of light elements which scatter electrons at relatively low angles, so BF and LAADF detectors were selected for STEM image acquisition.

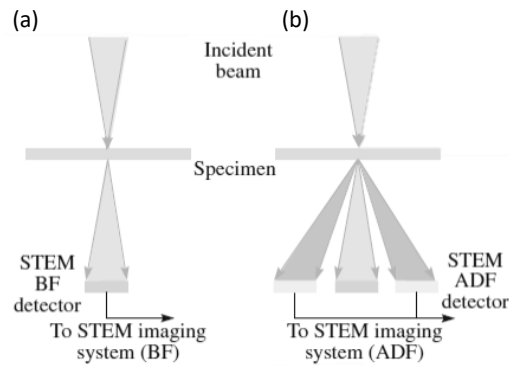


Figure 3.14 In STEM, (a) an on-axis detector was used to collect direct electrons to form BF image, and (b) an off-axis annular detector was used to collect scattered electrons to form ADF images.

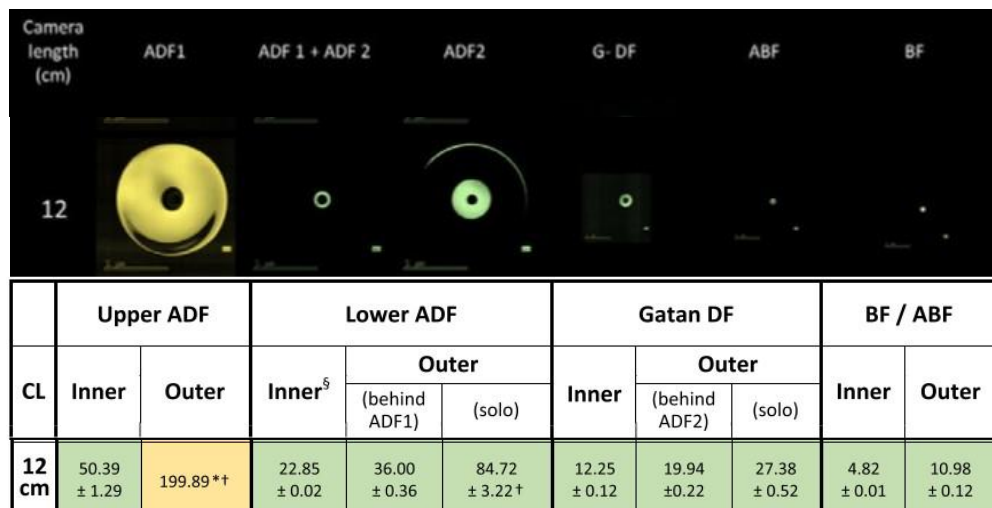


Figure 3.15 Collecting angles of detectors measured by swung-beam⁹⁷ scanning across all the available camera-lengths and for various detector configurations shown with the same relative scale: these include the upper dark-field (ADF1), the lower dark-field (ADF2), and the Gatan dark-field (GDF). As a special case, the scans of ADF2 when it is inserted behind ADF1 is also shown. The JEOL bright-field detector (whose outer-angle is defined by an aperture) is shown both with and without the beam-stop giving ABF and BF modes, respectively.

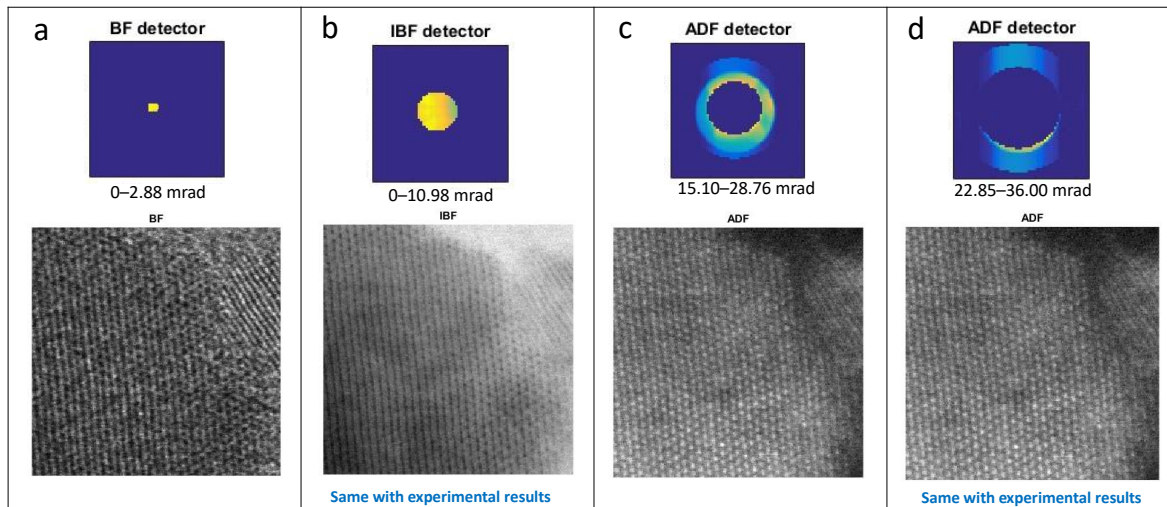


Figure 3.16 Synthetic images using 4D-STEM data from PEN and plotted with ptychography codes. (a) The bright-field detector of 0~2.88mrad, and the corresponding synthetic BF image. (b) The bright-field mask of 0~10.98mrad and corresponding synthetic image. The BF detector used for experimental image is the same as this mask. (c) A lower angle ADF mask and corresponding synthetic image. (d) ADF mask with the same collecting angle as experimental LAADF imaging. The contrast of features in a and d are highly matched with experimental BF-STEM and LAADF images. The images in b and d are achieved with signals selected by masks from the range of collecting angles same with experimental BF-STEM and LAADF images, and the contrast of features are the same as the corresponding images in Figure 3.17.

3.4 STEM imaging of PEN, PET with low-dose condition

In each of STEM imaging modes, a single type of signal would be detected and plotted as a function of the probe position. The scattering angle determined the type of detector to use. Bright-field images include BF- and ABF-STEM images; ADF images include LAADF, MAADF, and HAADF images according to the range of scattered angles across dark-field.

Because of the light elements that compose polymers, the scattering angle of majority electrons is relatively low, so BF and LAADF were the appropriate imaging modes chosen to accomplish work of imaging PEN and PET specimens. Shown in Figure 3.17, BF and LAADF images were acquired simultaneously on JEOL ARM200F under low dose condition with the parameters in Table 3.4. The BF and LAADF images in Figure 3.17 – experimental acquired images, are consistent with Figure 3.16(b) and (d) – synthetic images using 4D-STEM data.

The main features in specimen can be revealed by LAADF imaging (Figure 3.17), but further details beyond the strongly diffracted planes remain unresolved. Because LAADF is a dark-field image formed by summing signals of low angle scattered electrons, and the proportion of scattered electrons is generally low for light element materials like polymers. Hence the dose efficiency of LAADF is lower than bright-field imaging techniques.

Table 3.4 Microscope parameters of BF-STEM and LAADF images acquired from PEN specimen

Microscope condition		e-beam	Imaging parameters					Scanning		
Accelerating voltage	Spot size	Emission current	Detector	β	α	Camera Length	\times Mag	Pixel number	Pixel Size	Dwell time
kV	C	μ A	\	mrاد	mrاد	cm	M	x-direction	nm	μ S/pixel
200	8	3	GATAN BF	10.98	14.38	12	20	1024	0.01	1.6
			JEOL ADF2	22.85 ~ 36.00				2048	0.005	

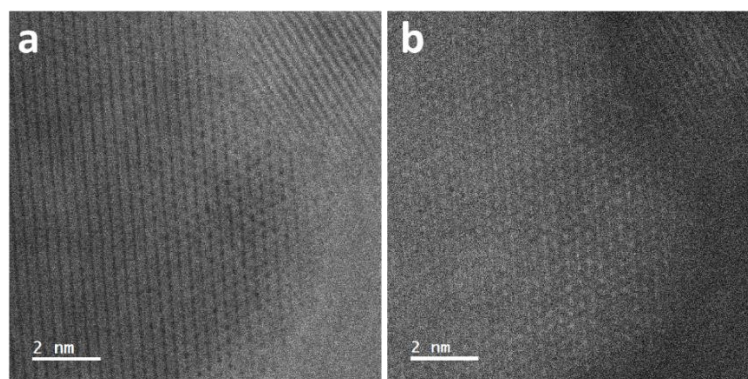


Figure 3.17 Microscopic (a) BF-STEM image and (b) LAADF image acquired simultaneously from PEN specimen, using the parameters in Table 3.4. The specimen region in these images is the same area where the 4D-STEM data was acquired, which was used in Figure 3.16.

3.5 STEM reconstructed images of polymer

3.5.1 Ptychography Single Side Band (SSB) reconstruction

STEM ptychography Single Side Band (SSB) reconstruction utilizes the overlap between the first- and zero-order scattered discs². The fast pixelated detector records the diffraction pattern at every probe position, resulting in a 4D dataset. The 4D STEM dataset comprises the two real-space dimensions of the probe scan and the two reciprocal-space dimensions of the diffraction pattern recorded at the STEM detector plane. STEM ptychography^{2,76,77} is a powerful application of the 4D data set for reconstructing the specimen complex transmission function, including the phase.

It has been shown experimentally that the phase image is robust to low-dose conditions⁴ suggesting that ptychography may be a powerful method for low-dose conditions. Taking the Fourier transform of the 4D dataset with respect to probe position results in a complex 4D matrix $G(K_f, Q_p)$, which carries the phase information of the interference between diffracted and undiffracted beams. Figure 3.18a, b shows an example of the modulus and phase of the complex matrix $G(K_f, Q_p)$ at a single spatial frequency Q_p where two diffracted beams $+Q_p$ and $-Q_p$ (indicated by dashed lines) overlap with the undiffracted direct beam. The areas labelled as area ① are double-overlap regions where one diffracted beam interferes with the direct beam and area ② is the triple-overlap region where both diffracted beams and the direct beam interfere. Area ③ has no interfering beams and is only noise and is therefore not used in the ptychography reconstruction. By using the phase from all spatial frequencies, the phase image can be reconstructed⁴ (Figure 3.19). The resolution of reconstructed image was corresponding to highest scattered angle.

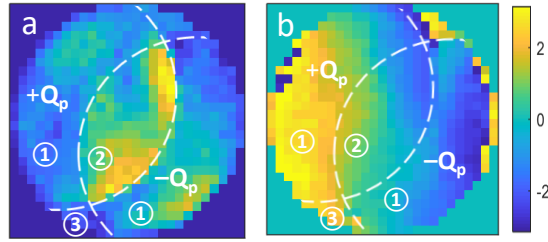


Figure 3.18 An example of the (a) modulus and (b) phase of the complex matrix $G(K_f, Q_p)$ at a single spatial frequency Q_p where two diffracted beams $+Q_p$ and $-Q_p$ (indicated by dashed lines) overlap with the undiffracted direct beam.

3.5.2 Reconstructed images with SSB and compared to other algorithms

The established sample preparation method, dosage control, and microscope parameters optimization have enabled the successful acquisition of ptychography phase images, BF- and LAADF-STEM images. The microscope parameters selection was based these assumptions:

- i. the illumination source is a perfect point source, i.e., illumination incoherence that will introduce blur was not considered;
- ii. the specimen is assumed to be thin with single scattering;
- iii. the inelastic scattering can be neglected. In practice, we carefully selected spot size and emission current to minimize unwanted incoherence. The reconstruction parameters should be consistent with experimental parameters, with the additional factor of the rotation of diffraction space with respect to scanning direction, which needs to be correctly determined.

Table 3.5 illustrates the microscope parameters used in the acquisition of 4D-STEM datasets.

The ptychography phase image obtained with SSB reconstruction is shown in Figure 3.19, from where more details can be observed compared to the BF-STEM, LAADF images directly acquired from the detectors, and the phase images possess sufficient contrast for further structural study. Therefore, an analysis of polymer crystalline structure can be conducted, which will be discussed in subsequent chapters.

Table 3.5 Microscope parameters of ptychography data acquisition

Microscope condition		illumination	Imaging parameters				Scanning		
Accelerating voltage	Spot size	emission current	Detector	α	Camera Length	\times Mag	pixel number	Pixel Size	Dwell time
kV	C	μ A	-	mrad	cm	M	x-direction	\AA	μ S/pixel
200	8	3	PN CCD	14.38	12	20	256	0.4	250
							512	0.2	

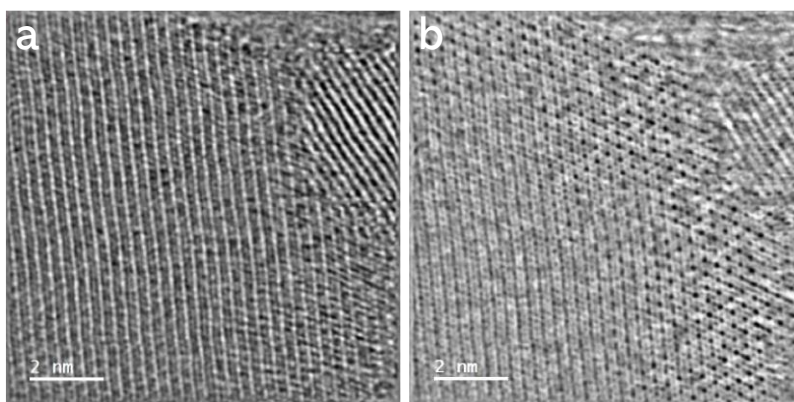


Figure 3.19 Ptychography (a) phase and (b) amplitude obtained from SSB reconstruction with 4D-STEM data acquired with microscope parameters in Table 3.5.

To gain a complete vision of the capability of ptychography reconstruction algorithms, we also run the same 4D-STEM dataset with the other non-iterative method – WDD (Figure 3.20). To obtain WDD images, more computation capabilities are required and the process is more time consuming. For polymer specimen that satisfies the WPO approximation, SBB can achieve the same quality image with less computation and time resources.

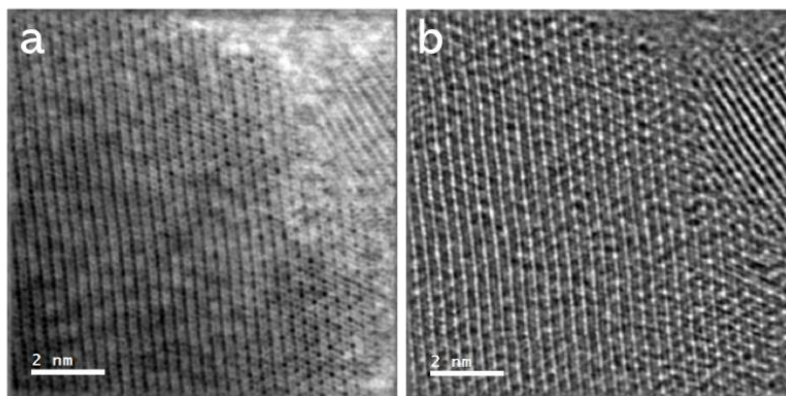


Figure 3.20 (a) Amplitude and (b) phase of WDD reconstruction with the same dataset used for SSB.

Benefit from the pixelated detector that resolves CBEDs for ptychography reconstruction, we can obtain DPC images from the same dataset by selecting specific proportion of signals to run DPC algorithm. DPC is not a preferred method for my work because CTF of DPC is easily affected by low spatial frequency noise. Although DPC can reconstruct images from the same dataset with SSB, the aberration correction algorithm in SSB cannot work for DPC. Additionally, DPC cannot work under defocus conditions. In conclusion, DPC is not a good option for my work after checking the reconstructed images and the inherent drawbacks of the algorithm.

3.5.3 Optical sectioning applied to polymer semi-crystalline thin film

The concept of optical sectioning⁹⁸ has been used in fluorescence microscopy to enhance image quality. Optical sectioning is a technique used in confocal microscopy to obtain images of thin slices of a thick specimen by removing the contribution of out-of-focus light in each image plane. By removing unwanted light, greater contrast is achieved, and three-dimensional (3D) reconstructions are possible by combining the data from a stack of images computationally.

A microscope's 'depth of field'⁶⁷ is defined as the amount of the *object* being observed that remains in focus at the same time. Cosgriff *et al.*⁹⁹ found that the depth of field in STEM is inversely proportional to the square of the aperture size. The theoretical focal depth of field¹⁰⁰ in STEM can be expressed as follows:

$$\Delta z = \frac{1.7\lambda}{\alpha^2} \quad (3.4)$$

where Δz is depth of field, λ is the electron wavelength and α is the aperture semi-angle. The depth of field determined by formula (3.4) with the accelerating voltage used in this work are at the scale is of tens of nanometres, i.e., 20.6nm at 200kV, and 12.5nm at 300kV (Table 3.6). This means the structure within tens of nanometre along the depth would be in focus at the same time.

The difference in depth $\Delta z'$ was generated by changing the defocus value df , and the relative difference in structure at df_1 and df_2 can be observed. Hence, by comparing the images at df_1 and df_2 , the structure along the depth can be resolved. Furthermore, since $\Delta z'$ is known, the distance and size of features along depth can be calculated.

Table 3.6 Depth of field for the accelerating voltage used to form the probe for imaging.

Accelerating Voltage (kV)	λ (nm)	α (rad)	Depth of Field Δz (nm)
300	1.97×10^{-3}	16.40×10^{-3}	12.45
200	2.51×10^{-3}	14.38×10^{-3}	20.64

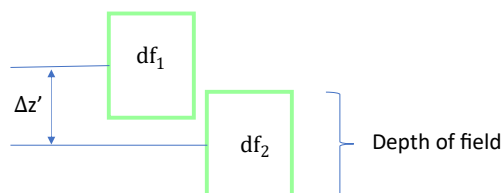


Figure 3.21 Methodology of resolving structure along the viewing direction (z-axis) in this chapter.

In conventional optical sectioning, three-dimensional imaging is realized by recording a series of images at various defocus C_1 values, in a manner that is similar to confocal optical microscopy. The primary advantage of optical sectioning with 4D STEM dataset over tomography is the shorter acquisition time (<5min rather than several hours), because only one scan is needed⁴ which significantly reduces the exposure of beam sensitive materials to radiation. Optical sectioning will be used frequently in PEN and PET image analysis, to identify feature of interest at specific defocus C_1 level, where C_1 is relative to actual probe cross-over in the microscope.

4 Beam damage study and Critical dose measurement

The beam damage was assessed with PEN before imaging it with (S)TEM, because the PEN specimen degraded rapidly, and no useful information could be obtained under standard STEM imaging conditions. The purpose of this pre-study is to observe how the specimen would be damaged when exposed to the beam and to determine whether the new sample preparation method would result in high quality specimens.

4.1 Acquisition of time-resolved diffraction patterns from PEN

4.1.1 Microscope setup for low dose condition

The first challenge to imaging polymer in (S)TEM is the standard dose for optics alignment damages the specimen immediately once it is exposed to the beam, but the extremely low dose was too low to detect the feature in the specimen. Therefore, the experiment was designed to align the optics of the diffraction mode at a region without features of interest with normal illumination, then switch to low dose illumination and observe the monitor of a digital camera while moving the specimen to look for the diffraction patterns of crystalline feature. Once a good DP is displayed on the monitor, a multi-frame DP will be recorded throughout the entire process of DP degradation. The dose applied to generate a diffraction pattern from polymer specimens must be low enough to ensure that the sample will not be completely damaged at the beginning of exposure. The procedure of beam damage can only be recorded if the structure is constantly changing during the data recording.

4.1.2 Time-resolved electron diffraction patterns acquisition

The change in crystallinity of polymers exposed to an electron beam with an accelerating voltage of 300 kV was investigated using time-resolved electron diffraction patterns (DPs). Data used to calculate time-resolved electron DP was derived from multi-frame diffraction patterns (MFDPs), which were acquired using an in-house developed code installed on the microscope (JEOL 3000F).

MFDP series consisted of a stack of electron DPs acquired with identical exposure time (0.3s) and uniform interval time (17s), each slice of DP could be analysed independently. A complete stack of MFDPs included the DPs of a specific area within the specimen, from the pristine structure to the damaged structure. A signal tracing the degradation of each crystallographic plane was based on the intensity of the diffraction spots corresponding to a set of planes. Consequently, the entire process of structure evolution was recorded as the electron dose accumulated along the exposure time.

The entire data acquisition process was conducted under low-dose conditions. The dose of illumination was reduced by applying a small condenser aperture and a small spot size. For a shorter exposure time, the specimen was focused at one area and a new area was used for data acquisition, and the beam was unblanked (valve opened) only during data acquisition. Chapter 3 describes the calibration of the dosage.

4.2 Connect the signal of diffraction planes with exposure time

4.2.1 Quantify the intensity of planes from the DPs

The first slice of DP - 'slice0' in a MFDP from PEN specimen shown in Figure 4.1 illustrates the procedure for identifying planes and intensities that can be used to trace their change under electron beam exposure. DP acquired from platinum nanoparticles under identical microscope

conditions was used as a spacing-known sample for calibration before measurements. Figure 4.1b shows the calibrated DP and how the centre was identified using DigitalMicrograph tools. The radius profile (Figure 4.2a) was then calculated from the DP by averaging the intensity along the circles where each diffracted arc was found. The position of beam-stop is the same in the whole image series, its influence to each image is the same and can be neglected.

The radius profile could be used to measure the spacing and diffraction intensity of each plane. The planes are not indexed because from the DP, each plane spacing might correspond to multiple planes as listed in Table 4.1. In order to ensure that the change in intensity reflects only the degradation of crystalline structure, the amorphous background, which is the area below the peaks, should be removed, as shown in Figure 4.2a. As shown in Figure 4.2b, the intensity of peaks would only include the diffraction intensity from crystalline planes.

Since the signal used to quantify the damage was the integrated area of the peak in the radius profile after background subtraction, the intensity was the integrated area of the peak. The baseline of integration was defined as the amorphous background same as the intensity profiles in the DP where no peaks of diffraction were observed (Figure 4.2a), so that the integrated intensity of peaks reflected purely the crystallinity of the specimen. Therefore, the change in intensity was indicative of the degradation of crystalline structure in the semi-crystalline PEN thin film.

The steps were then repeated on each slice of DP throughout the entire stack of MFDP. The intensity integrated from each peak in the radius profile through the MFED was used as the signal to trace the change in crystalline structure in the specimen over exposure time.

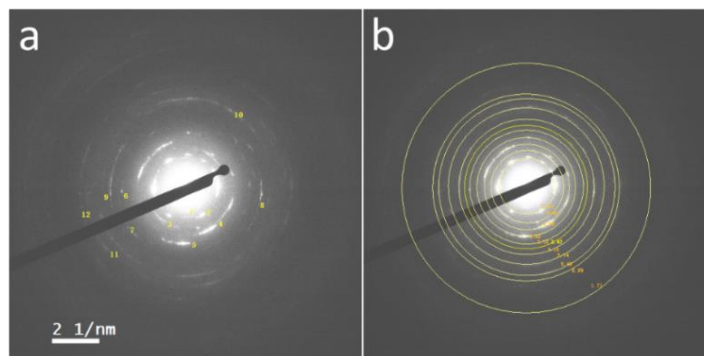


Figure 4.1 (a) Diffraction pattern of PEN specimen in one slice of MFDP stack, acquired from thin film annealed at 240°C for 30min. (b) Centre determination and spacing measurement in DigitalMicrograph.

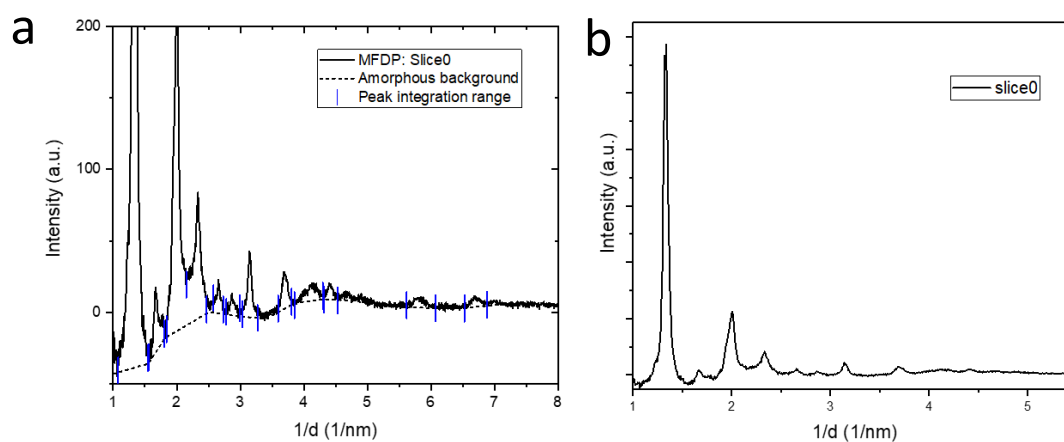


Figure 4.2 Radius profile of the first DP image, marked as 'Slice0', in the MFDP stack. (a) amorphous background determined (dash line) and range of peak integration (vertical short blue lines at edge of peaks). (b) radius profile of DP after amorphous background subtraction.

Table 4.1 All possible indexes of the planes in DP of Figure 4.1

Slice0 in MFDP			Model of PEN crystalline			Spacing discrepancy
d_{FT}	Integrated Intensity	Relative Intensity	Crystalline form	Index	d_{mol}	$d_{FT} - d_{mol}$
Å	a.u.	%	\	hkl	Å	Å
7.48	68.49	100.0%	α -triclinic	(0 0 1)	7.77	-0.29
			β -monoclinic	($\bar{1}$ 1 1)	7.72	-0.23
			β -triclinic	($\bar{1}$ 0 1)	7.62	-0.14
4.97	13.14	19.2%	β -monoclinic	(0 2 1)	5.33	-0.36

			β -triclinic	$(\bar{1} \bar{1} 1)$	5.38	-0.41
4.27	5.73	8.4%	β -monoclinic	$(1 2 0)$	4.73	-0.46
			β -triclinic	$(0 2 0)$	4.78	-0.51
3.78	0.70	1.0%	α -triclinic	$(1 0 0)$	3.83	-0.04
			β -triclinic	$(\bar{2} 0 2)$	3.81	-0.03
3.52	0.63	0.9%	β -monoclinic	$(\bar{2} 2 1)$	3.61	-0.09
3.17	2.97	4.3%	β -monoclinic	$(2 0 0)$	3.36	-0.18
			β -triclinic	$(2 0 0)$	3.32	-0.15
			α -triclinic	$(\bar{1} 1 0)$	3.33	-0.16
2.30	0.93	1.4%	β -monoclinic	$(\bar{3} 1 1)$	2.61	-0.31
			β -monoclinic	$(\bar{1} 5 2)$	2.45	-0.15

4.2.2 Time-resolved evolution of DP

The metadata of the MFDP included the interval time between every two slices and the acquisition time for each slice. Using the extracted metadata, each DP could be pinned to an exact point in the timeline of structural degradation. The dose rate had been calibrated in Chapter 3 and the timeline could be converted to accumulated dose. So, the time-resolved intensity evolution versus dose could be obtained.

Figure 4.3 shows the time-resolved intensity data for a whole MFDP stack. The data points represent the intensity of a crystallographic plane at a given value of accumulated dose. According to the curves in Figure 4.3, it appears that all planes degrade at a similar rate, but the degradation function of each plane is not exactly the same.

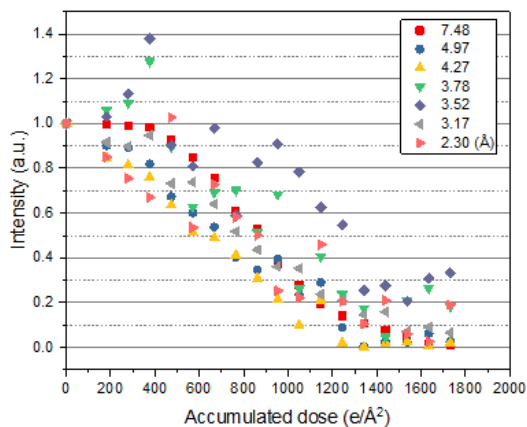


Figure 4.3 Time-resolved intensity versus accumulated dose curves for all planes from a MFDP dataset.

4.3 Damage model construction

4.3.1 Intensity evolution analysis – model fitting

The individual curves of the time-resolved intensity evolution of each peak should provide the information necessary to understand the degradation of the specific plane. Figure 4.4 shows the time-resolved data of the plane with spacing 7.48\AA , which possess the highest intensity and the degradation of the corresponding plane was well traced throughout the whole evolution observation. When exposed to electron beams, the intensity did not immediately decrease, but there was a 'stage' before the exponential decay occurred.

The fitting was performed using different decay models (Table 4.2), and the model was selected based on the R-square combined with the observed phenomenon, e.g., latency found in specific plane. The first few points not showing intensity decay were considered as "latent dose". The latent stage was excluded from the decay model fitting due to its uncertain decay pattern. For each diffraction peak, the number of data points treated as latent dose was adjusted according to the R-square of fitting (Table 4.2). Function (4.5) and Function (4.6) were used to determine the best fit for a 'latent stage' followed by an exponential decay as described in the 'Phenomenon match' section of Table 4.2. The R-square of both fitting results was similar. Function (4.7) was not able to interpret the latent dose 'stage', although the R-square was also close to one, therefore Function (4.7) was excluded. The same comparison has been made for all diffracted planes. All observed diffraction peaks were best fit by Function (4.6) (Table 4.3).

Function (4.6) was used as the decay model to fit the curve of intensity versus exposure time (Figure 4.4). In this MFDP dataset, the dose rate was measured as $5.96\text{ e}/(\text{\AA}^2\text{s})$, so the curve can also be plotted as intensity versus accumulated dose (Figure 4.5), which can then be used

to determine the 'critical dose', that is the critical point where the material structure is altered by the accumulated dose.

The decay model for each diffraction peak indicated that the damage rate of the different planes was similar, although distinct in details (Table 4.3). Contrary to earlier proposals that short-range periodicity is lost more rapidly than long-range periodicity²⁵, the results in this work (Figure 4.3) did not demonstrate a clear correlation between damage rate and plane spacing.

Table 4.2 Functions used for fitting the degradation curve in Figure 4.4

Functions for fitting	Phenomenon match
$y = A(1 - Be^{-\frac{x}{t_1}}) \cdot e^{-\frac{x}{t_2}}$ (4.5)	Exponential growth \times an exponential decay
$y = A \cdot e^{-\frac{x-x_0}{t_1}}$ (4.6)	Exponential decay with a delay
$y = A \cdot e^{-\frac{x}{t_1}}$ (4.7)	Exponential decay from beginning

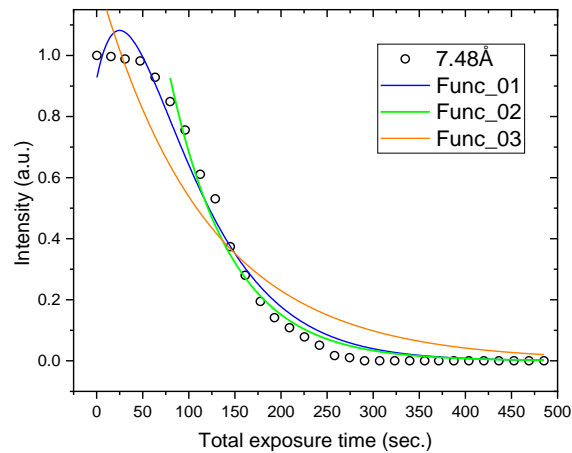


Figure 4.4 Model fitting for the intensity evolution versus time.

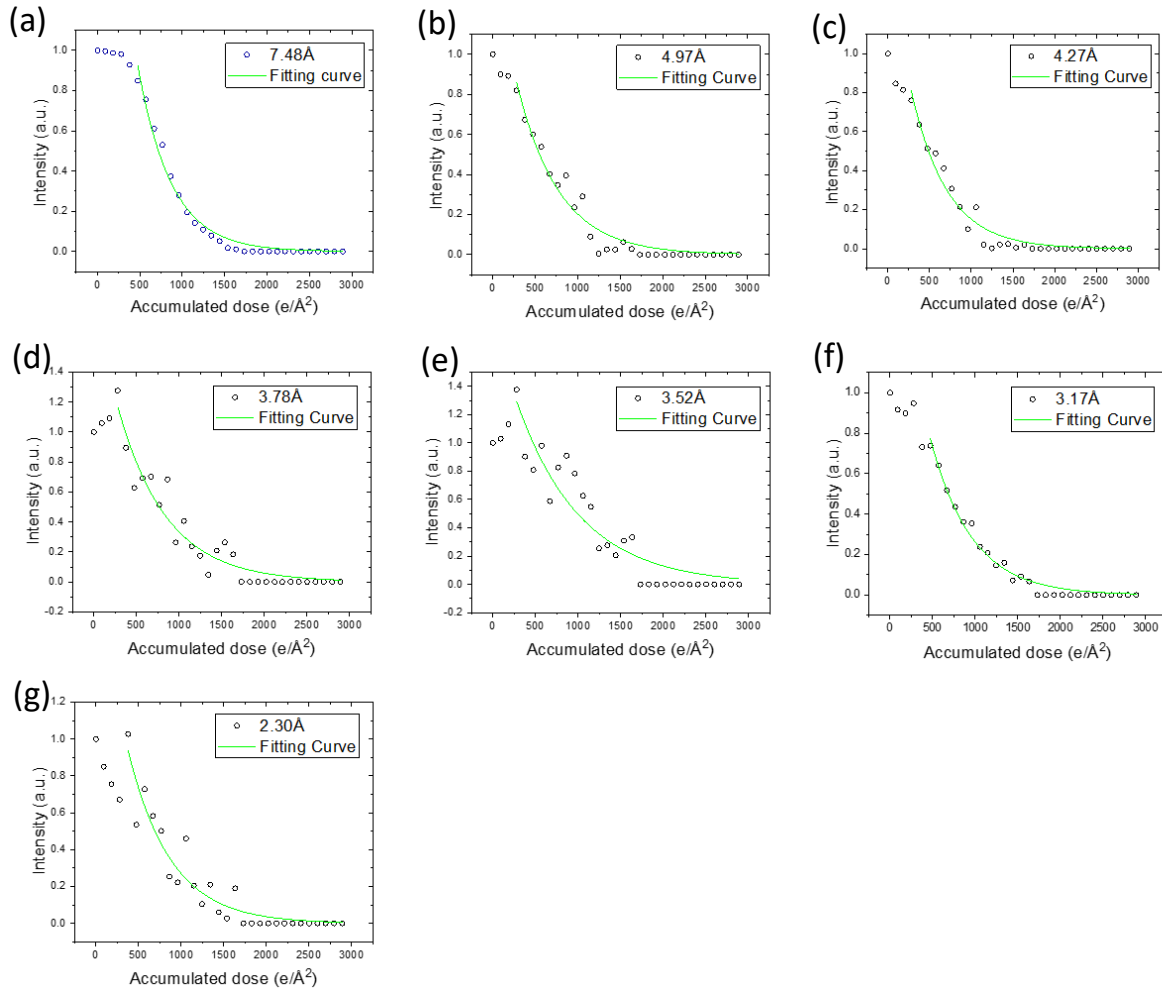


Figure 4.5 Fitting curve of each plane with Intensity (a.u.) versus Accumulated dose ($e/\text{\AA}^2$)

4.3.2 Critical dose determined from the decay model

The decay model expressed in the form of intensity versus accumulated dose could be expressed as below:

$$S_{(D)} = S_{(0)} \exp\left(-\frac{D - D_0}{D_c}\right) \quad (4.6)$$

$S_{(D)}$ is the measured signal, which is the intensity of the diffraction plane in radius profile, recorded after being exposed to accumulated dose D . $S_{(0)}$ is the intensity recorded after exposure of dose D_0 .

The critical (or characteristic) dose³⁹ is at the point where the intensity reduces by a factor $1/e \approx 0.37$. In this decay model, $S_{(D)} = S_{(0)} \exp(-1)$ when $D - D_o = D_c$. So, the 'actual critical dose' should be $(D_o + D_c)$.

The critical dose of all the planes in a stack of MFDP was illustrated in Table 4.3. It was found that the critical dose differs for different planes but are all in the range of 850 ± 150 ($e/\text{\AA}^2$). The low illumination in use may cause this relatively large error range (fluctuating data points), because of the measurements have approached the minimum reading limit of equipment. The critical dose of PEN was relatively high compared to the organic materials reported before³.

Table 4.3 Crystallinity decay quantities versus plane spacing. The planes were not indexed in this table, because each plane spacing might correspond to multiple planes from DP as listed in Table 4.1.

Spacing d_{FT} \AA	Points skipped in fitting	$S_{(D)} = S_{(0)} \exp\left(-\frac{D - D_o}{D_c}\right)$				Critical dose ($e/\text{\AA}^2$)
		$S_{(0)}$	D_o	D_c	R-square	$D_o + D_c$
7.48	5	0.888	492.45	395.51	0.98216	887.96
4.97	3	0.828	300.56	498.18	0.95509	798.74
4.27	3	0.779	298.21	429.88	0.96161	728.10
3.78	3	1.280	228.71	575.23	0.92161	803.94
3.52	3	1.293	280.60	750.54	0.87033	1031.14
3.17	5	0.767	480.15	485.38	0.98354	965.53
2.30	4	0.968	362.28	501.57	0.90167	863.84

The diffraction intensity evolution of plane 7.48\AA showed a latency, dropping by about 10% ($S_{(0)}=0.89$) at D_o followed by an exponential decay (with decay rate of $1/D_c$ (Figure 4.5a). As modelled, D_o stands for the dose after which the intensity started to decay exponentially, with accumulated dose – D_o , after which a more typical exponential decay mechanism is observed. Calculated by the model fitted, the “latent dose” D_o was $492 e/\text{\AA}^2$, and the critical dose ($D_o + D_c$) was $887 e/\text{\AA}^2$.

Although the latency was not so obvious for other planes, the best fitting of the decay model was still the same, function (4.6) – exponential decay with delay represented by D_o . The mechanism of the latency was not clear: there might be “adjustment” at the electronic level before the observable change happened at a molecular level. It means that the initial dose could cause minor electronic or binding changes in the material, which then allow for the loss of order with further dose. Once the order starts breaking down, it will propagate depending on the concentration of order that can be lost, which is exponential decay.

The concept of a latent dose of in organic samples has been reported¹⁰¹ before, but in data were recorded with sample-cooling, whereas this dataset was acquired at room temperature. It implied the latency observed in this work was not caused by extra-low temperature used to mitigate damage^{33,101}, but the material itself. A possible explanation is the resonant structure, naphthalate, is relatively stable hence can prevent nearby sensitive groups like C-H bonds from being quickly broken, and the rapid energy dissipation along the long chain molecules result in the energy not locating at a specific bond to break it until activated species have been accumulated to sufficient concentration.

Though the low dosage used might be considered as a factor that reveals the latency, which means the latency might exist in previous works but was not revealed in high dose illumination because the degradation was too fast. With low illumination, the damage takes longer to accumulate to the level of ‘observable’ change. However, the “latent dose” was not reported in previous investigation⁴² of beam damage with only low dose condition. Low dose methods mentioned in earlier works usually lack details of how the measurements been done, therefore due to the absence of quantified dosage data, a quantitative comparison is difficult.

From the damage study, the behaviour of PEN exposed in electron beam have been characterized. The damage model of latency followed by exponential decay should be taken

as reference in the imaging work, although the specific critical points might be distinct in different imaging modes.

4.4 Conclusion

The critical dose and beam damage of PEN have been studied by tracing the evolution of diffraction intensity versus accumulated dose. The decay model for crystallographic planes had been constructed as: $S_{(D)} = S_{(0)} \exp\left(-\frac{D-D_0}{D_c}\right)$. The decay model was constructed with the intention of interpreting the curve of 'intensity versus dose' as a latency followed by an exponential decay. The critical dose was determined as $(D_0 + D_c) \text{ e}/\text{\AA}^2$; where D_0 was the "latent dose" from where the exponential decay started, and D_c is the dose at which the intensity had decayed to 1/e of the intensity at the start of the exponential decay. The critical dose calculated based on this decay model was in the range of 700-1000 $\text{e}/\text{\AA}^2$, which was relatively high compared to empirical data of organic materials. Accordingly, we might have a relatively wide "operational window" of dose for PEN in (S)TEM imaging.

In the study of crystallinity decay for all the crystallographic planes, a "longest" latency was found for the plane with the largest spacing in multiple datasets, but no obvious correlation between spacing and damage rate ($1/D_c$) was found. Therefore, in the stage of exponential decay, the planes with smaller spacing were not observed to necessarily decay faster than planes with larger spacing.

The fact that the study was conducted at room temperature instead of low temperature condition suggests that the latency may be due to the chemical structure of PEN. Although the mechanism was not yet clear, it may imply an "adjustment" at the electronic level before the observable change at the molecular level. Nevertheless, once the dose exceeded the "latent

dose", all crystallographic planes decayed in a similar exponential manner with a rate that was non-correlated to the spacing.

5 Imaging the structure of PEN crystallinity with STEM ptychography

5.1 Images obtained from PEN – a beam sensitive and light element material

High resolution images of PEN were obtained after the primary obstacles including sample preparation, beam damage and low dosage condition have been studied, and corresponding solutions had been developed as described in the previous chapters.

PEN molecules are long chains involving a complex chemical structure, which brings a challenge to resolve the atoms. Compared to the atomic structure in metal and ceramic crystals, the arrangement of atoms in polymers contains superpositions of complex chemical structures, and the rotation of sub-molecular chemical units would induce subtle changes in intensity in the diffraction patterns acquired with X-rays or TEM, so typically it is not possible to determine the details of the structure directly from this.

In this chapter, the imaging methodology of low dose STEM ptychography, with which high resolution phase images of PEN crystallinity was successfully acquired will be demonstrated with the highest signal-to-noise ratio achieved from polymers so far. The methodology of analysis of the PEN structure from the ptychography images will be developed and discussed in detail, and as a result, the local molecular conformation within the crystals in a polymer semi-crystalline thin film will be analysed.

5.1.1 Dosage used in PEN image acquisition

The first set of critical doses of PEN was measured from time-resolved electron diffraction patterns (DP) acquired in TEM. The intensities of DP spots were used as the signal indicator and the evolution of intensity versus accumulated dose was used to calculate the critical dose

for crystalline PEN, giving a critical dose around 700~800 ($e/\text{\AA}^2$). This value can be converted to damage cross section⁴⁴ (σ_D) which is reciprocal of critical dose, noted by Egerton³ as $\sigma_D(\text{Mb}) = 100/D_c$, where D_c ($e/\text{\AA}^2$) is critical dose. So, the damage cross section of PEN is 0.12~0.14Mb ($1\text{b} = 10^{-28}\text{m}^2$). Compared with measurements on polymers in other works, PEN belongs to the highly sensitive group for all beam sensitive materials, but can be categorized as relatively resistant among the polymers that have been measured with EELS¹⁰². This might be caused by the “protective effect” of naphthalate ring in the PEN molecular structure³⁰.

In STEM imaging mode for PEN image acquisition, the beam current was 0.56pA. For BF-STEM image acquisition with dwell time of 1.6 μS , the dose at each probe position was 5.6 e . In ptychography with scanning speed of 4000fps (250 μS), the dose at each probe position was 880 e . If converted to fluence when the probe-step was 0.4 \AA with magnification of 20M, the fluence was calculated as around 5500 $e/\text{\AA}^2$ for one ptychography image. Noticeably, the dose in STEM ptychography mode is much higher than the dose measured from TEM diffraction mode. Similar phenomenon were reported earlier^{103,104}, but the reason is not yet clear.

We investigate images acquired from the same region of specimen with smaller probe step and calculate the dose of each image series being exposed, to resolve the concern that structure in ptychography images might had been damaged under such high dose. Figure 5.1 shows four ptychography image series that acquired from same region of specimen, but no observable structural changes were found after two ptychography images in each series. The beam current used for all these images are the same as the calibrated setting in Chapter 3, so the calibrated dose (electron number per probe position = 887.38 e) applies to these image series. We multiply calibrated electron per probe position to the pixel number for the dose of one image, and sum up the dose of all images in the same image series, i.e.:

- i. Dose in each image = (e/probe) * total pixel number of one image

- ii. Total dose of the image series = sum up the dose of all images.

Take one image series in Figure 5.1 as example:

- i. Dose of Figure 5.1a: $(e/\text{probe}) * \text{total pixel number} = 887.38 e * 512^2 = 2.33\text{E}+08 e$
- ii. Dose of Figure 5.1b: $(e/\text{probe}) * \text{total pixel number} = 887.38 e * 512^2 = 2.33\text{E}+08 e$
- iii. Total dose of the image series = $4.65\text{E}+08 e$

Following the same calculation protocol, dose of the other image series in Figure 5.1 are shown in Table 5.1. The dose of images in Figure 5.1 - using 1/4 (~0.2Å) or 1/16 (~0.1Å) pixel size of Figure 5.2a (~0.4Å) that being investigated extensively for structure analysis, is significantly higher; and the structure was not found damaged. The results from these image series (Figure 5.1) refresh our expectation of specimen dose tolerance in ptychography imaging and eliminate the concerned of structure alteration in upcoming ptychography images that will be analyzed.

Table 5.1 Dose calculation of images series in Figure 5.1. Distinct parameters are bolded.

Image	e-beam	DigiScan Free Mode		pnCCD	Dose calculation				
	Emission current	pixel number	Dwell time	Pixel Size	Counts/probe-position	$e^-/\text{probe-position}$	e^-/image	Total e^- in series	Energy absorbed in series
Figure 5.1	μA	Row	μS/pixel	Å	\	e	$e/\text{Å}^2$	e	C
a	3	512	250	0.207	22057.5	887.38	2.33E+08	4.65E+08	7.45E-11
b	3	512	250	0.207	22057.5	887.38	2.33E+08		
c	3	512	250	0.277	22057.5	887.38	2.33E+08	4.65E+08	7.45E-11
d	3	512	250	0.277	22057.5	887.38	2.33E+08		
e	3	512	250	0.277	22057.5	887.38	2.33E+08	4.65E+08	7.45E-11
f	3	512	250	0.207	22057.5	887.38	2.33E+08		
g	3	512	250	0.207	22057.5	887.38	2.33E+08	5.89E+08	9.44E-11
h	3	512	133	0.164	11734.59	472.08	1.24E+08		
i	3	512	250	0.164	22057.5	887.38	2.33E+08	5.89E+08	9.44E-11

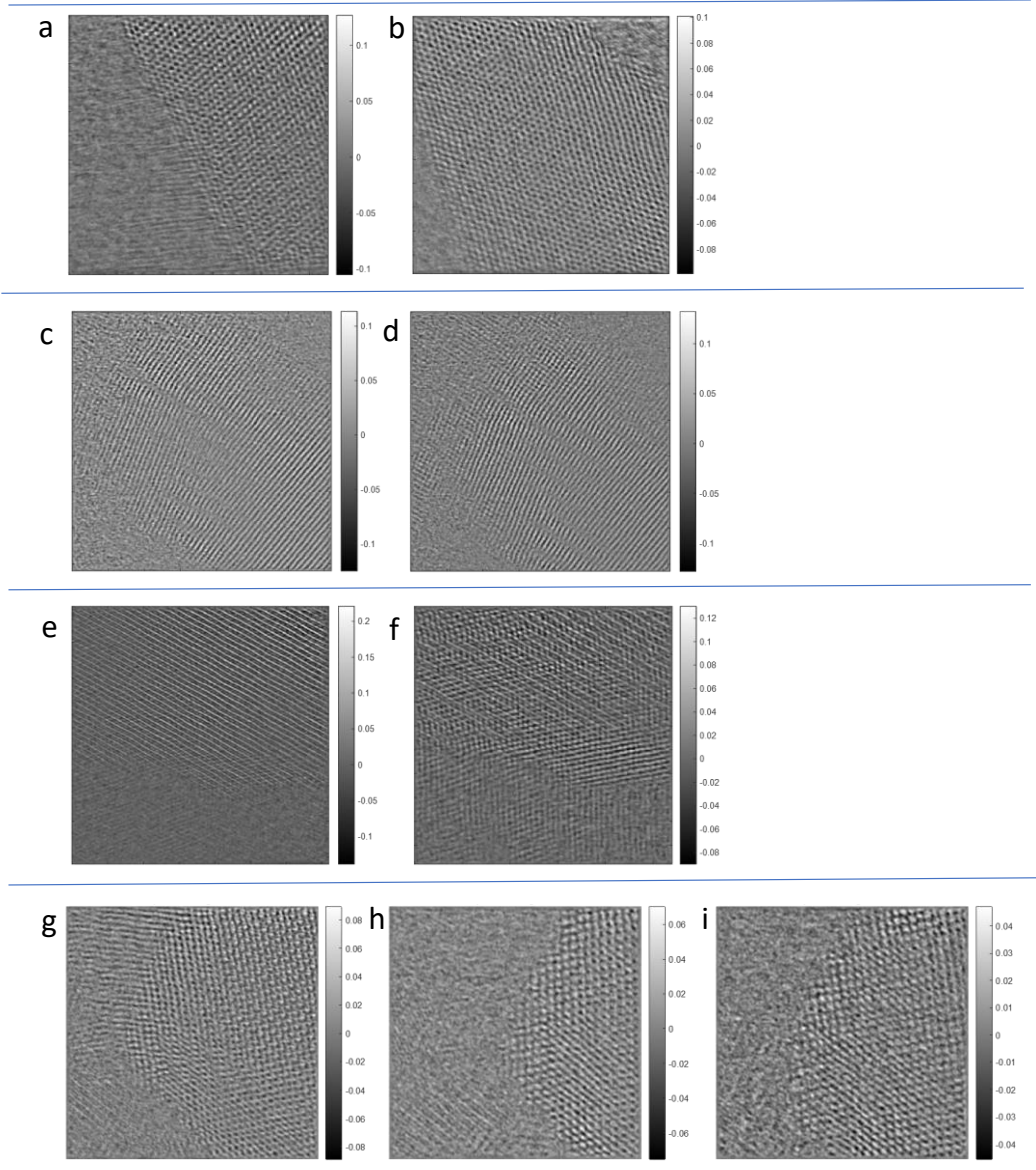


Figure 5.1 The series of images acquired over the same region of the specimen with ptychography. (a) and (b) are the images on the same region (some sample drifting involved), same as (c) (d), (e) (f) and (g) (h) (i). The structure was not found changed in two images acquired in series on the same region.

5.1.2 Data recording and processing

All the ptychography data in this chapter were acquired using the JOEL ARM-200F, with accelerating voltage of 200kV, spot size 8, convergent semi-angle (α) is 14.38mrad, camera length 12cm. The low dose condition was achieved by using a low emission current ($3\mu\text{A}$). The scanning speed used in this work was 4000fps, i.e., the dwell time was $250\mu\text{s}/\text{pixel}$. The probe-

step is 0.40\AA or 0.27\AA . Data processing and analysis were done with in-house developed MATLAB codes of Single Side Band (SSB) reconstruction^{4,77}.

For the BF-STEM image acquisition, a GATAN bright-field detector was used along with a DigiScan image acquisition unit controlled by the Digital Micrograph suite. The same α and camera length as the ptychography data acquisition were used, but a shorter dwell time ($1.6\mu\text{S}/\text{pixel}$) was applied. BF-STEM Image calibration and analysis was done with the Digital Micrograph suite.

5.1.3 Image pixel size calibration

The images were calibrated to ensure the measurements were correct before analysis. Even in the low dose setting that applied the available shortest dwell time, the acquisition time of ptychography data ($250\mu\text{S}/\text{pixel}$) was still much longer than BF-STEM data (here $1.6\mu\text{S}/\text{pixel}$). This introduced the problem of sample drift during data acquisition, which can cause random variation in dimension measurements of the same feature from different images.

To overcome this issue, the ptychography phase image was calibrated using a BF-STEM image acquired on the same feature. This 'faster' BF-STEM imaging allows a more accurate measurement of the $(2\ 0\ 0)$ plane spacings observed in the PEN, which was consistently measured as 3.17\AA in BF-STEM images, while a variation was found among different ptychographic images. The BF-STEM images used here were calibrated using lattice images of silicon viewed along $[1\ 1\ 0]$. The $(2\ 0\ 0)$ plane spacing of PEN measured from the BF-STEM image was applied to the spacing of $(2\ 0\ 0)$ measured from ptychographic phase image, hence the pixel size in each ptychographic phase image was calibrated.

5.2 Image analysis method development with ptychography data from PEN

5.2.1 PEN crystal model and structural analysis with diffraction

The crystal model of PEN developed with XRD from PEN fibres by Heuvel *et al.*¹⁰ was used as the reference for structure analysis. This model is a β -form crystal of four-chain monoclinic unit cell with space group $P2_1/a$ and cell parameters $a = 9.49$, $b = 13.31$, $c = 12.61\text{\AA}$, $\alpha = 90$, $\beta = 135$, $\gamma = 90^\circ$. Although the unit cell parameters do not differ much from the earlier model developed by Liu *et al.*⁹ based on single crystal ($a = 13.04$, $b = 9.26$, $c = 13.00\text{\AA}$, $\alpha = 131.47$, $\beta = 90$, $\gamma = 90^\circ$, space group $P2_1/n 1 1$), the new space group inferred a different packing of molecules in the unit cell. The PEN crystalline model proposed by Heuvel *et al.* can not only explain their fibre XRD pattern but also the ED patterns observed by Liu *et al.*⁹ from β -form single crystal, which was verified by comparing the simulated electron DP from their reported model and Liu *et al.*'s ED pattern⁹. Therefore, Heuvel's model is the appropriate model to be used for PEN β -form crystal indexing.

5.2.2 Measurements of crystalline planes and indexing

The image of PEN crystallinity with defocus value $C_1 = 8\text{nm}$ relative to probe cross-over was chosen for analysis, because the image of this C_1 value reveals all the major features with sufficient contrast as shown in Figure 5.2a. Based on the correlation between FT of image and crystalline structure, the FT pattern of the image/region-of-interest (ROI) was applied to measure the plane spacing and angles of the large grain in Figure 5.2a. The plane angle stands for the angle between each plane and the strongest plane in FT, here θ represents the angle between the measured plane and (2 0 0) plane.

Plane spacing can also be directly measured with line-profiles, which measure the average peak-to-peak distance. This method requires well resolved and separated peaks of the plane

to be clearly visible in the image. Spacing directly measured from the image with line-profile was applied to avoid the discrepancy introduced by spot centre determination in FT. The plane spacing d_{img} in Table 5.2 were from line-profiles, because the fringes of planes in Figure 5.2a were resolved, i.e., peaks were well separated. In practice, the plane spacing measurement in the image was done by rotating the line-profile initially from (2 0 0) by θ of corresponding plane measured from the FT. Usually, a broadened line-profile is needed to increase the signal to noise ratio for accurate measurement. Multiple line-profiles were applied to measure the spacing for each plane, and the average result was used as the value of the specific plane spacing.

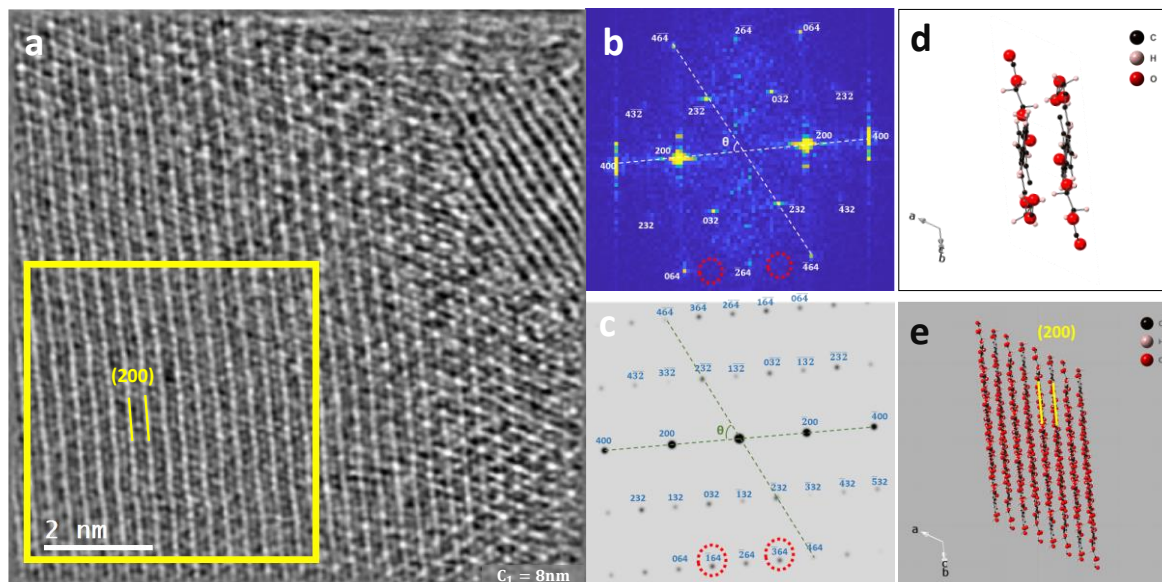


Figure 5.2 (a) Phase image of PEN crystallinity obtained from SSB reconstruction. There are multiple grains with different orientations in this area. There is one large dominant grain on the left and a smaller grain in upper right corner. The ROI in the large grain indicated by the yellow rectangle only includes the uniform lattice and excludes the lattice with disruption in the corners. Plane (2 0 0) was highlighted along the strong layer, between which a weaker layer of periodic features was also resolved. (b) The modulus of the FT of image ROI indexed by reference to panel (c), where the angle between plane (2 0 0) and each plane measured from the FT is denoted by θ . (c) Simulated single-crystal electron diffraction (ED) pattern using the model in d. The spots in the red dashed circles are the discrepancies found compared to FT of phase image. The absent spots in FT are marked with red dashed circles in b. (d) Unit cell of PEN β -form crystal model built from XRD data¹⁰ (monoclinic, with space group $P2_1/a$) viewed along the $[0\ 2\ \bar{3}]$ direction. (e) Plane (2 0 0) in the PEN model¹⁰ containing multiple cells, view from zone axis $[0\ 2\ \bar{3}]$.

Table 5.2 The plane spacing d_{img} and plane angle θ measured from ROI of Figure 5.2a. d_{img} represents the plane spacing directly measured from the phase image of Figure 5.2a with line-profile, the phase image has been calibrated by BF-STEM images. The plane angle θ is measured with respect to the (2 0 0) planes; and these parameters are compared with corresponding planes in the model.

Spacing in phase image	Plane angle in FT	Model ¹⁰			Spacing discrepancy
		hkl	d_{mot}	Angle to (2 0 0) model	
\AA	$^{\circ}$	β -monoclinic	\AA	$^{\circ}$	\AA
3.22	0	2 0 0	3.36	0.0	-0.14
1.61	0	4 0 0	1.68	0.0	-0.07
3.20	61	$2\bar{3}\bar{2}$	3.24	63.2	-0.04
1.60	61	$4\bar{6}\bar{4}$	1.62	63.2	-0.02
1.84	30	$4\bar{3}\bar{2}$	1.93	32.2	-0.10
3.11	60	0 3 2	3.15	60.1	-0.04
1.56	60	0 6 4	1.57	60.1	-0.02
1.75	30	2 3 2	1.88	31.1	-0.12
1.86	88	$\bar{2}\bar{6}\bar{4}$	1.81	88.0	0.05

5.2.3 PEN crystalline structure investigation with ptychography image

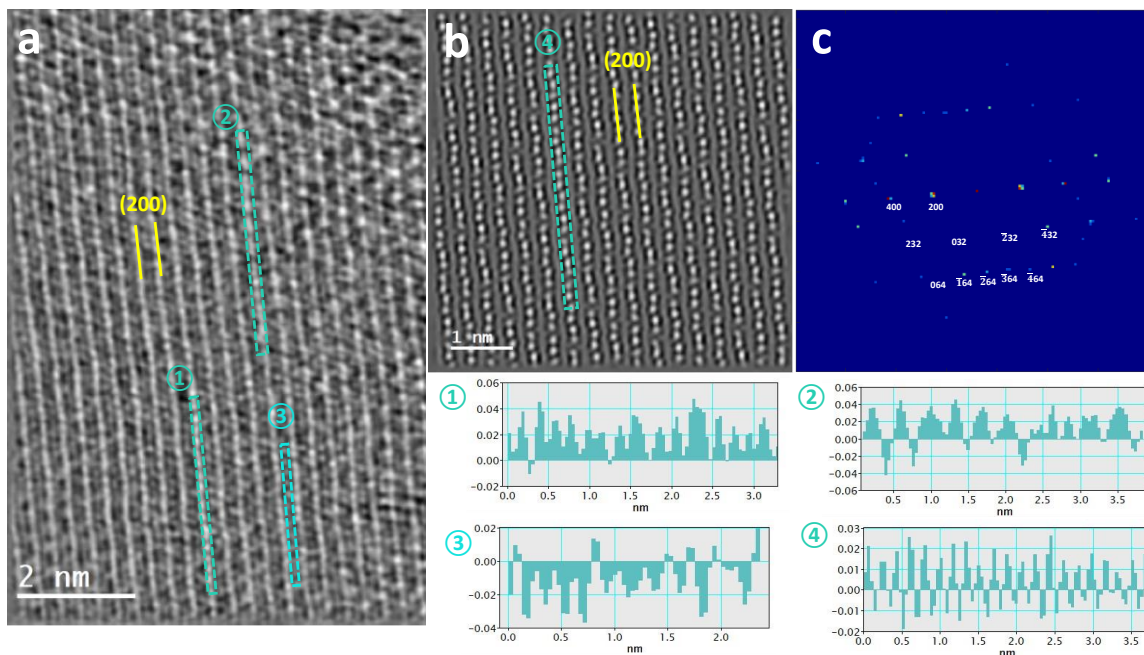
The spots in the FT of the phase image (Figure 5.2b) broadly match with the major features (spots) in the simulated DP from the model¹⁰ for an electron beam incident along the $[0\ 2\ \bar{3}]$ direction although some discrepancies exist. This result was obtained by comparing the FT to the simulated ED from the model along various orientations.

According to values of spacing discrepancy ($d_{img} - d_{mot}$) in Table 5.2, the spacing of most planes measured from Figure 5.2a are slightly smaller than the corresponding planes in the model, except for plane $(\bar{2}\ \bar{6}\ \bar{4})$ which is slightly larger. The range of discrepancy is from -0.14 to +0.05 \AA . The largest spacing discrepancy is found with plane (2 0 0), which is -0.14 \AA , 4% smaller than the model. This range of error is within a commonly acceptable error of 10%.

Plane (2 0 0) represents the inter-planar distance of planes parallel to bc -plane in the unit cell, a smaller spacing of (2 0 0) implied the chemical structure in molecules led to a “flatter” planar structure allowing the planes to get closer. In addition, a weak layer of periodic features was resolved between (2 0 0) planes.

The spacing of (2 0 0) planes was measured as 3.14-3.22Å from multiple ptychography phase images; while the average spacing of (2 0 0) is 3.36Å based on multiple empirical data^{10,9,94,105,24} and the model. To verify the value of measured from images, spacing of (2 0 0) was also measured from electron DP in TEM and BF-STEM images. The spacing of (2 0 0) measured from these PEN samples with electron DP was in range of 3.15-3.17Å. The average spacing of (2 0 0) measured from multiple BF-STEM images was 3.17Å from the same PEN sample. The experimental results from the same specimen fall within the range of spacings obtained from the phase images. Therefore, all the measurements from different methods agree well, the spacing of (2 0 0) in crystal of this PEN specimen is smaller than the model based on previous experimental data¹⁰.

The structural discrepancy was also reflected by plane angle θ . The discrepancies of θ were 1 – 2° for the planes that are not perpendicular or parallel to *c*-axis. The angle of (2 $\bar{6}$ $\bar{4}$) measured from image is exactly the same as the value in model: this plane distributing along the direction of molecule and almost perpendicular (88°) to the backbone (*c*-axis) as shown in Figure 5.5a.



Average repeated distance (Å)	a. Experimental phase image			b. Simulated phase image
Line-profile	①	②	③	④
Strong layers (200)	1.86 ± 0.04	3.67 ± 0.04	1.87 ± 0.04	1.80 ± 0.04

Figure 5.3 (a) Majority of the large grain in Figure 5.2a. Line-profile ① is one example of the measurements of periodic feature along the strong layers (2 0 0) in the experimental phase image, with repeat distance of 1.86Å. Line-profile ② is measurement of the periodic features in strong layers (2 0 0) from another part of the image, while the repeat distance became 3.67Å. ③ is the line-profile measuring the periodic features along the weak layers, where the repeat distance was 1.87Å. (b) Simulated SSB phase image from model¹⁰ built with XRD data obtained with the same parameters as a. ④ is the line-profile measuring the features within the strong layers in this simulated phase image, the repeat distance of which was 1.80Å. (c) FT of the simulated phase image. The 'Average repeated distance' in the table is taken average from around three measurements of the line-profile.

Image simulation was conducted by Dr Chen Huang to assist the interpretation of the discrepancies. A simulated ptychography phase image (Figure 5.3a) was obtained from the 4D-STEM dataset acquired from the crystalline model built in-house with reference¹⁰ viewed along vector $[0\ 2\ \bar{3}]$ and conducted by SSB reconstruction. This is a direct comparison of the crystal structure in the PEN specimen and the model, because the parameters used for obtaining the image of Figure 5.3a experimentally and Figure 5.3b by simulation were identical.

The intensity of strong plane (2 0 0) is found not to be uniform but contains periodic features along the plane direction. These periodic features were found in (2 0 0) lattice of both

experimental and simulated phase images. In Figure 5.3a, the average repeat distance in the strong layer (2 0 0) is 1.86Å measured by line-profile ①, but 3.67Å by line-profile ② from different parts of Figure 5.3a. The repeat distance from line-profile ① is half that of line-profile ②, which implies that even for the same feature, the details resolved can be locally different. The periodicity of the feature within (2 0 0) in the simulated image is 1.80Å measured by line-profile ④ in Figure 5.3b, but the periodicity of 3.67Å was not found in the simulated image.

Periodic weak (2 0 0) layers lying between the strong layers were only found in the experimental image (Figure 5.3a) but not observed in the simulated image (Figure 5.3b). The absence of periodic features between the principal (2 0 0) planes in the simulated image correctly reflect the structure of model (Figure 5.2c) from which this simulation data was generated. The repeat distance of periodic features along the weak (2 0 0) planes is 1.87Å measured by line-profile ③ in the experimental image (Figure 5.3a).

According to the indexing result in Figure 5.2b, the periodicity within (2 0 0) planes correspond to the $(2 \bar{6} \bar{4})$ plane spacing. The plane spacing of $(2 \bar{6} \bar{4})$ in the model is 1.81Å, close to measurement of line-profile ① in the experimental image (Figure 5.3a) and match with the measurement of line-profile ④ in simulated image (Figure 5.3b). The periodicity of weak layer found in experimental image was also well matched to the spacing of $(2 \bar{6} \bar{4})$. The periodic feature on the strong layer and weak layer might be generated by the same structure in the molecule.

Discrepancies of the same features in the ROI observed from different types of data have been summarized in Table 5.3, with the proposed explanations. The planes under discussion are listed in the column of '*hkl*'. The spacing of each plane was measured from phase image with two exceptions – plane $(\bar{1} 6 4)$ and $(\bar{3} 6 4)$ were absent in the FT of experimental phase image

(Figure 5.2b), but visible in FT of simulated image (Figure 5.3c) and simulated DP (Figure 5.2c), so their spacings were calculated from the model.

Illustrated in Table 5.3, the 'visibility' of spots in FT of simulated phase image agrees with the simulated ED. This means, in the simulated condition, the planes that can be resolved by electron diffraction, should be resolved in ptychography phase image as well.

The comparison with the fibre XRD pattern¹⁰ can help confirm that the missing spots in the FT are not contradictions of the crystalline form. In the fibre XRD pattern obtained from PEN fibre (Figure 5.4), only the strongest diffracted plane (2 0 0) and (4 0 0) match with the spots in FT. According to the two main factors that determine whether a spot is visible (not considering forbidden spots here, because the spots being checked are visible in my data) – the resolution limit and relative intensity, (0 3 2) and ($\bar{2}$ 3 2) should be visible in XRD. Because, firstly, their spacing ($>3\text{\AA}$) is within resolving limit of X-ray; secondly, the square of structure factor is linearly correlated to the intensity of spots in DP, the structure factor of (0 3 2) and ($\bar{2}$ 3 2) are at the same level with plane (2 0 $\bar{4}$), which has high relative intensity in the fibre XRD pattern in Figure 5.4.

A systematic absence of spots was observed in the FT of experimental image (Figure 5.2b), when compared to the simulated DP (Figure 5.2c). Among the row of planes (h 3 2) in the FT, (2 3 2) and (0 3 2) are visible but (1 3 2) is not, i.e., planes of ' $h=\text{odd number}$ ' were absent among planes of (h 3 2). However, in simulated DP, all the spots of (h 3 2) planes are visible, but the planes of $h=\text{odd number}$ are less intensive than those of $h=\text{even number}$. The absent spots in FT appeared in simulated DP might be caused by the 'low' intensity cut-off setting in the Crystal Maker simulation software. So, in the FT of experimental image, the planes might be there but the intensity of those spots of $h=\text{odd number}$ were too low to be visible.

According to the simulated DP, there ought to be two intense spots in the $(h\ 6\ 4)$ row that are absent in the FT, i.e. $(\bar{1}\ 6\ 4)$ and $(\bar{3}\ 6\ 4)$ (Figure 5.2c). The spacing of $(\bar{1}\ 6\ 4)$ and $(\bar{3}\ 6\ 4)$ are 1.74Å and 1.77Å. In principle, they can be resolved in the ptychography phase image, because the spacing of $(0\ 6\ 4)$ and $(\bar{4}\ 6\ 4)$ are smaller: 1.57Å and 1.62Å respectively, and these were both resolved. This discrepancy also should not be caused by the simulation cut-off setting either, because spots of $(\bar{1}\ 6\ 4)$ and $(\bar{3}\ 6\ 4)$ are more intense than $(0\ 6\ 4)$ and $(\bar{4}\ 6\ 4)$ according to the simulated DP. Besides, they were found visible in FT of the simulated phase image, which means these two planes in the model should be resolved in ptychography. So, the absence of plane $(\bar{1}\ 6\ 4)$ and $(\bar{3}\ 6\ 4)$ in the phase image implies their absence in the PEN crystalline structure that was measured.

The discrepancies found in the ptychography data compared to model include the disappearance of planes $(\bar{1}\ 6\ 4)$ and $(\bar{3}\ 6\ 4)$. Also, the periodicity of feature within plane $(2\ 0\ 0)$ were found match with plane $(\bar{2}\ 6\ 4)$, and the periodic feature resolved between the strong $(2\ 0\ 0)$ layers shows periodicity with the same plane, $(\bar{2}\ 6\ 4)$.

Table 5.3 A summary of discrepancies of the same crystalline feature observed from different types of data, including the FT of experimental ptychography phase image, the simulated ED pattern in Figure 5.2; the FT of the simulated phase image in Figure 5.3c, and the fibre XRD in Figure 5.4.

Data for comparison in this table:

- **Simulated ED:** electron diffraction pattern simulated by Crystal Maker from model built with XRD data¹⁰.
- **Simulated phase image:** the phase image obtained by SSB reconstruction with simulated 4D STEM dataset from model built from XRD data¹⁰.
- **FT of simulated phase image:** result of Fourier Transform conducted on simulated phase image.
- **FT of experimental phase image:** result of Fourier Transform conducted on SSB reconstructed phase image, which was obtained experimentally in this work.
- **Fibre XRD:** experimental XRD data obtained from fibre (Figure 5.4) by Heuvel *et al.*¹⁰

Viewed from zone axis: $[0\ 2\ \bar{3}]$							
Plane info.		Simulation with model ¹⁰		Experimental results		Proposed explanation for absent spots	
<i>hkl</i>	Spacing (Å)	Simulated ED	FT of simulated phase image	FT of experimental phase image	Fibre XRD ¹⁰	FT of phase image	Fibre XRD
2 0 0	3.22	visible	visible	visible	visible	\	\
4 0 0	1.61	visible	visible	visible	visible		\

0 3 2	3.11	visible	visible	visible	absent		Based on the structure factors for XRD, the (032) and ($\bar{2}$ 3 2) reflections should be visible in XRD but absent in this fibre XRD pattern.
$\bar{2}$ 3 2	3.20	visible	visible	visible	absent		
2 3 2	1.75	visible	visible	visible	absent		
4 3 2	1.84	visible	visible	visible	absent		
0 6 4	1.56	visible	visible	visible	absent		
$\bar{4}$ 6 4	1.60	visible	visible	visible	absent		
$\bar{2}$ 6 4	1.76	visible	visible	visible	absent		
$\bar{1}$ 6 4	1.74*	visible	visible	absent	absent	These two planes ought to be resolvable in the phase image, because (064) and ($\bar{4}$ 64) with smaller spacings are well resolved.	When the spacing is smaller than 2Å, the planes cannot be resolved by a standard XRD.
$\bar{3}$ 6 4	1.77*	visible	visible	absent	absent		

*Note: plane spacing values of absent plane in the experimental image are from model.

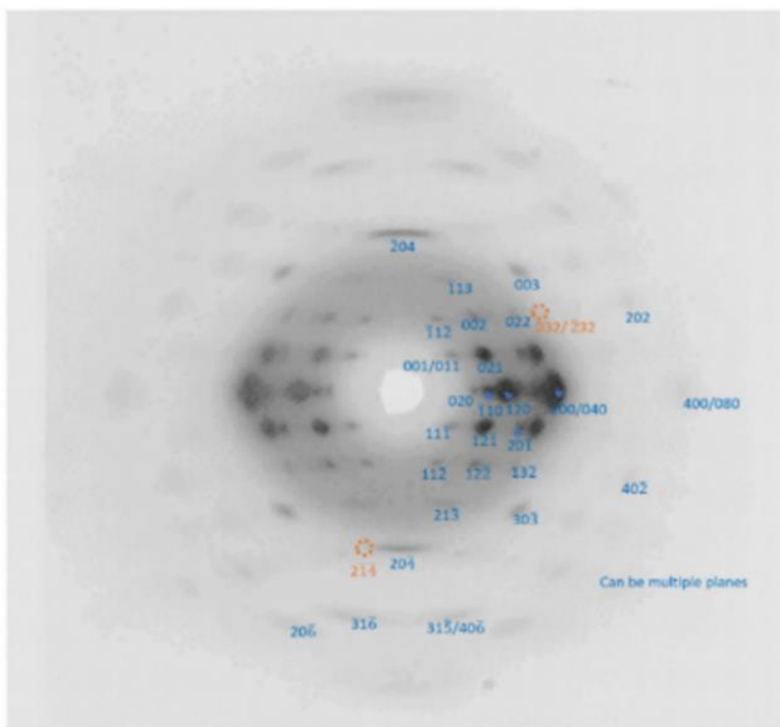


Figure 5.4 XRD pattern obtained from PEN fibre by Heuvel *et al.*¹⁰ is used for contradiction check, i.e., the visible and absent spots in FT were compared to the fibre XRD pattern to check whether any contradictions were found in data. From the XRD pattern, β -form crystalline modification had been recognized. As the pattern should include invisible planes with $[0\ 0\ 1]$ perpendicular to viewed direction, it is a good reference to check whether those spots either visible or absent in FT of phase images agree with the XRD pattern. As marked with orange dashed circles, these spots observed in the FT were not found in this XRD pattern. According to structure factor and resolution capability, plane $(2\ \bar{1}\ \bar{4})$, $(0\ 3\ 2)$ and $(2\ \bar{3}\ \bar{2})$ should be visible in XRD pattern.

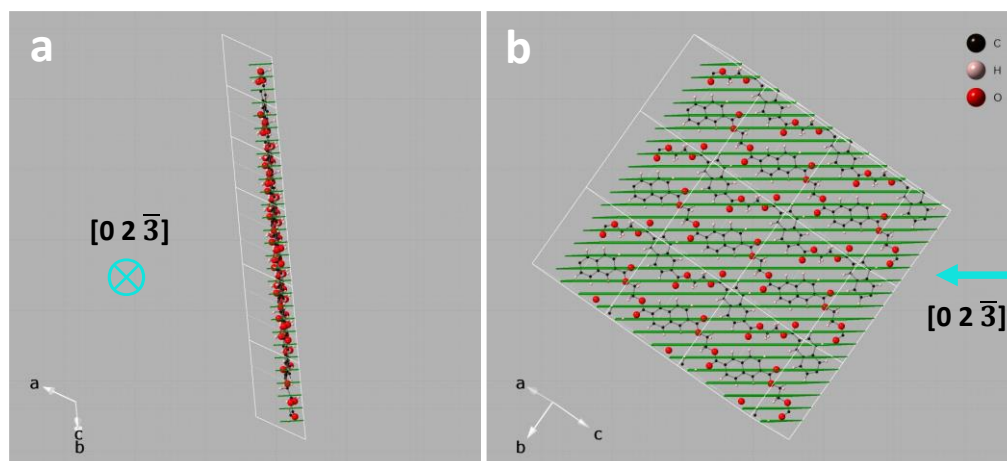


Figure 5.5 (a) One 'slice' molecular layer parallel to bc -plane viewed along $[0\ 2\ \bar{3}]$ with the plane $(\bar{2}\ 6\ 4)$ marked out (green lines). The direction of viewing axis is illustrated by the light blue arrows in the figures. (b) The slice of molecular layer was rotated by 90° and is viewed from left of its original viewed axis $[0\ 2\ \bar{3}]$, i.e., the viewing vector $[0\ 2\ \bar{3}]$ comes from the right. The intersection of the $(\bar{2}\ 6\ 4)$ planes with this layer is shown as the green lines. The repeating distance in plane $(\bar{2}\ 6\ 4)$ is found to be related to the periodicity of oxygens connected to aliphatic carbons.

A closer investigation about plane $(\bar{2} 6 4)$ and its associated chemical structure was conducted. Observation of the model from another perspective can offer insights. A 'slice' of the molecules parallel to bc -plane and the viewing lattice vector $[0 2 \bar{3}]$ was separated from the crystal model (Figure 5.5a), then rotated the vector $[0 2 \bar{3}]$ by 90° around the axis pointing up in the plane of image so the stacking of atoms in the plane became visible (Figure 5.5b).

The periodic feature within the $(2 0 0)$ planes measured by Line-profile ① in Figure 5.3 are highly matched with the planes $(\bar{2} 6 4)$ shown in Figure 5.5a, including the periodicity 1.86\AA and the distribution in $(2 0 0)$. According to the periodic of the parallel lines corresponding to plane $(\bar{2} 6 4)$ in Figure 5.5b, the repeated distance in $(2 0 0)$ is similar to the periodic distribution of oxygen atoms connected to aliphatic carbons. This allows the understanding of the observed periodicity and perhaps provides a hint that there might be some bond rotation between oxygen atoms and the connected aliphatic carbons, which generated the feature between the strong $(2 0 0)$ planes in the experimental image (Figure 5.3a).

5.2.4 Crystalline structure analysed with ptychography image revealed discrepancy compared to diffraction data.

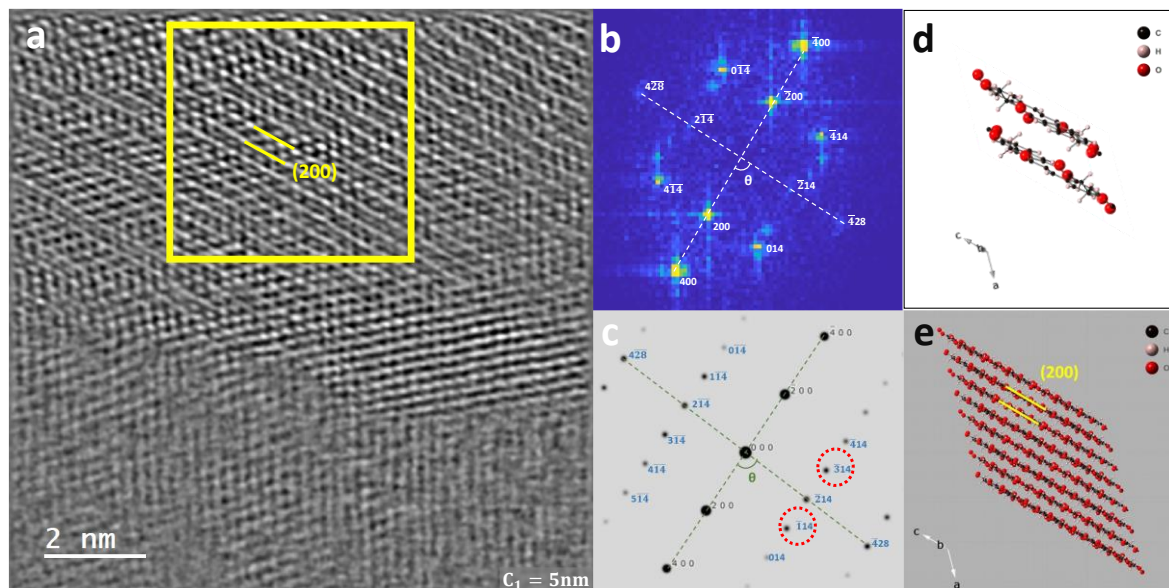


Figure 5.6 (a) Phase image of PEN with a dominant crystal occupying the upper two thirds of the whole area. The central region of this grain was selected as ROI (yellow rectangle). The (2 0 0) interlayer spacing is highlighted in the image. (b) The modulus of the FT of ROI in image (a) was indexed by reference to panel (c). The angle between (2 0 0) and each plane measured from the FT is denoted by θ . (c) Simulated single-crystal electron diffraction pattern (DP) from the model in d. The spots in red circles are the discrepancies found compared to FT of the phase image. (d) Unit cell of PEN β -form crystal model built from XRD data¹⁰ (monoclinic, with space group $P2_1/a$) viewed along vector $[0\ 4\ \bar{1}]$. | Plane (2 0 0) in PEN crystal model of multiple cells viewed from lattice vector $[0\ 4\ \bar{1}]$.

Another image (Figure 5.6a) was obtained from a different region of the same specimen with more probe positions (512 pixel) at the same magnification ($\times 20M$), i.e., finer pixel size generating the same level of contrast but smoother gradient in the phase image. (Figure 5.2a was acquired with 256 pixel)

The region of Figure 5.6a is dominated by one grain occupying the upper two thirds of the imaged area. The lattice in this dominant grain at defocus value of $C_1 = 5nm$ reveals the most detail and was used for structural study. Following the same calibration procedure described with previous dataset, the plane spacing d_{img} and plane angle θ were measured from FT

(Figure 5.6b) and tabulated in Table 5.4. The grain in Figure 5.6a can be determined to be viewed along lattice vector $[0\ 4\ \bar{1}]$, by comparing the FT with simulated ED patterns from different orientations of model, because of the broadly good match, albeit with some discrepancies, found in the plane spacings and angles.

The spacing of strong plane (2 0 0) measured from the image is 3.14Å, which is 0.22Å (6.5%) smaller than the model. This value of spacing is still within the range of results from same type of samples measured from ED and BF-STEM images. Also, there are two vague spots close to (0 1 4) and (4 $\bar{1}$ $\bar{4}$) that cannot match with any spot in the simulated DP. The largest discrepancy of plane angle θ is found for (0 1 4) as 5.8°, second largest plane angle discrepancy was found for (4 $\bar{1}$ $\bar{4}$) as 4.5°. Additionally, the ratio of spacing between plane (2 0 0) and ($\bar{2}$ 1 4) is reversed. In the model, the spacing of (2 0 0) is 0.3Å larger than ($\bar{2}$ 1 4); but in the image, the spacing of (2 0 0) is 0.3Å smaller than ($\bar{2}$ 1 4). Overall, the discrepancy for all plane spacing ranges from -0.22 to 0.38Å (Table 5.4), larger than the range of discrepancy found in Figure 5.2a.

Table 5.4 The plane spacings and angles measured from image and indexing. d_{img} represents the plane spacing directly measured from the ROI in phase image of Figure 5.6a with line-profile. The plane angle θ is measured with respect to the (2 0 0) planes from FT of ROI in Figure 5.6b; and these parameters are compared with corresponding planes in the model.

Spacing in phase image	Plane angle in FT	Model ¹⁰			Spacing discrepancy
		hkl	d_{mol}	Angle to (2 0 0) model	
d_{img}	Angle to (2 0 0): θ	β -monoclinic	Å	°	$d_{img} - d_{mol}$
Å	°		Å	°	Å
3.14	0	2 0 0	3.36	0.0	-0.22
1.57	0	4 0 0	1.68	0.0	-0.11
3.44	88	$\bar{2}$ 1 4	3.06	86.6	0.38
1.72	88	$\bar{4}$ 2 8	1.53	86.6	0.19
2.50	45	4 $\bar{1}$ $\bar{4}$	2.33	49.5	0.17
2.21	40	0 1 4	2.20	45.8	0.01

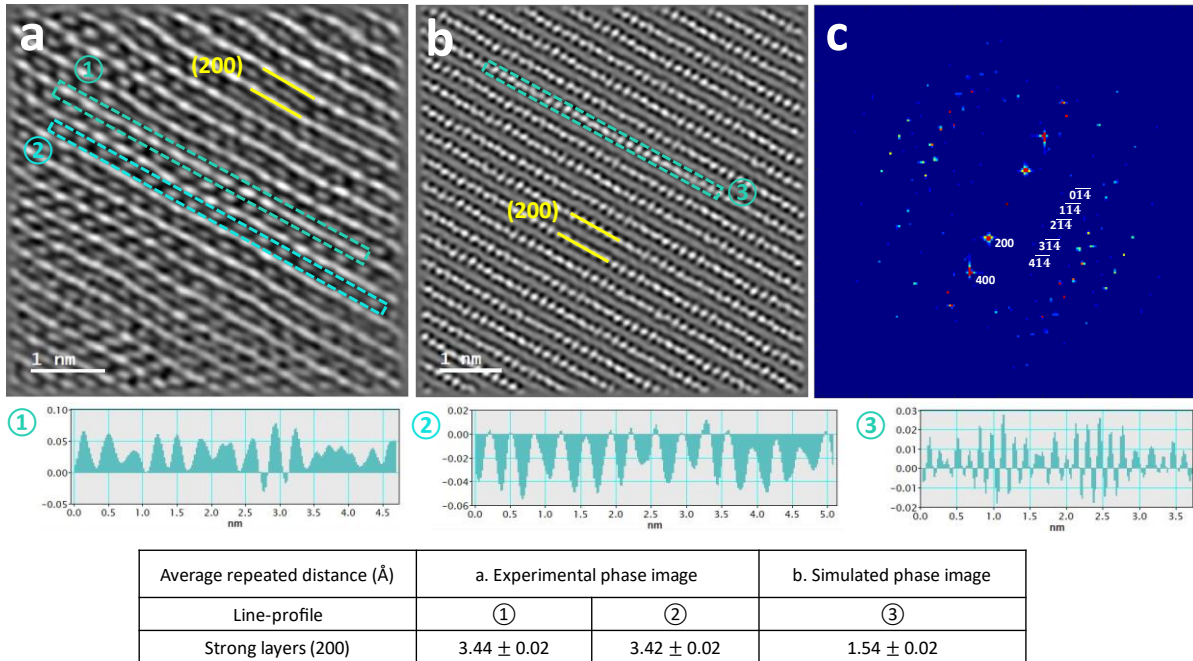


Figure 5.7 (a) ROI of experimental phase image in Figure 5.6a. There are periodic features within strong layer (2 0 0) and in the weaker layer between the strong (2 0 0) planes. Line-profile ① is one measurement of the periodic feature within strong layers (2 0 0) in the experimental phase image, the average peak-to-peak distance of which is 3.44Å. ② is one line-profile measuring the periodicity of weak layers, in which the average repeat distance is 3.42Å. (b) Simulated phase image reconstructed with 4D-STEM data obtained from model¹⁰ viewed from lattice vector $[0\ 4\ \bar{1}]$ with the same microscope parameters of a. ③ is one line-profile measuring the periodic feature within strong layers (2 0 0) in the simulated phase image, where the repeat distance is measured as 1.54Å. (c) FT of simulated image b.

The corresponding simulated image with the model viewed from $[0\ 4\ \bar{1}]$ was obtained as shown in Figure 5.7b. In the experimental phase image (Figure 5.7a), the average repeat distance within the strong layer (2 0 0) is 3.44Å measured by line-profile ①, but is 1.54Å in the simulated phase image (Figure 5.7b) by line-profile ③. Checking crystalline planes in experimental image with line-profiles, plane $(\bar{2}\ 1\ 4)$ and $(\bar{4}\ 2\ 8)$ were found distributing in the same direction as these periodic features within (2 0 0).

The spacing of plane $(\bar{2}\ 1\ 4)$ is 3.44Å measured from the experimental phase image (Table 5.4), which is identical to the repeat distance of the feature along the strong layer (2 0 0) found in Figure 5.7a, this implies the periodic feature within (2 0 0) can be $(\bar{2}\ 1\ 4)$ planes. The spacing of plane $(\bar{4}\ 2\ 8)$ is 1.53Å in the model, this is well matched with the repeated distance of feature

within (2 0 0) measured by Line-profile ③ in simulated phase image Figure 5.7b, which was generated from the same model. So, the periodic feature resolved in the strong layer (2 0 0) in experimental image (Figure 5.7a) can be plane $(\bar{2} 1 4)$, and the feature resolved in the strong layer of simulated phase image (Figure 5.7b) should be plane $(\bar{4} 2 8)$ that with half spacing of $(\bar{2} 1 4)$.

A periodic feature along the weak layers parallel to (2 0 0) was resolved in the experimental image. The periodicity of this feature was measured to be 3.42Å by line-profile ② in Figure 5.7a, and this value is very close to spacing of plane $(\bar{2} 1 4)$ 3.44Å. Whereas no feature between (2 0 0) is found in the simulated phase image (Figure 5.7b), where the zero contrast indicates vacuum.

In the experimental image (Figure 5.7a), the periodicity of features within (2 0 0) is 3.44Å, equal to plane spacing of $(\bar{2} 1 4)$ in image, and the periodicity of weak layer feature between (2 0 0) is 3.42Å. While in simulated image (Figure 5.7b), periodicity of feature within (2 0 0) is 1.54Å, equal to the plane spacing of $(\bar{4} 2 8)$ and half spacing of $(\bar{2} 1 4)$ in the model, no features between the strong (2 0 0) planes was resolved.

Combining all this information, it is reasonable to suppose the feature between the strong (2 0 0) repeats in the experimental image can be related to the vanishing of the feature within (2 0 0) with half-spacing of $(\bar{2} 1 4)$. There might be some conformational change in the molecular structure that results in the vanishing of plane $(\bar{4} 2 8)$ and the appearance of the features between the strong (2 0 0) repeats in the experimental image (Figure 5.7a).

Table 5.5 A summary of discrepancies found for the same ROI between the ptychography data in Figure 5.6, the simulated ED pattern, the FT of the simulated phase image (Figure 5.7c), and the fibre XRD in Figure 5.4.

Data that will be compared in this table:

- **Simulated ED:** electron diffraction pattern simulated by Crystal Maker from model built with XRD data¹⁰.
- **Simulated phase image:** the phase image obtained by SSB reconstruction with simulated 4D STEM dataset from model built from XRD data¹⁰.
- **FT of simulated phase image:** result of Fourier Transform conducted on simulated phase image.
- **FT of experimental phase image:** result of Fourier Transform conducted on SSB reconstructed phase image, which was obtained experimentally in this work.
- **Fibre XRD:** experimental XRD data obtained from fibre (Figure 5.4) by Heuvel *et al.*¹⁰

Viewed from zone axis: [0 4 $\bar{1}$]							
Plane info.		Simulation with model ¹⁰		Experimental results		Proposed explanation for invisible spots	
<i>hkl</i>	Spacing (Å)	Simulated ED	FT of simulated phase image	FT of phase image	Fibre XRD ¹⁰	FT of phase image	Fibre XRD
2 0 0	3.14	visible	visible	visible	visible	\	\
4 0 0	1.57	visible	visible	visible	visible	\	\
$\bar{2}$ 1 4	3.44	visible	dim	dim	absent	dim: spots are visible but not intense. absent: the absence of ($\bar{1}$14) and ($\bar{3}$14) spots are evidence of structural difference, because the plane ($\bar{4}$28) with smaller spacing was resolved, and they have high intensity in simulated ED pattern.	Based on the structure factor in XRD, i.e., relative intensity, ($\bar{2}$ 14) should be visible, and (014) should NOT be visible in XRD.
0 1 4	2.50	visible	visible	visible	absent		When spacing smaller than 3Å, spots in fibre XRD become very weak, and each spot can be from multiple planes.
$\bar{4}$ 1 4	2.25	visible	visible	visible	absent		
$\bar{1}$ 1 4	2.73*	visible	dim	absent	absent		
$\bar{3}$ 1 4	2.85*	visible	dim	absent	absent		
$\bar{4}$ 2 8	1.72	visible	visible	dim	absent		When the spacing is smaller than 2Å, the plane cannot be resolved in the XRD data.

*Note: plane spacing values of absent plane in the image are from model.

The discrepancies found between FT of the experimental image and the simulated data are summarized in Table 5.5. The intensity of spot ($\bar{2}$ 1 4) is noticeably 'dim' in the FT of the experimental image and simulated image compared with the simulated ED. As measured in Figure 5.7a, planes ($\bar{2}$ 1 4) are distributed along (2 0 0) with spacing 3.44Å, and the periodicity of the weak features between high intensity layer (2 0 0) is 3.42Å. The periodicity of plane ($\bar{2}$ 1 4) and the features between (2 0 0) are similar but out of phase. Therefore, the signal of ($\bar{2}$ 1 4) in the frequency domain was cancelled out by the parallel periodic feature between layer (2

0 0), and the spot of $(\bar{2} 1 4)$ in FT is the residual signal after being cancelled by the anti-phase features. This explains why the relative intensity of $(\bar{2} 1 4)$ in the FT is much lower than that in simulated DP, although the fringe is clearly resolved in the phase image. This phase cancelling effect is also observed in the FT of simulated phase image (Figure 5.7c).

Two intense spots of $(\bar{1} 1 4)$ and $(\bar{3} 1 4)$ in the simulated DP were absent in the FT of the experimental image (Figure 5.6b), but visible in the FT of the simulated phase image although the spots are relatively low intensity, which means they can be resolved by ptychography. Spacing of $(\bar{1} 1 4)$ and $(\bar{3} 1 4)$ are 2.73 and 2.85Å respectively, which are larger than the spacing of visible planes $(0 1 4)$ and $(\bar{4} 1 4)$. Also, their intensity in simulated DP is higher than $(0 1 4)$ and $(\bar{4} 1 4)$. Meanwhile, the fibre XRD pattern cannot determine whether the absence of $(\bar{1} 1 4)$ and $(\bar{3} 1 4)$ are contradictions, because the spots from planes with spacing smaller than 3Å are vague and can correspond to multiple planes. Therefore, the absence of spots $(\bar{1} 1 4)$ and $(\bar{3} 1 4)$ in the FT of experimental image indicates the structural difference in this PEN specimen, i.e., $(\bar{1} 1 4)$ and $(\bar{3} 1 4)$ may not exist due to structural discrepancy in the grain in Figure 5.6a.

Additionally, plane $(\bar{2} 1 4)$ and $(0 1 4)$ are not found in the fibre XRD pattern, as marked with orange dashed circles in the fibre XRD (Figure 5.4). Plane $(\bar{2} 1 4)$ should be visible as its spacing is larger than 3Å, and its structure factor is higher than the intense spot $(2 0 \bar{4})$, referring to value in software of CrystalDiffract. Whereas it makes sense that $(0 1 4)$ is invisible in fibre XRD, as its structure factor is too low although its spacing is within the resolution limit. This observation means the XRD data did not disprove the absent spots in FT of experimental image and may contain different molecular conformation to the crystal structure of PEN fibre.

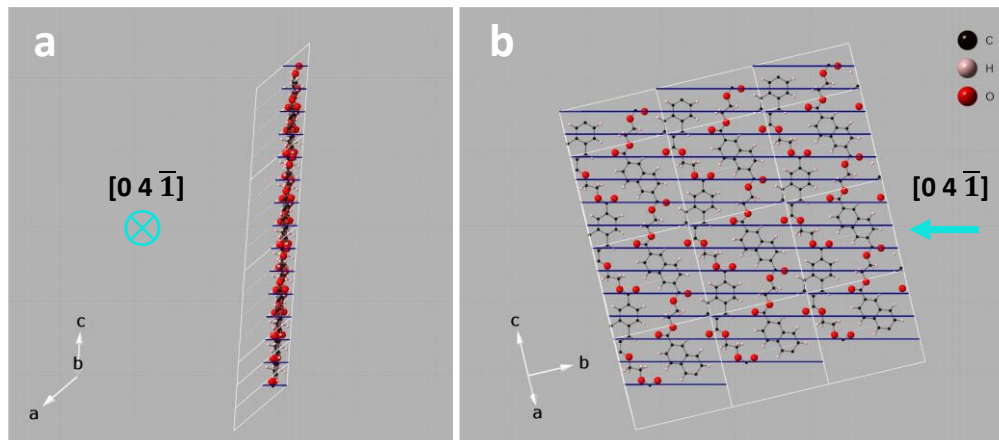


Figure 5.8 (a) One 'slice' of molecular layer parallel to bc -plane viewed along $[0\ 4\ \bar{1}]$ was separated from the rest of model. Short parallel lines represent plane $(\bar{2}\ 1\ 4)$. (b) the molecular slice was rotated for 90° and the vector $[0\ 4\ \bar{1}]$ comes from the right. The intersection of the $(\bar{2}\ 1\ 4)$ planes with this layer is shown as the blue lines throughout the slice of model. It can be observed that the repeating distance in plane $(\bar{2}\ 1\ 4)$ well match the periodicity of oxygens connected to aliphatic carbons.

A study was conducted to observe the model from a different perspective in an attempt to interpret the conformational difference between experimental and simulated images. As shown in Figure 5.8a, a 'slice' of plane $(2\ 0\ 0)$ viewed from zone $[0\ 4\ \bar{1}]$ was separated from the multi-cell model, then rotated for 90° around axis pointing up in the image plane to reveal the conformation details inside the slice as shown in Figure 5.8b.

The parallel lines in Figure 5.8a are plane $(\bar{2}\ 1\ 4)$ viewed along $[0\ 4\ \bar{1}]$ in the grain. When the slice was viewed from another perspective, the repeating chemical structures corresponding to plane $(\bar{2}\ 1\ 4)$ can be visualized. Following the lines representing plane $(\bar{2}\ 1\ 4)$ in Figure 5.8b, it can be found the spacing of planes $(\bar{2}\ 1\ 4)$ match with the periodicity of oxygens connected to aliphatic carbons. This implies the structural difference might be generated from single bond rotation of oxygen atoms connected to aliphatic carbons. This conformal rotation can lead to a model that explain this observation. This image (Figure 5.6a) may be another evidence for the local structural difference that is not generating a distinct diffraction pattern, and that the local conformation can only be revealed with high-resolution imaging.

This structural difference between the experimental results and the model could be caused by the newly developed sample-prep methodology, in which the PEN thin film crystallized from a perfect amorphous state, whereas the samples used to generate the model were mostly from fibres or samples crystallized from the melt. However, this imaging and analysis methodology could provide evidence of the true local structure, where slight differences in atomic arrangement do not generate a clearly distinct diffraction pattern. The slight difference in plane spacing and angles captured by ptychography image, would not be reflected in X-Ray or electron diffraction patterns as these discrepancies are too subtle to generate a distinct DP. Therefore, the conformational details resolved in ptychography image can lead to a new model of the PEN crystal structure.

5.3 Conclusion

In this chapter, the image analysis methodology for understanding PEN crystal structure has been established. The low dose STEM ptychography imaging methodology developed in previous chapters has been applied to acquire images from semi-crystalline PEN thin film. The images revealed the local molecular conformation of the crystalline structure. With the sufficient contrast of images obtained from polymer specimen, the discrepancy of local structure against the average structure proposed from conventional diffraction methods, e.g., XRD, electron diffraction, can now be identified.

A periodic feature was resolved between (2 0 0) and this feature was only found in experimental image. The periodicity of feature between strong layer (2 0 0) was identical to periodicity of a plane within (2 0 0), while the half-spacing of this plane vanished in experimental image but resolved in simulated image. Hence, the chemical structure related to this vanished half-spacing plane in experimental image is likely where the structural discrepancy formed. This

discrepancy might correspond to rotation of some molecular segments, e.g., the oxygen atoms connected to aliphatic carbons. Additionally, smaller inter-planar distance of (2 0 0) was found, which implies there may be 'chain extension' or 'bond rotation' in the molecules leading to 'flatter planes' that can get closer together.

All these discrepancies indicated distinct local structure compared to the structure predicted by the model built from XRD data, hence implies a modified model. The discrepancy observed between the experimental and simulated ptychography phase image revealed the corresponding chemical structure where it may form. Therefore, a tool to capture the local crystal structure and the analysis protocol has been established, hence more precise measurements on features in different part of a heterogeneous material can be conducted. This can be a starting point to study the local conformational structural variation in crystals of macromolecules.

6 Analysis of features dispersed in 3D with 2D images

The polymer specimens used in this work have typical thickness of ~50nm, therefore multiple grains may be present in the region of one image, distributed along the viewing direction through the thin film. The grains at various depths could be adjusted to be “in-focus” and studied using optical sectioning. In addition, the relative orientation and location in three dimensions can be determined.

The advantage of optical sectioning is that not only can the local molecular structure be resolved, but the size of the structure along the viewing direction can also be determined. Thus, the distribution and dimensions of the feature can be determined in both lateral and viewing directions. The objective of this chapter is to develop an analysis methodology for ptychography images involving multiple domains using optical sectioning, to resolve structural information along the viewing direction.

6.1 Spatial relation of multiple grains distributing in three dimensions

Figure 6.1a shows the image obtained from a PEN specimen at a defocus of $C_1=+5$ nm relative to probe cross over, which appears to show only one grain captured in the acquisition area of this image and the grain was relatively small. There was the best resolution of the central grain lattice at $C_1=+5$ nm, and the FT of the ROI (Figure 6.1b) was found to broadly match the simulated DP from $[0\ 4\ \bar{1}]$ (Figure 6.1c), despite some discrepancies. Most plane spacing discrepancies between measured values and model were within 10% (Table 6.1), except for plane $(\bar{2}\ 1\ 4)$. The spacing of $(\bar{2}\ 1\ 4)$ in the image is -0.36\AA (11.8%) smaller than that of the model. Parallel to this, discrepancy of plane $(\bar{2}\ 1\ 4)$ has also been observed in the other PEN images in Chapter 5 (Figure 5.6), and the values of discrepancy are almost equal (Table 5.4).

Both the grain in Figure 6.1 and the grain in Figure 5.6 of Chapter 5 are viewed parallel to the lattice vector $[0\ 4\ \bar{1}]$. The FT in Figure 6.1b shows clear spots, unlike the FT in Figure 5.6b, which contains several vague spots that cannot be indexed. In addition, spot $(2\ 1\ 4)$ was observable in Figure 6.1b, which means the features in the weak (relatively low intensity in the image) layers between $(2\ 0\ 0)$ plane is now in phase with those in the strong layers (relatively high intensity, it means the fringes of plane (200) here), different from previous chapter.

The central grain is relatively small. The lateral size of the grain in the centre is smaller than $10\times 10\text{nm}$ (Figure 6.1a), which would be equivalent to approximately 10 unit-cells, assuming that the c-axis is approximately parallel to the projection (image) plane, as shown in Figure 6.1d. Because the boundary of the crystal in Figure 5.6 was beyond the image, the exact size of the grain cannot be determined, but the part within the image was larger than the central grain in Figure 6.1a. Both grains were viewed along the same vector $[0\ 4\ \bar{1}]$. When comparing the two images, the smaller crystal (Figure 6.1b) generates a clearer FT, while the FT from the larger grain (Figure 5.6b) is characterized by some vague spots and more noise, which may be indicative of structural defects. It is reasonable to assume that a larger number of defects could form as the crystal grows larger.

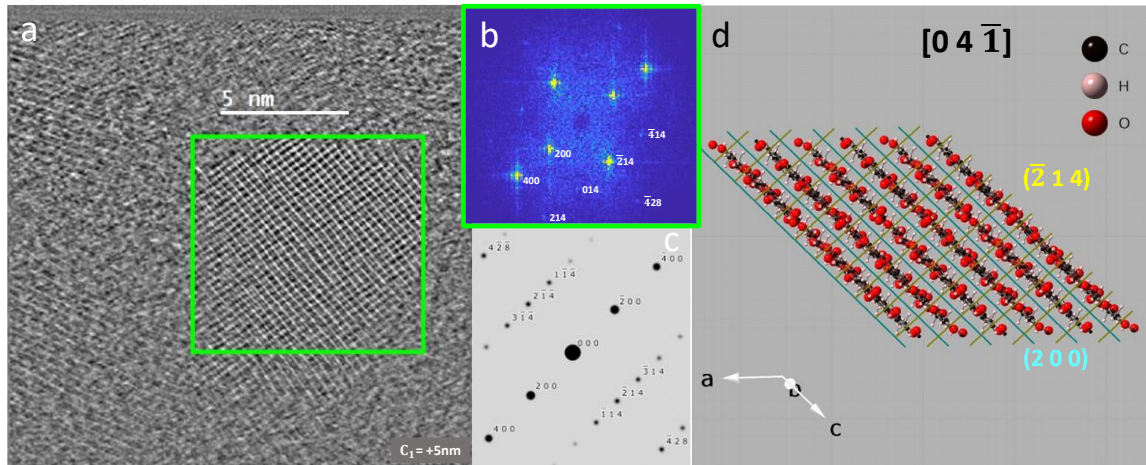


Figure 6.1 (a) The grain in centre is in-focus at C_1 value of +5nm. The diameter of the grain is less than 10nm. (b) FT of the ROI of central grain in-focus. (c) Simulated electron DP from (d) the model¹⁰ viewed from lattice vector $[0\ 4\ \bar{1}]$.

Table 6.1 Indexing FT pattern in Figure 6.1b with Model¹⁰ of PEN crystal along $[0\ 4\ \bar{1}]$

Plane spacing & angle in FT		Model ¹⁰ of PEN crystal along $[0\ 4\ \bar{1}]$				Spacing discrepancy
d_{FT}	Angle to (200): θ	hkl	d_{mol}	Angle to (200) model	Relative Intensity	$d_{FT} - d_{mol}$
Å	°	β -monoclinic	Å	°	%	Å
3.15	0	2 0 0	3.36	0.0	100.0	-0.20
1.55	0	4 0 0	1.68	0.0	10.4	-0.13
2.70	86	$\bar{2}$ 1 4	3.06	86.6	0.4	-0.36
1.34	86	$\bar{4}$ 2 8	1.53	86.6	0.4	-0.19
2.13	49	$\bar{4}$ 1 4	2.33	49.5	0.1	-0.20
1.96	46	0 1 4	2.20	45.8	0.0	-0.23
1.28	29	2 1 4	1.44	27.9	0.0	-0.16

In the process of determining the optimal depth to resolve the central grain and measuring its thickness with optical sectioning, more features were revealed at other depths in the rest of the image area (Figure 6.2). By $C_1=+35$ nm (Figure 6.2h), the central grain was no longer distinctly discernible. In Figure 6.2i, other grains around the central grain were best resolved at $C_1=+40$ nm, while the central grain became out of focus. The lattice around the central grain exhibits periodicity along diverse directions, implying these grains were viewed from different orientations.

The dataset demonstrated that optical sectioning could be used to identify and separate multiple grains distributed in three dimensions. In a specimen that contains multiple grains at different depths, the lattice of each grain can be analysed by adjusting the defocus value, thus allowing the grains that were originally 'out of focus' to become 'in focus'.

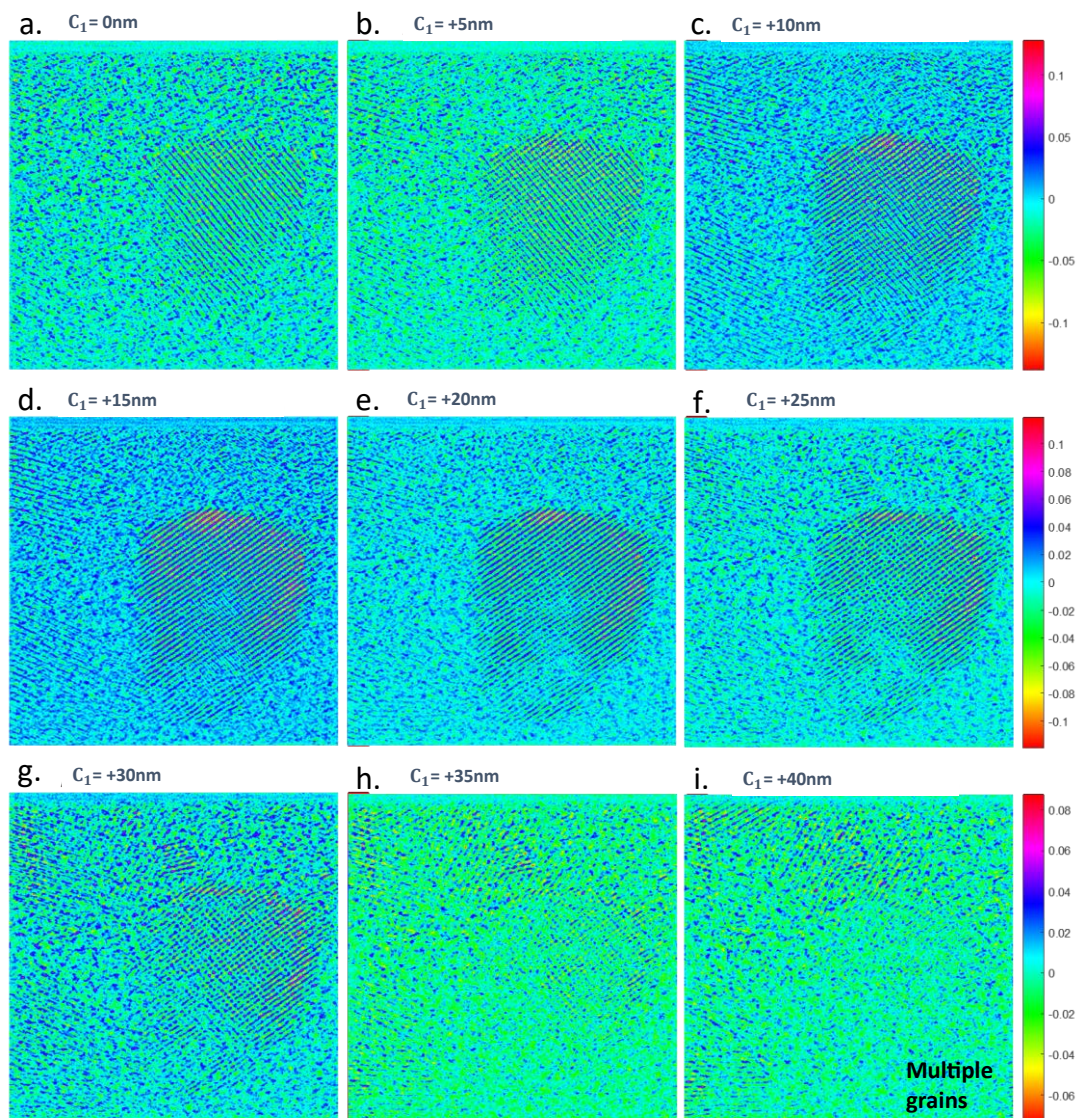


Figure 6.2 Ptychography phase images of C_1 series ranging from 0~40nm. The HSV colour map was chosen to enhance the distinction of the grains. Multiple grains with different orientation and at distinct depth in the region could be separated by optical sectioning.

6.2 Resolve lattices forming Moiré fringes

6.2.1 Moiré fringes formed by stacked lattices

One commonly observed feature in semi-crystalline materials is moiré fringes formed by two lattices stacked at different orientations that form an angle between them. It is difficult to resolve the individual sets of lattices separately with conventional STEM imaging techniques. Here optical sectioning offers a simple method to directly measure the angle between the lattices without calculation, as well as visualize each of the stacked lattices.

This methodology is demonstrated by a depth profile of an image containing Moiré fringes as shown in Figure 6.3. The moiré fringes were observed at $C_1 = -1\text{nm}$ (Figure 6.3b). The stacked lattices were separated by optical sectioning to produce images involving only one feature of those forming the synthetic fringes. The lattice underneath was independently resolved at $C_1 = -21\text{nm}$ (Figure 6.3a), and the lattice on the top was independently resolved at $C_1 = +19\text{nm}$ (Figure 6.3c).

A widely used method for separating the lattices that form Moiré fringes is to perform FT on the image, mask one set of spots, and then reverse FT to visualize the lattice with the corresponding spatial frequency. But the grain of an organic crystal may contain partial defects; therefore, the FT would contain extra spots or arches produced by the defective planes, making it difficult to isolate the stacked lattices.

However, with optical sectioning, the lattices at different depths could be separated into independent images containing the specific set of lattices. The imperfections in the lattice would not affect the separation result and can be observed in the image. As an example, the top layer lattice in the image $C_1 = +19\text{nm}$ contained some bending (Figure 6.3c), whereas this defect did not affect the optical section and could be visualized after the lattice was isolated. The method is suitable for organic materials that contain crystals of tens of nanometres in thickness, while

the application to monoatomic layer 2D materials remains unknown but may be worth exploring.

It can be observed that each set of lattices is 20nm distant from the image where Moiré fringes form ($C_1 = -1\text{nm}$), and the angle between the lattices is 17.40° . The relatively large distance between the two layers of lattices and angle between fringes weaken the possibility that they are part of the same grain.

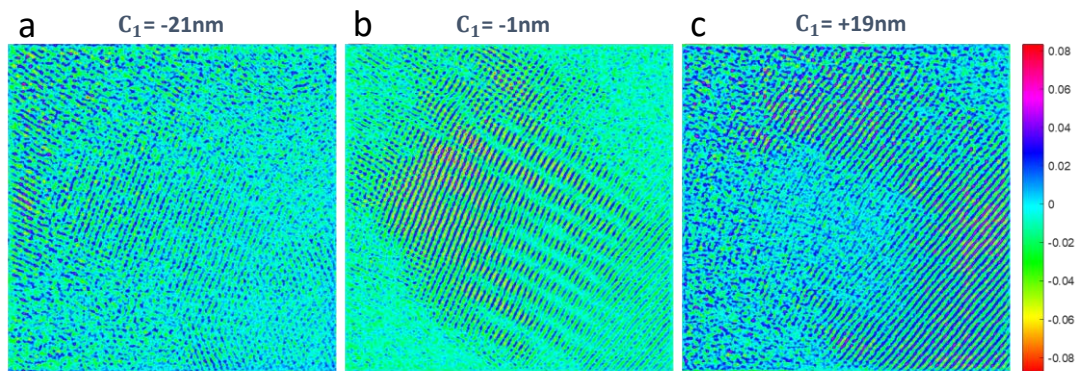


Figure 6.3 Separation of stacking lattices forming Moiré fringes by Optical Sectioning. (a) The image at $C_1 = -21\text{nm}$ contains only one set of lattices at the bottom. (b) The image at $C_1 = -1\text{nm}$ where Moiré fringes were observed. (c) The image at $C_1 = +19\text{nm}$ contains the lattice of top layer.

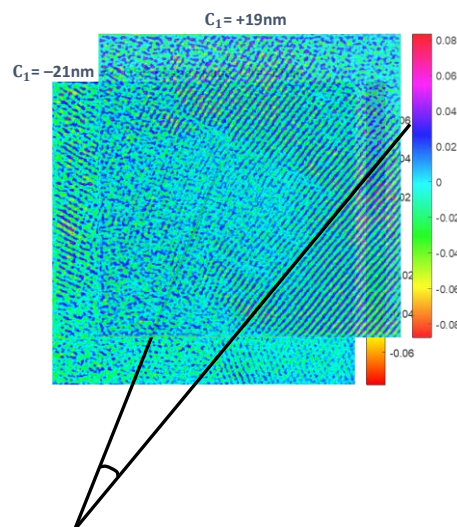


Figure 6.4 The angle between stacked lattices directly measured from the images was 17.40° .

6.2.2 Moiré fringes formed by local plane twisting within one grain

Moiré fringes found in another image appeared to be produced by lattices in the same grain, which may suggest internal plane twisting. A crystal edge as shown in Figure 6.5, where a depth profile ranging from -27nm to -7nm with interval depth of 5nm was used to study the crystalline structure along the viewing direction. The lattice structure appeared uniform in the image at $C_1 = -27\text{nm}$ but kept changing as C_1 increased. Noticeably at $C_1 = -17\text{nm}$, the bottom left corner showed some “ripples” of Moiré fringes (Figure 6.5c). A clear lattices differentiation appears at the depth of $C_1 = -12\text{nm}$, where the uniform lattice became two distinct parts, which were separated as indicated by the black line in Figure 6.5d. The FT of the two distinct parts revealed the same FT pattern with different relative intensities for the spots (Figure 6.6b, c), suggesting they are part of the same grain but slightly tilted in orientation. The crystal split into two parts above and below the $C_1 = -17\text{nm}$, where the lattice twist around the viewing direction, and the lattice superposition form Moiré fringes. Crystal twisting has been reported in crystalline morphology observed with TEM image (Figure 6.7), while the depth profile in Figure 6.5 resolve the twisting at molecular level with lattice images.

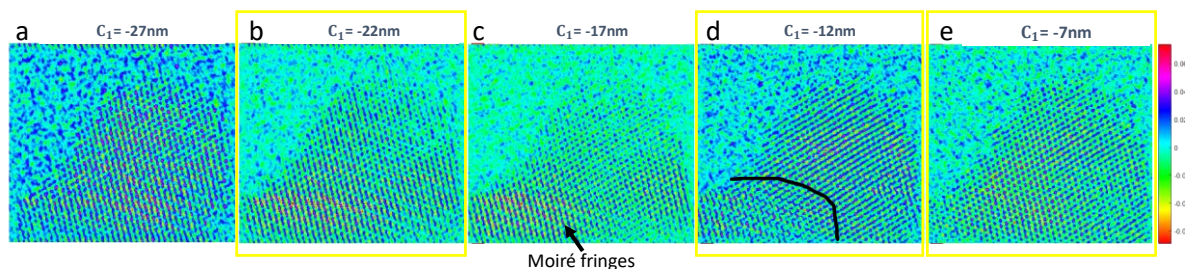


Figure 6.5 The depth profile of a ptychography image from PEN specimen, which were plotted with HSV colormap to enhance the feature for ease of observation. (a) Uniform and continuous crystalline feature at $C_1 = -27\text{nm}$. (b) at $C_1 = -22\text{nm}$, the lattices in upper part of the grain started to fade. (c) The bottom left corner showed some ripples of Moiré fringes at $C_1 = -17\text{nm}$. (d) at $C_1 = -12\text{nm}$, the grain contained two types of features separated by the line. (e) at $C_1 = -7\text{nm}$, the lattice became uniform again. The images in yellow boxes will be further analysed for the crystalline structure with indexing.

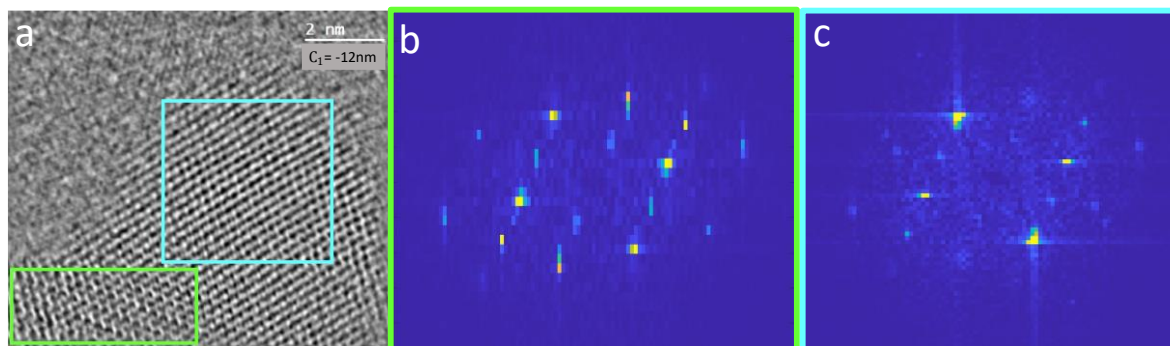


Figure 6.6 (a) Phase image at $C_1 = -12\text{nm}$. Two parts of the grain with different features were selected separated to conduct FT. (b) The FT of ROI in green rectangle in a, (c) FT of the ROI in blue rectangle in b. FT in b and c correspond to the same lattice patterns, but some spots in b were stretched.

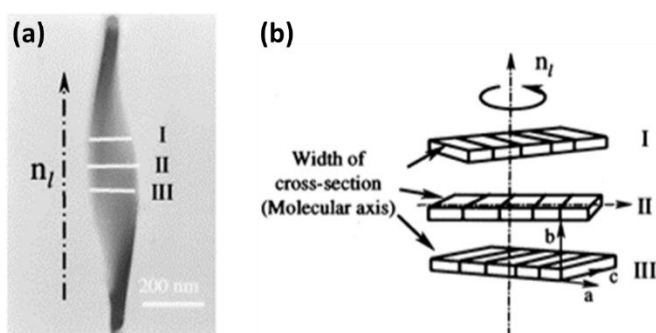


Figure 6.7 Single-twist model of the helical lamellar crystals.^{106,107} (a) TEM image of the helical lamellar crystal. I, II, and III represent three cross sections. (b) Enlarged and isolated cross sections I, II, and III in the single-twist model. There is only one helical axis (n) in this model.

Although the lattice may contain some local tilting or twisting that changes the relative intensity in FT spots, the FT pattern remains the same. The FT pattern was indexed to analyse the local tilting of planes. According to the defocus series in Figure 6.5, the crystalline lattice at $C_1 = -22\text{nm}$ was continuous and uniform (Figure 6.5b), and therefore the FT was used for indexing. In accordance with Table 6.2, the plane spacing and angles in the FT matched the model very well with simulated DP from lattice vector $[\bar{3} \bar{7} \bar{4}]$ (Figure 6.8c). According to the mechanism of phase image formation, the reconstruction was based on the diffraction signals of crystalline

planes, therefore the lattice resolved in the phase image (Figure 6.8a), should correspond to planes $(\bar{1} 1 \bar{1})$ and $(2 2 \bar{5})$ in the crystalline structure as highlighted in the model (Figure 6.8d).

When the C_1 continued increasing in the depth profile, the lattice at $C_1=-7\text{nm}$ (Figure 6.9a) appeared to be one uniform grain again. Plane $(2 2 \bar{5})$ was still well resolved in this image, but the other intense spot was due to plane $(4 0 \bar{3})$. The corresponding planes in the model were also marked in Figure 6.9d. The discrepancy between the FT and simulated DP is the relative intensity of plane $(4 0 \bar{3})$, which is in accordance with the observation in Figure 6.9b that plane $(4 0 \bar{3})$ became a strong plane.

The change of relative intensity of spots along the depth profile implied that orientation of planes relative to the viewing direction can change subtly. The crystal is bifurcating such that the lattice splits into two slightly different orientations which then overlap leading to the Moiré fringes.

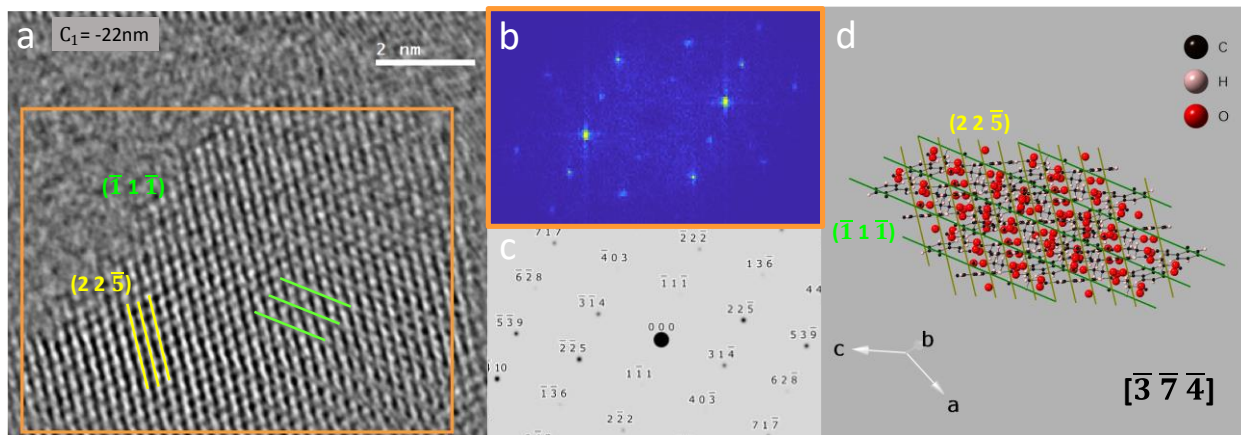


Figure 6.8 (a) Ptychography SSB phase image at $C_1 = -22\text{nm}$. (b) FT of the ROI in a. (c) Simulated DP produced from d. (d) PEN crystalline model of β -monoclinic form viewed from $[\bar{3} \bar{7} \bar{4}]$. The lines stand for the planes of $(\bar{1} 1 \bar{1})$ in green, and $(2 2 \bar{5})$ in yellow colour in the image.

Table 6.2 Indexing of FT pattern in Figure 6.8b with Model¹⁰ of PEN crystalline $[\bar{3} \bar{7} \bar{4}]$

Plane spacing & angle in FT		Model of PEN crystalline along $[\bar{3} \bar{7} \bar{4}]$				Spacing discrepancy
d_{FT}	Angle to $(\bar{1}\bar{1}\bar{1})$: θ	hkl	d_{mol}	Angle to $(\bar{1}\bar{1}\bar{1})$ model	Relative Intensity	$d_{FT} - d_{mol}$
Å	°	β -monoclinic	Å	°	%	Å
4.00	0	$\bar{1} \bar{1} \bar{1}$	3.95	0.0	0.0	0.05
2.00	0	$\bar{2} \bar{2} \bar{2}$	1.98	0.0	0.0	0.02
2.37	56	$4 0 \bar{3}$	2.33	54.7	0.0	0.04
2.86	89	$3 1 \bar{4}$	2.85	89.3	0.3	0.01
1.42	89	$6 2 \bar{8}$	1.42	89.3	0.0	-0.01
2.31	54	$2 2 \bar{5}$	2.30	53.7	1.6	0.01
1.18	54	$4 4 \bar{1}0$	1.15	53.7	2.5	0.03
1.64	35	$1 3 \bar{6}$	1.61	34.5	0.0	0.03
1.21	26	$0 4 \bar{7}$	1.19	24.7	0.1	0.02

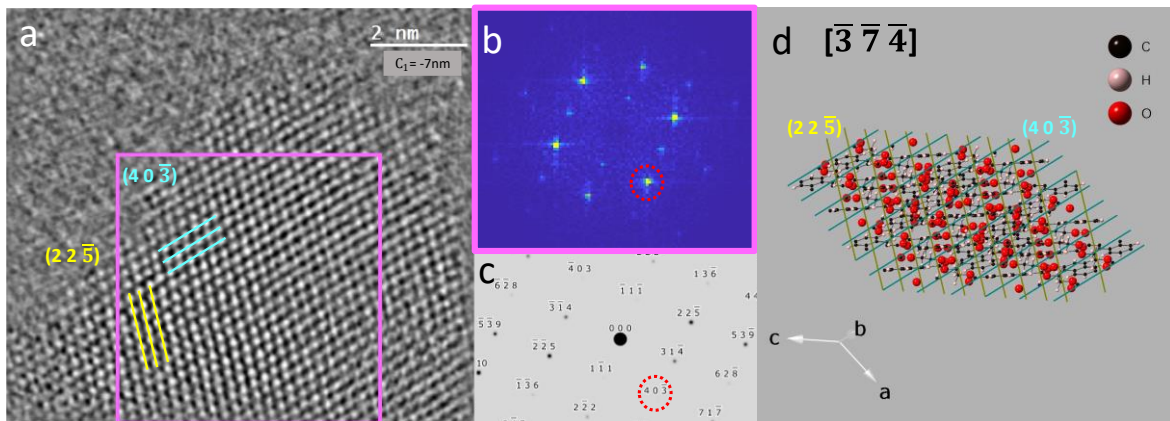


Figure 6.9 (a) The phase image at $C_1 = -7\text{nm}$. (b) FT of the ROI in yellow rectangular in a. (c) Simulate DP with model from lattice vector $[\bar{3} \bar{7} \bar{4}]$. (d) PEN crystalline model viewed from $[\bar{3} \bar{7} \bar{4}]$ involved multiple unit cells, plane $(2 2 \bar{5})$ and $(4 0 \bar{3})$ were shown in the model.

6.3 Partial plane tilting/defect within one grain measured along the viewing direction

6.3.1 Identify local plane tilting within one grain

The majority of crystals found in the semi-crystalline PEN specimen were thicker than 10nm. Besides Moiré fringes, the partial plane tilting can also be observed in other forms. In some cases, the partial tilting is found as a type of defects inside the crystal. The defects could be resolved in the phase image if it was at an observable level by a change in the lattice fringes. By

analysing the depth profile produced by optical sectioning, the location and dimensions of the defects could be determined. The purpose of this section is to discuss partial distinct features along the viewing direction within a grain identified by optical sectioning.

In order to identify the discrepancies associated with indexes, the first step is to determine the orientation of the grain. One large grain dominates this image, and the continuous lattice at $C_1 = +10\text{nm}$ (Figure 6.10a) was chosen for indexing. The viewing direction was parallel to the lattice vector $[0\ 2\ \bar{3}]$ determined by indexing with the FT (Figure 6.10b). Then the lattice was observed by resolving the lateral morphology at various depths (Figure 6.11) along the viewing direction, with an interval length of 2.5nm all the way upwards starting from $C_1 = +10\text{nm}$. In the images at $C_1 = +10\text{nm}$ and $+12.5\text{nm}$, the crystal lattice was clearly resolved and continuous. As the image at $C_1 = +15\text{nm}$ progressed, the lattice in the lower-right part of the image became blurry, while the lattice in the upper part of the image remained sharp. The boundary between the two regions is indicated by the black line (Figure 6.11c). Upon changing the C_1 to $+17.5\text{nm}$ and $+20\text{nm}$ (Figure 6.11d,e), the lattice at the lower-right part became distinct from the original feature at $C_1 = +10\text{nm}$ (Figure 6.11a).

A further investigation into the lattice differentiation in the image at $C_1 = +15\text{nm}$ (Figure 6.11c) was conducted. Although the lattices in two regions are visually distinguished, there is a broad fit between FT patterns from each part (Figure 6.12b, d) and the simulated DP along $[0\ 2\ \bar{3}]$. The intensity of spots in FT from the lower part of the image became dimmer (Figure 6.12b), but the pattern remains the same. Similar for the upper part (Figure 6.12d), but more discrepancies are observed. The spots of FT in Figure 6.12d became more diffuse compared to those at $C_1 = +10\text{nm}$ (Figure 6.10b), for example, the spots of $(2\ 0\ 0)$ and $(4\ 0\ 0)$ became more intense, while the spots of $(0\ 3\ 2)$, $(0\ 6\ 4)$, $(4\ \bar{3}\ \bar{2})$ and $(\bar{2}\ 6\ 4)$ became vague and can only be roughly identified. The indexes of the three FT are presented in Table 6.3.

It appears that the two distinct lattices are still part of the same grain because of the same FT patterns they generated, and the change of relative intensity of spots indicated slight tilting of the orientation. This can be supported by results obtained with simulated DP by rotating the model viewed from $[0\ 2\ \bar{3}]$ by 0.8° (Figure 6.12e), which shows not only the pattern but also relative intensity are similar to FT in Figure 6.12d.

Therefore, despite the lattice was found to change along the depth, the possibility of multiple grain stacking can be excluded because the FT patterns of the two distinct lattices both matched with the simulated DP from $[0\ 2\ \bar{3}]$. The difference in the feature may indicate a local structural discrepancy within the crystal. It is possible that part of the crystallography planes tilt, hence the local orientation of lattices would slightly change within small range, leading to crystal bending and blurring of lattices. The morphology of crystal bending was also observed in AFM images (Figure 6.13). By using optical sectioning, this crystal bending caused by partial plane tilting is directly observed at lattice level. The crystal bending might be the result of relatively weak intermolecular force in polymers.

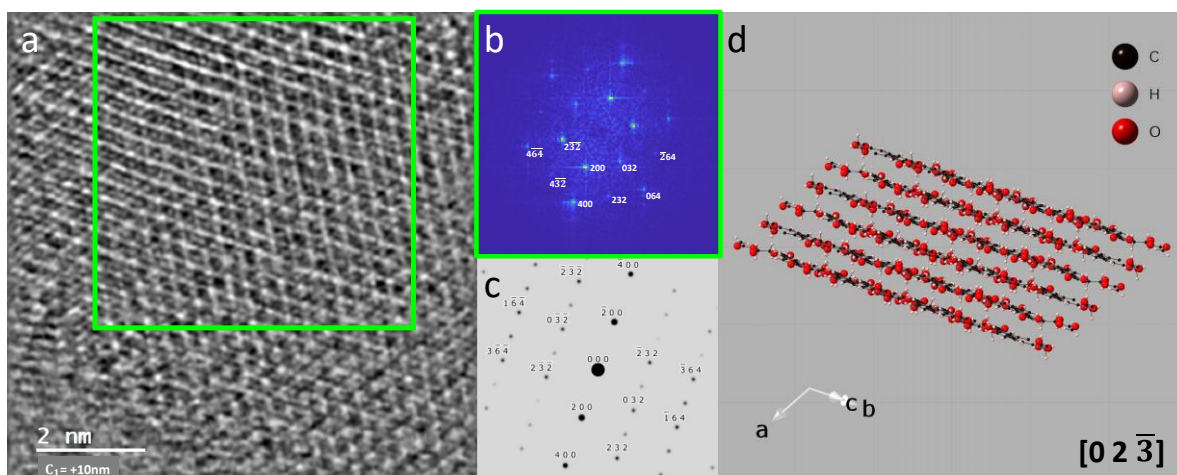


Figure 6.10 (a) The feature was continuous in the phase image of $C_1 = +10\text{nm}$. Majority of the grain was selected for structural analysis. (b) FT pattern of the ROI in a. (c) Simulated DP produced from (d) unit cell of PEN crystalline model viewed from lattice vector $[0\ 2\ \bar{3}]$.

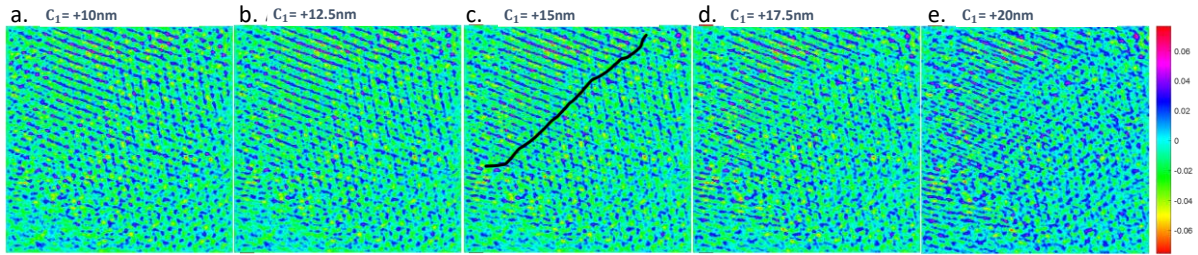


Figure 6.11 Depth profiling of the Figure 6.10a ranging from +10nm to +20nm. (c) A black-line highlights where the lattice appears two parts of distinct features starting at $C_1=+15\text{nm}$ while the C_1 value increasing, i.e., use optical sectioning to “slice” through the structure downwards from the top.

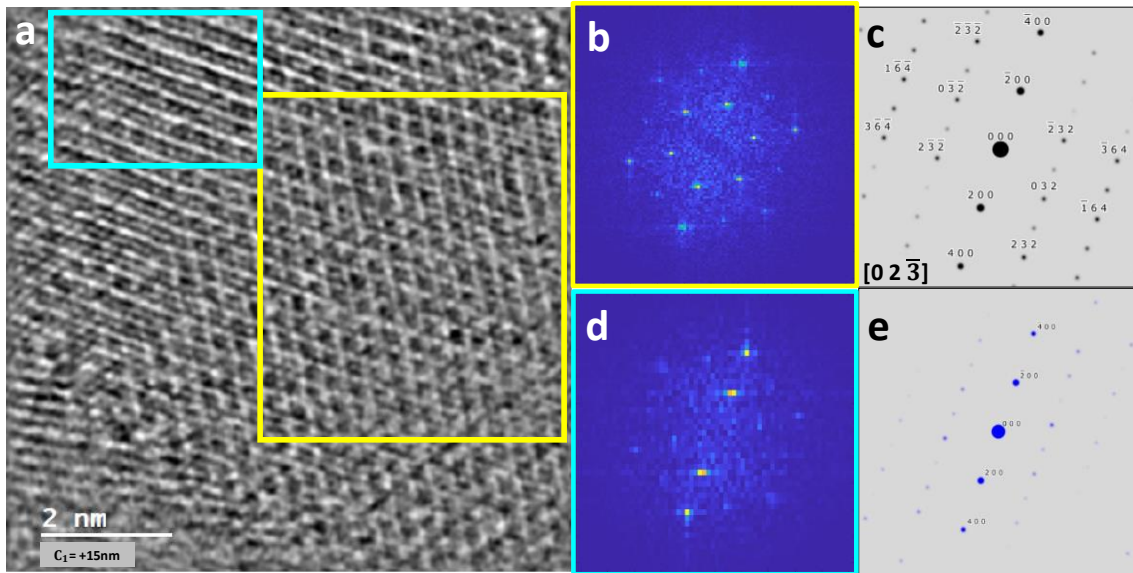


Figure 6.12 (a) The phase image at $C_1= +15\text{nm}$ where the grain become two parts of distinct features. (b) The FT of ROI in yellow rectangle in a. (c) Simulated DP from model along zone axis $[0\ 2\ \bar{3}]$. (d) The FT of the ROI in blue rectangle in a. (e) Simulated DP with model rotated 0.8° from the orientation in c.

Table 6.3 Comparison table of the discrepancies found in images at different C_1 values.

Model of PEN crystalline $[0\ 2\ \bar{3}]$			Figure 6.10b $C_1= +10\text{nm}$		Figure 6.12b $C_1= +15\text{nm}$		Figure 6.12d $C_1= +15\text{nm}$	
hkl	d_{mot}	Angle to (200) model	d_{FT}^*	Angle to (200)	d_{FT}	Angle to (200)	d_{FT}	Angle to (200)
β -monoclinic	\AA	$^\circ$	\AA	$^\circ$	\AA	$^\circ$	\AA	$^\circ$
200	3.36	0.0	3.15	0	3.00	0	3.11	0
400	1.68	0.0	1.57	0	1.56	0	1.56	0

$2\bar{3}\bar{2}$	3.24	63.2	3.14	60	3.17	60	3.06	58
$4\bar{6}\bar{4}$	1.62	63.2	1.61	60	1.59	60	1.61	58
032	3.14	60.1	3.19	57	3.11	59	*	\
064	1.57	60.1	1.58	57	1.60	59	\	\
$4\bar{3}\bar{2}$	1.93	32.2	1.82	31	1.81	30	\	\
232	1.87	31.1	1.80	28	1.76	29	1.79	27
$\bar{2}64$	1.81	88.0	1.89	89	1.90	89	\	\

d_{FT}^* : spacing measured from FT

*: spot not found in the FT

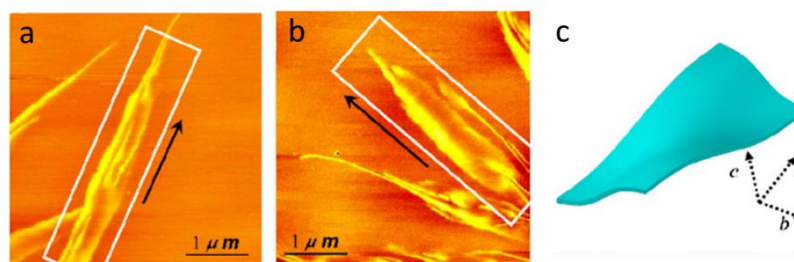


Figure 6.13 AFM images (a-b) and the scheme (c) showing the curvature of the lamella of PHBHHx crystals. The arrows indicate the radial growth direction (a axis) and the rectangular frames indicate the lamella with complicated curvature.

6.3.2 Local small range defect within a grain

There is a type of internal defect that appears as lattice blurring over a small range at specific depths. This feature was observed in the large grain in Figure 6.14a, and the defect will be characterized based on the planes in the corresponding crystalline structure.

To identify the defect related to the crystalline planes, the FT of the ROI in the large grain was indexed. The lattice in the large grain in Figure 6.14a was best resolved at $C_1 = 0\text{nm}$, and the FT pattern of ROI matched with simulated DP from model¹⁰ viewed along lattice vector $[0\bar{2}\bar{9}73]$. In Figure 6.14a, the strongest lattices are planes $(2\ 0\ 0)$ and $(\bar{1}\ 5\ 2)$. Similar to other PEN images, features resolved between the strong intensity $(2\ 0\ 0)$ planes in the image were not present in the model. Meanwhile, the spacing of $(\bar{1}\ 5\ 2)$ measured by line-profile from the image was $2.50\ \text{\AA}$, which is exactly the same as the model. According to the indexing result demonstrated in Table 6.4, the FT pattern (Figure 6.14b) and simulated DP (Figure 6.14c) are

highly matched. All these observations indicate the crystalline structure of the grain can be well interpreted using the PEN crystalline model¹⁰, hence the discrepancy found in the image implies the defect in the crystalline structure.

According to the depth profile in Figure 6.15, the lattice in the upper part of large grain started to become less sharp at $C_1 = -5\text{nm}$ and kept becoming more blurred as the C_1 value increased. In the image at $C_1 = 0\text{nm}$, only the strong planes (2 0 0) and $(\bar{1} 5 2)$ are still visible, but both become non-continuous; and some lattice of $(\bar{1} 5 2)$ become curvy in the image. However, the lattice did not change into a completely different type of feature. This appears to be a range of local defects that might be crystal bending or twisting within the crystal, which result in lattices blurring in some areas of the image. This defect ranges from C_1 of -5nm to $+5\text{nm}$ along the viewing axis, takes around 1/3 of the thickness of the grain (approx. 35nm).

Adjacent to the large grain, another grain on the left side was also resolved during the optical sectioning process. Its orientation appears to be different from the large grain, but the number of FT spots is insufficient to determine the viewing orientation. This grain on the left is thinner than the dominant grain. The depth profile indicates that this thinner grain is located between $C_1 = -15\text{nm}$ and $+10\text{nm}$ (Figure 6.15), which is thicker than the range of internal defects in the big grain. It is not clear whether the existence of this 'neighbour' grain could be related to the internal defect in the large grain.

The internal defect of the dominant grain resolved in the depth profile is a new type of structural information resolved by polymer ptychography image. This function can be potentially applied in material failure analysis in real world products.

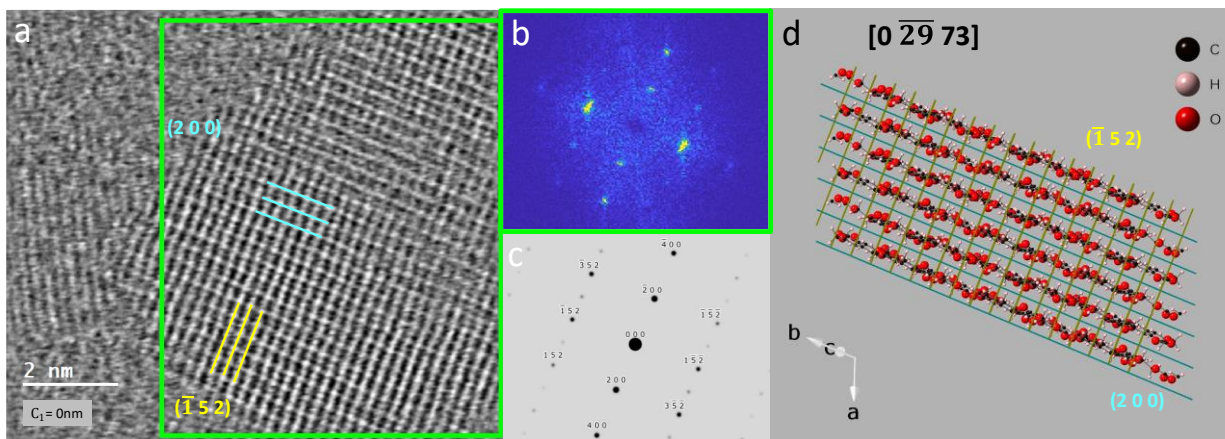


Figure 6.14 (a) Phase image at $C_1=0\text{nm}$. In the large grain, plane (2 0 0) and $(\bar{1} 5 2)$ were resolved. (b) FT of the ROI in a. (c) simulated DP from model viewed from lattice vector $[0 \bar{2} 9 73]$. (d) PEN crystalline model viewed from $[0 \bar{2} 9 73]$. Plane (2 0 0) and $(\bar{1} 5 2)$ were marked with parallel lines in the model.

Table 6.4 Indexing of FT pattern in Figure 6.14 with Model¹⁰ of PEN crystalline $[0 \bar{2} 9 73]$

Plane spacing & angle in FT		Model of PEN crystalline $[0 \bar{2} 9 73]$				Spacing discrepancy
d_{FT}	Angle to (200): θ	hkl	d_{mol}	Angle to (200) model	Relative Intensity	$d_{FT} - d_{mol}$
Å	°	β -monoclinic	Å	°	%	Å
3.17	0	2 0 0	3.36	0.0	100.0	-0.18
1.60	0	4 0 0	1.68	0.0	10.4	-0.08
2.50	89	$\bar{1} 5 2$	2.45	88.7	4.0	0.05
1.25	89	$\bar{2} 10 4$	1.23	88.7	0.1	0.02
2.00	52	$3 \bar{5} \bar{2}$	2.00	54.7	6.4	0.00
1.96	51	1 5 2	1.96	53.0	0.6	0.00
1.32	31	3 5 2	1.37	34.0	0.1	-0.05

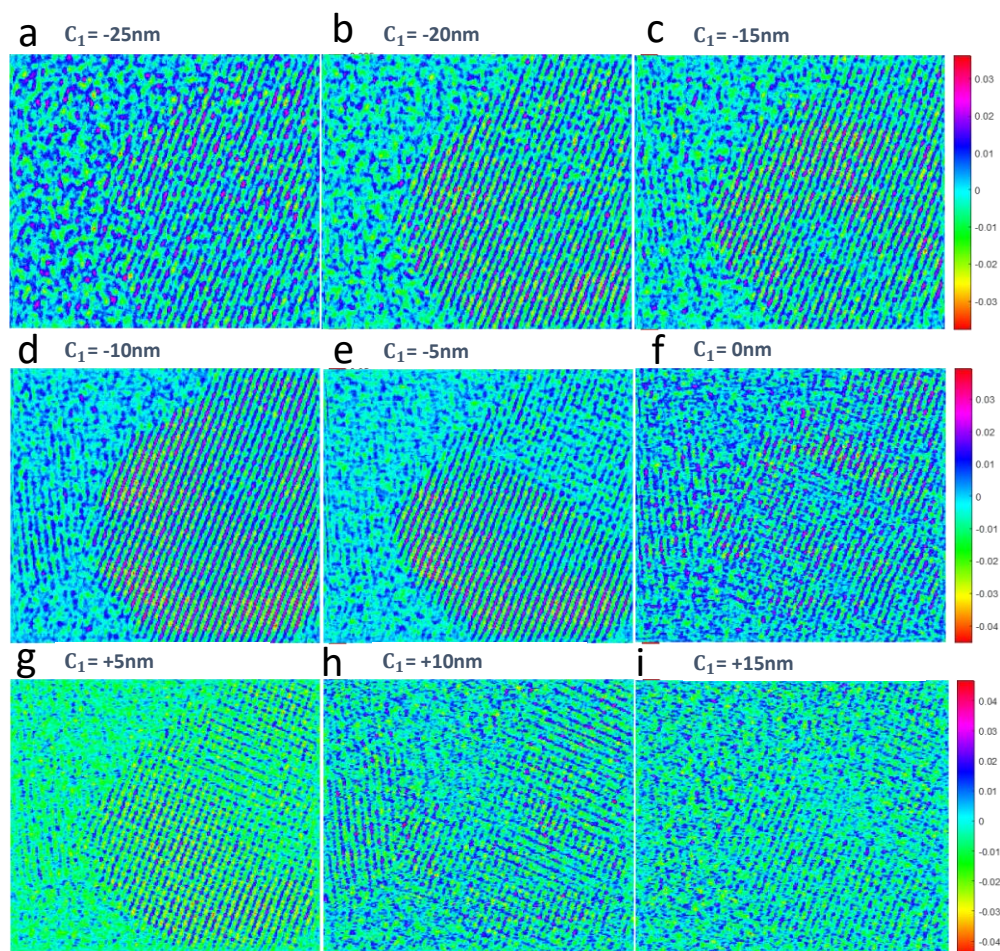


Figure 6.15 Depth profile of Figure 6.14a. (a) – (i) are images of C_1 series ranging from -25nm to $+15\text{nm}$, where the features were enhanced by applying the HSV colormap.

6.4 Resolve imperfectly aligned planes

In practice of imaging polymer specimens in STEM, it is impossible to tilt the specimen to an optimal orientation before the feature become damaged, hence a method that can recover the slight misaligned planes would be helpful.

For example, the first impression of Figure 6.16a is that the structure of the grain cannot be analysed because the lattice appeared to be at an angle to viewing. Whereas, through the depth profile shown in Figure 6.16, the inclined lattice was found better aligned to the viewing

direction hence can be resolved at $C_1 = +27\text{nm}$, which implies the crystal bent. Therefore, the orientation of the grains was determined as vector $[0\ 4\ \bar{1}]$ (Figure 6.17a). Noticeably there were extra spots in the FT pattern that could not be indexed, as highlighted with red circles in Figure 6.17b. Also, considerable ($>10\%$) discrepancies were found in the spacings of plane $(\bar{2}\ 1\ 4)$ and $(\bar{4}\ 2\ 8)$ in the column of $(d_{FT} - d_{mol})$ in Table 6.5. These phenomena might be caused by fact that the planes are slightly inclined and crystal bent, therefore information from other surrounding features and the bent lamella was included.

In this semi-crystalline PEN thin film, the orientations of grains were not modified by experiment, and there is not time to tilt the sample during imaging because the exposure time needs to be short. But with carefully “slicing” through the feature along the depth, some planes that are slightly inclined but still close to parallel to the viewing direction could be resolved at specific C_1 values, because the crystal slightly changes orientation at different depths.

This is very useful for imaging polymers, because it was usually hard to find the perfect alignment of specimen while imaging due to real-time low contrast shown on monitor, and it was also very challenging to tilt the polymer sample *in situ* because of beam damage. In fact, the orientation of crystal could only be determined post-acquisition, and the crystalline structure had gone in the experiment. Therefore, this optical sectioning technique offered an opportunity to analyse the structure of crystal close to but not perfectly aligned, especially when there is only one chance to acquire the data.

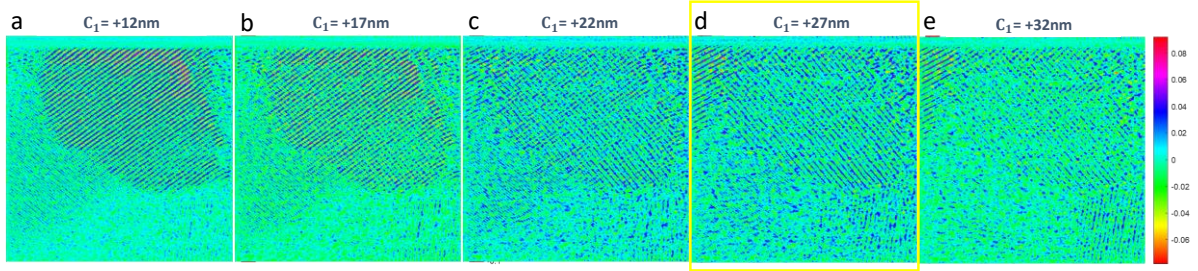


Figure 6.16 In the depth profile of a grain with planes not well parallel to the projection direction, the plane can be resolved at a specific depth, where $C_1 = +22\text{nm}$.

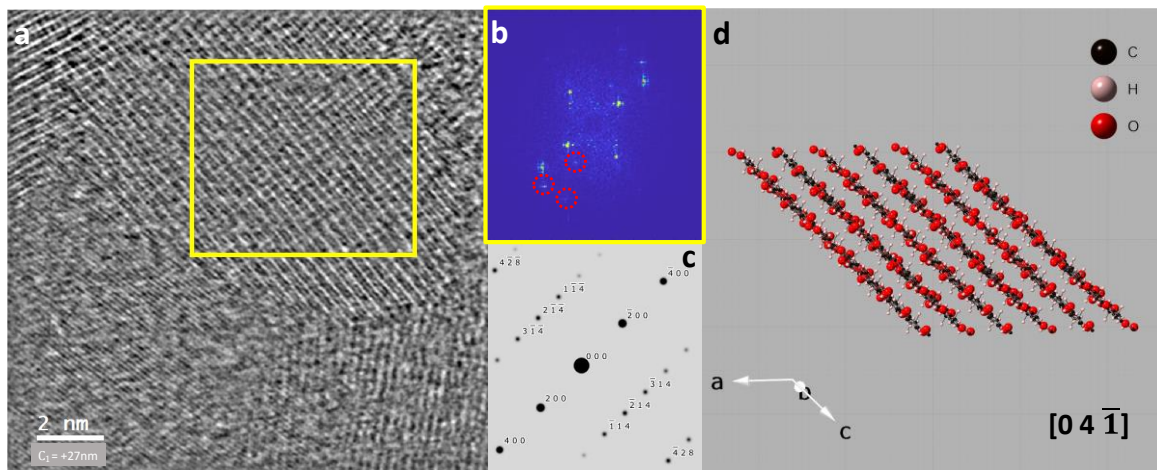


Figure 6.17 (a) Ptychography phase image at $C_1 = +27\text{nm}$. (b) FT of the ROI in a. The extra spots cannot be indexed are circled. (c) Simulated electron DP from the model in d. (d) The PEN crystal model¹⁰ viewed from zone axis $[0\ 4\ \bar{1}]$.

Table 6.5 Indexing the FT pattern in Figure 6.17b with Model¹⁰ of PEN crystalline along $[0\ 4\ \bar{1}]$. Large spacing discrepancies are colour coded in red.

Plane spacing & angle in FT		Model of PEN crystalline along $[0\ 4\ \bar{1}]$				Spacing discrepancy
d_{FT}	Angle to (200): θ	hkl	d_{mol}	Angle to (200) model	Relative Intensity	$d_{FT} - d_{mol}$
Å	°	β -monoclinic	Å	°	%	Å
3.10	0	(2 0 0)	3.36	0.0	100.0	-0.26
1.56	0	(4 0 0)	1.68	0.0	10.4	-0.12
2.60	86	($\bar{2}$ 1 4)	3.06	86.6	0.4	-0.46
1.29	86	($\bar{4}$ 2 8)	1.53	86.6	0.4	-0.25

6.5 Conclusion

In a polymer crystal as thick as tens of nanometres, optical sectioning is an efficient method to obtain high resolution images from various depths by changing the defocus value C_1 to obtain the depth profile. With the “slices” along the viewing direction, the variation of structure along the z-axis could be visualized.

In a semi-crystalline PEN thin film specimen with thickness of around 50nm, multiple grains of various size dispersed in the film at different depths. By optical sectioning, not only the crystalline structure at different depth can be resolved, but also the relative orientation of the grains could be visualized. It was discovered with optical sectioning that the Moiré fringes can be formed by stacking lattices from different domain or internal lattice tilting in one grain.

The depth profiles of PEN specimens shows that polymer crystalline lattices will tend to distort/bend, likely due to the relatively weak intermolecular interactions which will allow for some variation of interatomic distances. In Chapter 5, the distortion was found within plane; in this chapter, the distortion was found along the viewing direction by optical sectioning.

7 Structural analysis of semi-crystalline PET with STEM ptychography

7.1 Models selected for PET structure analysis

The methodology developed in previous chapters was applied to fabricate semi-crystalline PET specimens and analyse them. Images acquired from semi-crystalline specimens included both 'ordered' and 'partially-ordered' features. The analysis of these features will follow the protocol developed in previous chapters of PEN crystalline structural analysis. This is the first time a 'pre-crystalline' morphology has been directly observed. This chapter will discuss the analysis of this partially ordered structure as well as the crystalline structure.

7.1.1 Crystalline structure of PET

In this chapter, the protocol developed in previous chapters for crystalline structure analysis will be applied to the fully crystallized regions in the PET images. Based on the crystalline structure analysis in literature^{12,13,20,14,15,16,17,18,23}, as discussed in Chapter 2, a triclinic crystalline structure has been constructed by Fu *et al.*¹⁸ by XRD with cell parameter of $a=4.5087$, $b=5.8818$, $c=10.7873\text{\AA}$, $\alpha=100.01^\circ$, $\beta=118.36^\circ$, $\gamma=110.56^\circ$, space group of $P_{\bar{1}}$ was applied as the model for indexing the FT patterns of PET ptychography images. Fu's model¹⁸ was built with the crystalline structure formed when internal strain was released by annealing, which is most similar to the specimen fabricated in this work that was crystallized from strain-free amorphous thin film.

Based on the study done by Fu *et al.*¹⁸, during annealing, the a and b cell parameters become smaller, while c becomes larger. These results implied the molecules became more compact or closer to each other with less strain and each molecular chain might be more extended. If

this pattern observed by Fu *et al.* could be applied here, the intermolecular distance in the specimen obtained from the new sample-prep methodology could be even smaller than that of Fu's model. Using the newly developed sample-prep method developed for PEN earlier in this work, the PET crystals were formed from a strain-free amorphous thin film, thereby extending the molecules.

7.1.2 Periodic non-crystalline and pre-crystalline structures in polymer

Crystals have structures where atoms are arranged in ordered and repeated patterns in all three dimensions, but the newly discovered disordered feature found in the PET specimen illustrated only "partial" crystalline characteristics, i.e., periodicity along specific direction. Various forms of "partial" crystalline structures might be considered to assist the interpretation of the disordered feature found in the PET images. A review of several periodic non-crystalline features observed in polymers is presented to interpret the 'disordered' structure discovered in PET images.

A commonly known "partial" crystalline structure is a liquid crystal. Liquid crystalline¹⁰⁸ mesophases possess some typical properties of a liquid, such as fluidity and the inability to support shear, and formation and coalescence of droplets. These mesophases also have certain crystalline properties, such as anisotropy of optical, electrical, and magnetic properties, as well as a periodic arrangement of molecules in one or more spatial directions (Figure 7.1).

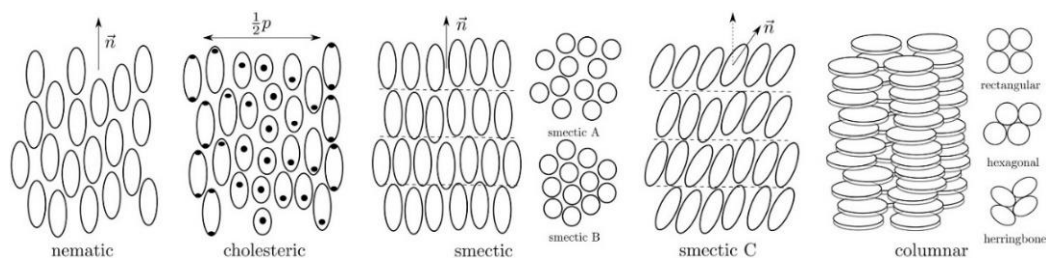


Figure 7.1 Molecular arrangements in liquid crystalline mesophases.¹⁰⁸

In terms of why molecules may show partial ordering, one explanation could be that the molecules were ordering themselves in a step of crystallization. The actual procedure of crystallization in polymers is still debatable, works had been reported attempting to understand it with indirect characterization methodologies. Wurm *et al.*¹⁰⁹ reported an interesting study trying to understand polymer crystallization as a multiple step process. They claimed their observation during simultaneous dielectric and SAXS experiments strongly supports the idea of pre-order in polymer melts before the formation of crystals. They found an increasing permittivity that might be explained by formation of internal surface. And the additional dipole moments or interfaces might be created before crystallinity can be detected by SAXS or DSC. F. Jin *et al.*¹¹⁰ characterized the local chain trajectory with ¹³C-labeled semicrystalline PLA crystallized from glass and melt, with an effect on the ¹³C–¹³C double-quantum (DQ) nuclear magnetic resonance (NMR) signal. They concluded that (i) folding occurs prior to crystallization and (ii) melt and cold crystallization do not induce the additional folding but proceed with rearrangements of polymer chains in the existing templates. It is likely the result implied the molecules ‘pre-order’, while the folding is still debatable.

Besides the PET crystalline structure, this chapter will also illustrate the newly discovered ‘partially ordered’ features in PET specimens, as well as the analysis method that uses line profiles to measure peak-to-peak distances to characterize the molecules arrangements.

7.2 Analysis of PET crystalline feature

7.2.1 One large crystalline dominant in the image

Images of the semicrystalline PET showed regions of good crystalline order, which will be focused on first. The phase image in Figure 7.2a was dominated by one crystalline grain of size larger than the recording area of the image, and there was no sign of the boundary indicating the edge of the grain. The crystalline feature was continuously uniform and not disrupted by other grains. The image suggested that the region captured in this image might be inside a relatively large grain, which would explain the absence of disruption from grain boundaries. There was some lattice in the upper-right corner that appeared less perfect, so this was not included in the analysis of the dominant grain.

The orientation of the grain was determined as $[10 \bar{1} 2]$ by indexing the FT in the ROI marked with a green rectangle in Figure 7.2a. According to the model in Figure 7.2d, molecules in this orientation are viewed along the direction where the planes of the naphthalate rings are perpendicular to viewing direction. This might explain the well-defined peaks in the phase image because the peaks implied the stack of aligned atoms along the viewing direction according to the depth profile from optical sectioning.

The plane spacing and angles in the FT of the phase image were highly matched with the model (Table 7.1). Among the plane spacings, the largest discrepancy was found for plane $(0 \bar{2} \bar{1})$, which, at 0.20 \AA , is within 10% of the spacing measured from the model. This discrepancy is in scale equal to the probe-step used for recording this ptychography dataset (0.207 \AA theoretically) and is within reasonable range of error.

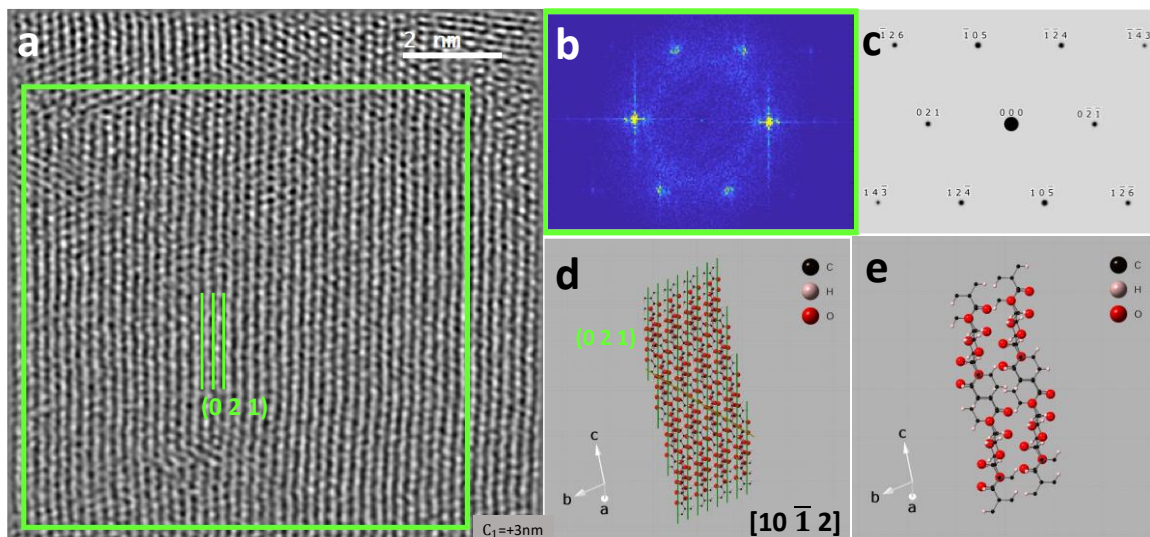


Figure 7.2 (a) PET phase image at $C_1 = +3nm$. (b) FT of the ROI in a. (c) Simulated DP with model viewed along $[10 \bar{1} 2]$ in d and e. (d) PEN crystalline model of multiple cells, the parallel lines overlaid represented plane $(0 2 1)$. (e) Unit cell of PET crystalline model.

Table 7.1 Indexes of FT pattern from the experimental image in Figure 7.2b

Plane spacing & angle in FT		Model ¹⁸ of PET crystalline structure				Spacing discrepancy
d_{FT}	Angle to $(0 \bar{2} \bar{1})$: θ	hkl	d_{mol}	Angle to $(0 \bar{2} \bar{1})$ model	Relative Intensity	$d_{FT} - d_{mol}$
Å	°	Triclinic $P_{\bar{1}}$	Å	°	%	Å
2.38	0	$(0 \bar{2} \bar{1})$	2.18	0.0	7.3	0.20
2.11	68	$(1 0 \bar{5})$	2.11	67.1	24.4	0.00
1.95	61	$(\bar{1} \bar{2} 4)$	1.94	57.8	10.4	0.01
1.28	38	$(1 \bar{2} \bar{6})$	1.29	34.1	4.8	-0.01
1.23	34	$(\bar{1} \bar{4} 3)$	1.17	30.7	2.3	0.05

7.2.2 Two crystals with grain boundary in between

An image acquired from another region of the PET specimen appears to contain multiple grains. For instance, Figure 7.3a involves two regions with distinct features. Each part generated clear spots in the FT, therefore implying the existence of a crystalline structure. Simply based on observation of the image, the upper part highlighted in the yellow rectangle looked more like a well-formed crystal with molecules in a compact arrangement, while the lower part (indicated

in the green rectangle) seemed to be crystalline structure viewed along lower-order axis thereby showing larger spacings (Table 7.2).

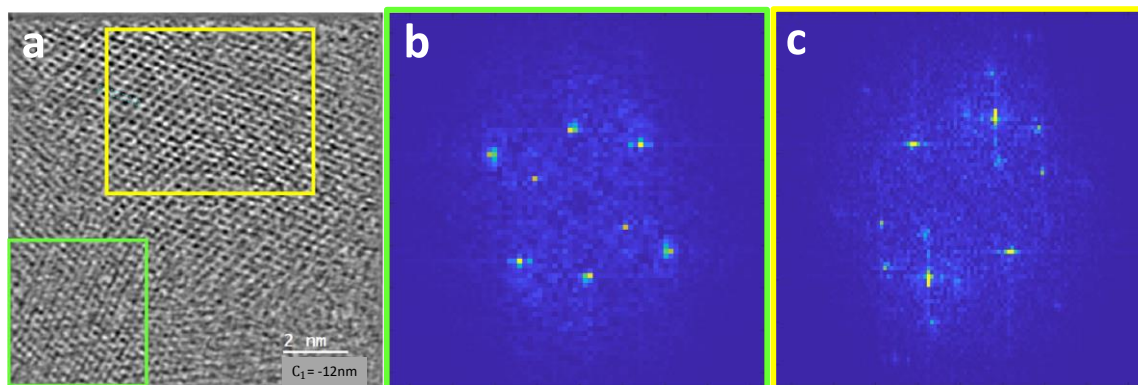


Figure 7.3 (a) PET phase image at $C_1 = -12\text{nm}$. (b) FT of the region at the left lower corner. (c) FT of the region at upper right part.

The feature in the lower-left part of Figure 7.3a appears to be a series of parallel molecules that show a large interplanar space compared to the commonly observed crystalline structure, but the FT (Figure 7.3b) shows clear and sharp spots indicating the presence of long-range 3-dimensional periodic structure in this region, as there is no blurred rings observed which indicates amorphous/disordered structures.

Indexing the FT pattern (Figure 7.4b) with reference to the simulated DP from the PET model¹⁸ revealed that the viewing direction was closest to lattice vector $[0 \bar{1} \bar{2}]$, however there were significant discrepancies between the image and the model. A large discrepancy was found with the spacing of plane $(1 0 0)$. The spacing measured from the image was 4.33 \AA , while the spacing in the model was 3.43 \AA . The spacing of $(2 0 0)$ measured from FT was 0.40 \AA larger than that in the model. There was also an apparent discrepancy in the relative intensity of $(1 \bar{2} 1)$ and the angle between $(1 \bar{2} 1)$ and $(1 0 0)$. The spot of $(1 \bar{2} 1)$ was not visible in the simulated DP (Figure 7.4c), but pretty sharp in the FT pattern.

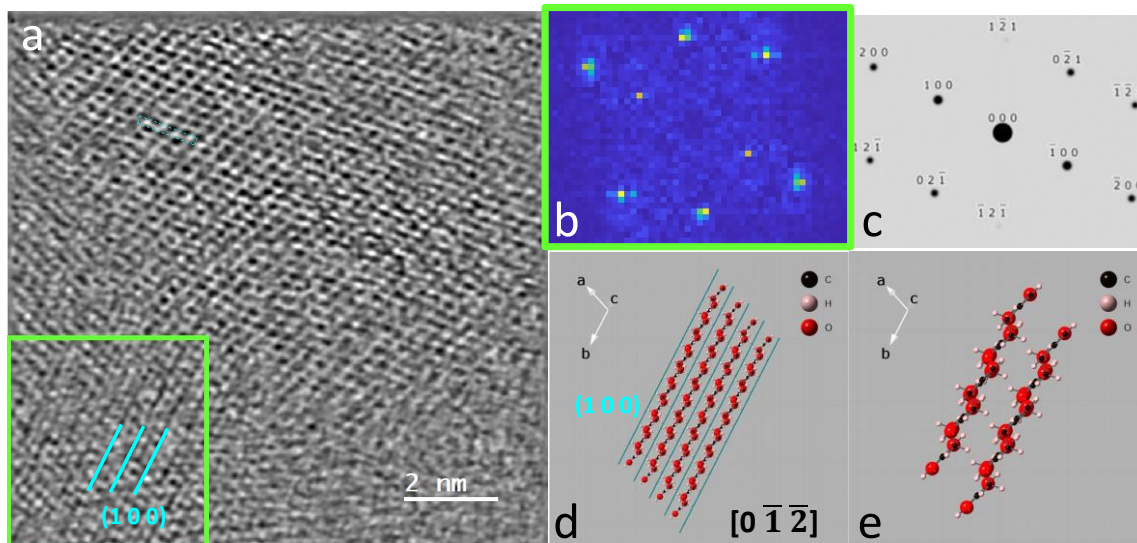


Figure 7.4 (a) The lower left feature is highlighted in image at $C_1 = -12\text{nm}$. (b) FT of the ROI in a. (c) Simulated DP from model in d. (d) plane (1 0 0) is noted in PET crystalline model of multiple cells. (e) Unit cell of PET crystalline model. Both models in d and e are viewed along $[0 \ 1 \ \bar{2}]$.

Table 7.2 Indexes of the spots of FT pattern in Figure 7.4b. The relatively large values of discrepancies are highlighted in red.

Spacing in phase image	Plane spacing & angle in FT		Model ¹⁸ of PET crystalline structure				Spacing discrepancy
	d_{img}	d_{FT}	Angle to (100): θ	hkl	d_{mol}	Angle to (100) model	Relative Intensity
Å	Å	°	Triclinic $P\bar{1}$	Å	°	%	Å
4.33	4.17	0	(1 0 0)	3.43	0.0	100.0	0.73
2.17	2.12	0	(2 0 0)	1.72	0.0	9.6	0.40
2.88	2.88	55	(1 $\bar{2}$ 1)	2.65	65.0	0.0	0.23
*	2.53	73	(0 2 $\bar{1}$)	2.73	68.8	10.5	-0.20

*: the spacing of plane in the image could not be determined.

The structure in the upper right part of Figure 7.3a showed more clear periodic features than the other region, but the FT pattern of this region (Figure 7.6b) could not be indexed by only one simulated DP from any orientation of the hkl model. To cover all the spots of the FT pattern,

two simulated DPs were required. This can be caused by either the presence of defects or the stacking of multiple lattices, which can explain the formation of combined DP.

The combination of simulated DP from lattice vector $[1 \bar{1} \bar{2}]$ and $[2 2 \bar{1}]$ matched with the FT in Figure 7.6b. The angle between $[1 \bar{1} \bar{2}]$ and $[2 2 \bar{1}]$ is 43° . Although the stacking lattices in this region are viewed from different orientations, but the lattices showed similar features in the phase images. For instance, plane $(1 \bar{1} 1)$ in $[1 \bar{1} \bar{2}]$ and plane $(0 1 2)$ in $[2 2 \bar{1}]$ were in similar positions, hence were not quite distinguishable if overlapped in the phase image.

Through the use of optical sectioning, the features in a specific depth range could be observed, and therefore the distinct structures could be separated (Figure 7.5) if they are located at different depths. In the depth profile, one of the two orientations could be clearly distinguished from the other, as the FT pattern of $C_1 = -2\text{nm}$ (Figure 7.5f) contains only the same spots as the simulated DP from $[1 \bar{1} \bar{2}]$ (Figure 7.6e). This implied that $[1 \bar{1} \bar{2}]$ was the dominant orientation of crystals in the region, while $[2 2 \bar{1}]$ only occupied a small portion of the region, which is why the $[2 2 \bar{1}]$ FT spots cannot be distinguished from those of the other orientation (Figure 7.5d).

The discrepancies observed in spacings, and angles, shown in Table 7.3 and Table 7.4, might be caused by either the intrinsic structural differences, or the exist of the other set of stacking lattices. The image in this section shows that larger discrepancies were observed around the boundary of multiple domains, while the structure within one large grain (Figure 7.2) matches the model very well.

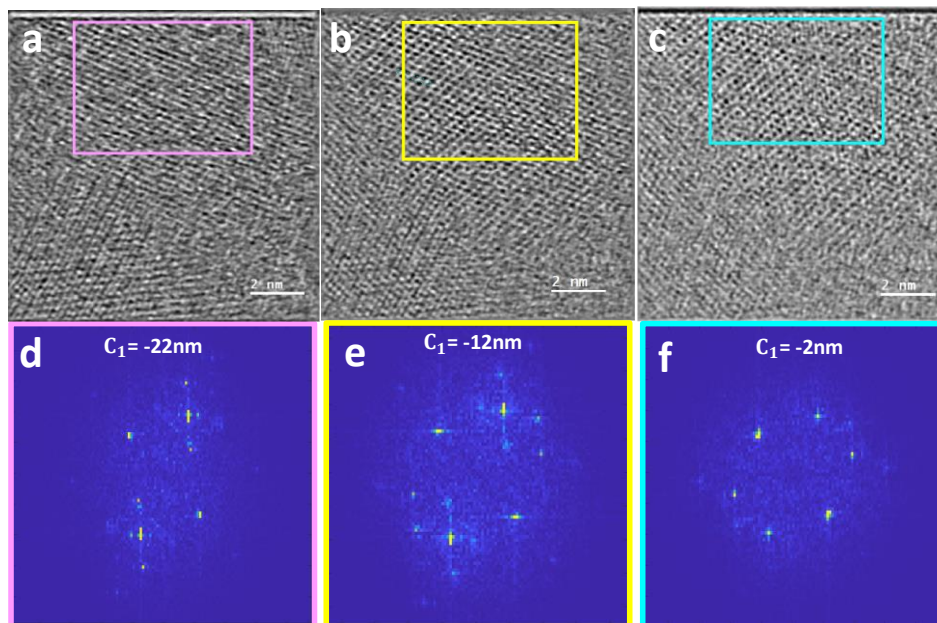


Figure 7.5 The lattice of distinct orientations separated with optical sectioning. (a) Phase image at $C_1 = -22\text{nm}$. (b) Phase image at $C_1 = -12\text{nm}$. (c) Phase image at $C_1 = -2\text{nm}$. (d) FT of ROI in a. (e) FT of ROI in b. (f) FT of ROI in c.

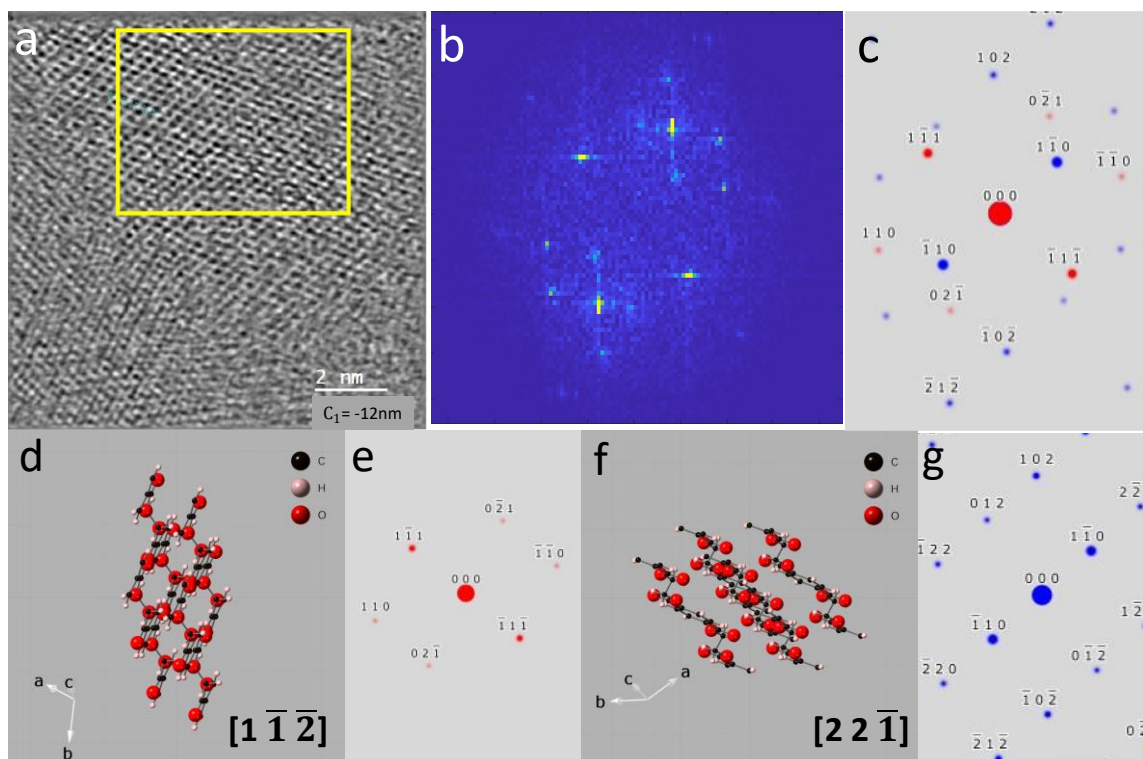


Figure 7.6 (a) The phase image at $C_1 = -12\text{nm}$. (b) FT of the ROI in a. (c) Combination of simulated DP from e (red spots) and g (blue spots). (d) The model¹⁸ viewed from $[1 \bar{1} \bar{2}]$ generating the simulated DP in (e). (f) The model¹⁸ viewed from $[2 \bar{2} \bar{1}]$ generating DP in (g) The pattern in FT can be indexed with combining the simulated DP from d and f, though some obvious discrepancies were still found.

Table 7.3 Indexing FT in Figure 7.6b with simulated DP viewed along lattice vector $[1 \bar{1} \bar{2}]$ in Figure 7.6d. Relatively large discrepancy was found in the angles of $(0 \bar{2} 1)$ and $(1 1 0)$ to benchmark plane $(1 \bar{1} 1)$.

Plane spacing & angle in FT		Model ¹⁸ of PET crystalline structure				Spacing discrepancy
d_{FT}	Angle to $(1 \bar{1} 1)$: θ	hkl	d_{mol}	Angle to $(1 \bar{1} 1)$ model	Relative Intensity	$d_{img} - d_{mol}$
Å	°	Triclinic $P_{\bar{1}}$	Å	°	%	Å
2.89	0	$(1 \bar{1} 1)$	3.16	0.0	43.9	-0.27
1.45	0	$(2 \bar{2} 2)$	1.58	0.0	0.0	-0.13
2.39	66	$(0 \bar{2} 1)$	2.73	77.2	10.5	-0.34
2.50	64	$(1 1 0)$	2.34	56.7	0.5	0.16

Table 7.4 Indexing FT in Figure 7.6b with simulated DP viewed from lattice vector $[2 2 \bar{1}]$ in Figure 7.6f.

Plane spacing & angle in FT		Model ¹⁸ of PET crystalline structure				Spacing discrepancy
d_{FT}	Angle to $(1 \bar{1} 0)$: θ	hkl	d_{mol}	Angle to $(1 \bar{1} 0)$ model	Relative Intensity	$d_{img} - d_{mol}$
Å	°	Triclinic $P_{\bar{1}}$	Å	°	%	Å
2.89	88	$(0 1 2)$	2.76	84.2	0.3	0.13
1.45	88	$(0 2 4)$	1.38	84.2	0.4	0.07
2.39	\	\	\	\	\	\
2.50	\	\	\	\	\	\
4.07	0	$(1 \bar{1} 0)$	3.88	0.0	48.1	0.19
2.01	0	$(2 \bar{2} 0)$	1.94	0.0	0.4	0.07
2.53	46	$(1 0 2)$	2.15	50.8	1.2	0.38
1.65	33	$(2 \bar{1} 2)$	1.52	33.2	1.2	0.13

7.2.3 Two grains with overlap region

Figure 7.7 involved three regions with distinctive features, which were sequenced according to decreased level of ordering in the structure.

Region ① is the most “ordered” part consisting of long-range periodic features and could be categorized as crystalline because of the clear spots in FT, although some defects were observed.

In Region ②, long lattice features were found along the diagonal direction from left to right. There was bending in the lattices, and they were not perfectly continuous.

Region ③ contains some mixed features including features in Region ① and ②. It appears to be an overlap of two grains. Amorphous structures would not exhibit spots or 'dash-line' like features as observed in Figure 7.7b-③.

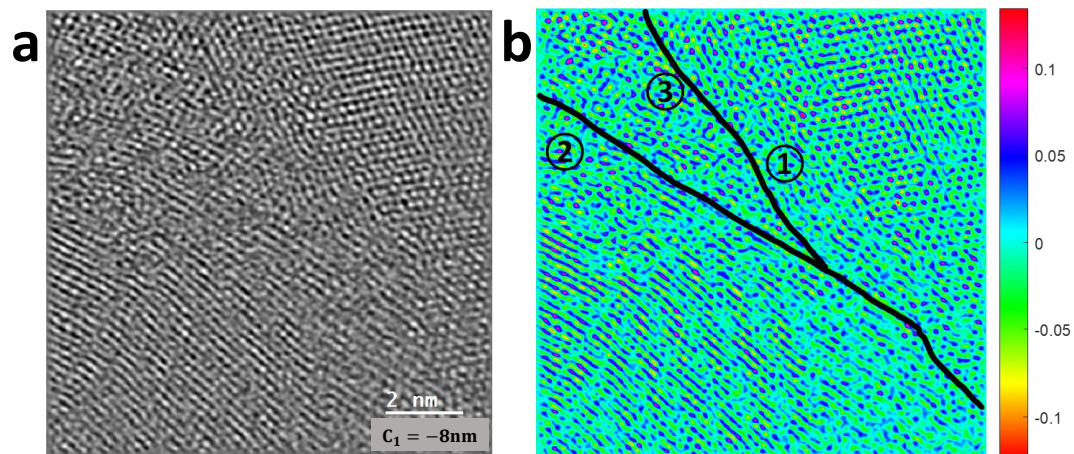


Figure 7.7 (a) Three distinct features were resolved in the PET phase image. (b) The same phase image HSV colormap to enhance the visibility of features. The three distinctive features are labelled in this image: ① an ordered feature that looks like crystalline structure; ② some clearly resolved lattice but not strictly ordered, with some bending and curvy shapes; ③ a region in between where the molecules illustrated partially-ordered feature, which is neither completely amorphous nor crystalline.

Region ① of the phase image at -8nm (Figure 7.7b) contains the most ordered crystalline feature of the whole image, therefore it was analysed by indexing the FT shown in Figure 7.7b. Several orientations of the model generated simulated DPs that matched with most spots, but none of these simulated DPs could match all spots in the FT, i.e., the FT could not be indexed with a sole simulated DP.

The FT was found best matched with the combination of simulated DPs from lattice vectors $[\bar{1} 1 \bar{3}]$ (Figure 7.8c) and $[\bar{1} 2 \bar{4}]$ (Figure 7.8f). According to the relative intensities, $(0 2 1)$ is the strongest plane (7.3%) in simulated DP along $[\bar{1} 2 \bar{4}]$, and $(\bar{2} 1 1)$ is the strongest diffracted plane (8.1%) in the simulated DP of $[\bar{1} 1 \bar{3}]$; they corresponded to the highest intensity spots in the combined FT pattern. The discrepancies of plane spacing and angles for both orientations are small (Table 7.5, Table 7.6).

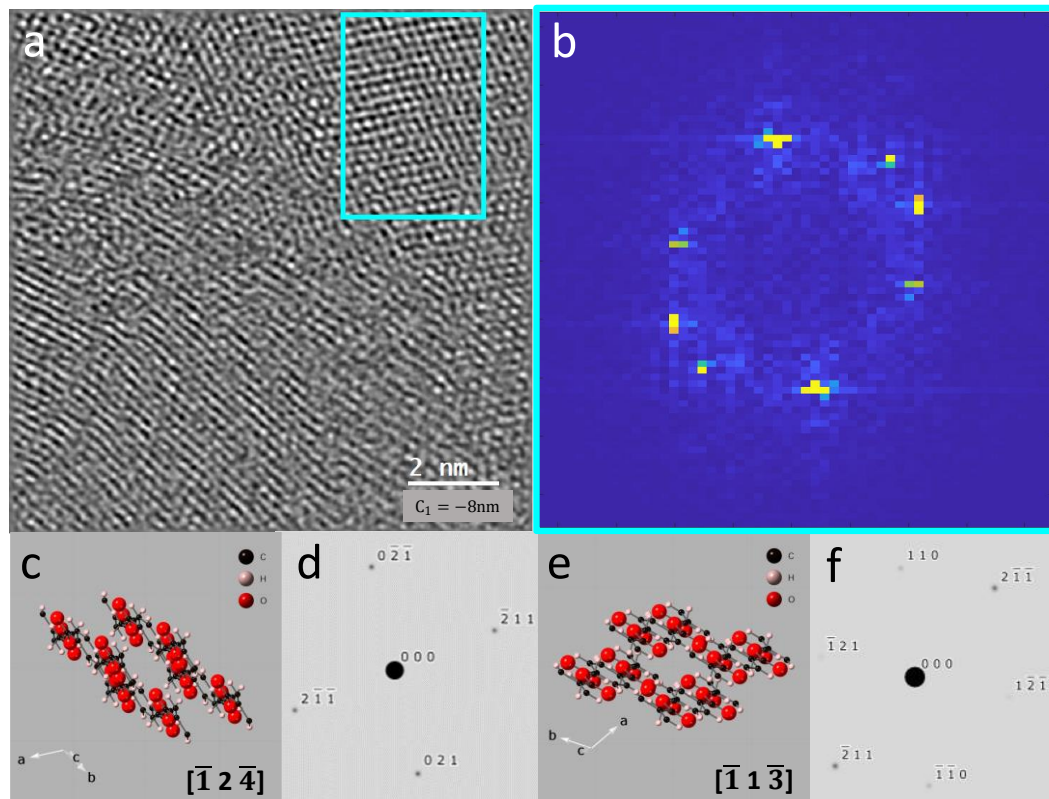


Figure 7.8 (a) Region ① with ROI indicated by blue rectangle for further analysis. (b) FT of the ROI in a. (c) Unit cell of PET crystalline model viewed from lattice vector $[\bar{1} 2 \bar{4}]$. (d) Simulated DP from e. (e) Unit cell of PET crystalline model viewed from $[\bar{1} 1 \bar{3}]$. (f) Simulated DP from c. The angle between vector $[\bar{1} 1 \bar{3}]$ and $[\bar{1} 2 \bar{4}]$ is 3.9° .

Table 7.5 Indexing the FT in Figure 7.8b with simulated DP viewed from lattice vector $[\bar{1} 1 \bar{3}]$ and discrepancies.

Plane spacing & angle in FT		Model of PET crystalline structure along $[\bar{1} 1 \bar{3}]$				Spacing discrepancy
d_{FT}	Angle to $(\bar{1} \bar{1} 0)$: θ	hkl	d_{mol}	Angle to $(\bar{1} \bar{1} 0)$ model	Relative Intensity	$d_{img} - d_{mol}$
Å	°	Triclinic $P_{\bar{1}}$	Å	°	%	Å
2.36	0	$(\bar{1} \bar{1} 0)$	2.34	0.0	0.5	0.02
2.15	75	\	\	\	\	\
2.44	73	$(1 \bar{2} \bar{1})$	2.67	70.7	8.1	-0.23
2.11	52	$(\bar{2} 1 1)$	2.15	49.3	0.8	-0.04

Table 7.6 Indexing the FT in Figure 7.8b with simulated DP viewed from lattice vector $[\bar{1} 2 \bar{4}]$ and discrepancies.

Plane spacing & angle in FT		Model of PET crystalline structure along $[\bar{1} 2 \bar{4}]$				Spacing discrepancy
d_{FT}	Angle to $(0 2 1)$: θ	hkl	d_{mol}	Angle to $(0 2 1)$ model	Relative Intensity	$d_{img} - d_{mol}$
Å	°	Triclinic $P_{\bar{1}}$	Å	°	%	Å
2.36	0	$(0 2 1)$	2.18	0.0	7.3	0.18
2.15	75	$(2 \bar{1} \bar{1})$	2.15	80.9	0.8	0.00

The two sets of spots in the FT pattern were separated using optical sectioning (Figure 7.9). FT of Region ① at $C_1 = -18\text{nm}$ (Figure 7.9d) only involved the spots corresponding to simulated DP from vector $[\bar{1} 2 \bar{4}]$ (Figure 7.8d). The FT pattern at $C_1 = +2\text{nm}$, however, contained not only the same spots as the simulated DP of vector $[\bar{1} 1 \bar{3}]$ (Figure 7.8f) as expected, but also spots from another orientation. In other words, it contained all the spots of the combined FT pattern, but the relative intensity was different from the combined FT (Figure 7.9e). It is possible that the above observation implies that lattices along vector $[\bar{1} 2 \bar{4}]$ were dominant, while the rest of the lattices were viewed along vector $[\bar{1} 1 \bar{3}]$. Due to the small angle (4°) between vectors $[\bar{1} 2 \bar{4}]$ and $[\bar{1} 1 \bar{3}]$, lattice tilting with this angle is highly likely. The depth profiling results support the hypothesis that the crystals in Region ① contain multiple oriented lattices stacking along the viewed direction.

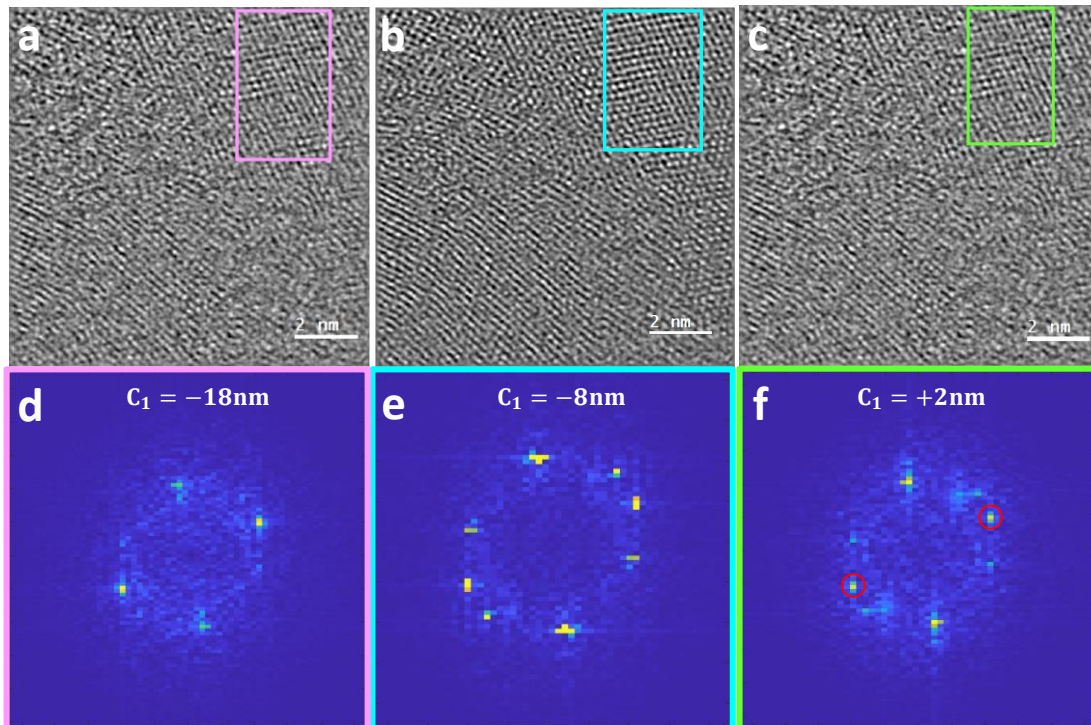


Figure 7.9 Separate the two orientations in Region ① of Figure 7.7b by optical sectioning. (a) Phase image at $C_1 = -18\text{nm}$. (b) Phase image at $C_1 = -8\text{nm}$. (c) Phase image at $C_1 = +2\text{nm}$. (d) FT of ROI in a. (e) FT of ROI in b. (f) FT of ROI in c.

Region ② clearly contains a crystalline lattice. The spacing of the fringes is around 2\AA , measured by line-profiles. Because of the limited information revealed in the FT pattern (Figure 7.10b), it is difficult to determine the orientation of this lattice. There is a high density of defects including breaking and bending of the linear features and no clearly resolved peaks in region ② that could be characterized with line-profiles.

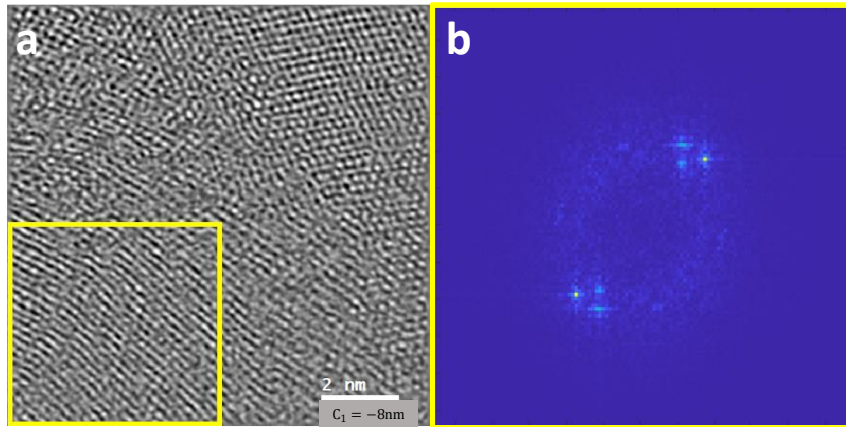


Figure 7.10 (a) Region ② in the phase image at $C_1 = -8\text{nm}$. (b) The FT of ROI in image a.

The low discrepancies found in the planes of Region ① indicated a good match of its crystalline structure to the model¹⁸. Thus, feature in Region ① is crystalline structure with low impact from the junctional non-crystalline structure in Region ③. The feature in Region ③ appear to be similar but more ordered than the partially-ordered features which will be discussed in next section.

7.3 Analysis of ‘partially-ordered’ region in PET semi-crystalline thin film

Among the various ptychography phase images acquired from the semi-crystalline PET, besides the crystalline features, features that appeared to be neither crystalline nor amorphous state were found. The arrangement of molecules in these features was at some level of ordered but not yet of forming a long-range periodic structure in three-dimensions. The clear spots of intensity roughly equidistant from one another, but not arranged into a regular array over a significant number of repeats cannot be explained as amorphous material and lends itself to the idea that the molecules are aligned along viewing direction but were not fully packed into a crystalline array. In these regions of images exhibiting ‘partially-ordered’ non-crystalline

structures, line-profiles were applied to measure the peak-to-peak distances with the goal of identifying the nature of these features.

7.3.1 Image involving ordered and partially-ordered structures

Figure 7.11a illustrates the semi-crystalline PET specimen with multiple features, involving 'ordered' and 'partially-ordered' structures. There is a large area of 'partially-ordered' features in the centre of the image, and some 'ordered' crystalline grains in the upper part and near the opposite and right edges. The grains were not continuous and were "broken down" by grain boundaries filled with partially-ordered features.

Understanding how the molecules are arranged in these partially-ordered features is of interest. Because the boundaries between ordered and disordered features are vague, the ordered crystalline structure may contain structural information about the surrounding partially-ordered feature. The information about the molecule conformation in the crystals may provide a clue about the molecular conformation in the partially-ordered region nearby. Thus, the ordered and partially-ordered features of each image would be analysed together.

7.3.1.1 Crystalline region: orientation of the largest grain

The largest grain among the crystalline features was selected for analysis to determine the orientation of the crystalline region in Figure 7.11a. The FT pattern of ROI in Figure 7.11a as shown in Figure 7.11b broadly matched the simulated DP from the model¹⁸ viewed from $[2 \bar{1} \bar{2}]$, which is almost parallel to *c*-axis that is the molecular axis, as demonstrated in Figure 7.11e. The high contrast planes within the ROI in Figure 7.11a are planes $(0 \bar{2} 1)$ that are also marked in the model (Figure 7.11d), which are echoed in the FT (Table 7.7) in that the spots of plane

$(0 \bar{2} 1)$ possess the highest relative intensity among the three planes. The sequence of relative intensity of the planes in the model agreed with the sequence observed from the FT of ROI.

The discrepancies found in plane spacings of $(0 \bar{2} 1)$ and $(\bar{1} 0 \bar{1})$ were both slightly larger than 10%, which is the commonly accepted range of error from such experimental data. For instance, the plane spacing of $(0 \bar{2} 1)$ is 2.46 Å measured from the phase image with line-profile, which is 11% smaller than 2.73 Å in the model. Noticeably, the FT pattern is closer to a hexagonal structure than the simulated DP, which is echoed in the discrepancy found in the plane angles. This may reflect a greater symmetry perpendicular to the viewing direction arising from disorder in the orientation of the molecules (randomness in the rotation of the molecule about an axis parallel to the molecular axis) aligned along the viewing direction. The high symmetry of FT from the ordered region implies an orientation of molecules in which are almost parallel to the *c*-axis. Therefore, the discrepancy might be raised from the slight tilt of determined viewing vector $[2 \bar{1} \bar{2}]$ relative to the *c*-axis.

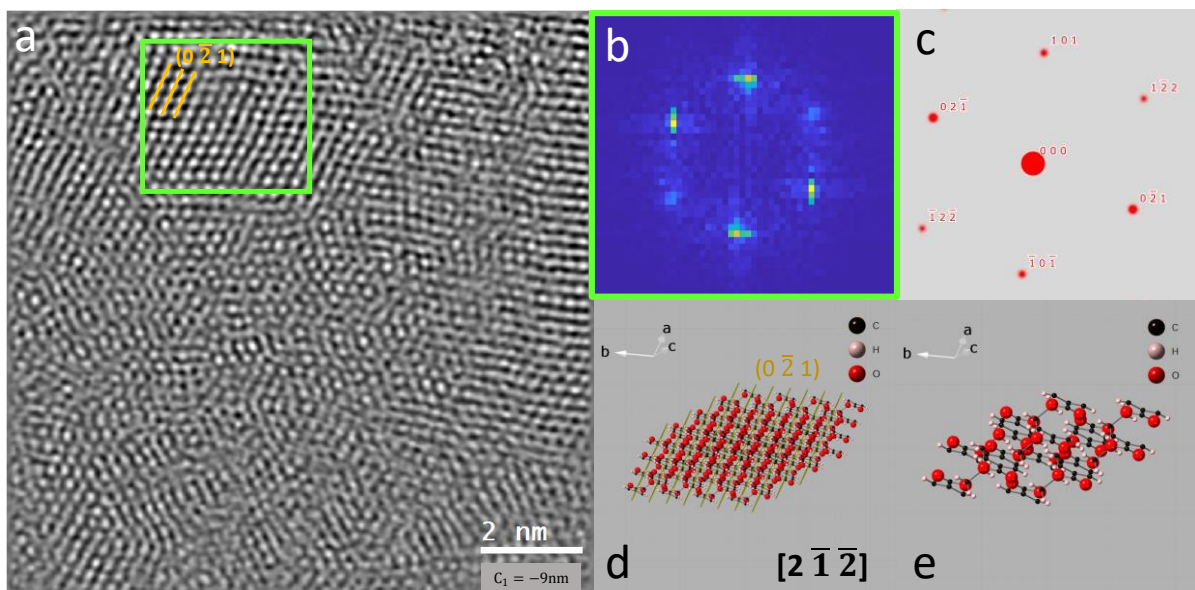


Figure 7.11 (a) PET image with multiple features involved. (b) FT of ROI from a. (c) Simulated single-crystal ED from model shown in e. (d) PET crystalline Model¹⁸ of multi-cells viewed along vector $[2 \bar{1} \bar{2}]$. The plane $(0 \bar{2} 1)$ is marked with parallel yellow lines. (e) Unit cell of in the PET crystalline model in d.

Table 7.7 Indexing the FT in Figure 7.11b with simulated DP viewed from lattice vector $[2 \bar{1} \bar{2}]$.

Plane spacing & angle in FT		Model ¹⁸ of PET crystalline structure				Spacing discrepancy
d_{FT}	Angle to $(0 \bar{2} 1)$: θ	hkl	d_{mol}	Angle to $(0 \bar{2} 1)$ model	Relative Intensity	$d_{img} - d_{mol}$
Å	°	Triclinic $P\bar{1}$	Å	°	%	Å
2.43	0	$(0 \bar{2} 1)$	2.73	0.0	10.50	-0.30
2.39	68	$(\bar{1} 0 \bar{1})$	2.70	71.0	1.90	-0.31
2.24	57	$(1 \bar{2} 2)$	2.34	55.0	0.90	-0.09

7.3.1.2 Partially-ordered non-crystalline regions

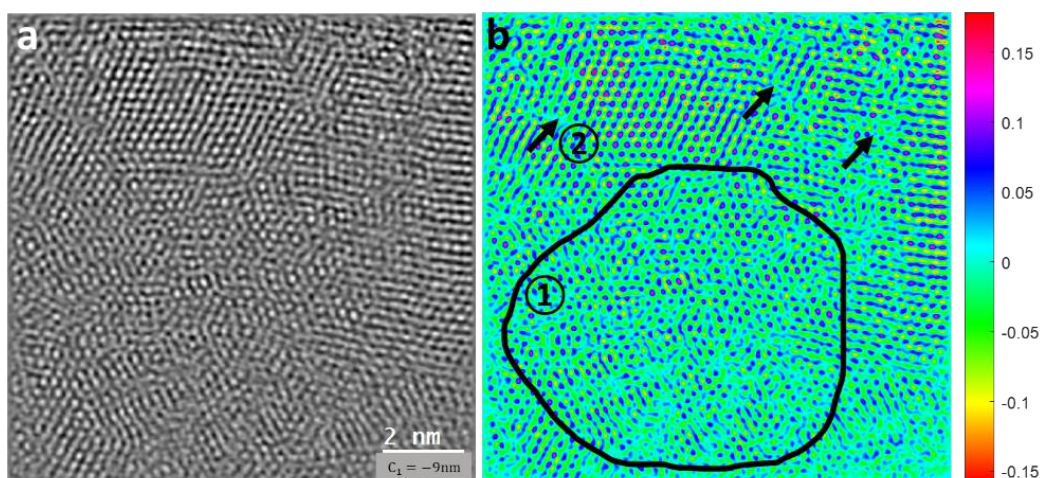


Figure 7.12 (a) The partially-ordered features are observed in the phase image. (b) image a in HSV colormap, scale in radian. The partially-ordered features were highlighted as ① circled region involving clear 'peaks' indicating molecules with certain level of ordering, neither full crystallinity nor amorphous. ② as indicated by the arrows, the features between crystal grains are not amorphous, but partially-ordered.

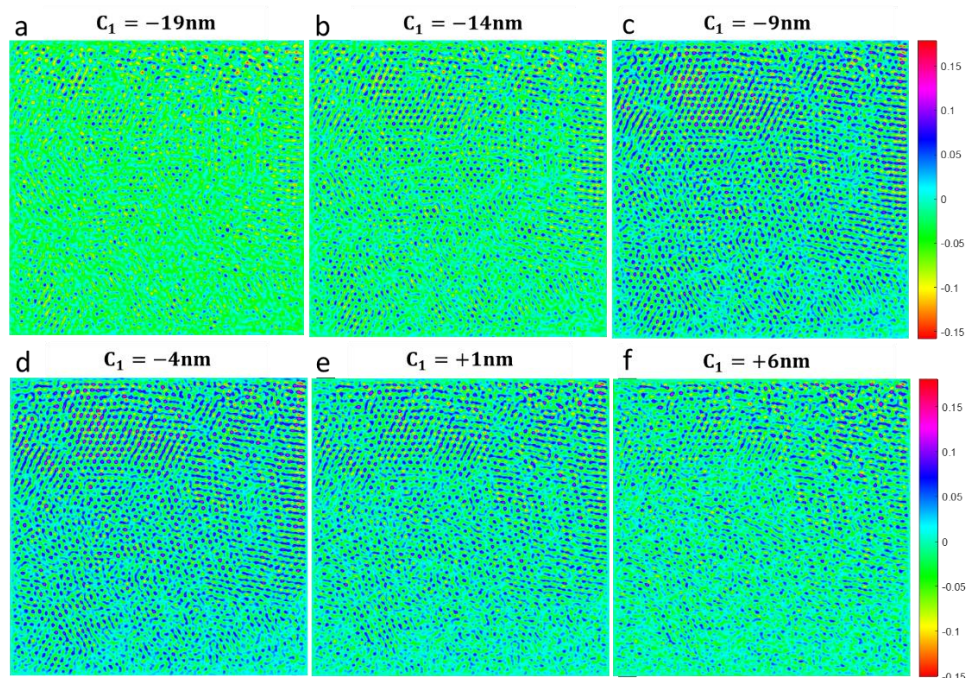


Figure 7.13 Depth profile of Figure 7.12. The peaks of partially-ordered feature was well resolved through the depth of 25nm.

This phase image contained two types of disordered features. The first was the large area circled in the centre of Figure 7.12b-①, which indicated partially order as the 'clear spots' implied a long range order. According to the depth profile of this image (Figure 7.13), these clear spots remained for approximately 25 nm throughout the depth profile. These peaks represent the molecules approximately aligned with the viewing direction.

The second type of disordered feature was found between grains. Figure 7.12b-② shows that the crystals formed were not perfectly one grain, but several grains separated by non-crystalline structures indicated by arrows. The features between each of the two grains were not completely amorphous, but similar to features in region ①, were peaks implying partially ordered structure where the molecules aligned to viewing direction. This contrasts with images of PEN, in which no non-crystalline structure was observed between grains, either in amorphous or non-crystalline form.

An attempt was made to understand the structure of the partially-ordered features by measuring the peak-to-peak distances using line profiles. The peak-to-peak distances were measured using approx. 60 line-profiles in the image, and the distribution of values was illustrated with the histogram in Figure 7.14c.

The measurement results of peak-to-peak (peak means the high intensity spots in the image) distances in Figure 7.12b-① region and crystalline regions in Figure 7.11a are summarized in Figure 7.14, which shows the distribution of distance in non-crystalline 'partially-ordered' and crystalline 'ordered' regions. The distance distribution in the partially-ordered region was wider than in the ordered region, but the most common values were both in the range of 2.6-2.8Å. The distribution in the partially-ordered region was close to a normal distribution. The distances in the ordered region are divided into two ranges, 2.7-2.8 Å and 3.0-3.2 Å, which are associated with orientations. Referring to the model, the mean of distances in the partially-ordered region is close to the spacing of plane (0 $\bar{2}$ 1) as listed in Table 7.7.

Table 7.8 Mean and standard deviation of distance in crystalline 'ordered' regions and non-crystalline 'partially-ordered'.

Region	Average of distance (Å)	StdDev of distance (Å)
Ordered	2.822	0.161
Partially-ordered	2.715	0.200
Average of both regions	2.750	0.194

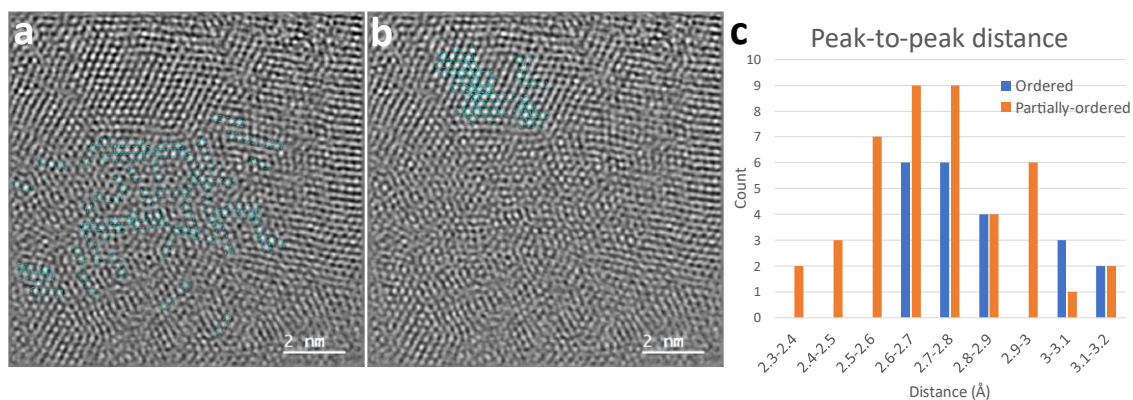


Figure 7.14 Statistics of the peak-to-peak distance in the partially-ordered and ordered features. (a) The line-profiles used to measure the peak-to-peak distance in the 'partially-ordered' region. (b) Line-profiles applied to measure peak-to-peak distance in the 'ordered' region. (c) Histograms of the peak-to-peak distances of both features in the image with colour coded. Mean of partially-ordered region was 2.7 Å, mean of ordered region was 2.8 Å.

The partially-ordered feature in Figure 7.12b-① may be similar to a liquid-crystal, which is a structure that possesses the characteristics of both a crystal and a liquid¹⁰⁸, as well as being a state distinct from crystalline and amorphous states. Liquid crystal exhibits orientational order but no positional order, which is why diffraction pattern of liquid-crystal would be arcs indicating the preferred orientation. If the feature in Figure 7.12b-① reminiscent of a liquid-crystal, the molecules could align along the viewing direction.

In Figure 7.12b-①, the material might be in the process of 'crystallizing', which means that the molecules are in the process of orienting themselves prior to forming a crystal. The image might have shown a snapshot of a pre-crystalline state, i.e., pre-order¹¹⁰ before crystallization starting. The close mean of distances in histogram also supports the supposition that the two features may be the two states in the transition process.

7.3.2 Random mixture of ordered and partially-ordered features

Among the images acquired from PET semi-crystalline specimen, Figure 7.15 contains the largest number of distinct regions showing crystalline and non-crystalline structure with diverse

periodicity. Crystalline regions are marked with black outlines as Region ① and ③; the lattice in Region ① possesses clear peaks while lattices in Figure 7.15b – Regions ③ contains only linear features, thus being labelled differently. The counterpart of Figure 7.15b is filled with the characteristic ‘peaks’ of partially-ordered structure, hence is overall labelled as Region ②.

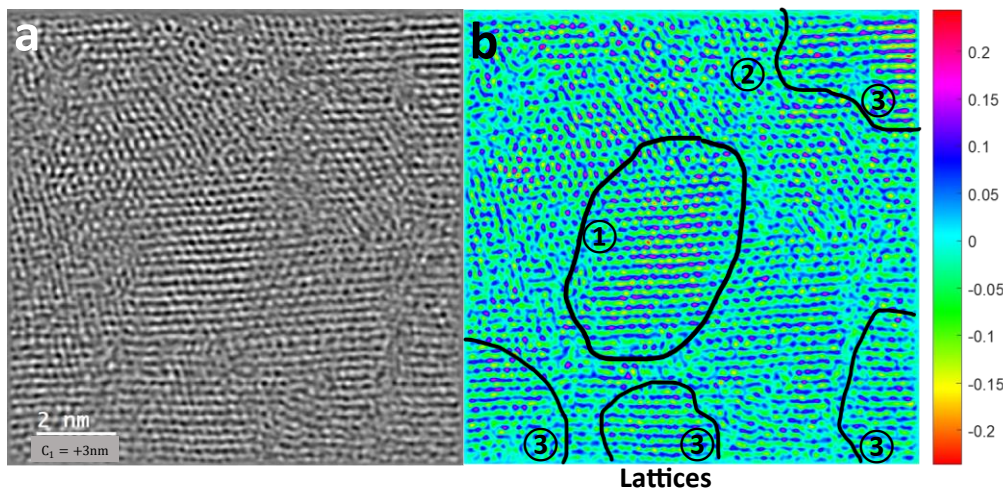


Figure 7.15 (a) Phase image of PET at $C_1=+3\text{nm}$ containing random mixture of ordered and partially-ordered features. (b) Phase image with HSV colormap that ease the identification of periodic features. ① the region containing lattice with clear peaks. ② the counterpart of the image showed characteristic peaks of partially-ordered feature that is different from crystalline and amorphous. ③ the lattices among ordered features containing only linear features without peaks.

The depth profile demonstrates the length of the molecular alignment along the viewing direction that form the peaks is around 25 nm in Figure 7.15b-②. The central grain (Figure 7.15b-①) is resolved in Figure 7.16b-e, where C_1 range from -2 to +13nm, so the thickness is around 15 nm. In Figure 7.16f, the crystalline lattices show shorter length, but the peaks of partially-ordered structure are still clearly resolved, which indicates the periodicity of the peaks are longer than the crystal thickness.

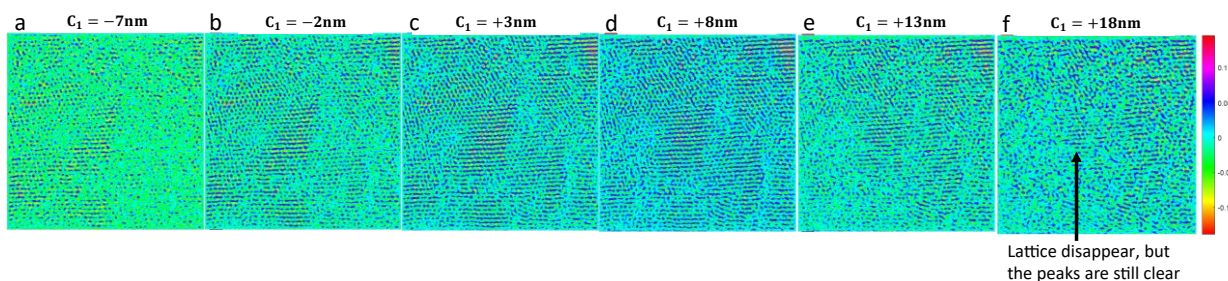


Figure 7.16 Depth profile of Figure 7.15. The partially-ordered structure remained throughout the depth profile, even while the lattice disappears at specific depth. The thickness of crystal in Region ① is around 15nm (b-e).

Because the whole image showed either the ordered or partially ordered structures, characterization of crystalline orientation in ordered regions might be particularly helpful for interpretation of the molecule orientation in the disordered region. The lattice would be analysed following the protocol developed previously – indexing the FT image to determine the orientation. The partially-ordered region would be analysed by measuring peak-to-peak distance with line-profiles.

Similarly, to the other images involving partially-ordered structure, the crystalline structure in the ordered region contained a high density of discrepancies that were found while indexing. Thus, it was hard to find a good fit in simulated DPs. The best five fits of different orientations are illustrated from Table 7.9 to Table 7.13, but large discrepancies were found in every orientation. Therefore, the orientation of the crystalline in the Figure 7.17a could not be determined.

This echoes back to the observation from the previous images: the crystalline structure in an area involving crystalline and non-crystalline structure could not be well characterized by the model. For instance, crystalline in Figure 7.11.

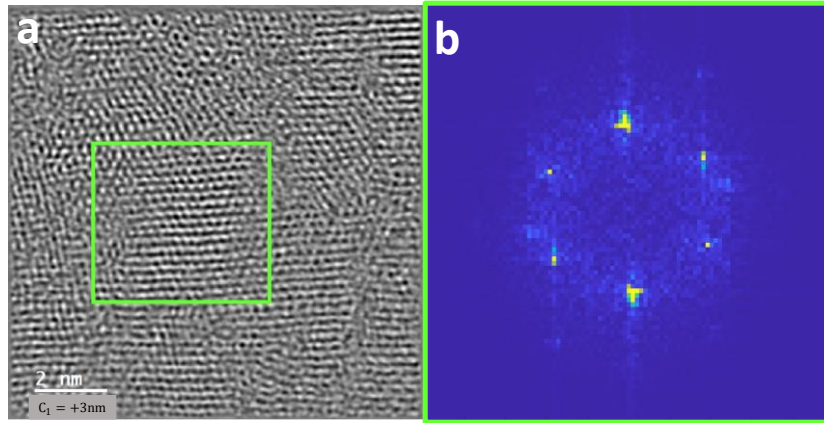


Figure 7.17 (a) Region ① in phase image at $C_1=+3\text{nm}$ highlighted the central grain. (b) FT of the ROI in a.

Table 7.9 Indexing FT in Figure 7.17b for the crystalline structure with Model¹⁸ of PET crystalline structure along $[\bar{1} \ 1 \ \bar{3}]$

Plane spacing & angle in FT		Model of PET crystalline structure along $[\bar{1} \ 1 \ \bar{3}]$				Spacing discrepancy
d_{FT}	Angle to $(\bar{1} \ 2 \ 1)$: θ	hkl	d_{mol}	Angle to $(\bar{1} \ 2 \ 1)$ model	Relative Intensity	$d_{img} - d_{mol}$
Å	°	Triclinic $P_{\bar{1}}$	Å	°	%	Å
2.49	0	$(\bar{1} \ 2 \ 1)$	2.67	0.0	8.1	-0.19
2.38	61	$(1 \ 1 \ 0)$	2.34	70.7	0.5	0.04
2.29	58	$(\bar{2} \ 1 \ 1)$	2.15	60.0	0.8	0.14
1.40	31	$(0 \ 3 \ 1)$	1.53	38.0	4.2	-0.13
1.34	31	$(\bar{3} \ 3 \ 2)$	1.37	33.6	0.3	-0.03

Table 7.10 Indexing FT in Figure 7.17b for the crystalline structure with Model¹⁸ of PET crystalline structure along $[1 \ \bar{1} \ 3]$

Plane spacing & angle in FT		Model of PET crystalline structure along $[1 \ \bar{1} \ 3]$				Spacing discrepancy
d_{FT}	Angle to $(\bar{2} \ 1 \ 1)$: θ	hkl	d_{mol}	Angle to $(\bar{2} \ 1 \ 1)$ model	Relative Intensity	$d_{img} - d_{mol}$
Å	°	Triclinic $P_{\bar{1}}$	Å	°	%	Å
2.49	0	$(\bar{2} \ 1 \ 1)$	2.15	0.0	0.8	0.34
2.38	61	$(\bar{1} \ 2 \ 1)$	2.67	60.0	8.1	-0.29
2.29	58	$(\bar{1} \ \bar{1} \ 0)$	2.34	49.3	0.5	-0.05
1.40	31	$(\bar{3} \ 3 \ 2)$	1.37	26.4	0.3	0.02
1.34	31	$(\bar{3} \ 0 \ 1)$	1.23	23.5	0.0	0.11

Table 7.11 Indexing FT in Figure 7.17b for the crystalline structure with Model¹⁸ of PET crystalline structure along [5 1 $\bar{2}$]

Plane spacing & angle in FT		Model of PET crystalline structure along [5 1 $\bar{2}$]				Spacing discrepancy
d_{FT}	Angle to ($\bar{1}$ 1 $\bar{2}$): θ	hkl	d_{mol}	Angle to ($\bar{1}$ 1 $\bar{2}$) model	Relative Intensity	$d_{img} - d_{mol}$
Å	°	Triclinic $P_{\bar{1}}$	Å	°	%	Å
2.49	0	($\bar{1}$ 1 $\bar{2}$)	2.50	0.0	1.2	-0.01
2.38	61	(0 $\bar{2}$ $\bar{1}$)	2.18	73.0	7.3	0.20
2.29	58	($\bar{1}$ 3 $\bar{1}$)	1.95	58.8	0.5	0.34
1.40	31	($\bar{1}$ $\bar{1}$ $\bar{3}$)	1.45	39.4	0.1	-0.05
1.34	31	($\bar{2}$ 4 $\bar{3}$)	1.25	33.4	0.6	0.09

Table 7.12 Indexing FT in Figure 7.17b for the crystalline structure with Model¹⁸ of PET crystalline structure along [5 7 1]

Plane spacing & angle in FT		Model of PET crystalline structure along [5 7 1]				Spacing discrepancy
d_{FT}	Angle to ($\bar{1}$ 0 5): θ	hkl	d_{mol}	Angle to ($\bar{1}$ 0 5) model	Relative Intensity	$d_{img} - d_{mol}$
Å	°	Triclinic $P_{\bar{1}}$	Å	°	%	Å
2.49	0	($\bar{1}$ 0 5)	2.11	0.0	24.4	0.37
2.38	61	($\bar{2}$ 1 3)	2.21	51.2	0.1	0.17
2.29	58	(1 $\bar{1}$ 2)	2.50	61.9	1.2	-0.21
1.40	31	($\bar{3}$ 1 8)	1.20	25.0	0.0	0.20
1.34	31	(0 $\bar{1}$ 7)	1.33	28.1	1.8	0.01

Table 7.13 Indexing FT in Figure 7.17b for the crystalline structure with Model¹⁸ of PET crystalline structure along [1 $\bar{3}$ $\bar{2}$]

Plane spacing & angle in FT		Model of PET crystalline structure along [1 $\bar{3}$ $\bar{2}$]				Spacing discrepancy
d_{FT}	Angle to ($\bar{1}$ 1 $\bar{2}$): θ	hkl	d_{mol}	Angle to ($\bar{1}$ 1 $\bar{2}$) model	Relative Intensity	$d_{img} - d_{mol}$
Å	°	Triclinic $P_{\bar{1}}$	Å	°	%	Å
2.49	0	($\bar{1}$ 1 $\bar{2}$)	2.50	0.0	1.2	-0.01
2.38	61	($\bar{1}$ $\bar{1}$ 1)	2.69	63.4	0.9	-0.31
2.29	58	(0 2 $\bar{3}$)	2.46	54.8	1.5	-0.17
1.40	31	($\bar{2}$ 0 $\bar{1}$)	1.52	30.4	0.0	-0.13
1.34	31	($\bar{1}$ 3 $\bar{5}$)	1.40	27.6	1.9	-0.05

The peak-to-peak distance of ‘partially-ordered’ feature in Figure 7.15b-② is compared with the ‘ordered’ feature in Region ①, which contains clear peaks. As shown in Figure 7.18c, the histograms of distances for ‘partially-ordered’ and ‘ordered’ features are both normal

distribution and highly overlap. The 'Average of distance' of both regions are around 2.8 Å. But the distribution of distance in Region ① is narrower the mean slightly shifted to left, which imply the molecules in ordered structure are more close-packed.

The PET molecules in this image might be in the transient state from amorphous to crystalline, which could explain the difficulty of fitting the FT pattern of crystalline region to any of the simulated DP. Also because of the 'transiant state', the mean of peak-to-peak distance in crystalline and non-crystalline region were both around 2.8 Å, and similar to the mean of 'partially-ordered' non-crystalline feature in other images.

Table 7.14 Mean and standard deviation of distance in non-crystalline and crystalline regions in Figure 7.18.

Region	Average of distance (Å)	StdDev of distance (Å)
Partially-ordered	2.842	0.214
Ordered	2.808	0.149
Average of both regions	2.829	0.191

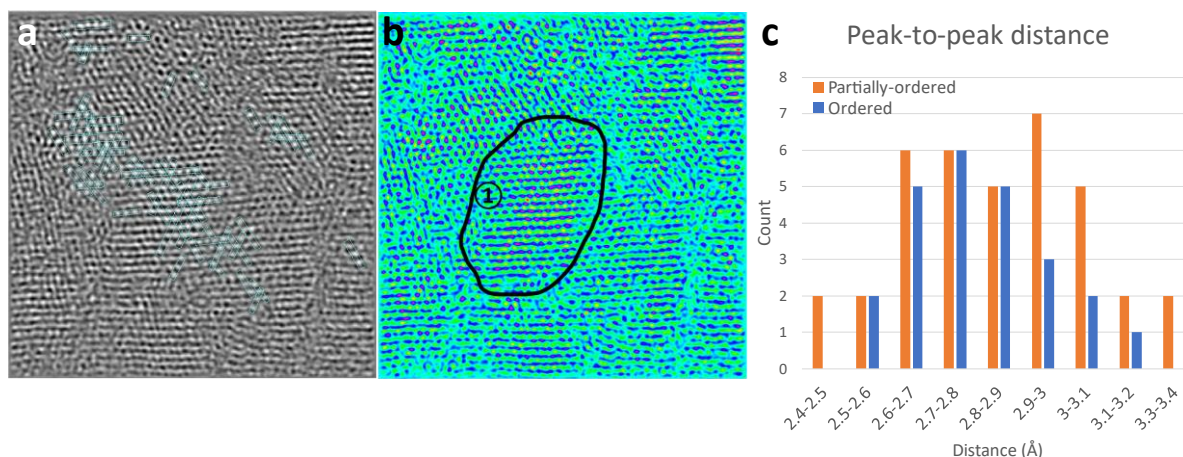


Figure 7.18 (a) Line-profiles applied to measure the peak-to-peak distance in the Region ① and ② of Figure 7.15b. (b) The central grain is the 'ordered' region, and Region ② of the image is the 'partially-ordered' region. (c) To characterize the distances measured from the image, distance measured in ordered and partially-ordered features were colour coded in the histogram.

7.4 Discussion about the newly found disordered feature in PET images

7.4.1 Summary of distances of partially-ordered features

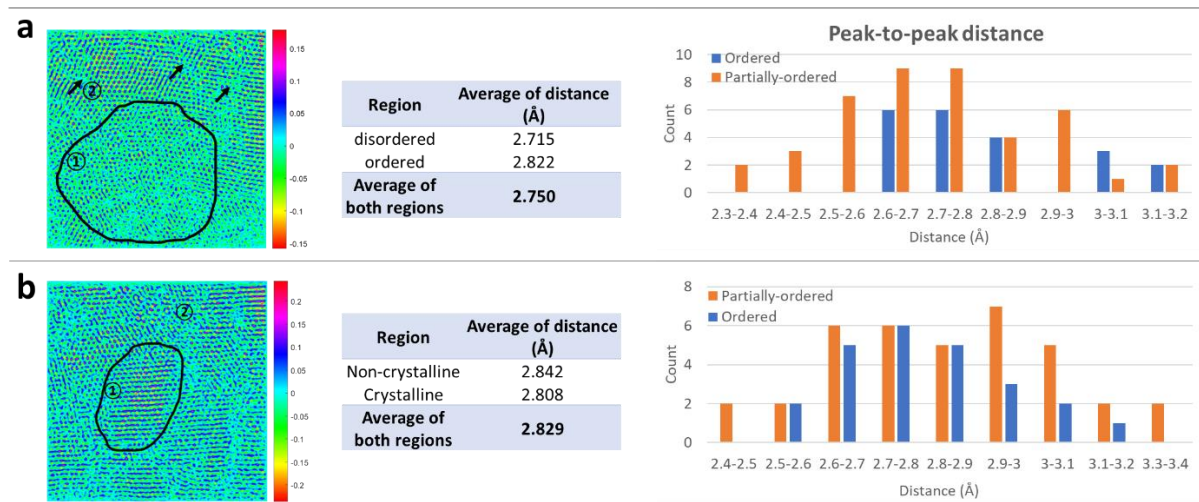


Figure 7.19 Images involving partially-ordered feature.

In these images (Figure 7.19), the peak-to-peak distances of the partially-ordered features share the character of normal distribution, and the value of 'Average of distance' are all around 2.8Å.

For the images of Figure 7.19(a) and (b), the impact from the partially-ordered feature on the ordered feature is visible in the histogram and value of mean. The histograms of distances from ordered features highly overlap with those from partially-ordered features and share the mean of 2.8Å. Therefore, the ordered feature in Figure 7.19(a) and (b) might not be crystalline structure, because they cannot be interpreted by the model¹⁸, and it has been verified the crystalline structure in PET images match very well with the model. Therefore, these two images support the assumption that the partially-ordered features represent a transition state of molecule orientating before crystallization process.

Assuming the molecules in partially-ordered features are aligned to viewing direction, and peak-to-peak distance represents intermolecular distance, the intermolecular distances from different regions of PET specimen are consistently smaller than that in the model¹⁸.

7.4.2 Intermolecular distance measured from crystalline model

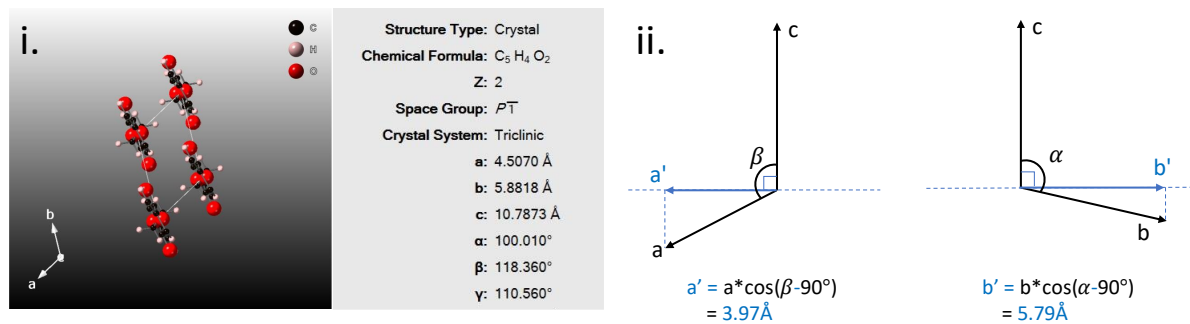


Figure 7.20 Intermolecular distance in unit cell of PET crystal. (i) Unit cell of PET crystalline model¹⁸ and the cell parameters. (ii) Projection of a and b when c -axis parallel to viewed direction. Length of the projections $a'=3.97 \text{ \AA}$ and $b'=5.97 \text{ \AA}$, which are supposed to be the minimum distance between molecules if c -axis pointed along viewed direction and the molecular conformation was the same as predicted by this model.

According to the unit cell parameters in the model built by Fu *et al.*¹⁸, the projection of a and b onto the plane perpendicular to c are the corresponding intermolecular distances when the molecular pointing out, i.e., c -axis parallel to viewing direction. Projection of a noted as a' is equal to 3.97 \AA , and projection of b noted as b' is 5.97 \AA (Figure 7.20), which are thought of as the minimum distances between molecules if c -axis was parallel to viewing direction and the molecular conformation was the same as predicted by this model. The crystalline structure is the most compact way molecules 'settle' in a periodic structure when energy level is low for the molecular conformation and intermolecular interaction.

The model¹⁸ was constructed with the sample annealed and released strain in solid state - fibre, whereas the specimen fabricated in this work was thin film cast from diluted solution. Molecular conformations in specimens prepared using these two sample preparation methods may differ.

Due to the consistency of peak-to-peak distance measured as 2.8\AA from the partially-ordered features, which is much smaller but not far from half of 3.97 and 5.97\AA . It suggests the best explanation for this would be there might be rotational symmetry along the molecular axis, and the atoms in the side groups stacked on one another and aligned to the molecular backbones between molecules.

7.5 Conclusion of PET images analysis

In this chapter, images of the PET semi-crystalline specimens revealed a variety of structures, using techniques of STEM ptychography and optical sectioning. In addition to the fully crystalline 'ordered' structure, a type of 'partially-ordered' structure, distinct from either crystalline or amorphous, was discovered for the first time.

In the partially-ordered regions, there are clear 'peaks' suggesting molecular alignment along the viewing direction for $20\text{-}30\text{nm}$, but only random short-range periodicity in the lateral dimension, which is in some respects reminiscent of a 'liquid crystal' structure. The PET molecules possess intrinsic periodicity along the molecular axis, hence the 'peaks' could be molecules aligned to the viewing direction, and the peak-to-peak distance represents intermolecular distance.

Theoretically, the intermolecular distance obtained from the close-packed van de Waals radius of atoms should be the smallest distance, and intermolecular distance should be smallest in crystalline status. Across all partially-ordered features from multiple images, the average peak-to-peak distance is consistently around 2.8\AA , which is much smaller but not far from half of the intermolecular distance in crystalline model. The newly developed sample preparation methods may result in a change in molecular conformation. Assuming the molecules of the partially-

ordered feature are aligned with the viewing direction, there may be rotational symmetry along the molecular axis and the stacked atoms of side groups could form some of the peaks.

The ordered features in PET images can be either crystalline or non-crystalline structure based on their connection with the partially-ordered features. Part of the crystalline structures in the ordered region can be well interpreted with PET model constructed from empirical diffraction data, especially the grains in images without partially-ordered features. These ordered features should be crystalline in nature.

Nevertheless, some ordered structures in images involving partially-ordered features show considerable discrepancies to the model, which indicates its significant structural difference with the presence of these partially-ordered features. These ordered features showed a high degree of overlap in peak-to-peak distances and shared a mean of 2.8\AA with the partially ordered features. These ordered features appear to be a form of more closely packed molecules of the partially ordered features. This suggests that these ordered features might be in a 'pre-crystalline' state, and together with the junctional partially-ordered feature, a "snapshot" of the transition status has been obtained.

Therefore, the PET images involving the partially-ordered features might reveal pre-order of molecules before the procedure of crystallization, and there is rotational symmetry along the molecular axis. A new model could offer evidence and enhance the understanding of polymer crystallization mechanism.

8 Conclusions and future work

My DPhil project has achieved the initial research goal of obtaining high-resolution ($<2\text{\AA}$) images of polymer materials and revealing the conformation details of their crystalline structures. The methodology for observing molecular conformation in polymer crystals has been developed, providing a foundation for analysing organic materials with STEM imaging.

8.1 Contribution to the field

8.1.1 New experimental methodology

A valid sample preparation method has been developed to produce high quality polymer thin film specimens. Specimens with consistent quality can be achieved, for instance, the thickness is maintained around 50 to 100nm (Section 3.1.2), using a water-soluble substrate for sample casting and annealing.

Better understanding of the beam damage in PEN has been achieved by studying the change of diffraction pattern versus accumulated illumination dose. The damage process of PEN in TEM diffraction mode has been described using a model consisting of 'latency followed by exponential decay'.

Using the study of the beam damaging behaviour of PEN, the microscope conditions applied to acquire data from polymer specimens were designed to take advantage of the latency. Firstly, the dose of illumination should be enough to generate sufficient intensity on the detector with a sufficient signal to noise ratio in the image. Secondly, the dose should be low enough so that the data can be acquired before the structure is altered. The experiment ended with a viable condition with dosage within a critical dose for STEM ptychography imaging, which was found to be higher than in TEM diffraction mode.

8.1.2 New science

STEM ptychography with controlled dosage was successfully used to acquire images of high resolution and contrast from PEN and PET samples. Besides identifying the crystal phase, the local molecular conformational structure within the crystals can also be analysed. Since this type of data is available for the first time, a methodology for analysis is required.

Comparing to the empirical diffraction data which is generated from average structural information and the model built from the diffraction data, a discrepancy was found in PEN crystals. The crystal structure in PEN image broadly fits with β -form monoclinic unit cell with spacing of the strong plane (200) slightly smaller than the model. However, additional features were resolved in the (200) as weaker features between the strong (200) repeats. It is suggested that the 'additional features' between the primary (200) planes in the PEN experimental images might be generated from rotation of chemical segments in molecules, which create features half-way between the strong (200) repeats. The resolved discrepancy in the image could provide a starting point for studying the local molecular structure of polymer crystallinity.

An intrinsic capability of ptychography, optical sectioning was applied to the PEN image analysis and enabled the discovery of structural features along the viewing direction. For instance, resolving multiple grains with various relative orientations, internal local plane tiling, and separating overlapping lattices forming moiré fringes.

Equipped with the imaging and analysis methodologies established, a type of new feature was discovered in PET specimens. Besides the crystalline structure, several regions involving molecules pointing along the viewing direction, appeared to be in the transitional procedure of "ordering" before full crystalline order was resolved in semi-crystalline PET specimens. This

novel discovery of molecule pre-ordering before crystallization is empowered by the newly established sample preparation, imaging, and structural analysis methodologies.

8.2 Future work and potential application

8.2.1 Future work suggestions

According to the discrepancies found in high resolution images compared to the model built from empirical diffraction data, a modified model can be constructed. In PEN crystals, the details resolved within and between the strong plane (200) repeats indicate a new model of β -form crystalline structure with monoclinic unit cell. Therefore, the study on influence of crystallization conditions to the molecular conformation in crystalline structure is possible.

The pre-ordering feature in PET was directly imaged for the first time in polymers. Modelling this type of structure would be useful to understand the complete procedure and underlying mechanisms of polymer crystallization, which will solve the long-standing mystery. More factors that may influence polymer crystallization can be characterized, for example, the differences based on different thermal or strain histories of the specimen, further analysis of the interactions of one crystal with another, and interaction of materials in blend of copolymers.

In terms characterization methods, tomography can be tried on thicker specimens, and cryo-EM for more beam sensitive polymers.

8.2.2 Potential application proposal

Since the entire analysis process is a coding base, it can readily be transformed into software once a user interface has been developed. The whole set of tools would facilitate the analysis

of organic crystalline structure with data acquired by STEM ptychography, including polymers and other organic molecules.

In terms of potential applications of the methodology established in this thesis, functional polymers are widely used in the electronics industry. Understanding the relationship between local crystalline structure and material properties can potentially assist in optimizing the fabrication process and leveraging the material hence device performance.

In addition, the pharmaceutical industry is another niche field that uses a lot of organic materials and pays attention to their molecular structure. The imaging method for beam sensitive materials would enable the acquisition of high-resolution images from molecule medicines and organic samples that would assist in the development of new medicines.

Reference

1. French, A. D. & Gardner, K. H. *Fibre diffraction methods*. (American Chemical Society, 1980).
2. Nellist, P. D., McCallum, B. C. & Rodenburg, J. M. Resolution beyond the 'information limit' in transmission electron microscopy. *Nature* **374**, 630–632 (1995).
3. Egerton, R. F. Radiation damage to organic and inorganic specimens in the TEM. *Micron* **119**, 72–87 (2019).
4. Yang, H. *et al.* Simultaneous atomic-resolution electron ptychography and Z-contrast imaging of light and heavy elements in complex nanostructures. *Nat. Commun.* **7**, 12532 (2016).
5. Yang, H., Pennycook, T. J. & Nellist, P. D. Efficient phase contrast imaging in STEM using a pixelated detector. Part II: Optimisation of imaging conditions. *Ultramicroscopy* **151**, 232–239 (2015).
6. Young, R. J. *Introduction to polymers*. *Polymer International* **27**, (CRC PRESS, 1987).
7. Mencik, Z. Crystal structure of polycondensate of naphthalene-2,6-dicarboxylic acid with ethylene glycol. *Chem. Prum.* **17**, 78 (1967).
8. Buchner, S., Wiswe, D. & Zachmann, H. Kinetics of crystallization and melting behaviour of poly(ethylene naphthalene-2,6-dicarboxylate). *Polymer (Guildf)*. **30**, 480–488 (1989).
9. Liu, J. *et al.* Crystal Structures and Morphology of Thin-Film, Melt-Crystallized, and Polymerized Poly(ethylene Naphthalate). *J. Macromol. Sci. Part B Phys.* **37**, 567–586 (1998).
10. Van Den Heuvel, C. J. M. & Klop, E. A. Relations between spinning, molecular structure and end-use properties of polyethylene naphthalate tyre yarns. *Polymer (Guildf)*. **41**, 4249–4266 (2000).
11. Plummer, C. J. G. High resolution electron microscopy of β -poly(ethylene naphthoate). *Macromol. Rapid Commun.* **20**, 157–161 (1999).
12. Astbury, W. T. & Brown, C. J. Structure of Terylene. *Nature* **158**, 871 (1946).
13. Daubeny, P., Bunn, C. W. & Brown, C. J. The Crystal Structure of Polyethylene Terephthalate. *Source Proc. R. Soc. London. Ser. A, Math. Phys. Sci. Proc. R. Soc. London. Ser. A* **226**, 531–542 (1954).
14. Fakirov, S., Fischer, E. W. & Schmidt, G. F. Unit cell dimensions of polyethylene terephthalate. *Die Makromol. Chemie* **176**, 2459–2465 (1975).
15. Kitano, Y., Kinoshita, Y. & Ashida, T. Morphology and crystal structure of an a axis oriented, highly crystalline poly(ethylene terephthalate). *Polymer (Guildf)*. **36**, 1947–1955 (1995).
16. Sun, T., Zhang, A., Li, F. M. & Porter, R. S. Crystal lattice deformation and the mesophase in poly(ethylene terephthalate) uniaxially drawn by solid-state coextrusion. *Polymer (Guildf)*. **29**, 2115–2120 (1988).

17. Zhang, A., Jiang, H., Wu, Z., Wu, C. & Qian, B. Internal stress, lattice deformation, and modulus of polymers. *J. Appl. Polym. Sci.* **42**, 1779–1791 (1991).
18. Fu, Y., Busing, W. R., Jin, Y., Affholter, K. A. & Wunderlich, B. Poly(ethylene terephthalate) Fibres. 1. Crystal Structure and Morphology Studies with Full-Pattern X-ray Diffraction Refinement. *Macromolecules* **26**, 2187–2193 (1993).
19. Fu, Y., Annis, B., Boller, A., Jin, Y. & Wunderlich, B. Analysis of structure and properties of poly(ethylene terephthalate) fibres. *J. Polym. Sci. Part B Polym. Phys.* **32**, 2289–2306 (1994).
20. Tomashpol'skii, Y. Y. & Markova, G. S. An electron diffraction study of the crystalline structure of polyethylene terephthalate by means of the Fourier synthesis. *Polym. Sci. U.S.S.R.* **6**, 316–324 (1964).
21. Wakelyn, N. T. Observations from an X-ray diffraction study of poly(ethylene terephthalate) film and fibre. *Journal of Applied Polymer Science* **28**, 3599–3602 (1983).
22. Yuhiko, Y. Single crystal of poly (ethylene terephthalate). *J. Polym. Sci. Part A* **3**, 81–92 (1965).
23. Liu, J. & Geil, P. H. Crystal structure and morphology of poly(ethylene terephthalate) single crystals prepared by melt polymerization. *J. Macromol. Sci. Part B Phys.* **36**, 61–85 (1997).
24. Yoshioka, T. *et al.* Morphological study by TEM on uniaxially oriented thin films of PET, PEN and their blends. *Polymer (Guildf)*. **46**, 4987–4990 (2005).
25. Grubb, D. T. Radiation damage and electron microscopy of organic polymers. *J. Mater. Sci.* **9**, 1715–1736 (1974).
26. Yeh, G. S. Y. Order in Amorphous Polystyrenes as Revealed by Electron Diffraction and Diffraction Microscopy. *J. Macromol. Sci. Part B* **6**, 451–463 (1972).
27. Charlesby, A. *Atomic radiation and polymers*. (Elsevier, 1960). doi:10.1016/c2013-0-07861-9
28. Franck, J. & Rabinowitsch, E. Some remarks about free radicals and the photochemistry of solutions. *Trans. Faraday Soc.* **30**, 120–130 (1934).
29. *The Radiation Chemistry of Macromolecules*. (Elsevier, 1973). doi:10.1016/b978-0-12-219801-4.x5001-0
30. Alexander, P. & Charlesby, A. Energy transfer in macromolecules exposed to ionizing radiations. *Nature* **173**, 578–579 (1954).
31. Partridge, R. H. Excitation energy transfer in alkanes. I. Exciton model. *J. Chem. Phys.* **52**, 2485–2490 (1970).
32. Alexander, P., Hamilton, L. D. G. & Stacey, K. A. Disorganization of the secondary structure in proteins exposed to ionizing radiations in the solid state. *Nature* **184**, 226–228 (1959).
33. Grubb, D. T. & Groves, G. W. Rate of damage of polymer crystals in the electron microscope: Dependence on temperature and beam voltage. *Philos. Mag.* **24**, 815–828 (1971).

34. Gejvall, T. & Löfroth, G. Radiation Effects Radiation induced degradation of some crystalline amino acids RADIATION INDUCED DEGRADATION OF SOME CRYSTALLINE AMINO ACIDS. **25**, 187–190 (1975).
35. S'Ari, M. *et al.* Toward Developing a Predictive Approach to Assess Electron Beam Instability during Transmission Electron Microscopy of Drug Molecules. *Molecular Pharmaceutics* (2018). doi:10.1021/acs.molpharmaceut.8b00693
36. Henderson, R. The Potential and Limitations of Neutrons, Electrons and X-Rays for Atomic Resolution Microscopy of Unstained Biological Molecules. *Q. Rev. Biophys.* **28**, 171–193 (1995).
37. Giorgio, S. & Kern, R. High-resolution electron microscopy of polyethylene and paraffin crystals: Stability in the electron beam. *J. Polym. Sci. Polym. Phys. Ed.* **22**, 1931–1951 (1984).
38. Giorgio, S. & Kern, R. DEFECTS IN A LAMELLAR POLYMER BY HIGH-RESOLUTION ELECTRON MICROSCOPY. *Ultramicroscopy* **21**, 157–170 (1987).
39. Glaeser, R. M. Limitations to significant information in biological electron microscopy as a result of radiation damage. *J. Ultrastructure Res.* **36**, 466–482 (1971).
40. Kumar, S. & Adams, W. W. Electron beam damage in high temperature polymers. *Polymer (Guildf)*. **31**, 15–19 (1990).
41. Martin, D. C., Chen, J., Yang, J., Drummy, L. F. & Kübel, C. High resolution electron microscopy of ordered polymers and organic molecular crystals: Recent developments and future possibilities. *J. Polym. Sci. Part B Polym. Phys.* **43**, 1749–1778 (2005).
42. Leijten, Z. J. W. A., Keizer, A. D. A., de With, G. & Friedrich, H. Quantitative Analysis of Electron Beam Damage in Organic Thin Films. *J. Phys. Chem. C* **121**, 10552–10561 (2017).
43. Egerton, R. F., Lazar, S. & Libera, M. Delocalized radiation damage in polymers. *Micron* **43**, 2–7 (2012).
44. Egerton, R. F. Mechanisms of radiation damage in beam-sensitive specimens, for TEM accelerating voltages between 10 and 300 kV. *Microsc. Res. Tech.* **75**, 1550–1556 (2012).
45. Kirkland, A. I., Chang, S. L. & Hutchison, J. L. 1. Atomic Resolution Transmission Electron Microscopy. in *Handbook of Microscopy* 3–47 (2019).
46. Huang, C. Ultra High Resolution Imaging of Radiation-Sensitive Materials. (University of Oxford, 2016).
47. DOBB, M. G., HINDELEH, A. M., JOHNSON, D. J. & SAVILLE, B. P. Lattice resolution in an electron-beam sensitive polymer. *Nature* **253**, 189–190 (1975).
48. Dobb, M. G., Johnson, D. J. & Saville, B. P. Direct observation of structure in high-modulus aromatic fibres. *J. Polym. Sci. Polym. Symp.* **58**, 237–251 (1977).
49. Galiotis, C. *et al.* High-modulus polydiacetylene single-crystal fibres. *J. Polym. Sci. Polym. Phys. Ed.* **22**, 1589–1606 (1984).
50. Chanzy, H., Folda, T., Smith, P., Gardner, K. & Revol, J.-F. Lattice imaging in polytetrafluoroethylene single crystals. *J. Mater. Sci. Lett.* **5**, 1045–1047 (1986).

51. Revol, J.-F. & Manley, R. S. J. Lattice imaging in polyethylene single crystals. *J. Mater. Sci. Lett.* **5**, 249–251 (1986).
52. Uemura, A., Tsuji, M., Kawaguchi, A. & Katayama, K. I. High-resolution electron microscopy of solution-grown crystals of poly(p-phenylene sulphide). *J. Mater. Sci.* **23**, 1506–1509 (1988).
53. Tsuji, M., Isoda, S., Ohara, M., Kawaguchi, A. & Katayama, K. Direct imaging of molecular chains in a poly(p-xylylene) single crystal. *Polymer (Guildf)*. **23**, 1568–1574 (1982).
54. Tsuji, M., Roy, S. K. & Manley, R. S. J. Direct lattice imaging in single crystals of isotactic polystyrene. *Polymer (Guildf)*. **25**, 1573–1576 (1984).
55. Isoda, S., Tsuji, M., Ohara, M., Kawaguchi, A. & Katayama, K. Structural analysis of β -form poly(p-xylylene) starting from a high-resolution image. *Polymer (Guildf)*. **24**, 1155–1161 (1983).
56. Young, R. J. & Yeung, P. H. J. Molecular detail in electron micrographs of polymer crystals. *J. Mater. Sci. Lett.* **4**, 1327–1330 (1985).
57. Yeung, P. H. J. & Young, R. J. Direct imaging of molecules in polydiacetylene single crystals. *Polymer (Guildf)*. **27**, 202–210 (1986).
58. Apgar, P. A. & Yee, K. C. Poly[1,6-di(*N*-carbazolyl)-2,4-hexadiyne]. *Acta Crystallogr. Sect. B Struct. Crystallogr. Cryst. Chem.* **34**, 957–959 (1978).
59. Enkelmann, V., Leyrer, R. J., Schleier, G. & Wegner, G. Macroscopic single crystals of polymers by solid-state polymerization: a study of the monomer to polymer phase transformation of 1,6-dicarbazolyl hexadiyne. *J. Mater. Sci.* **15**, 168–176 (1980).
60. Blundell, D. J. & Keller, A. Nature of Self-Seeding Polyethylene Crystal Nuclei. *J. Macromol. Sci. Part B* **2**, 301–336 (1968).
61. Bunn, C. W. & Howells, E. R. Structures of molecules and crystals of fluoro-carbons. *Nature* (1954). doi:10.1038/174549a0
62. Tabor, B. J., Magré, E. P. & Boon, J. The crystal structure of poly-p-phenylene sulphide. *Eur. Polym. J.* **7**, 1127–1133 (1971).
63. Iwamoto, R. & Wunderlich, B. Crystal structure of poly-p-xylylene. I. The α form. *J. Polym. Sci. Part A-2 Polym. Phys.* **11**, 2403–2411 (1973).
64. Niegisch, W. D. & Iegiscii, W. D. N. Crystallography of Poly-p-Xylylene. *J. Appl. Phys.* **37**, (1966).
65. KLUG, A. & DE ROSIER, D. J. Optical Filtering of Electron Micrographs: Reconstruction of One-Sided Images. *Nature* **212**, 29–32 (1966).
66. Smith, D. J. & Fryer, J. R. Molecular detail in electron micrographs of quaterrylene C₄₀H₂₀. *Nature* **291**, 481–482 (1981).
67. Williams, D. B. (David B. & Carter, C. B. *Transmission electron microscopy : a textbook for materials science*. (Springer, 2009).
68. Stejny, J., Dlugosz, J. & Keller, A. Electron microscope diffraction characterization of the fibrous structure of poly(sulphur nitride) crystals. *J. Mater. Sci.* **14**, 1291–1300

- (1979).
69. Kawaguchi, A., Isoda, S., Petermann, J. & Katayama, K. High resolution electron microscopy of (SN)x. *Colloid Polym. Sci.* **262**, 429–434 (1984).
 70. Sugiyama, J., Harada, H., Fujiyoshi, Y. & Uyeda, N. Lattice images from ultrathin sections of cellulose microfibrils in the cell wall of *Valonia macrophysa* Kutz. *Planta* **166**, 161–168 (1985).
 71. Zhou, X., Marks, T. J. & Carr, S. H. Direct Imaging of The Lattice In Poly(Phthalocyaninato-Germoxane) Single Crystals. *Mol. Cryst. Liq. Cryst.* **118**, 357–360 (1985).
 72. Nellist, P. D. 2. Scanning Transmission Electron Microscopy. in *Handbook of Microscopy* (eds. Pennycook, S. J. & Nellist, P. D.) 49–99 (Springer New York, 2019). doi:10.1007/978-1-4419-7200-2
 73. Pennycook, S. J. & Nellist, P. D. *Scanning Transmission Electron Microscopy: Imaging and Analysis*. (Springer, 2011). doi:10.100/978-1-4419-7-200-2
 74. Nellist, P. D. The Principles of STEM Imaging. in *Scanning Transmission Electron Microscopy* 91–115 (Springer New York, 2011). doi:10.1007/978-1-4419-7200-2_2
 75. Rothmann, M. U. *et al.* Atomic-scale microstructure of metal halide perovskite. *Science (80-.)*. **370**, (2020).
 76. Rodenburg, J. M. M., McCallum, B. C. C. & Nellist, P. D. D. Experimental tests on double-resolution coherent imaging via STEM. *Ultramicroscopy* **48**, 304–314 (1993).
 77. Rodenburg, J. M.; Bates, R. H. T. The theory of super-resolution electron microscopy via Wigner-distribution deconvolution. *Philos. Trans. R. Soc. London. Ser. A Phys. Eng. Sci.* **339**, 521–553 (1992).
 78. Pennycook, T. J., Martinez, G. T., Nellist, P. D. & Meyer, J. C. High dose efficiency atomic resolution imaging via electron ptychography. *Ultramicroscopy* **196**, 131–135 (2019).
 79. Rodenburg, J. M. & Faulkner, H. M. L. A phase retrieval algorithm for shifting illumination. *Appl. Phys. Lett.* **85**, 4795–4797 (2004).
 80. Humphry, M. J., Kraus, B., Hurst, A. C., Maiden, A. M. & Rodenburg, J. M. Ptychographic electron microscopy using high-angle dark-field scattering for sub-nanometre resolution imaging. *Nat. Commun.* **2012 31 3**, 1–7 (2012).
 81. Maiden, A. M. & Rodenburg, J. M. An improved ptychographical phase retrieval algorithm for diffractive imaging. *Ultramicroscopy* **109**, 1256–1262 (2009).
 82. O’Leary, C. M. *et al.* Phase reconstruction using fast binary 4D STEM data. *Appl. Phys. Lett.* **116**, 124101 (2020).
 83. O’Leary, C. M. *et al.* Contrast transfer and noise considerations in focused-probe electron ptychography. *Ultramicroscopy* **221**, 113189 (2021).
 84. Rose, H. Phase Contrast in Scanning Transmission Electron Microscopy. *Optik (Jena)* **39**, 416–436 (1974).
 85. Dekkers, N. H. & de Lang, H. Differential Phase Contrast in a Stem. *Opt.* **41**, 452–456

(1974).

86. Shibata, N. *et al.* Direct Visualization of Local Electromagnetic Field Structures by Scanning Transmission Electron Microscopy. *Acc. Chem. Res.* **50**, 1502–1512 (2017).
87. Yang, H., Ercius, P., Nellist, P. D. & Ophus, C. Enhanced phase contrast transfer using ptychography combined with a pre-specimen phase plate in a scanning transmission electron microscope. *Ultramicroscopy* **171**, 117–125 (2016).
88. Song, J. *et al.* Atomic Resolution Defocused Electron Ptychography at Low Dose with a Fast, Direct Electron Detector. *Sci. Reports 2019 91* **9**, 1–8 (2019).
89. Lozano, J. G., Martinez, G. T., Jin, L., Nellist, P. D. & Bruce, P. G. Low-Dose Aberration-Free Imaging of Li-Rich Cathode Materials at Various States of Charge Using Electron Ptychography. *Nano Lett.* **18**, 6850–6855 (2018).
90. Nellist, P. D. *et al.* (Invited) Imaging light elements in beam sensitive materials using electron ptychography. in
91. Shinotsuka, K. Crystallization in Thin Films of Polyesters and Copolyesters. (University of Oxford, 2009).
92. Chen, B. T. Investigation of the solvent evaporation effect on spin coating of thin films. *Polym. Eng. Sci.* **23**, 399–403 (1983).
93. Walsh, C. B. & Franses, E. I. Thickness and quality of spin-coated polymer films by two-angle ellipsometry. *Thin Solid Films* **347**, 167–177 (1999).
94. Miyata, K., Kikutani, T. & Okui, N. Fibre structure formation in ultra-high-speed melt spinning of poly(ethylene 2,6-naphthalene dicarboxylate). *J. Appl. Polym. Sci.* **65**, 1415–1427 (1997).
95. Tsuji, M., Novillo, F. A., Fujita, M., Murakami, S. & Kohjiya, S. Morphology of melt-crystallized poly(ethylene 2,6-naphthalate) thin films studied by transmission electron microscopy. *J. Mater. Res.* **14**, 251 (1998).
96. Williams, D. B. & Carter, C. B. Amplitude Contrast. in *Transmission Electron Microscopy* 371–388 (Springer US, 2009). doi:10.1007/978-0-387-76501-3_22
97. Jones, L., Varambhia, A., Sawada, H. & Nellist, P. D. An optical configuration for fastidious STEM detector calibration and the effect of the objective-lens pre-field. *J. Microsc.* **270**, 176–187 (2018).
98. Conchello, J.-A. & Lichtman, J. W. Optical sectioning microscopy. *Nat. Methods 2005 212* **2**, 920–931 (2005).
99. Cosgriff, E. C. & Nellist, P. D. A Bloch wave analysis of optical sectioning in aberration-corrected STEM. *Ultramicroscopy* **107**, 626–634 (2007).
100. Cosgriff, E. C. *et al.* Three-dimensional imaging using aberration-corrected scanning transmission and confocal electron microscopy. *J. Phys. Conf. Ser.* **126**, (2008).
101. Siegel, G. *Der Einfluß tiefer Temperaturen auf die Strahlenschädigung von organischen Kristallen durch 100 keV-Elektronen.* *Z. Naturforsch* **27**, (1972).
102. Egerton, R. F., Crozier, P. A. & Rice, P. Electron energy-loss spectroscopy and chemical change. *Ultramicroscopy* **23**, 305–312 (1987).

103. Jones, L. *et al.* Managing dose-, damage- and data-rates in multi-frame spectrum-imaging. *Microscopy* **67**, i98–i113 (2018).
104. Ilett, M., Brydson, R., Brown, A. & Hondow, N. Cryo-analytical STEM of frozen, aqueous dispersions of nanoparticles. *Micron* **120**, 35–42 (2019).
105. Wu, G., Li, Q. & Cuculo, J. A. Fibre structure and properties of poly(ethylene-2,6-naphthalate) obtained by high-speed melt spinning. *Polymer (Guildf)*. **41**, 8139–8150 (2000).
106. Li, C. Y. *et al.* Double-twisted helical lamellar crystals in a synthetic main-chain chiral polyester similar to biological polymers. *Macromolecules* **32**, 524–527 (1999).
107. Li, C. Y. *et al.* Double twist in helical polymer “soft” crystals. *Phys. Rev. Lett.* **83**, 4558–4561 (1999).
108. Andrienko, D. Introduction to liquid crystals. *J. Mol. Liq.* **267**, 520–541 (2018).
109. Wurm, A., Soliman, R., Goossens, J. G. P., Bras, W. & Schick, C. Evidence of pre-crystalline-order in super-cooled polymer melts revealed from simultaneous dielectric spectroscopy and SAXS. *J. Non. Cryst. Solids* **351**, 2773–2779 (2005).
110. Jin, F. *et al.* Polymer Chains Fold Prior to Crystallization. *ACS Macro Lett.* **11**, 284–288 (2022).